The development of experimental and analytical techniques for the study of aligned fluorophores

by

Alan Matheson Wemyss

A thesis submitted in partial fulfilment of the requirements of the degree of Doctor of Philosophy in Mathematical Biology with Biophysical Chemistry

MOAC Doctoral Training Centre, University of Warwick

December, 2016

Contents

List of Figures

List of Tables

Acknowledgements

I would like to thank my chemistry supervisor, Professor Alison Rodger, for all of her support, advice and optimism during this project, as well as Dr Nikola Chmel for his help throughout. I would also like to thank my supervisor in life sciences, Dr David Roper, for his advice in molecular biology.

Thank you to everyone at the MOAC doctoral training centre, especially Sarah Shute, Naomi Grew and Anne Maynard, for organising so many great seminars and departmental conferences. I would also like to thank all of my colleagues in biophysical chemistry and life sciences. In particular Dr Claire Broughton and Dr Joe Jones for so many helpful discussions, and most of all, for their friendship.

Thank you to all of the Nagórski family. Robert, Bogusława and Michał for providing so many meals and fun breaks during the long period of writing up, and most especially to Agnieszka, for all of her love and encouragement.

Finally, I would like to thank my brother Graham and my dad for their continual support, and my mum, who has been so active in helping me throughout my life. This would have been an impossible task without you.

Declaration

The work performed in this thesis was carried out in the Departments of Chemistry and Life Sciences, University of Warwick between October 2012 and September 2016. Unless otherwise stated, it is the work of the author and has not been submitted in whole or in part for any degree at this or any other university.

The content has not previously been published, except as detailed in the publications listed below:

[1] C. E. Broughton, H. A. Van Den Berg, A. M. Wemyss, D. I. Roper, and A. Rodger, "Beyond the Discovery Void : New targets for antibacterial compounds," *Science Progress*, vol. 99, no. 2, pp. 153–182, 2016

[2] D. P. Lobo, A. M. Wemyss, D. J. Smith, A. Straube, K. B. Betteridge, A. H. J. Salmon, R. R. Foster, H. E. Elhegni, S. C. Satchell, H. A. Little, R. Pacheco-Gómez, M. J. Simmons, M. R. Hicks, D. O. Bates, A. Rodger, T. R. Dafforn, and K. P. Arkill, "Direct detection and measurement of wall shear stress using a filamentous bio-nanoparticle," *Nano Research*, vol. 8, no. 10, pp. 3307–3315, 2015

Symbols

A_{iso} Isotropic absorbance 11

I_0 Incident intensity 24, 25

S Orientation factor 11

α Angle between transition moment and molecular orientation 11

$\boldsymbol{E}(t)$ Electric field magnitude 9

$\boldsymbol{\mu}$ Electric dipole operator 8

$\boldsymbol{r}$ Position of particle 8

λ Wavelength 15

ν Frequency of light 8

ω Angular frequency 9

ϕ Quantum yield 24

ψ_f Wavefunction of the final state 8

ψ_i Wavefunction of the initial state 8

h Plank's constant ($6.62607004 \times 10^{-34} m^2 kgs^{-1}$) 8

t Time 9

Å Ångström 51

V Volts 23, 31, 157

Abbreviations

AC alternating current 16, 17, 25, 26, 32, 47

CD circular dichroism 13, 81, 94, 95, 97, 99, 123

DC direct current 16, 17, 23, 25, 26, 32, 47, 55

FDCD fluorescence detected circular dichroism 20, 59

FDLD fluorescence detected linear dichroism 4, 8, 20, 21, 23–27, 29–37, 39–44, 46–49, 52, 55, 56, 59, 60, 63, 66, 67, 70–73, 98, 99, 123, 124

LD linear dichroism 2–4, 10–13, 16, 17, 21, 25–27, 29–37, 39, 40, 42–44, 47–49, 51–53, 55, 58–60, 62, 63, 65, 67–70, 72, 73, 98, 123, 125

AMR antimicrobial resistance 76

DAPI 4',6-diamidino-2-phenyindole 53–55, 61–66, 73, 123

DNA deoxyribonucleic acid 3–5, 12, 49, 51–59, 61–67, 70, 72, 73, 81, 83–85, 87–89, 123

DPH 1,6-diphenyl-1,3,5-hexatriene 29, 30, 38–40, 48

EtBr ethidium bromide 54–60

GEnCs human conditionally immortalised endothelial cells 101–103, 117, 119, 120

HT high tension voltage 23, 25, 26, 31

IPTG isopropyl β-D-1-thiogalactopyranoside 84, 89

LS light source 13

MPB 4-methylphenyl benzoate 30, 41–46, 48

MreB bacterial actin homologue MreB xiii, 6, 76–82, 88–95, 97–99, 123, 124

NMR nuclear magnetic resonance 58

NRMSD normalised root mean square deviation 96

OD optical density 21, 22

PCR polymerase chain reaction 5, 12, 82–84

PE^{OX} oxidised polyethylene 11, 32, 34–36, 47, 71, 123

PEM photoelastic modulator 13–16, 24

PI propidium iodide 54, 55, 60

PIV particle image velocimetry 101, 120

PMT photomultiplier tube 14, 16, 20, 23, 26, 27, 34, 55, 59, 98, 123

PTV particle tracking velocimetry 101, 120

RNA ribonucleic acid 5

ROI region of interest 121

SDS-PAGE sodium dodecyl sulfate polyacrylamide gel electrophoresis 90–93, 99, 124, 157

TRITC tetramethylrhodamine isothiocyanate 102, 103, 108, 114, 117–120

UV ultraviolet 8, 14, 32, 33, 37, 38, 40, 41, 55, 58, 61, 64, 65, 67, 69, 73, 94, 96, 123

WGA wheat germ aglutinnin 102, 103, 108, 117–120

WSS wall shear stress 6, 101, 114, 116–121, 124, 125

Summary

The objective of the work described in this thesis was to develop novel experimental and analytical methods to study samples of anisotropically oriented fluorophores. The primary development was the fluorescence detection method for linear dichroism spectroscopy ($FDLD$). The experimental configuration of the measurement has the detector placed facing the propagation direction of the exciting incident light. Long-pass edge filters, selected so that their cut-off wavelength lies between the excitation and emission maxima of the sample's fluorophore, were placed between the sample and detector to block transmitted incident light, whilst allowing Stoke's shifted fluorescence emissions to pass freely. The experiment was designed to be conducted using a commercial circular dichroism (CD) spectropolarimeter, which has been adapted to measure linear dichroism (LD). A theoretical framework to calculate $FDLD$ spectra using the output of such an instrument is presented, and used to generate the $FDLD$ spectra of small molecules oriented on stretched oxidised polyethylene films and biological samples oriented in Couette flow. It was found that much of the information that can be obtained from LD may also be derived from $FDLD$ spectra, however, $FDLD$ possessed two clear advantages: i) fluorescence detection is highly sensitive, which significantly lowered the sample volume requirement of a measurement, and ii) fluorescence detection is more selective than absorption methods, as only chromophores that are also fluorophores are detected.

A method for the cloning, expression and purification of the *Escherichia coli* actin homologue MreB is also presented. The composition of secondary structure elements within the protein obtained was analysed using CD and found to be in good agreement with literature values, taken from the crystal structure of *Caulobacter crescentus* MreB. Fluorescence spectra of the protein were recorded, which indicated that it may be possible to study its *in vitro* polymerisation kinetics using $FDLD$. Unfortunately, we were unable to obtain our *Escherichia coli* MreB in a sufficient yield to develop this assay.

Finally, a novel method for detecting the wall shear stress (WSS) exerted on a specific point of a surface by a fluid flowing over it is reported. This information was derived from the response to a shear flow of a fluorescently labelled particle of M13 bacteriophage, which was tethered to the surface. The focus of this thesis was primarily on the analysis of the fluorescence signals. Using a custom made algorithm, microscopy images of the tethered phage particle were segmented to define the region of each image occupied by the particle, and to calculate its orientation and length at all time points. These data were used to calculate the WSS at the point of the particle's attachment, and show that it varied when the surface was not uniform — highlighting a potential problem with commonly used methods for determining WSS that average over surface dynamics, such as particle image velocimetry and particle tracking velocimetry.

CHAPTER 1

Introduction

Investigations of matter using polarised light have been conducted for centuries, since at least the time of Arago's observations of optical activity in 1811 [3]. Studies of dichroism, which is the anisotropic absorption of light by matter, followed quickly, and among the early reports was Ambronn's observation of linear dichroism in dye stained membranes in 1888 [4]. Since this time, the application of polarised light spectroscopy to biological systems has grown steadily.

The work reported in this thesis is part of a wider programme of research to develop novel experimental methods for electronic absorption spectroscopies, so to extend their utility and effectiveness in probing the properties of biological samples. As biological samples are often only obtainable in small amounts, reducing the sample volume requirements for these spectroscopies is a key objective. Examples of where this has been achieved in recent work at the University of Warwick are: the development of a micro-volume Couette flow cell, which enables linear dichroism spectra to be recorded using samples volumes as low as 25 μL [5]; and an extruded quartz capillary sample holder for circular dichroism, which only requires 3 μL of sample to record a spectrum [6].

The work of this thesis continues with the theme of lowering the sample volume requirements by developing a methodology for obtaining much of the information that can be gained from linear dichroism, through detecting the fluorescence emissions of a sample. This is because fluorescence measurements are intrinsically more sensitive than absorbance measurements, providing that a fluorophore is present [7]. An additional advantage of fluorescence detection is that only chromophores that are also fluorophores are detected, which can greatly enhance the selectivity of measurements.

This chapter provides a general introduction to the work of this thesis. Fuller introductions to each topic are given at the beginning of each chapter.

1.1 Linear dichroism and fluorescence detected linear dichroism

The spectroscopic technique linear dichroism (LD) is used to examine the physical orientation of highly anisotropic systems by measuring differences in the absorption of light polarised parallel ($A_{\parallel}$) and perpendicular ($A_{\perp}$) to the sample's orientation axis, as stated in Equation 1.1. This technique is well known and its application requires that the sample contains suitable chromophores, in addition to an efficient alignment on the macromolecular level — the two most common orientation methods currently being Couette flow [5, 8, 9] and mechanical stretching [10, 11].

$$LD = A_{\parallel} - A_{\perp} \tag{1.1}$$

Historically, the main biomolecular applications of LD were studies of deoxyribonucleic acid (DNA) and DNA-drug systems [12]; however, more recent reports include the structural and kinetic characterisation of lipid vesicles and proteins bound to lipid membranes [13], in addition to steady-state kinetic studies of fibrous protein polymerisation [14]. In these instances, the technique relies on the characteristic absorbance regions of the protein under investigation. In the mid-ultraviolet region, the $\pi^* \leftarrow \pi$ and $\pi^* \leftarrow n$ transitions of the ubiquitous peptide bond dominate [15]. This is not an ideal chromophore for an orientationally sensitive technique, as the large number of residues in a typical protein means that the ensemble average of these transitions does not necessarily possess a high degree of preferential alignment. Proteins with tryptophan residues can be investigated using the intrinsic absorbance of the indole chromophore, although in some cases this can be complicated by external, overlapping absorbance signals (*e.g.* from the nucleotides whose hydrolysis commonly initiates and drives protein polymerisation). Measuring fluorescence emissions eliminates this problem by limiting what is detected to the light emerging from fluorophores.

Coupling LD with other analytical techniques was first proposed in 1972 by Akiyoshi Wada [16], however, there have been very few reports on coupled LD until recently. The development of a capillary micro-volume Couette flow accessory for LD has

allowed the first measured fluorescence detected flow linear dichroism spectra, thus opening the door for biological applications [5].

We define fluorescence detected linear dichroism ($FDLD$) as measuring the difference in the fluorescence emission intensity, following excitation with incident light polarised parallel and perpendicular to the sample's orientation axis. This is stated in Equation 1.2.

$$FDLD = F_{\parallel} - F_{\perp} \tag{1.2}$$

The method we have developed for measuring $FDLD$ uses commercial instruments, which have been adapted for LD. The development process required a full understanding of what the instrument output was from an LD measurement, and how to calculate $FDLD$ from the collected data. Full experimental and theoretical descriptions of both LD and the $FDLD$ developed here are given in Chapter 2.

Our $FDLD$ experiments were first performed using a simple test system of small fluorescent molecules, oriented on a stretched oxidised polyethylene film. This allowed us to optimise the experimental setup to achieve the best quality data. The molecules we selected for this were: anthracene, 1,6-diphenyl-1,3,5-hexatriene (DPH), and 4-methylphenyl benzoate (MPB). The results of these experiments, and a discussion of what they show, is given in Chapter 3.

From the $FDLD$ of small molecules on polyethylene films we moved on to experiments of DNA-dye complexes, oriented in solution using micro-volume Couette flow. Developing a system whereby the relative orientation of chromophores in a biological sample can be examined, with an enhanced sensitivity when compared with conventional LD, is the primary aim of this study, and so these experiments would really determine whether this aim has been achieved. A comparative analysis of the LD and $FDLD$ of these systems is given in Chapter 4, as well as those of an additional biological sample: M13 bacteriophage in solution.

Information on the rates at which some proteins polymerise to form fibres in solution — and therefore factors such as the preferred pH or salt concentration for the process to occur — can be obtained by monitoring the LD of the polymerising protein in

Couette flow [17]. We had hoped to emulate this using $FDLD$, where we would be able to take advantage of the techniques increased measurement sensitivity and selectivity. However, in the end we were unable to collect any $FDLD$ data from the model protein we selected: the *Escherichia coli* actin homologue MreB. Although we did express and purify the protein using a number of techniques from molecular biology, and the results we did collect are presented in Chapter 5 .

1.2 Molecular biology

Molecular biology is the study of the intracellular processes and molecular interactions that come together to produce a functioning organism [18]. Several key discoveries from the middle of the 20th century gave rise to molecular biology as a recognised field in its own right, where previously such studies may have been considered as part of biochemistry or genetics. Among the earliest of these works was the 1944 publication by Avery *et al.*, who showed that DNA is responsible for the transmission of one phenotype of an organism to another through transformation [19]. A short while later, and most famously, Crick and Watson proposed the double helical structure of DNA [20], though Crick's later publication 'Central dogma of molecular biology' was just as important for molecular biology [21].

The central dogma describes the mechanism by which the genetic information stored in DNA is used to form a functioning organism. An overview of this mechanism is that sections of DNA known as genes are copied into ribonucleic acid (RNA) by a process called transcription [22]. The sequence of bases in the RNA are then translated into proteins, which perform a huge number of the functions vital to an organism's survival [21].

For the purpose of copying a gene, and producing enough replicate DNA fragments of the gene to transform them into a cell, a significant advance was the invention of the polymerase chain reaction (PCR) by Kary B. Mullis in 1983 [23]. PCR is used to amplify a given sequence of DNA using a small amount of genomic DNA, two short DNA primers that are complementary to opposite ends of the target sequence, and a DNA polymerase that is able to withstand high temperatures, such as the *Taq*

polymerase found in the bacterium *Thermus aquaticus* [24]. Combing the ability to produce large quantities of a desired DNA fragment with the ability for DNA ligase to join fractions of DNA together — a discovery made by Weiss and Richardson in 1967 [25] — made it possible to introduce a new gene into a cell, as well as control its expression with additional DNA sequences.

A common method used to control the expression of a gene that has been transformed into a new cell is the negative control mechanism of the Lac repressor, first isolated by Gilbert and Müller-Hill in 1966 [26]. We also used this system to control the expression of MreB.

These key techniques of molecular biology allowed us to obtain MreB from *E. coli*. We then were able to analyse its structure using circular dichroism. A full description of the methods we used to obtain the protein, in addition to its structural analysis is given in Chapter 5.

1.3 Wall shear stress

The final results chapter of this thesis, Chapter 6, describes a novel method for detecting the wall shear stress (WSS) exerted on a surface by a fluid flowing over it. In particular it describes in detail the methods of image analysis and data processing that were used in the publication: 'Direct detection and measurement of wall shear stress using a filamentous bio-nanoparticle' [2].

Developing a method to accurately measure WSS is highly important in a number of fields, such as micro-fluidics [27] and lab-on-a-chip technologies [28]. However, it is of particular importance in medicine, where abnormal WSS in the vasculature is associated with diseases such as atherosclerosis [29], and it also plays a key role in molecular transportation in the microvasculature [30–32]. A problem with existing methods is that they average many of the WSS dynamics over a surface. The method given in Chapter 6 calculates the WSS at a given point on a surface, allowing greater resolution of how it varies across a surface.

CHAPTER 2

The development of a fluorescence detection methodology for linear dichroism spectroscopy

2.1 Introduction

Our fluorescence detection methodology for linear dichroism spectroscopy was applied to a number of spectrometers during the course of this PhD. The basic setup was the same for all of them, with a long pass edge filter in place before the photomultiplier tube detector, which faces the propagation direction of the incident light. The key differences, and where the technique needed to be optimised, lay in the software settings of the detector and the subsequent data processing. This chapter begins with an in-depth discussion of the two spectroscopic techniques that have been combined — linear dichroism and fluorescence excitation spectroscopy — which is followed by a practical and theoretical explanation of fluorescence detected linear dichroism ($FDLD$).

2.2 Spectroscopy in the ultra-violet to visible region

Spectroscopy may be defined as the study of the interaction between radiated energy and matter. The form this interaction takes is widely varied, and largely depends on the frequency of the radiated energy used. In the ultraviolet (UV) to visible region, the electric field generated by photons may have sufficient energy to change the electron distributions in molecules — for one or more electrons to be excited from the ground state to an excited state. For such an electronic transition to take place, the energy of the incoming light must equal the energy gap between the two states (*i.e.* $h\nu = E_f - E_i$, where h is Plank's constant, ν is the frequency of the light, and E_i and E_f are the energies of the initial and excited states, respectively) and the transition dipole moment between the states must be non-zero:

$$\boldsymbol{\mu}_{fi} = \int \psi_f^* \boldsymbol{\mu} \psi_i d\tau \neq 0 \tag{2.1}$$

$$\boldsymbol{\mu} = -e\boldsymbol{r} \tag{2.2}$$

where ψ_f and ψ_i are the wavefunctions of the final and initial states, respectively, the

* denotes that the complex conjugate is being used, and $d\tau$ is the volume element. The electric dipole moment operator, $\boldsymbol{\mu}$, is the distance between the centres of positive and negative charges in a molecule ($\boldsymbol{r}$) multiplied by the magnitude of these charges. The transition dipole moment is a measure of the degree to which an electron in state i is polarised by incoming incident light, such that its spatial distribution is similar to that of state f. In short: an oscillating electric field interacts with a molecule through its dipole moment. The energy of this interaction, $H(t)$, can be described as:

$$H(t) = \boldsymbol{\mu} \cdot \boldsymbol{E}(t) \tag{2.3}$$

where $\boldsymbol{E}(t)= \boldsymbol{E}_0 \cos(\omega t)$ — ω represents the angular frequency of the light, t denotes time and $\boldsymbol{E}_0$ is a uniform electric field. Both the electric dipole and the electric field are vector properties, and their dot product can be zero even if their magnitudes are not. A simple example of this is when the instantaneous electric dipole of the molecule is polarised perfectly along some Z axis and the electric field is polarised on the Y axis of the same coordinate system. In this instance, $H(t)$ would be equal to zero. Conversely, the value of $H(t)$ will be maximised when the polarisation of the incident light is exactly aligned with the polarisation of the electric dipole moment for a transition, and so will simply be equal to $\mu E(t)$. Equation 2.1 states that $\boldsymbol{\mu}_{fi}$ is the dipole moment associated with a transition between two states, and that it is a vector property (as in Cartesian coordinates, there will be an element associated with the x, y and z directions). The scalar quantity $|\boldsymbol{\mu}_{fi}|^2$ is proportional to the transition probability, and so by maximising the interaction energy we are also maximising the probability that a given transition between two states will occur.

Using simple unit vectors to describe the polarisation states, Figure 2.1 illustrates the effect of rotating the electric field 90° in the YZ plane, whilst fixing the electric dipole along a Z axis. It is this dependency on the relative orientations of the electronic transition dipole moment and the electric field vector of the incident light that gives rise the property of dichroism.

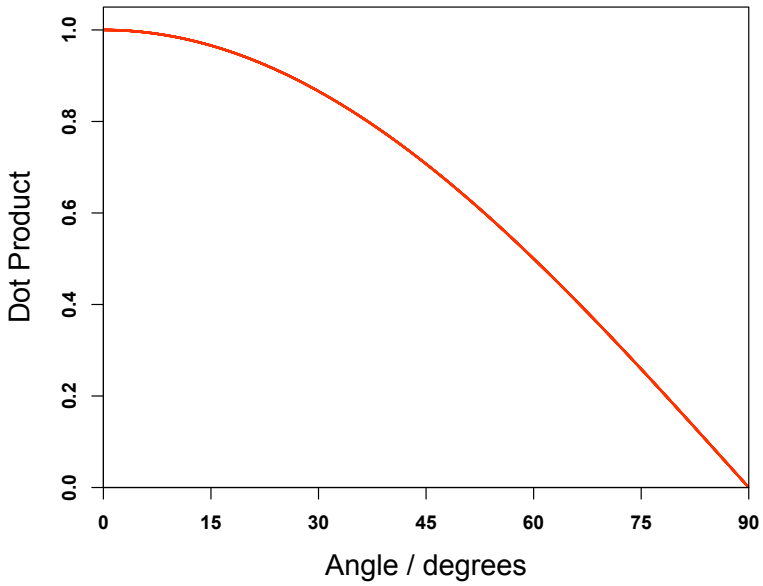

Figure 2.1: *The figure shows the dot product between two unit vectors, one of which is being rotated 90° relative to the other. This illustrates the effect rotating the axis of the electric field vector relative to the polarisation direction of a molecule's electric transition dipole moment has on* $|\boldsymbol{\mu}_{fi}|^2$*, and therefore, on the probability of a transition.*

2.2.1 Linear dichroism

As discussed above, the probability of a molecule absorbing a photon of light is dependent on the extent to which the electric field vector aligns with the molecule's electric dipole transition moment. This principle enables the measurement of a linear dichroism (LD) spectrum, as in an anisotropically oriented sample there will be a difference in the absorbance spectra when using incident light polarised parallel to the sample's orientation axis, compared with when light polarised perpendicular to this axis is used (with the rare exception of cases where the transition angles are at an average of the magic angle ($\sim 54.7°$) to the orientation axis) [1]. With reference to Figure 2.2, LD may be defined as:

[1]Here and throughout this section we are considering only the ideal case where a sample has a single chromophore per absorption band, with each of the chromophores having an equal probability of being oriented by the orientation apparatus. Overlapping chromophore absorbances, chromophores stereochemically fixed with respect to each other, or anisotropic light scattering, may distort a measured LD spectrum.

$$LD = A_Z - A_Y \tag{2.4}$$

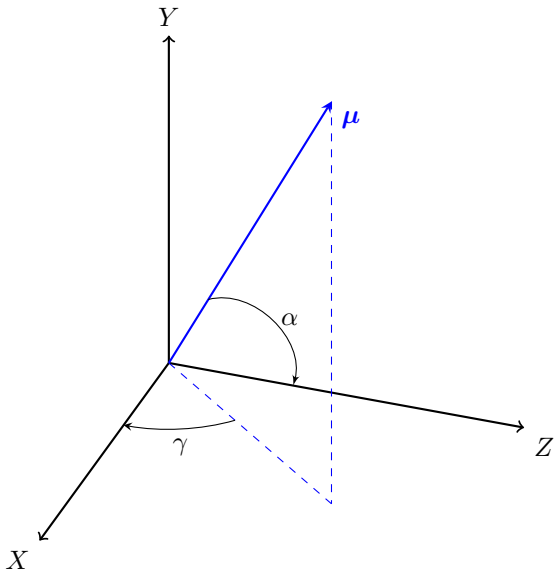

Figure 2.2: *The orientation of an electric dipole transition moment ($\boldsymbol{\mu}$) in a Cartesian coordinate system, where Z is the orientation axis and X is the propagation direction of the incident light. The angle between $\boldsymbol{\mu}$ and the molecular orientation axis is denoted α, and the angle it makes with the propagation direction of the incident light is γ.*

From Equation 2.4 we can derive the more familiar LD equation [33]:

$$LD = \frac{3}{2} A_{iso} S(3\cos^2\alpha - 1) \tag{2.5}$$

where α is the angle between the transition's polarisation and the orientation axis; A_{iso} is the isotropic absorbance of the sample; and S is an orientation factor, which equals 1 for a perfectly oriented sample and 0 if the sample is isotropic [34].

A key part of an LD measurement is the method used to induce a preferential alignment in a sample. Small molecules may be oriented on untreated commercial polyethylene (PE) films or oxidised polyethylene (PE^{OX}) — see Chapter 3 for details of preparation — that are further stretched along the manufacture stretch direction. The mechanical stretching apparatus used in this work consists of two parallel double-ended dowel screws, which span the length of a metal frame. Each screw is attached to a cog at each end of the frame, which are both controlled synchronously

by a central cog. Set perpendicularly onto the screws, and at an equal distance from the central dowel, are two parallel clamps that move apart or together upon turning the central cog. To align a sample, a segment of PE^{OX} film is clamped between the jaws of the stretcher, and the cogs are turned to evenly stretch the film. Following the measurement of a baseline spectrum, typically 40 μL of sample was deposited onto the film, and the solvent allowed to evaporate. Molecules tend to preferentially align with their long axis along the stretching direction of the film. A photograph of a mechanical stretcher is given in Figure 2.3.

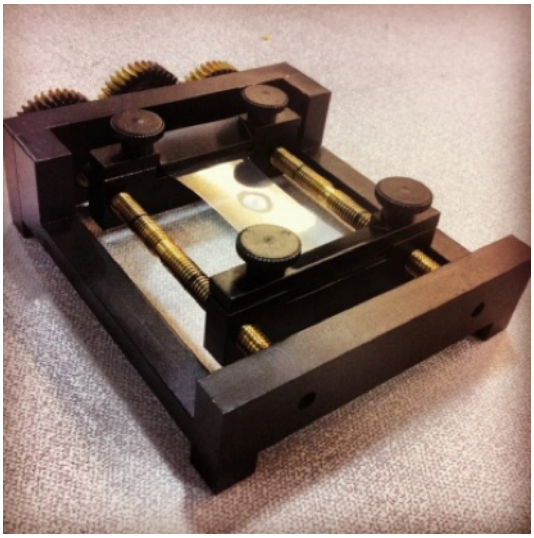

Figure 2.3: *Mechanical stretcher used to orient small molecules for LD measurements. This figure is reproduced from reference [35].*

For biological molecules, the most appropriate method to induce a preferential alignment in a sample is generally micro-volume Couette flow [5]. Using this experimental setup, the sample is held between two coaxial cylinders: a rotating outer quartz capillary, and a stationary inner quartz rod. The sample is subject to a viscous drag force, which at rotation velocities below that which initiates turbulent flow, causes the sample to orient in the plane perpendicular to the long axis of the rod. The orientational distribution of a sample aligned in this way is highly dependent on the distribution of aspect ratios of its component molecules, with higher aspect ratios orienting better. This property comes with a number of advantages, such as: the *LD* of a PCR mixture only detects the PCR product, since neither the primers nor the unpolymerised bases orient [36]; recording the *LD* of a DNA binding molecule in the presence of DNA exclusively detects the bound

molecules and DNA, as the free molecules will be isotropically oriented; and the kinetics of the formation of long chain polymers can be followed, as the LD value will increase as the molecules polymerise to form structures with increasing aspect ratios.

The instrument we use to record LD for this work is the Jasco J-815 circular dichroism (CD) spectropolarimeter (Jasco UK), which is illustrated schematically in Figure 2.4.

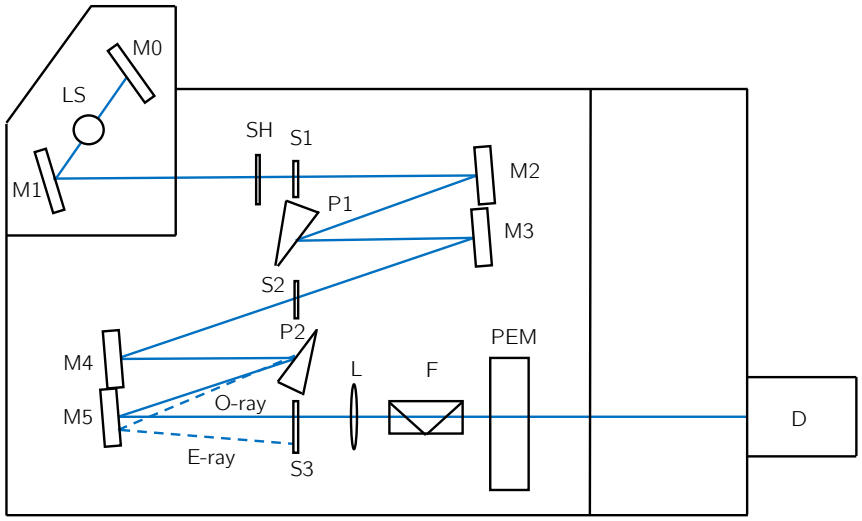

Figure 2.4: *A schematic of the Jasco J-815 CD spectrometer, redrawn from the user manual [37]. LS stands for light source, M for mirror, S for slit, P for prism, L for lens, F for polariser, PEM for photoelastic modulator, and D for detector. These components are discussed in the main text. E-ray and O-ray denote the extraordinary ray and ordinary ray, respectively.*

With reference to Figure 2.4, the Jasco J-815 CD spectrometer uses a xenon arc lamp light source (LS), which emits broad-spectrum radiation. This light then — either directly or by reflection from mirrors (M0 and M1) — travels through a system of two monochromators. A monochromator essentially has two components: a dispersing element (either a prism or a diffraction grating) and an exit slit, whose position relative to the dispersing element determines which wavelength passes through to the sample. Jasco instruments use crystal prisms (P1 and P2) to separate the incident light according to wavelength. A second effect of the prism monochromators is that their crystal axis orientations have been set such that the light exiting the third slit (S3) is to a good degree linearly polarised. To clean this up into linearly polarised light, the beam passes through a focussing lens (L) to a linear polariser

(F), which is necessary before the light passes through the photoelastic modulator (PEM) (Figure 2.4).

After the incident radiation passes through a sample, it reaches a photomultiplier tube (PMT) detector (D). The sequence of components making up a PMT begin with a photocathode, which emits electrons (or photoelectrons) when struck by light. These are directed towards a series of 'electron multiplier' dynodes *via* a focusing electrode [38]. It is through a series of secondary emissions from these dynodes that the gain on the original signal is achieved. This occurs in three stages: primary electrons, with energy of around a few hundred electron volts, are absorbed by the dynode and impart their energy to the electrons in its material; the energised electrons then diffuse through the material; and at the surface, electrons with sufficient energy are able to escape into the vacuum, on route to the next dynode. The multiplied electrons are finally collected by an anode, which generates the output signal [38]. Integrated over the time frame that the PMT is irradiated by each wavelength of incident light, this flow of electrons is proportional to the photon flux reaching the photocathode. If we had a similar detection system recording the photon flux of the incident beam prior to the sample, we could easily calculate the sample's absorbance spectrum using the Beer-Lambert law. However, as we want to calculate the difference of two absorbances, this spectrometer has a slightly more elaborate detection system. Before looking into how this calculation is achieved, it is important to first consider the output of a photoelastic modulator.

A photoelastic modulator (PEM) is a dynamic polarisation device — as opposed to the static polariser, F, mentioned above — and (for UV-visible radiation) consists of a silica bar, which is fused to a piezoelectric transducer [39]. Piezoelectric materials generate mechanical stress upon the application of an electric field, and silica is a photoelastic material, meaning its birefringence is altered upon the application of stress [40]. By setting the voltage applied to the piezoelectric material to be such that it vibrates at the natural resonance frequency of the silica bar (which in our case is set at 50 kHz), the birefringence of the bar is modulated. Considering the linearly polarised input beam, polarised at 45° to the stress axis of the bar, as the supposition of two, in-phase beams, the PEM will affect one of these components differently, in the time-dependent retardation (δ):

$$\delta = \delta_0 \sin(\omega t) \tag{2.6}$$

where δ_0 is the peak retardation (*i.e.* $\lambda/2$ — the drive voltage of the modulator must be altered at each wavelength (λ)), $\omega/2\pi$ is the modulation frequency (50 kHz); and t is time [41]. Therefore, the output of the PEM is an electromagnetic field, whose polarisation is alternating (continuously between the states) in a time dependent manner. It has been shown that the intensity of light transmitted by a sample is then [40]:

$$I = \frac{I_0}{2}\left[(e^{-a_\parallel} + e^{-a_\perp}) + (e^{-a_\parallel} - e^{-a_\perp})\cos(\delta)\right] \tag{2.7}$$

where I_0 is the intensity of light incident on the PEM and $a_\perp$ and $a_\parallel$ are the sample's absorbance of perpendicular (Y axis) and parallel (Z axis) polarised light, respectively [40]. We can use Equation 2.6 to expand the last term of Equation 2.7 in a Fourier-Bessel series:

$$\cos(\delta_0 \sin(\omega t)) = J_0(\delta_0) + 2J_2(\delta_0)\cos(2\omega t) \tag{2.8}$$

where $J_n(\delta_0)$ are Bessel functions of the first kind. Equation 2.8 allows us to split Equation 2.7 into static ($I(0)$) and dynamic ($I(2\omega)$) components:

$$I(0) = \frac{I_0}{2}\left[(e^{-a_\parallel} + e^{-a_\perp}) + (e^{-a_\parallel} - e^{-a_\perp})J_0(\delta_0)\right] \tag{2.9}$$

and, at twice the modulation frequency:

$$\begin{aligned} I(2\omega) &= I_0 J_2(\delta_0)(e^{-a_\perp} - e^{-a_\parallel}) \\ &= J_2(\delta_0)(I_\perp - I_\parallel) \end{aligned} \tag{2.10}$$

Our instrument is configured such that $J_0(\delta_0) = 0$, therefore Equation 2.9 may simply be written:

$$\begin{aligned} I(0) &= \frac{I_0}{2}(e^{-a_\parallel} + e^{-a_\perp}) \\ &= {}^{(I_\parallel + I_\perp)}/_2 \end{aligned} \tag{2.11}$$

Equation 2.11 shows that the $I(0)$ component is not a function of time, and so the current this will generate at the PMT will be continuous at each wavelength, *i.e.* a direct current (DC) is generated. When there is no sample between the PEM and the PMT, this is all the detector will see [42]. This is not true for the $I(2\omega)$ component, shown in Equation 2.10, which when an aligned sample is present, has intensity that varies sinusoidally at absorbing wavelengths, and so will generate an alternating current (AC) [43]. Therefore, when an aligned sample is in place, the output signal detected at the PMT anode consists of an AC component ($\propto (I_\perp - I_\parallel)$), produced by the differential absorbance of a sample, coupled to a DC component ($\frac{1}{2}(I_\parallel + I_\perp)$), which is proportional to the average photon flux reaching the PMT. These two components are separated into two channels. The AC channel contains an amplifier followed by a lock-in amplifier, which is phase-locked to twice the modulation frequency of the PEM (for LD measurements), and outputs a voltage that contains information on the differential absorbance of a sample. The signal in the DC channel passes through an operational amplifier that also outputs a voltage, this time being proportional to the mean beam intensity [42, 43].

The instrument then calculates the differential absorbance of the sample (the AC component) with respect to the average light throughput at each wavelength (the DC component) by taking their ratio [37]:

$$LD = \log_{10} \frac{I_\perp}{I_\parallel} = \log_{10} \frac{1 + {}^{AC}/_{2DC}}{1 - {}^{AC}/_{2DC}} \tag{2.12}$$

The $\log_{10} \frac{I_\perp}{I_\parallel}$ term in Equation 2.12 can be shown to equal $A_\parallel - A_\perp$ by using the Beer-Lambert law:

$$\begin{aligned} LD &= A_{\parallel} - A_{\perp} \\ &= -\log_{10} \frac{I_{\parallel}}{I_{0,\parallel}} + \log_{10} \frac{I_{\perp}}{I_{0,\perp}} \\ &= \log_{10} \frac{I_{\perp}/I_{0,\perp}}{I_{\parallel}/I_{0,\parallel}} \\ &= \log_{10} \frac{I_{\perp}}{I_{\parallel}} \end{aligned} \tag{2.13}$$

where $I_{0,\perp} = I_{0,\parallel}$ are the incident intensities of perpendicular and parallel light, respectively. As the AC component is much smaller than the DC component in Equation 2.12, LD can be approximated as [37]:

$$LD = k\frac{AC}{DC}\log_{10} e \tag{2.14}$$

where k is a machine constant. In normal operation, Equation 2.14 is simplified by amplifying or attenuating the AC and DC outputs simultaneously, such that the DC output is maintained at a constant value. This is achieved by calculating the difference between the DC value at time t, and the set value, which in our case is 1:

$$DC_e = DC_t - 1 \tag{2.15}$$

The variation or error from the value of 1 in the DC output, DC_e, is then used to vary the potential (or the high tension voltage) across the PMT *via* a servomechanism, to reduce its value to zero [37]. Equation 2.14 may then simply be expressed as:

$$LD = k'AC \tag{2.16}$$

2.2.2 Fluorescence excitation spectroscopy

Once an electron has absorbed the energy of an incoming photon in the ultraviolet or visible region, and is occupying one of the vibrational energy levels of an excited state, it immediately begins a process which will see it return to the ground state. In most chromophores, this is achieved through a non-radiative process, such as

vibrational decay or collisional quenching, however, in some cases, the electron releases energy by emitting a photon. Where there is no intersystem crossing from a singlet to a triplet state, this occurrence is termed fluorescence. Figure 2.5 is a Jabłoński diagram, which illustrates the processes through which an electron can return to the ground state.

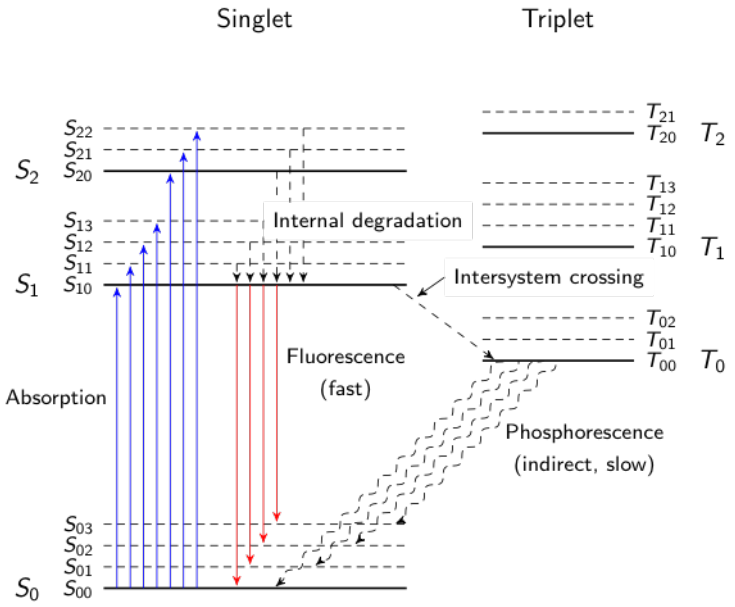

Figure 2.5: *Jabłoński diagram [44] illustrating the processes that occur following the absorption of a photon. Through absorption, an electron in one of the vibrational levels of the singlet ground state (S_{0i}) is excited to a first (S_1) or second (S_2) singlet state. It is most likely that it then decays down to the S_{10} state, from where it can release its energy radiatively and drop down to the S_0. An electron in the S_1 may also go through spin conversion to a triplet state (T_i), in a process called intersystem crossing. Radiative decay from a triplet state to the S_0 (phosphorescence) is spin forbidden, and occurs over a much longer time frame. This figure was adapted from a TikZ template on www.TEXample.net.*

From Figure 2.5 one can easily see that fluorescence emissions are lower in energy than the light that was absorbed. This energy difference is called the 'Stokes shift', after Sir G. G. Stokes who first observed the phenomenon [45]. It is less obvious from Figure 2.5, though generally true, that the energy of the emitted light is independent of the energy of the excitation light used; a phenomenon eponymously named: 'Kasha's' rule [46]. These features of fluorescence mean that one can relatively easily distinguish between fluorescence emissions and transmitted or Rayleigh scattered incident light; and also, one can measure variations in the fluorescence emissions

over a range of excitation wavelengths with little (or no) alterations to the detection system.

A schematic representation of a typical spectrofluorometer is given in Figure 2.6.

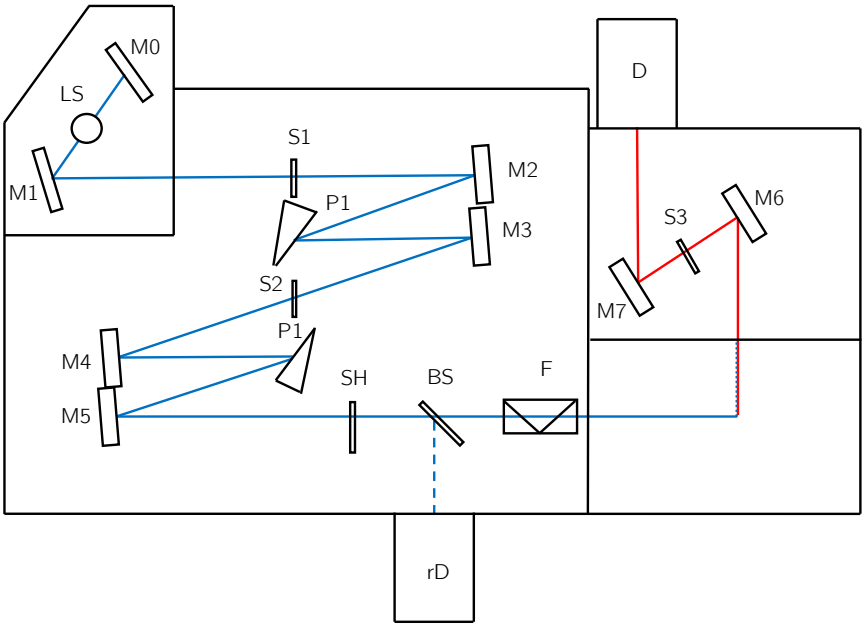

Figure 2.6: *Schematic of spectrofluorimeter. Many of the optical elements can be the same as in the CD spectrometer given in Figure 2.4. The different components are the beamsplitter (BS), which directs light towards a reference detector (rD) so that the incident light intensity can be recorded. This figure was drawn in Microsoft PowerPoint.*

Recording the variation in fluorescence intensity with the wavelength of exciting light gives a fluorescence excitation spectrum [47]. In an ideal case, where the detection efficiency of the instruments is exactly the same at all wavelengths and its wavelength calibration is accurate, a fluorescence excitation spectrum should be superposable onto an absorbance spectrum, when using a sample containing only a single chromophore, which is also a fluorophore [48]. However, an advantage of fluorescence measurements over absorbance methods is that they are intrinsically more sensitive, as they depend only on the incident light intensity and the instrument's ability to detect low light levels, and not its ability to differentiate between two, nearly equal signals from the incident and transmitted light beams (as shown in Equation 2.18).

When measuring a spectrum of a sample containing multiple chromophores, fluorescence detection can also be much more selective than detecting the absorbance directly, as in most cases only one of the chromophores will fluoresce. Though

with samples such as these (containing multiple chromophores with only a single fluorophore) one has to be cautious of the inner-filter effect, where the spectrum is distorted by the emitted light being reabsorbed before reaching the detector. The inner filter effect is usually not too much of a problem, as fluorescence detection permits the use of highly dilute samples.

2.3 Fluorescence detected linear dichroism

Our motivation for developing a fluorescence detection methodology for linear dichroism spectroscopy was to enable us to obtain information on the relative orientation of chromophores in a sample, with increased measurement sensitivity and chromophore selectivity than is possible with conventional absorbance linear dichroism. We begun by defining fluorescence detected linear dichorism ($FDLD$) as the difference in the intensity of fluorescence emissions after excitation by parallel ($F_{\parallel}$) and perpendicularly ($F_{\perp}$) polarised light:

$$FDLD = F_{\parallel} - F_{\perp}. \tag{2.17}$$

The following sections detail the development of $FDLD$'s experimental configuration, and the theoretical basis of the experiment.

2.3.1 Experimental procedure

In their work on fluorescence detected circular dichroism ($FDCD$), Muto *et al.* used the Stoke's shift of fluorescence emissions to separate them from transmitted incident light by placing 100 mm of saturated $NaNO_3$ solution between the sample and the detector [49]. We use similar reasoning in our $FDLD$ experiments, where we use long-pass edge filters with a high optical density through their attenuated wavelengths and as high a cut-off gradient as possible, to maintain the PMT facing the propagation direction of the incident light. The initial motivation for this was that when using a mechanical stretcher to orient a sample (Figure 2.3), it is not possible to detect a signal at 90° as it is blocked by the apparatus, however, we

have found that it also gives better results when using solution samples oriented by Couette flow.

When selecting a long-pass filter, the first thing that needs to be considered is the sample's excitation and emission wavelength maxima. These can be measured using standard absorbance and fluorescence spectrophotometers. The cut-off wavelength of the long-pass filter is selected to lie between these maxima. It is preferable that the Stoke's shift of the fluorophore is large, so that that there is no overlap between the excitation and emission peaks. This is generally the case when the fluorophore is excited into the S_2 state (Figure 2.5), although it is less common when exciting into S_1. When there is overlap between the excitation and emission spectra, a trade-off has to be made between the wavelength range of the measured spectrum and its signal intensity. Selecting a filter with a steep cut-off gradient reduces the sacrifice of both these parameters. The long-pass filters used in this work are given in Table 2.1.

Table 2.1: Long-pass filters used for fluorescence detected linear dichroism

Filter	**Cut-off Wavelength (nm)**
SCHOTT OG570	570
ThorLabs FEL0400	400
ThorLabs FELH0450	450
ThorLabs FEL0500	500
ThorLabs FEL0550	550
Semrock FF01-300/LP-25	300
Semrock FF01-341/LP-25	341
Semrock FF02-409/LP-25	409
Semrock LP02-568RU-25	568

In Table 2.1, the SCHOTT OG570 filter is included as an example of the coloured glass filters we used. This type of filter performs very poorly in our setup, as they transmit too much light through their attenuated wavelengths, and so spectra

measured using these are a mixture of LD and $FDLD$. All of the ThorLabs filters listed performed very well, with their maximum transmission intensity through their attenuated wavelengths being 0.01% (optical density (OD) 4). These filters blocked light over a large wavelength range, though their cut-off gradient was found to be quite shallow, with ∼15 nm between their maximum transmission and rejection regions.

The steepest cut-off gradient filter in Table 2.1 is the Semrock Razor Edge LP02-568RU-25, with only 3 nm between its maximum transmission and rejection regions. This filter, however, is designed for Raman spectroscopy and has a poor range of blocked wavelengths. Much better performers in this respect are the other Semrock filters, which are all from the BrightLine series. They have the range of blocked light achieved by the ThorLabs filters (with an increased blocking efficiency of OD 5-7), with only a 6 nm cut-off gradient. On occasions when an individual filter's blocking range did not cover the region we wished to measure, it was found to be very effective to 'piggyback' one filter on top of another, such that the incident light hit the filter with the longest cut-off wavelength first. This technique was used frequently throughout this work.

Once an appropriate long-pass filter has been selected, it needs to be fitted directly in front of the detector. As the filters given in Table 2.1 require that they are set at exactly 90° to the incident light to transmit all polarisations of light equally, we custom made a holder that fit them into a Jasco J-815 spectrometer. A diagram of the filter holder is given in Figure 2.7.

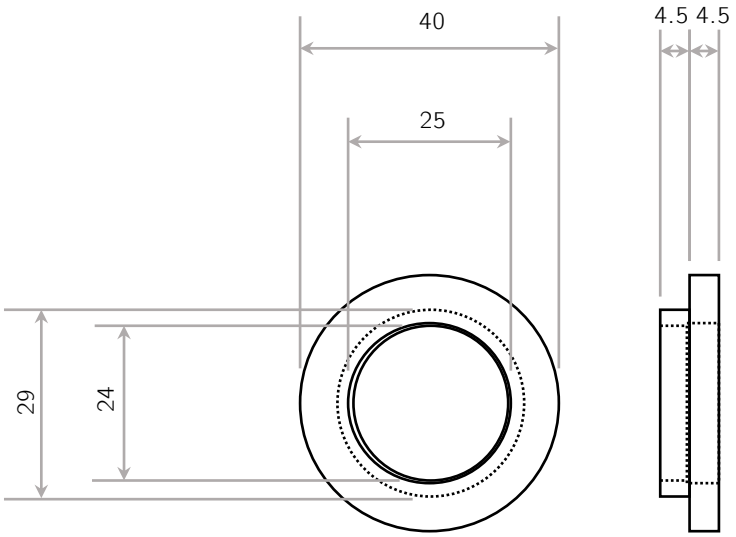

Figure 2.7: *Drawing of the custom made long-pass filter holder used to fit filters into a Jasco J-815 spectrometer. Once the ⌀25 mm filter was placed in the mouth of the fitting, a rubber o-ring was used to hold it in place. All dimensions shown are in millimetres.*

Once the filter and sample are in place, the other adjustments are made using the instrument's software. So that transmitted light is not recorded, the wavelength range must start before the cut-off wavelength of the long-pass filter that is in place in the instrument — the minimum number of wavelengths before depends on the steepness of its cut-off gradient — and the stop wavelength is set at the shortest wavelength of the range. Channel two of the instrument is set to record either the high tension voltage (HT) or the *DC* output from the PMT, depending on whether the DC is set to be constant (using Equation 2.15) or the HT is set at a constant value (normally 600 V), respectively. In either case, it is obvious from the trace of this channel whether the filters being used block transmitted light over the selected wavelength range, as regions where they transmit light will be seen as a sharp decrease in the HT value or a sharp increase in the *DC* output.

Whether to set the instrument to measure in fixed HT or fixed *DC* mode depends on the sample one is using. The reason for this, and an introduction to the theory of $FDLD$ is given below.

2.3.2 Theoretical introduction

Fluorescence emission may be defined as the absorbance of a sample, multiplied by the quantum yield of the fluorophore [50]:

$$F = \phi\big[I_0(1 - e^{-a})\big] \tag{2.18}$$

where ϕ is the quantum yield, I_0 is the intensity of the incident light, and a is the Eulerian absorbance of the sample. Assuming the long pass filter is 100% effective, ϕ is the same for both polarisations of exciting light, and that the fluorescence lifetime of the fluorophore is much shorter than the reciprocal of the frequency of the PEM [51], with reference to Equation 2.17, $FDLD$ may be described as follows.

In our experiment, we must expand Equation 2.18, in terms of the incident intensity of the two linear light polarisations, $I_{0,\parallel}$ and $I_{0,\perp}$, and their respective sample absorbance, $a_\parallel$ and $a_\perp$:

$$F = \phi\big[I_{0,\parallel}(1 - e^{-a_\parallel}) + I_{0,\perp}(1 - e^{-a_\perp})\big] \tag{2.19}$$

As $a_{\parallel/\perp} = \bar{a} \pm \dfrac{\Delta a_{LD}}{2}$, where $\bar{a}$ is the average absorbance of the two light polarisations, and Δa_{LD} is their difference, *i.e.* $\Delta a_{LD} = a_\parallel - a_\perp$, we can write Equation 2.19 as [52]:

$$F = \phi\big[I_{0,\parallel}(1 - e^{-(\bar{a} + \frac{\Delta a_{LD}}{2})}) + I_{0,\perp}(1 - e^{-(\bar{a} - \frac{\Delta a_{LD}}{2})})\big] \tag{2.20}$$

We again know that the incident intensity of each light polarisation on a sample is a time varying function of the phase shift, δ, produced by the PEM (Equation 2.7), where $I_{0,\parallel/0,\perp} = \dfrac{I_0}{2}(1 \pm \cos\delta)$ [52]. And so Equation 2.20 becomes:

$$\begin{aligned}
F &= \phi\big[\frac{I_0}{2}(1+\cos\delta)(1-e^{-(\bar{a}+\frac{\Delta a_{LD}}{2})}) + \frac{I_0}{2}(1-\cos\delta)(1-e^{-(\bar{a}-\frac{\Delta a_{LD}}{2})})\big] \\
&= \frac{\phi I_0}{2}\big[(1+\cos\delta)(1-e^{-(\bar{a}+\frac{\Delta a_{LD}}{2})}) + (1-\cos\delta)(1-e^{-(\bar{a}-\frac{\Delta a_{LD}}{2})})\big] \\
&= \frac{\phi I_0}{2}\big[2 - e^{-(\bar{a}+\frac{\Delta a_{LD}}{2})} - e^{-(\bar{a}-\frac{\Delta a_{LD}}{2})} - (e^{-(\bar{a}+\frac{\Delta a_{LD}}{2})} - e^{-(\bar{a}-\frac{\Delta a_{LD}}{2})})\cos\delta\big] \\
&= \frac{\phi I_0}{2}\big[2 - e^{-\bar{a}}((e^{\frac{\Delta a_{LD}}{2}} + e^{\frac{-\Delta a_{LD}}{2}}) - (e^{\frac{\Delta a_{LD}}{2}} - e^{\frac{-\Delta a_{LD}}{2}}))\cos\delta\big] \\
&= \frac{\phi I_0}{2}\big[2 - e^{-\bar{a}}(2 - \Delta a_{LD}\cos\delta)\big]
\end{aligned} \tag{2.21}$$

Using Equation 2.8 to expand $\cos\delta$, and remembering that our instrument is configured such that $J_0(\delta_0) = 0$, we get:

$$\begin{aligned}
F(0) &= \frac{\phi I_0}{2}\big[2 - e^{-\bar{a}}(2 - \Delta a_{LD} J_0(\delta_0)\big] \\
&= \phi I_0\big[1 - e^{-\bar{a}}\big]
\end{aligned} \tag{2.22}$$

and

$$\begin{aligned}
F(2\omega) &= \frac{\phi I_0}{2}\big[2e^{-\bar{a}}\Delta a_{LD} J_2(\delta_0)\big] \\
&= \phi I_0 e^{-\bar{a}} J_2(\delta_0)\Delta a_{LD}
\end{aligned} \tag{2.23}$$

Here, as for linear dichroism, we again have the measured AC ($F(2\omega)$) and DC ($F(0)$) components of the instrument output. The DC term is the average of the fluorescence emission intensity following excitation by the two orthogonal light polarisations. The AC term is proportional to the differential absorbance, Δa_{LD}, and so is also proportional to LD (as $\Delta a_{LD} = \ln(10)LD$). We divide the AC signal by the DC, which removes the incident light intensity term, I_0, which is unknown in our measurement. In this study, the sign of the $FDLD$ spectra has been changed so that signals are of the same sign as LD, and so measurements using the two techniques can be more easily compared.

$$FDLD = -\frac{AC}{DC} \tag{2.24}$$

In order to record a spectrum in fixed DC mode, using the mechanism described

in Equation 2.15, the AC signal should be much smaller than the DC output, or the average fluorescence intensity. Where the oriented sample fluorophore only weakly fluoresces, the DC output could be increased by including a non-interacting, unaligned fluorophore into the sample, which, if its concentration is low enough to avoid the inner filter effect, would increase the signal to noise ratio of the sample without effecting its sign or magnitude. This would only be possible for samples oriented in the solution phase, where small fluorescent molecules would not have a high enough aspect ratio to orient in flow — the mechanical stretching apparatus used for solid samples would orient all small molecules. For this reason, it was generally found to be better to fix the HT for solid samples, oriented on stretched polyethylene films, and to fix the DC for solution samples oriented in Couette flow. In fixed DC mode, $FDLD$ spectra are simply calculated using Equation 2.25.

$$FDLD = -AC \tag{2.25}$$

2.4 Methods summary

$FDLD$ was designed to combine the sensitivity and selectivity of a fluorescence excitation measurement, with the sensitivity to the relative orientation of chromophores in a sample, obtainable through LD. To perform an $FDLD$ measurement on a commercial LD instrument, a long-pass edge filter must be selected, which has a cut-off threshold wavelength that lies between the excitation and emission wavelengths of the fluorophore in the sample. As fluorescence emissions are longer in wavelength than the excitation light used (Stoke's shifted), this means that only the fluorescent light will reach the PMT and be detected.

Within the software settings of the instruments, it is possible to record a spectrum in two modes: one where the HT voltage is fixed and the varying DC trace is recorded; and in the other mode the DC output is fixed at 1, and one only needs to invert the trace from the AC channel to provide the $FDLD$ spectrum, as defined in Equation 2.17. If the spectrum is recorded using a fixed HT, then the both the AC and DC traces need to be used to calculate the $FDLD$ spectrum using

Equation 2.24.

2.5 Conclusions

In this chapter we have reviewed the theory behind LD, and how an instrument translates the currents generated in its PMT detector during a measurement into an LD signal. We then described our $FDLD$ experimental configuration — where the PMT is kept facing the propagation direction of the incident light and a high quality long-pass edge filter is placed in front of it, to block transmitted incident light, whilst allowing longer wavelength fluorescence emissions to pass freely — and defined $FDLD$ as the difference in fluorescence emission intensity following excitation with incident light polarised parallel and perpendicular to the orientation axis of a sample, respectively. The chapter closes with a method we propose will allow the calculation of $FDLD$ spectra from the currents generated in a PMT, much like is done in LD.

CHAPTER 3

Fluorescence detected linear dichroism of small molecules oriented on polyethylene film

3.1 Introduction

As stated in Equation 2.17, we define $FDLD$ as the difference in the fluorescence emission intensity from a sample, following excitation with light polarised parallel to the molecular orientation axis and light polarised perpendicular to that axis, respectively. Our initial proof of concept $FDLD$ experiments focussed on recording the spectra of small fluorescent organic molecules, oriented on stretched oxidised polyethylene films (PE^{OX}) [35]. Orienting molecules on stretched polymer films has been used for decades as a means to determine the polarisation directions of their electronic transitions, and the recent development of PE^{OX} has meant that this simple technique can be used for a wider range of compounds [35]. Anthracene (Figure 3.1A) is a molecule which has been well studied using LD [10, 35, 53–55], and so recording its $FDLD$ spectrum was an ideal starting point. It possesses two allowed transitions in the ultraviolet region: a long wavelength ^1L_a band at 379 nm and a short wavelength ^1B_b band at 254 nm — and following both of these excitations, some molecules return to the ground state through a radiative process [56].

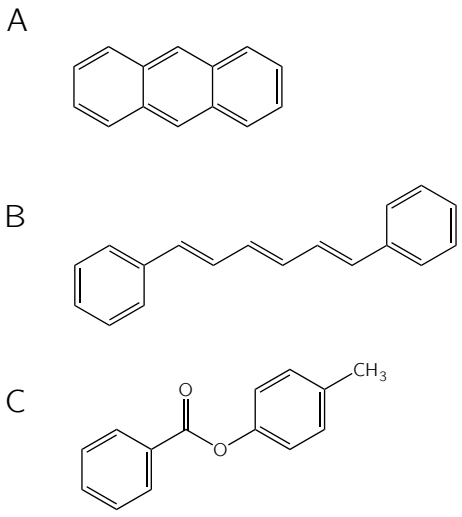

Figure 3.1: *Small fluorescent molecules used in stretched film $FDLD$ experiments. A: anthracene, B: trans-1,6-diphenyl-1,3,5-hexatriene (DPH), C: 4-methylphenyl benzoate (MPB).*

A representation of *trans*-1,6-diphenyl-1,3,5-hexatriene (DPH) is given in Figure 3.1B. DPH is another well studied molecule, particularly because of its use

as a fluorescent probe [57–60], but also because it is the smallest member of a class of linear diphenyl polyenes, which have intriguing spectroscopic properties [61, 62], and are used as model compunds for vitamin A [63]. The ground singlet state (S_0) and the first excited state (S_1) of DPH both have A_g symmetry, and so an $S_1 \leftarrow S_0$ transition is forbidden by the Laporte selection rule — that transitions must be accompanied by a change in parity [64]. The S_2 of DPH has B_u symmetry, and so an $S_2 \leftarrow S_0$ transition is allowed, and it is this band that is seen in a UV-visible absorption spectrum of the molecule. On the return to the ground state things are more complex. Fluorescence directly from the S_2 has been reported, as the $S_0 \leftarrow S_2$ transition is allowed, though generally it is the $S_1 \leftarrow S_2$ transition that occurs quickly through internal conversion [65]. As the S_1 and S_2 states are very close in energy, vibronic coupling between them allows the transition from the $S_1 \leftarrow S_0$ *via* the S_2 [66]. For these reasons DPH was also selected as an interesting molecule to investigate with $FDLD$.

Significantly less attention has been given to 4-methylphenyl benzoate (MPB, Figure 3.1C) in the literature, when compared with anthracene and DPH. It is reported to be an effective benzoate ester when used in Friedel-Crafts Fries rearrangement reactions [67], though there is next to nothing about its spectroscopy, which, as is demonstrated below, is quite interesting.

In this chapter we show the potential of fluorescence detected linear dichroism ($FDLD$) to be performed using a commercial linear dichroism (LD) instrument, by illustrating the information that can be extracted from spectra collected with stretched PE^{OX} and an appropriate long-pass edge filter.

3.2 Materials and methods

3.2.1 Materials

All chemicals were purchased from Sigma-Aldrich (Sigma-Aldrich Company Ltd., Dorset, UK) and used without further purification. The solvents used were chloroform (spectrophotometric grade, Sigma-Aldrich) and methanol (laboratory

grade, Fisher Chemicals).

3.2.2 Preparation of PE^{OX} films

3×5 cm^2 sections of polyethylene were cut from Glad® Snap Lock® bags, and oxidised in an Emitech K1050X Plasma Asher connected to an oxygen gas supply for 1 min at 50 W to generate PE^{OX} [35].

3.2.3 Spectroscopic techniques

Prior to measuring a spectrum, a section of PE^{OX} was clamped between the jaws of a mechanical stretcher (Figure 2.3), which were set to be 2.5 cm apart. The central cog of the stretcher was then turned to stretch the film 1.8×, so that the final distance between the jaws was 4.5 cm. To swell the film, 40 μL of solvent (without sample) was pipetted onto its surface and allowed to evaporate. The mechanical stretcher was then placed into a Jasco J-815 spectropolarimeter, and a baseline LD or $FDLD$ measurement was recorded using the parameters given in Table 3.1.

A range of high tension voltage (HT) values were tried for initial $FDLD$ measurements, and a value of 600 V was generally found to produce spectra with the best signal to noise ratio when using the molecules given in Figure 3.1 as analytes. Therefore, this value was used for all fixed HT $FDLD$ measurements in this thesis.

Table 3.1: Parameters used for film LD and $FDLD$ measurements

Parameter	LD	$FDLD$
D.I.T.	1 s	1 s
Bandwidth	1 nm	1 nm
Data Pitch	0.2 nm	0.2 nm
Scanning Mode	Continuous	Continuous
Scanning Speed	100 nm/min	100 nm/min
Accumulations	3	8
DC Output	Constant	Variable
HT Voltage	Variable	600 V

Following a baseline measurement, 40 μL of sample solution was deposited on to the film surface and the solvent was allowed to evaporate. The sample spectrum was then measured using the same parameters as was used for the baseline measurement. In cases where the sample molecule being used is not prone to photobleaching, it was found to be better to pipette additional sample solution onto the first film when recording a series of spectra with increasing analyte, instead of preparing fresh solutions of increasing concentration. This is because LD and $FDLD$ signals are not only proportional to the concentration of chromophore, but also to its alignment, and each sample aligns slightly differently on different films.

For LD measurements, where a variable HT voltage was used (Table 3.1), the baseline trace was simply subtracted from the sample trace to produce the final spectrum. As the $FDLD$ measurements were recorded using a fixed HT voltage, the baseline and raw sample spectra were calculated separately from the alternating current (AC) and direct current (DC) output of the instrument, using Equation 2.24. The resulting baseline traces were then subtracted from the sample traces to give the final $FDLD$ spectra, which are plotted in Section 3.3.

3.3 Results and discussion

The results of the LD and $FDLD$ spectroscopic measurements, recorded from small molecules oriented on stretched oxidised polyethylene (PE^{OX}), are given below. Unpolarised ultraviolet (UV)-visible and fluorescence emission spectra are also given, to illustrate how the choice of long-pass edge filter was made for $FDLD$ measurements.

3.3.1 Anthracene

Anthracene is a good test compound as its lowest energy short-axis polarised transition has overlaid vibronic progressions and significant intensity 'borrowed' from the 254 nm long-axis polarised transition [68]. It also shows different LD spectra (differing in both peak wavelength and sign) for oligomeric structures [35]. Anthracene's window between absorbance and emission is small, and so the long-pass edge filter had to be chosen carefully for $FDLD$ measurements.

Figure 3.2 shows the UV-visible absorbance and fluorescence emission spectra of anthracene deposited on a stretched PE^{OX} film, with the emission spectra being measured using an excitation wavelength of 254 nm. The bandwidths of the excitation and emission monochromators were both set at 1 nm.

The dashed grey line in Figure 3.2 indicates the cut-off wavelength of the Semrock 409 nm long-pass edge filter (Table 2.1). As can be seen from the figure, there is a slight overlap in the excitation and emission bands of the molecule. This filter was selected for $FDLD$ measurements to obtain a complete excitation spectrum, which in this case comes at the expense of some of the emission intensity that reaches the detector.

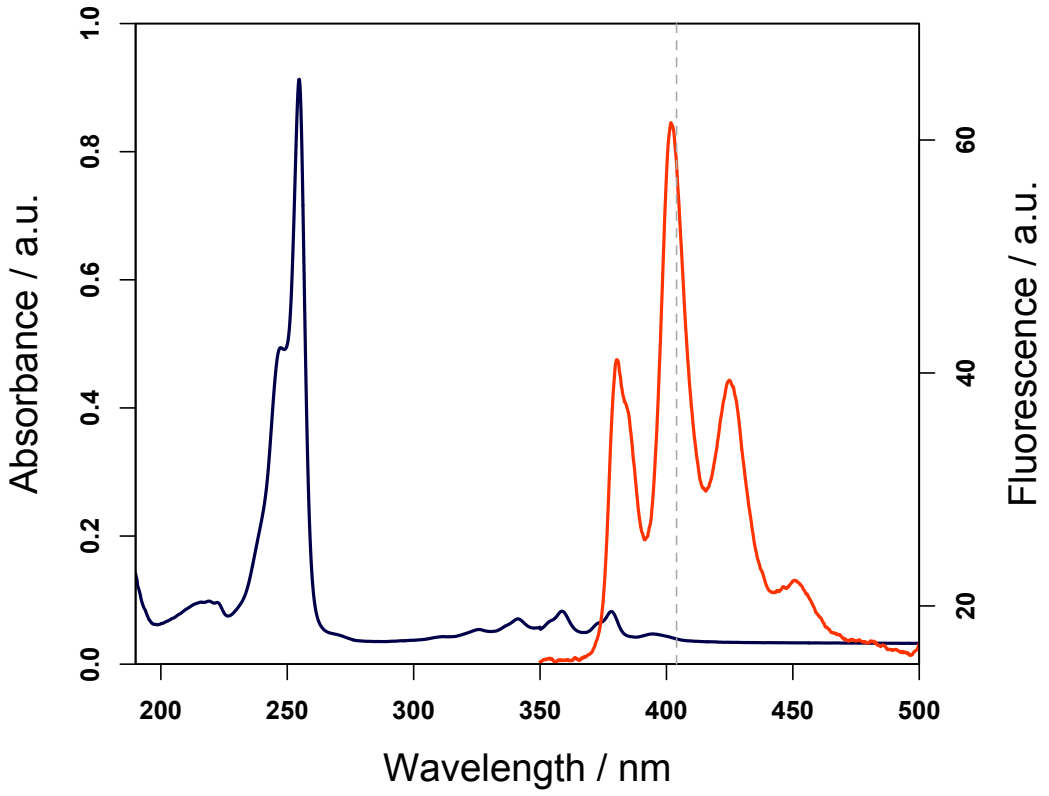

Figure 3.2: *Absorbance (blue) and fluorescence emission (red) spectra of 40 µL of 1 mg/mL anthracene solution (0.224 µmol) deposited on a stretched* PE^{OX} *film. The excitation wavelength for the emission spectrum was 254 nm. The dashed grey line shows the cut-off wavelength of the long-pass filter selected for recording* $FDLD$ *spectra.*

Figure 3.3 shows the LD and $FDLD$ spectra of monomeric anthracene. A Semrock long-pass edge filter 409 nm was placed in front of the photomultiplier tube (PMT) detector when measuring the $FDLD$ spectra. The instrument parameters given in Table 3.1 were used for recording all LD and $FDLD$ spectra in the figure. As anthracene is not prone to photobleaching, each set of spectra were recorded on the same section of PE^{OX}, with additional 40 µL aliquots of stock solution being added to the film prior to each spectrum being measured.

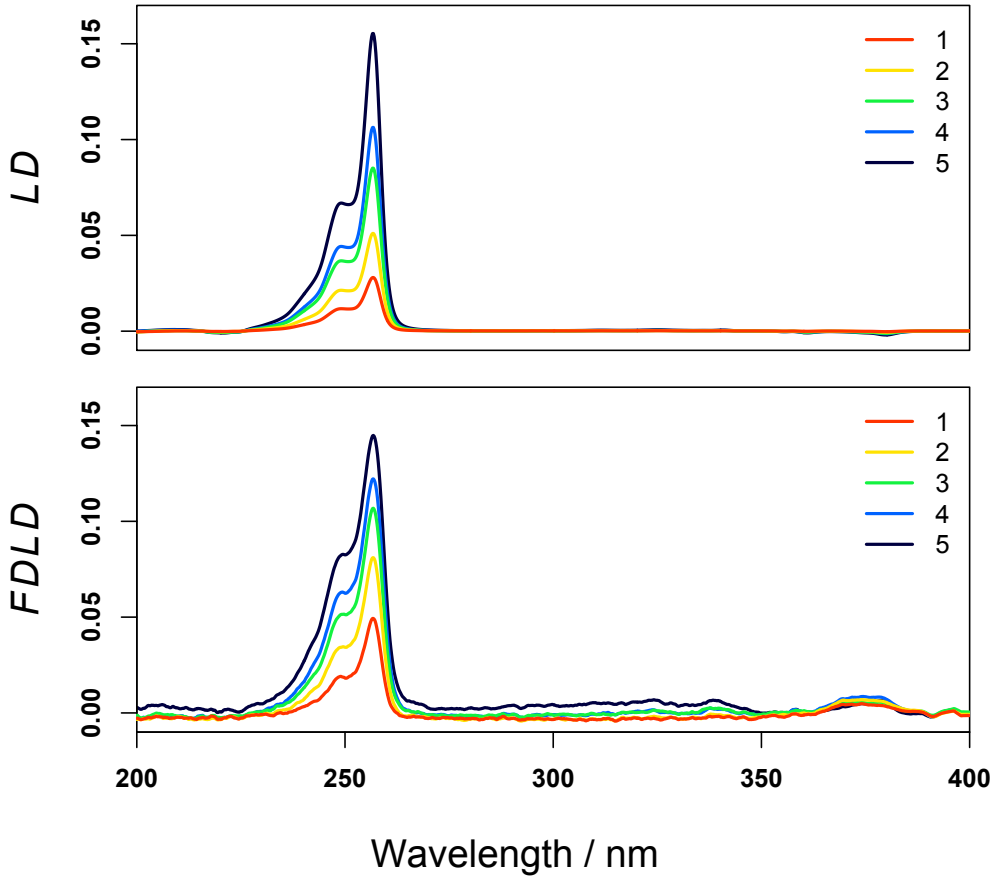

Figure 3.3: *LD (top) and FDLD (bottom) spectra of monomeric anthracene, oriented on stretched PE^{OX} films. The numbers given for each spectrum indicate the number of 40 µL aliquots of anthracene stock solution that was added to the film. For LD measurements a 10 µg/mL stock solution was used (following solvent evaporation, one 40 µL addition would leave 2.24 nmol of anthracene on the film), and for FDLD measurements a 100 ng/mL stock solution was used (leaving 22.44 pmol following solvent evaporation). Both LD and FDLD were measured using the settings given in Table 3.1, with the Semrock 409 nm long-pass edge filter being used for FDLD measurements.*

Figure 3.3 shows that in the region of the long axis transition (∼254 nm), the general shape of the *FDLD* spectra of anthracene is in good agreement with that of the *LD* spectra of monomeric anthracene, which is given in the same figure, and featured in a previous work by Razmkhah *et al.* [35]. However, as the figure shows, the concentrations of the stock solutions used differ by a factor of 100. This is because it was not possible to obtain *FDLD* spectra resembling the monomeric *LD* spectra when using equal concentrations.

A consequence of the low sample amount used for the *FDLD* measurements in

Figure 3.3 is that the spectra have a poor signal to noise ratio in the region of the short axis transition. This is improved when higher sample amounts are added to the film. An example of this is the LD and $FDLD$ spectra given in Figure 3.4. Here, 40 μL aliquots of a 10 μg/mL stock solution of anthracene in chloroform and methanol ($CHCl_3$(20):CH_3OH(80)) were deposited onto the PE^{OX} for each set of measurements.

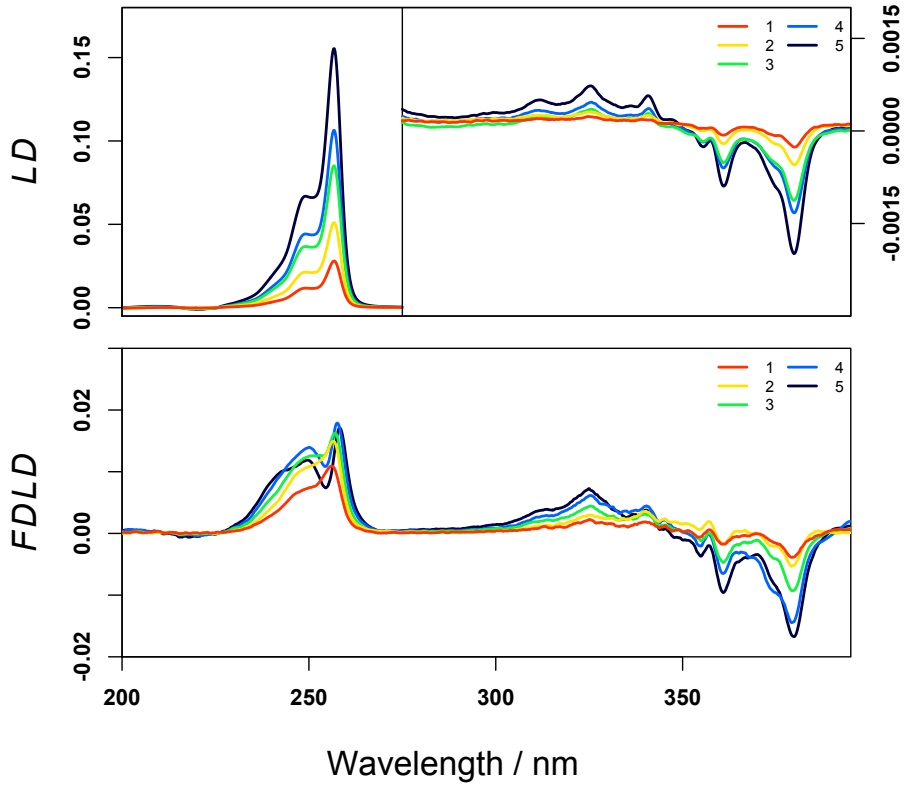

Figure 3.4: *LD (top) and FDLD (bottom) spectra of anthracene. For both sets of measurements, a 10 µg/mL stock solution in chloroform and methanol (20:80) was used to deposit anthracene on the PE^{OX}. The numbers in both figure legends indicate the number of 40 µL aliquots that were added to the film (leaving 2.24 nmol after solvent evaporation). These are the only film FDLD spectra presented in this work that were recorded using a variable HT voltage (fixed DC output). This was done to increase the dynamic range of the experiment, and in this case did not cause saturation (flattening) of the bands.*

From Figure 3.4, the 254 nm LD intensity is significantly larger than its $FDLD$, but the 379 nm $FDLD$ is larger than its LD reflecting the higher fluorescence quantum yield of the longer wavelength transition. Thus, in this example, $FDLD$ enhances the sensitivity of the weak long wavelength transition. Most noticeable from the

spectra, however, is the difference in the spectral shape of the short wavelength band when using the two techniques. It has been shown previously that when high sample amounts are deposited on the surface of PE^{OX}, an inversion of the 254 nm peak occurs due to layers of anthracene adopting higher order structures, such as dimers or trimers, and orienting differently on the film [35]. However, at these concentrations the inversion of the ^1B_b band peak at 254 nm begins to appear in the first of the $FDLD$ spectra, when only 2.24 nmol of anthracene had been deposited on the film. It is also apparent from the $FDLD$ spectra, that with increasing anthracene amounts, a shorter wavelength negative peak emerges at 248 nm, and a strong positive peak at 240 nm appears.

The long wavelength ^1L_a band of anthracene has a clear vibronic progression, which can be seen in both LD and $FDLD$ as illustrated in Figure 3.5. The fact we can see it in $FDLD$ also, with a good signal to noise ratio, is significant, as it may open the door to viewing such progressions when overlapping signals from non-fluorescent chromophores obscure them when using absorption methods. This may make it possible to see in greater detail how electronic states are effected by their environment.

The sign change of the near-UV short axis transition is a further interesting feature of anthracene's spectroscopy, and it can be clearly seen in both spectra in Figure 3.5. It arises as the ^1L_a band in anthracene is coupled to the strong ^1B_b band in the spectrum [54]. As the energy of the vibronic components of the ^1L_a band's progression increase, and become closer in energy to the ^1B_b band's excitation, the coupling becomes stronger [69], and the sign of the LD and $FDLD$ spectra changes around 340 nm.

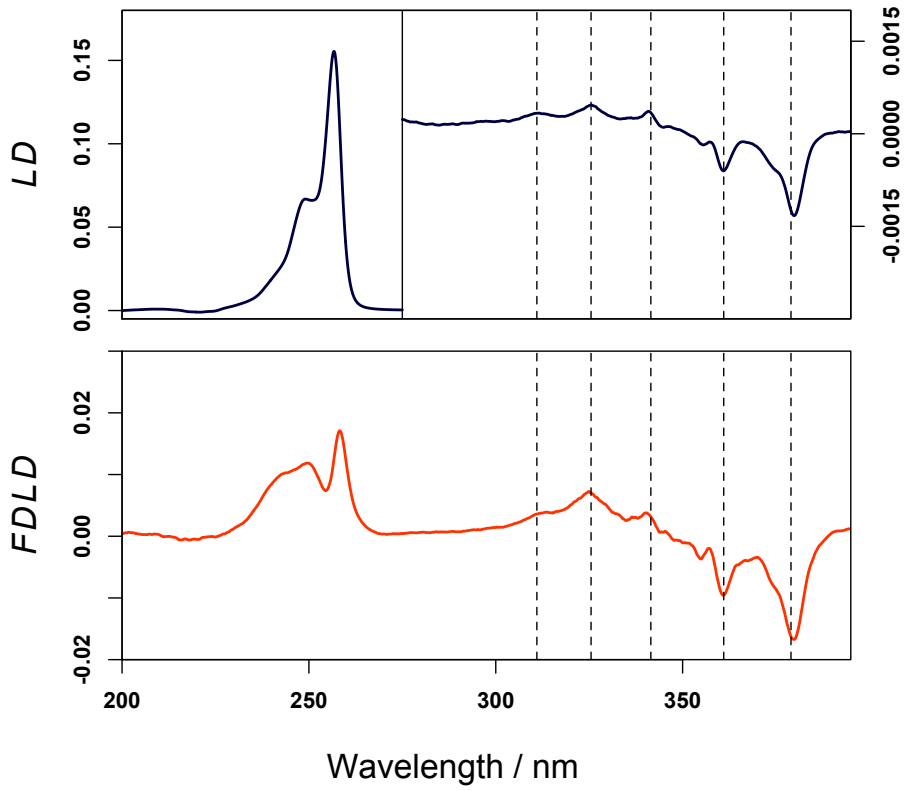

Figure 3.5: *The LD (top) and FDLD (bottom) spectra of anthracene after five 40 µL additions of a 10 µg/mL stock solution. These data are reproduced from Figure 3.4, with the addition of dashed lines to highlight the 1400 cm^{-1} vibronic progression at 379 nm, 361 nm, 342 nm, 325.5 nm and 311 nm.*

3.3.2 1,6-Diphenyl-1,3,5-hexatriene

The UV-visible absorbance and fluorescence emission spectra of 1,6-diphenyl-1,3,5-hexatriene (DPH) deposited on a stretched PE^{OX} film are given in Figure 3.6.

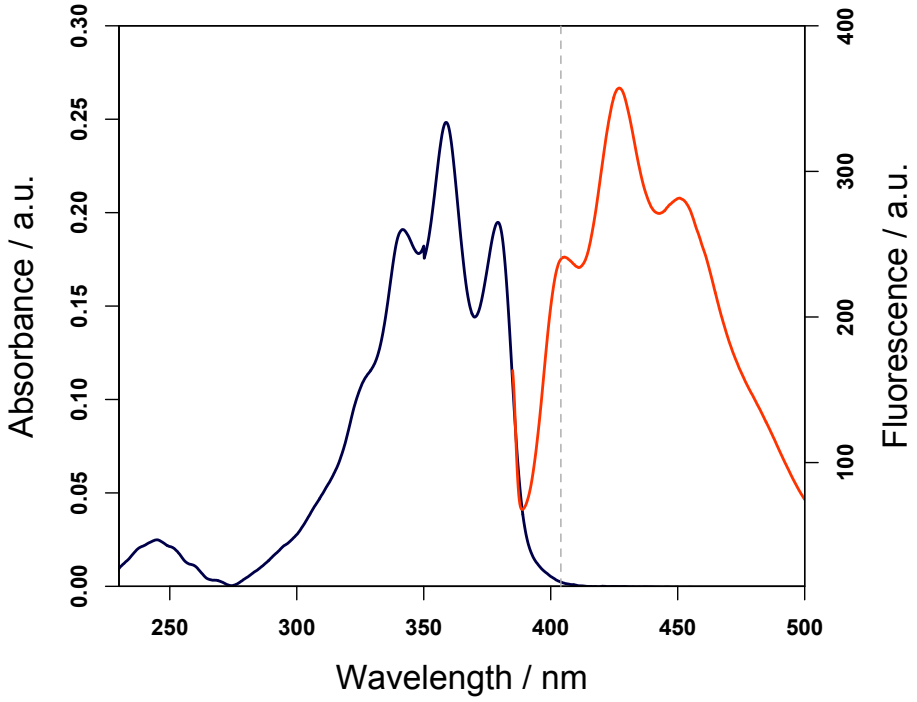

Figure 3.6: *Absorbance (blue) and fluorescence emission (red) spectra of 40 μL of a 1 mg/mL 1,6-diphenyl-1,3,5-hexatriene solution deposited on a stretched* PE^{OX} *film. The excitation wavelength used for the emission spectrum was 379 nm.*

The fluorescence emission spectrum in Figure 3.6 was measured using an excitation wavelength of 379 nm, and the bandwidths of the excitation and emission monochromators were set at 3 nm and 1 nm, respectively. The dashed grey line in the figure again represents the cut-off wavelength of the Semrock 409 nm long-pass edge filter, which was also selected for the $FDLD$ measurements of this molecule. In this case, there is a greater Stoke's shift when compared with anthracene, and so a full DPH excitation spectrum can be recorded with very little emission intensity being blocked by the filter.

DPH is a molecule with a particularly high quantum yield, so the stretched-film $FDLD$ data were able to be collected using pmol amounts, while the LD required nmol quantities to give a reasonable signal, showing the advantage of $FDLD$ for efficient fluorophores. The DPH spectra using both these techniques are given in Figure 3.7.

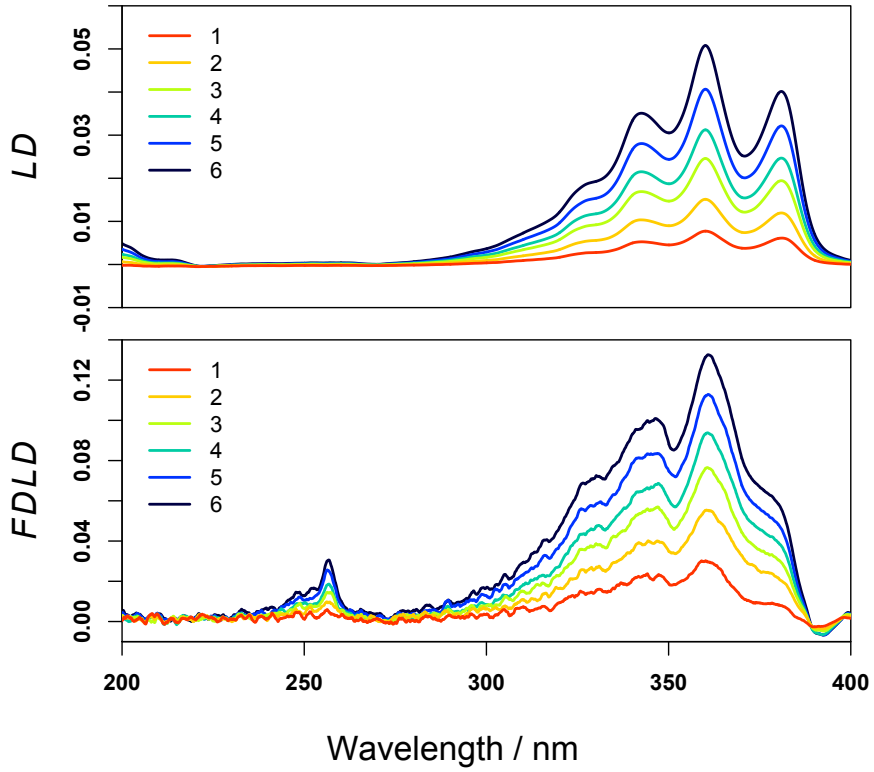

Figure 3.7: *The LD (top) and FDLD (bottom) spectra of DPH. The numbers in both figure legends indicate the number of 40 µL aliquots of stock solution that were added to the film. For LD measurements a 10 µg/mL stock solution was used (leaving 1.72 nmol after solvent evaporation) and for FDLD measurements a 10 ng/mL stock solution was used (1.72 pmol DPH after solvent evaporation). All spectra were recorded with the measurement parameters given in Table 3.1.*

The different vibronic components of the 300∼400 nm DPH transition illustrate features of $FDLD$ that need to be considered. The measured LD and $FDLD$ in Figure 3.7 look similar for the lowest three vibronic components of DPH, however, the highest component in the two sets of spectra is quite different. The underlying reason for this difference lies with the complex emission spectroscopy of DPH mentioned in the introduction to this chapter. DPH has at least two excited electronic states of similar energy (the lower state of ^1A_g symmetry whose transition to the ground state is forbidden and the higher ^1B_u state which is allowed) [61]. Non-radiative transfer between the states is possible resulting in different vibronic states having different quantum yields [70].

A further noticeable difference between the sets of spectra in Figure 3.7 is that the peak at 256.5 nm in the $FDLD$, which is also present in the unpolarised UV-visible

spectrum of Figure 3.6, appears to be completely absent from the LD spectra. Interestingly, this is in the region of the 0-0 transition of phenylethene (styrene), which is reported to be at 250 nm [71]. However, as styrene's emission is around 308 nm, and emissions of this wavelength would be blocked by the long-pass filter, it is unlikely that styrene contamination is what we are seeing here. It may be that this peak emerges due to DPH aggregates being formed on the film, which, as was observed with anthracene, $FDLD$ has increased sensitivity towards.

3.3.3 4-Methylphenyl benzoate

The UV-visible absorbance and fluorescence emission spectra of 4-methylphenyl benzoate (MPB) deposited on a stretched PE^{OX} film are presented in Figure 3.8. The figure also contains two dashed grey lines: one at the cut-off wavelength of the Semrock 300 nm long-pass edge filter and a second at the cut-off wavelength of the Semrock 341 nm long-pass edge filter. This is an example of when one has to think carefully about choosing a long-pass filter to use for $FDLD$ measurements. When using the 341 nm filter for MPB $FDLD$, it is possible to obtain a full excitation spectrum, however, it would seem from Figure 3.8 that a lot of the emission intensity is being blocked by the filter, in addition to transmitted incident light. Although in this case quality $FDLD$ spectra are still obtained using this filter, as is shown below.

It is also possible to collect MPB $FDLD$ spectra using a long-pass edge filter with a 300 nm cut-off wavelength. As is illustrated in Figure 3.8, this allows us to collect much more of the emission intensity of the fluorophore, however, we are unable to collect a spectrum over the full excitation range. $FDLD$ spectra of MPB recorded using this filter are also given below, where we found that we were able to collect data using much smaller amounts of sample.

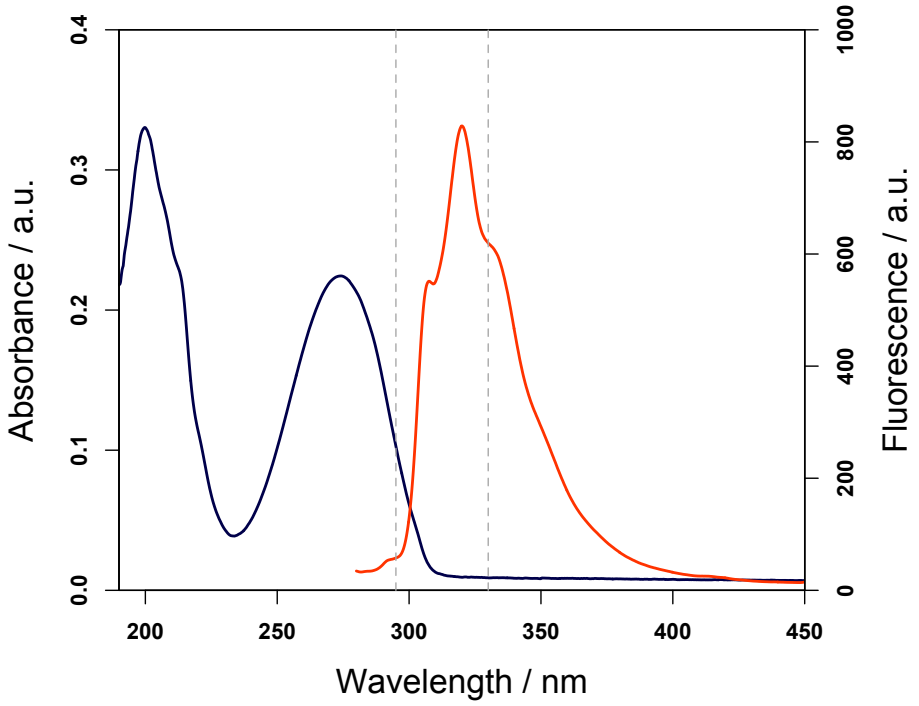

Figure 3.8: *Absorbance (blue) and fluorescence emission (red) spectra of 40 µL of 1 mg/mL 4-methyl phenylbenzoate solution deposited on a stretched* PE^{OX} *film. The excitation wavelength for the emission spectrum was 274 nm.*

The *LD* and *FDLD* spectra of MPB are presented in Figure 3.9. A Semrock 341 nm long-pass edge filter was used to collect the *FDLD* spectra displayed in this figure, and the parameters given in Table 3.1 were used for both *LD* and *FDLD* measurements.

MPB is another extremely efficient fluorophore. Its *FDLD* spectrum shows a greatly enhanced signal magnitude for its long wavelength transitions when compared with *LD*, further illustrating the potential increased sensitivity of *FDLD* measurements. The enhancement for the shorter wavelength band is less but still significant.

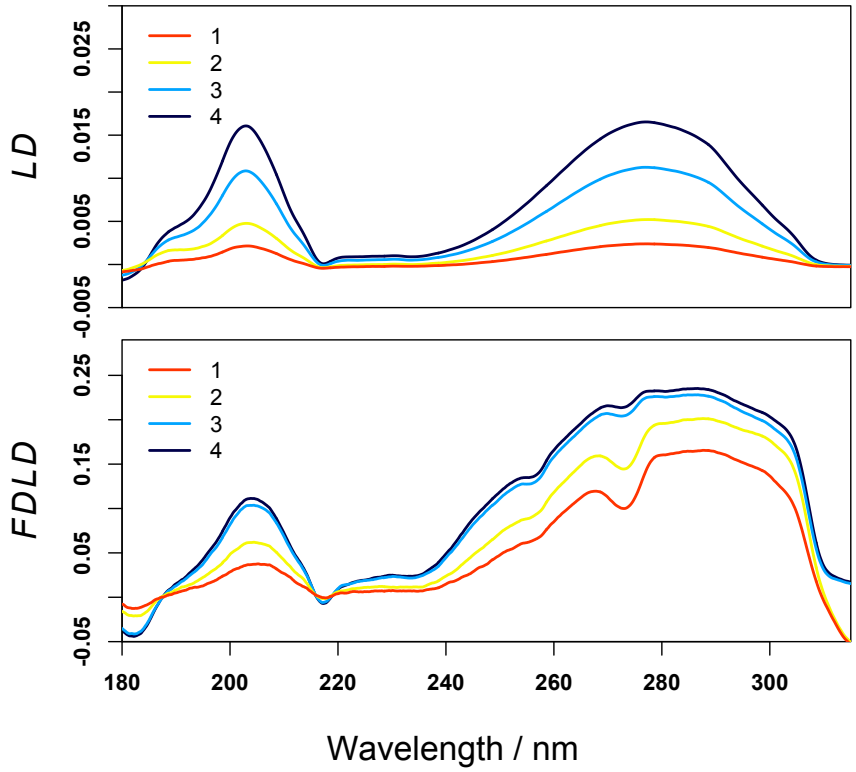

Figure 3.9: *The LD (top) and FDLD (bottom) spectra of MPB. The legend numbers indicate the number of 40 µL aliquots of MPB stock solution were pipetted into the surface of the* PE^{OX} *film. A 10 µg/mL stock solution was used for both sets of measurements, which, after solvent evaporation, left 1.88 nmol of MPB. All spectra were measured using the parameters given in Table 3.1. A Semrock 341 nm long-pass edge filter was used for FDLD measurements.*

The quantities of MPB used for the experiments in Figure 3.9 were chosen to be the same for both *LD* and *FDLD* to better compare the two techniques, and to demonstrate the increased measurement sensitivity of *FDLD*. However, though a greater amount of structure can be seen in the *FDLD* spectra, it is also clear that the detection system is beginning to be saturated and the bands are flattened.

The *FDLD* spectra of MPB were measured at lower concentrations to avoid the problem of absorption flattening, and the result is given in Figure 3.10. Here, the Semrock 341 nm long-pass edge filter was again used for the measurements.

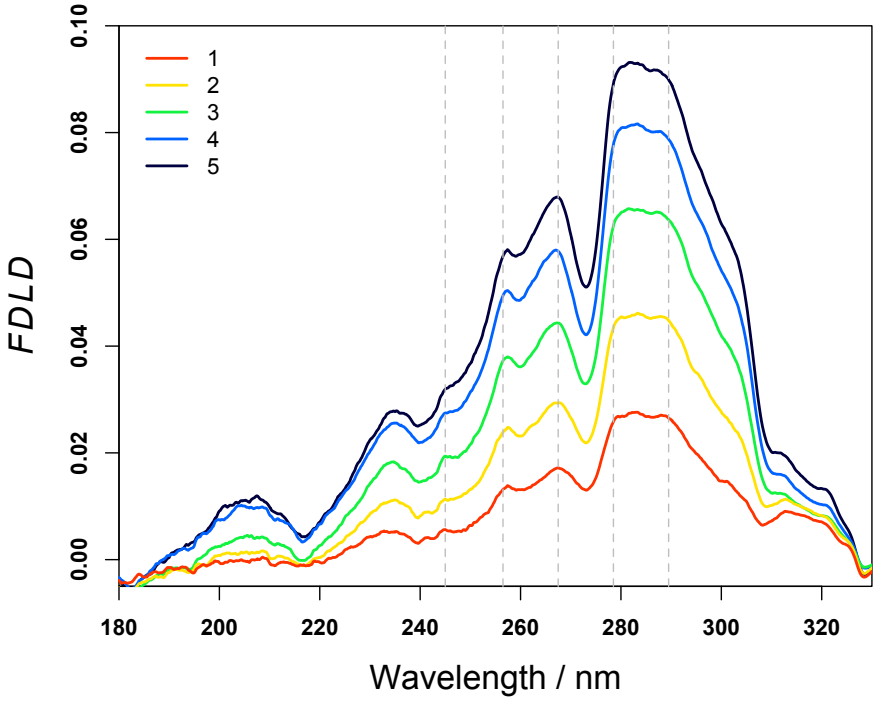

Figure 3.10: *FDLD spectra of MPB recorded using a Semrock 341 nm long-pass edge filter. For each measurement 40 µL of 500 ng/mL MPB solution in methanol was added to the surface of the film and allowed to evaporate (leaving 94.23 pmol of MPB) before recording a spectrum. The numbers in the legend indicate the number of aliquots that were added. All spectra were measured using the FDLD measurement parameters given in Table 3.1. The dashed lines at 289.5 nm, 278.5 nm, 267.5 nm, 256.5 nm and 245 nm indicate a 1457 cm^{-1} vibronic progression and referred to in Table 3.2.*

Figure 3.10 shows the *FDLD* spectra of MPB at lower amounts than were used for the spectra in Figure 3.9. The improved resolution of the vibronic structure within the bands compared with *LD* is striking, and we are able to pick out a 1457 cm^{-1} progression from the 289.5 nm maximum. The measured progression slightly differs from a theoretical one originating from that position, which is illustrated in Table 3.2. However, the clarity with which such vibronic detail can be obtained when using *FDLD* compared with absorption methods shows the potential advantage of using the technique to provide additional information about a molecule.

Table 3.2: Comparison of the observed positions of the vibronic progression shown in Figure 3.10 with theoretical values assuming a 1457 cm^{-1} progression from the band with maximum at 289.5 nm.

Calculated position of 1457 nm^{-1} vibronic components	**Observed position**
289.5 nm	289.5 nm
277.78 nm	278.5 nm
266.98 nm	267.5 nm
256.98 nm	256.5 nm
247.71 nm	245 nm

A further point about the spectroscopy of MPB deposited on stretched polymer films, is that its fluorescence excitation spectra show a hypsochromic shift in the 297 nm monomer peak to 280 nm with additional amounts of MPB. This is illustrated using the conventional unpolarised fluorescence excitation spectra in Figure 3.11. The spectrum was recorded on a Jasco FP-6500 fluorescence spectrophotometer. The emission wavelength for the measurement was fixed at 330 nm, and the bandwidth of both the excitation and emission monochromators was set to 3 nm.

The blue shift in the monomer peak of MPB is possibly due to the formation of H-aggregates on the film. H-aggregates are formed when the arrangement to molecules in a sample is such that the coupling between their dipoles leads to a blue shift in the absorption band [72]. Similarly, J-aggregates are formed when the molecules are stacked so that their transition dipoles are parallel, which causes a red (bathochromic) shift in their absorbance spectrum [72]. The fluorescence from H-aggregates is often strongly self-quenched, however, a number of reports show that this is not always the case, particularly when the sample is on film [73, 74].

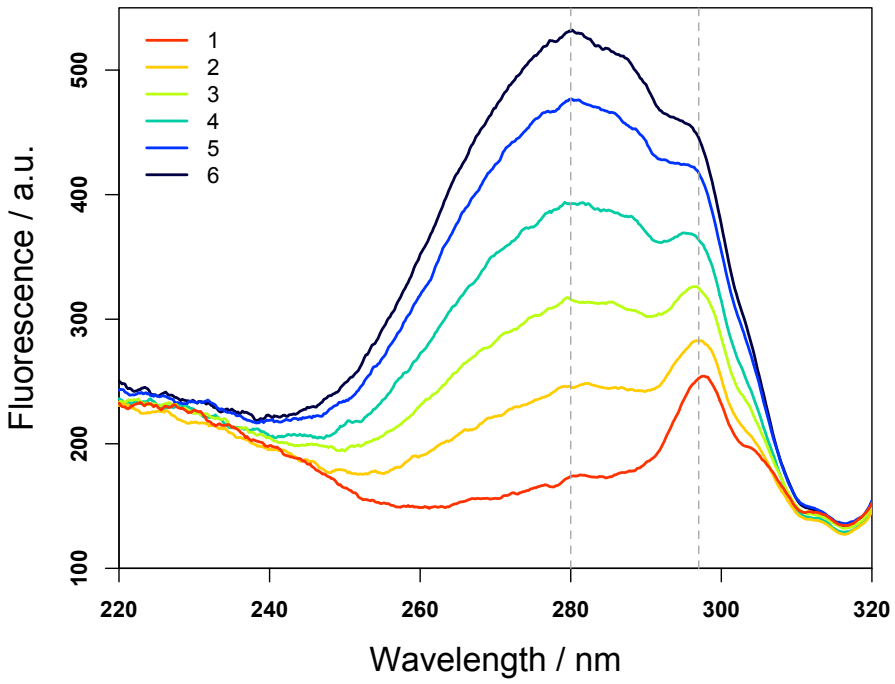

Figure 3.11: *Fluorescence excitation spectra of MPB on stretched PE^{OX} film. The legend numbers indicate the number of 40 µL aliquots of 10 µg/mL MPB stock solution was added to the film. The bandwidths of both the excitation and emission monochromators was set to 3 nm. The emission wavelength was set at 330 nm. The dashed lines illustrate the hypsochromic shift of the 297 nm monomer peak with increasing amounts of MPB.*

A final example of *FDLD* spectra measured using MPB is given in Figure 3.12. These spectra were recorded using a Semrock 300 nm long-pass edge filter, instead of the 341 nm filter that was used in the above *FDLD* measurements. As in this case much more of the emission intensity of the fluorophore is reaching the detector, we were able to use a lower amount of sample deposited on the film surface, with each 40 µL deposit of 10 ng/mL MPB solution leaving 1.88 pmol behind following solvent evaporation.

Figure 3.12 shows that the relative magnitude of peaks in these spectra are quite different to when higher amounts of MPB are deposited on the film. Although we are not able to see the longer wavelength maximum of the monomer peak, at 297 nm in Figure 3.11, it would appear that the 256.5 nm peak from Figure 3.10 is also from the monomer, as here it has an increased magnitude when compared with

the 280 nm aggregate peak. It may also indicate that the 280 nm peak may have an overlaid contribution from a red-shift of the 256.5 nm peak due to J-aggregates also being formed on the film. This is a further illustration of the significant effect that the stacking of MPB molecules deposited on a film has on its spectroscopy, and of the increased insight that an be obtained when using a fluorescence detection methodology.

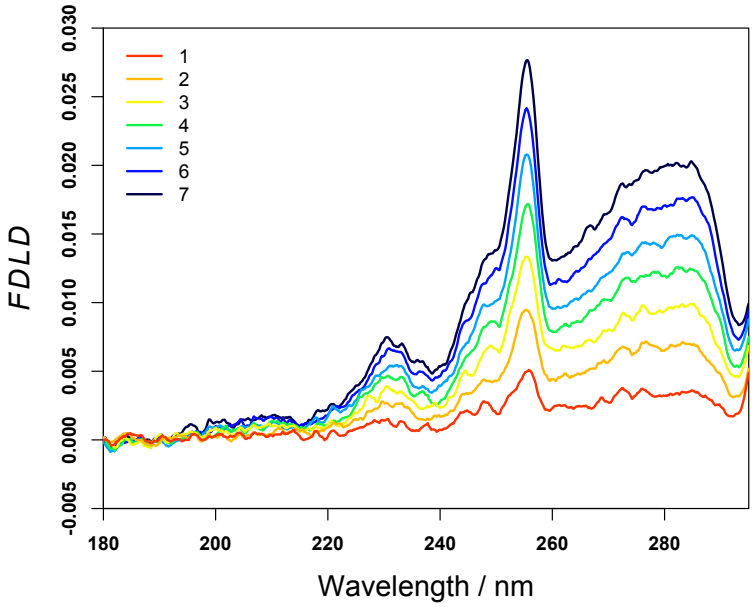

Figure 3.12: *FDLD spectra of MPB recorded using a Semrock 300 nm long-pass edge filter. For each measurement 40 µL of 10 ng/mL MPB solution in methanol was added to the surface of the film and allowed to evaporate (leaving 1.88 pmol of MPB) before recording a spectrum. The numbers in the legend indicate the number of aliquots that were added. All spectra were measured using the FDLD measurement parameters given in Table 3.1.*

3.4 Conclusions

Building on the theory detailed in Chapter 2, the results given in this section show that we can actually record *FDLD* spectra using a commercial instrument, adapted for *LD* spectroscopy. The *FDLD* spectra of a number of small organic molecules, deposited on stretched PE^{OX} films, were the starting point for our development of the method, due to the simplicity with which the mechanical stretching apparatus can orient a sample containing multiple copies of a single

molecule. We have confirmed that $FDLD$ spectra may be calculated from the AC and DC components of the instrument output, when recording with a fixed HT voltage using Equation 2.24. We have also shown that $FDLD$ spectra can be obtained using a variable HT voltage, as was done for the anthracene $FDLD$ spectra in Figure 3.4. Varying the HT voltage increases the dynamic range of the experiment, and so one does not have to lower it manually to record regions of high fluorescence emission that may otherwise flood the detector.

As demonstrated above, $FDLD$ can give similar information to that obtained from LD, often with only a fraction of the amount of sample. For all of the molecules used in the experiments in this section, their $FDLD$ spectra showed a large enhancement in signal magnitude compared with their LD spectra. The two most striking examples of this were: DPH, where we could see a similar signal magnitude with 1×10^{-3} of the amount of sample; and MPB, where comparing Figures 3.9 and 3.12 shows we can achieve similar signal magnitudes with 1×10^{-4} of the amount of sample.

In some cases, however, $FDLD$ spectra show differences when compared with LD spectra. $FDLD$ spectra seem to show an increased resolution of the vibrational structure of molecule, as is very apparent in the MPB spectra, and also has an increased sensitivity to oligomeric species, as we observed in the anthracene measurements. In the anthracene spectra, we can record the monomer spectrum using both LD and $FDLD$, which is demonstrated in Figure 3.3. It is only when $\sim$2.24 μmol of anthracene has been deposited on the film we begin to see the oligomeric species in LD. However, the anthracene $FDLD$ spectra show oligomeric species with much lower sample amounts.

Comparing the two sets of spectra of MPB, the increased ability to detect small signals when using $FDLD$ is very apparent. The LD spectra have poor resolution within the absorption bands, and seem to show only aggregate peaks, even when small amounts of sample are deposited on the film. In contrast, the $FDLD$ spectra show additional fine structure within the bands, even when we used the same sample as we used to record the LD spectra. The sensitivity of $FDLD$ then allows even smaller sample amounts to be recorded, which, as is shown is Figures 3.10 and 3.12,

reveals bands that are not observed in the absorption spectra, which we propose originates from the excitation of the monomer.

These measurements recorded using polymer films to orient a sample acted as a valuable tool for optimising our $FDLD$ methodology. They were key to working out the long-pass filters that should be selected, which software settings should be used for a given measurement, and how the information gained from $FDLD$ compares with that obtained from conventional LD. As the ultimate goal is for $FDLD$ to be used with biological systems, and a more useful alignment technique for these is Couette flow, the next chapter describes the use of this alignment method to record the $FDLD$ spectra of biological systems: deoxyribonucleic acid (DNA) with fluorescent probes and M13 bacteriophage.

CHAPTER 4

Couette flow fluorescence detected linear dichroism of DNA binding dyes

4.1 Introduction

The information for creating the fundamental components that combine to form all living things are encrypted into DNA. A scientific understanding of every aspect of this molecule, and its interactions with its environment, is therefore crucial to our understanding of the processes of life. In the field of medicine, the number of drugs approved for therapeutic use is growing at an exponential rate, and in the US the number reached 1453 by December 2013 [75]. It is therefore also crucial to our understanding of the efficacy and safety of these drugs that we understand the ways in which they interact with DNA and effect its function. In this chapter, some of the insights linear dichroism has provided to this subject are reviewed, and we show that in some cases fluorescence detected linear dichroism enhances our ability to obtain such information.

Aside from molecules that bind covalently to DNA, such as the well known chemotherapeutic cisplatin and the nerve gas alkylating agents, small molecules bind non-covalently to DNA through three established mechanisms: intercalation, groove binding, and external binding [76]. Intercalation — a mechanism first proposed by Lerman in his study of acridines in 1961 [77] — occurs when planar molecules insert between adjacent bases of the DNA chain, without breaking any hydrogen bonds of the Watson-Crick base pairs. Therefore, intercalated molecules stack perpendicular to the backbone of the DNA. Due to the geometry of the base pairs, the interhelical spaces between the two strands that form the backbone are of unequal size. The smaller of the two measures approximately 12 Å in B-DNA, and is called the minor groove. The larger, at approximately 22 Å, is called the major groove. Molecules binding to either of these sites are angled more in line with the DNA's major axis, with their long axis transition moments tending to lie between 35° and 45° from it [78]. Molecules may also bind electrostatically to external sites of DNA, however, this mode of binding is generally random and will not be considered further is this study.

Linear dichroism has a long history of being used to investigate the way in which small molecules interact with double stranded DNA [79–81]. Its sensitivity to the relative orientations of chromophores in a sample mean that molecules that are

intercalated into DNA, with their molecular long axis perpendicular to the DNA's orientation axis, are easily distinguishable from those that are groove bound, lying with their long axes less than 45° from this axis. The latter gives rise to positive *LD* signals for their long axis polarised transition, whereas the former results in a negative signals for the same transition.

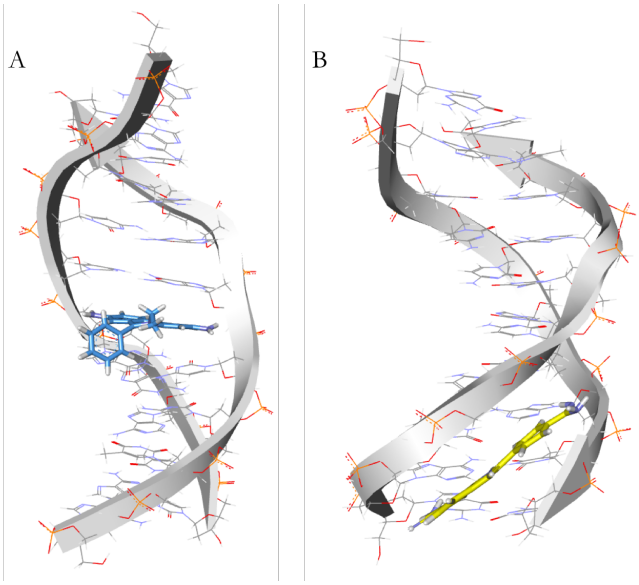

Figure 4.1: *Two of the modes in which small molecules can bind to double stranded DNA: A shows a molecule intercalated between adjacent base pairs, and B shows a molecule bound to the minor groove. These images were generated by Dr Shirin Jamshidi, King's College London, and have not previously been published.*

B-form DNA has its own intrinsic absorbance at 260 nm, mainly due to the $\pi^* \leftarrow \pi$ transitions of the bases that lie perpendicular to the DNA's molecular long axis (their combination giving an apparent transition dipole moment angle of 86°) [82]. *LD* spectra in this region are dominated by this absorption band, and the ultra-violet spectral features of bound small molecules are often overwhelmed, or obscured by its presence. As DNA is not a fluorescent molecule, in cases where the bound small molecules are fluorophores, these features may be unveiled by *FDLD*. As mentioned in Chapter 2, this increased measurement selectivity was one of the major motivations in our decision to develop this technique, along with the potential for increased measurement sensitivity, which is intrinsic to fluorescence measurements when compared with absorption methods. These effects are illustrated below using four fluorescent molecules (ethidium bromide, propidium iodide, 4',6-diamidino-2-phenyindole, and Hoechst 33258) bound to DNA.

This chapter closes with a proposed novel application of $FDLD$ to detect pathogenic bacteria using wild-type M13 bacteriophage as a bio-sensor, where the intrinsic fluorescence of the tryptophan residues on the pVIII capsid proteins give rise to strong $FDLD$ signals.

4.1.1 Fluorescent molecules

The fluorescent DNA stains used in this work are shown in Figure 4.2. Ethidium bromide was first synthesised by Watkins and Woolfe of the Boots company in 1952, as an enhancement on the trypanocidal activity of dimidium bromide in animals [83]. Since then, it has become one of the most widely used and extensively studied fluorescent DNA probes on the market. It binds to DNA through intercalation, as described above, and this action produces a striking enhancement of its fluorescence quantum yield due the ethidium ions being less exposed to solvent molecules [84]. Similarly, propidium iodide also binds to DNA through intercalation, which is accompanied by an increase in fluorescence intensity.

4',6-diamidino-2-phenyindole (DAPI) was first synthesised in 1971, once again for its enhanced trypanocidal activity [85]. The compound Hoechst 33258 was synthesised by the Hoechst AG company, and both it and DAPI are also very commonly used as fluorescent DNA stains.

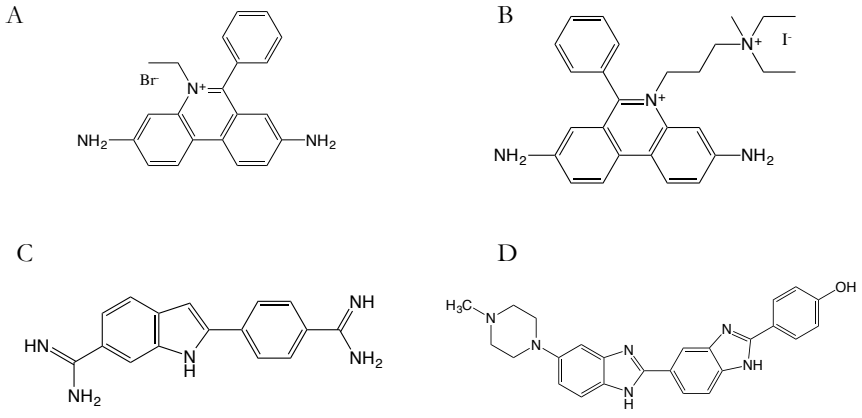

Figure 4.2: *Structures of Small Molecules. A: Ethidium Bromide B: Propidium Iodide C: DAPI D: Hoechst*

4.1.2 Couette flow orientation

M. Couette published the first experimental investigation of the flow of a liquid held between two rotating, concentric cylinders in 1887, and the rheological technique still bears his name today [86]. It is extremely useful for orienting biological macromolecules in solution, due to the relatively small sample volumes required when compared with other methods, such as flow-through channels. It was first used in the context of flow linear dichroism by A. Wada in 1964. In this setup, the annular gap between the outer and inner cylinders was 0.7 mm, and 2.6 mL of sample was required for a single experiment [87]. The more recent innovation by Marrington *et al.*, here at the University of Warwick, of the micro-volume Couette flow cell significantly reduced the sample volume requirement to 60 μL [5]. This made it possible for *LD* to probe the structure of protein fibres, which are often obtained in such small amounts that 2.6 mL would not be easily obtained. It is this Couette flow setup that is used in all experiments described in this work.

4.2 Materials and methods

This section gives the details of all of the chemicals and solvents that were used to prepare the samples for spectroscopic analysis, in addition to the instruments, materials and settings used for all measurements.

4.2.1 Materials

Deoxyribonucleic acid (DNA) sodium salt from salmon testes was purchased from Sigma-Aldrich and used for all DNA experiments. Stock solutions were prepared by weighing out approximately 10 mg of DNA, and leaving it to reconstitute in 10 mL of filtered and deionised water (18.2 MΩ·cm, Millipore Direct-QTM) overnight at 4°C. The final concentration of the stock solution was then measured using a Jasco V-660 UV-visible spectrometer, using the extinction coefficient: ε_{260} = 6600 $M^{-1}cm^{-1}$ [88].

The molecules ethidium bromide (EtBr), propidium iodide (PI),

4,6-diamidino-2-phenyindole (DAPI) and Hoechst 33258 were purchased from Sigma-Aldrich and used as received. Stock solutions were made by dissolving the powders in filtered and deionised water, and their concentrations were again determined spectrophotometrically using extinction coefficients of: $\varepsilon_{480} = 5680$ $M^{-1}cm^{-1}$ (EtBr, [89]), $\varepsilon_{494} = 5900$ $M^{-1}cm^{-1}$ (PI, [90]), $\varepsilon_{340} = 27000$ $M^{-1}cm^{-1}$ (DAPI, [91]), and $\varepsilon_{338} = 42000$ $M^{-1}cm^{-1}$ (Hoechst 33258, [92]).

Samples of M13 bacteriophage were a gift from Professor Tim Dafforn at the University of Birmingham.

4.2.2 Spectroscopic techniques

All UV-visible absorption measurements were recorded using a Jasco V-660 spectrophotometer. Samples of stated concentrations were prepared in 1.5 mL Eppendorf tubes, before being transferred to a 0.1 cm quartz cuvette and placed in the spectrometer. Baseline measurements were always taken separately, and subsequently subtracted, so to eliminate the possibility of an error due to baseline data propagating through the sample spectra, which may happen if the baseline solution is contaminated and the machine is set to subtract its spectrum automatically. Table 4.1 provides the measurement parameters for the UV-visible measurements conducted in this work.

Table 4.1: Parameters used for UV-visible absorbance measurements

Parameters	
D.I.T.	1 s
Bandwidth	1 nm
Data Pitch	0.2 nm
Scanning Mode	Continuous
Scanning Speed	100 nm/min
Accumulations	1

LD and *FDLD* measurements were made on a Jasco J-815 following the procedure

outlined in Chapter 2, using a fixed DC output. The parameter settings of the instrument are given in Table 4.2. For $FDLD$ measurements of DNA-EtBr and DNA-PI, a Semrock 568 nm long-pass filter was piggy-backed on top of a Thorlabs 550 nm long-pass filter and placed in front of the PMT using the holder illustrated in Figure 2.7. $FDLD$ measurements of DAPI and Hoechst 33258 were performed in a similar way, using Semrock 409 nm and Thorlabs 400 nm long-pass filters. Equation 2.25 was used to convert the instrument output to $FDLD$ spectra.

Table 4.2: Parameters used for LD and $FDLD$ measurements

Parameter	LD	$FDLD$
D.I.T.	1 s	1 s
Bandwidth	1 nm	1 nm
Data Pitch	0.2 nm	0.2 nm
Scanning Mode	Continuous	Continuous
Scanning Speed	100 nm/min	100 nm/min
Accumulations	3	8
DC Output	Constant	Constant
HT Voltage	Variable	Variable

4.3 Results and discussion

Presented below are the results of the spectroscopic measurements recorded using DNA-dye complexes and samples of M13 bacteriophage, in addition to a discussion of what they show, and in particular, how using $FDLD$ adds to the information that is obtainable using other techniques.

4.3.1 Ethidium bromide and propidium iodide

The UV-visible spectra of 50 μM EtBr with a range of DNA concentrations are given in the top left panel of Figure 4.3. It is clear that the addition of DNA has a dramatic effect on both the short and long wavelength absorption bands, with

a large decrease in absorption in the near-UV and a slight increase along with a bathochromic shift in the visible region. These are common characteristics of DNA intercalators [93]. The top right panel of Figure 4.3 tracks the absorbance at 480 and 526 nm, illustrating the red shift in the absorbance maximum in this region.

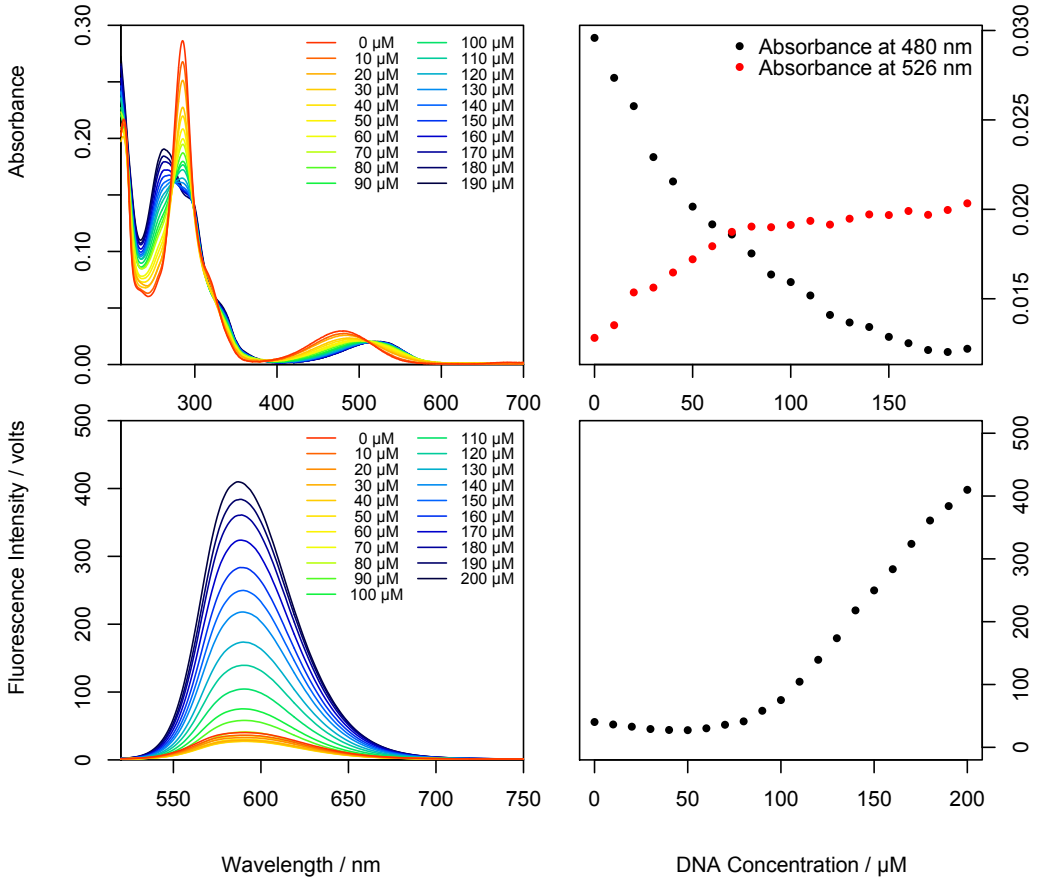

Figure 4.3: *UV-visible absorbance and fluorescence emission spectra of 50 µM Ethidium Bromide and a range of concentrations of salmon sperm DNA. Top left: UV-visible absorbance spectra. Top right: Plot of the peak values at 480 and 526 nm, showing the bathochromic shift of the EtBr peak upon binding DNA. Bottom left: Fluorescence emission spectra, recorded using an excitation wavelength of 506 nm. Bottom right: Plot showing the change in fluorescence intensity with DNA concentration, highlighting the increase in quantum yield when EtBr is bound to DNA.*

The bottom panels of Figure 4.3 show the fluorescence emission spectra of 50 μM EtBr with increasing concentrations of DNA. All of the spectra were measured using the same samples as were prepared for the UV-visible absorption spectra. They illustrate the approximately 25-fold increase in the fluorescence emission intensity from EtBr following the addition of DNA, which has been shown previously [94].

The reason for this increase in the quantum yield of the fluorophore is that when it is intercalated between the base pairs of DNA, there is a reduction in proton transfer to solvents molecules, which occurs rapidly when the free dye is dissolved in a protic solvent [84].

Figure 4.4 shows the UV-visible Couette flow LD spectra of 200 μM DNA with increasing concentrations of EtBr. This result is in agreement with LD spectra of DNA-EtBr complexes found in the literature [5, 95]. The DNA-only spectrum, shown in red in the figure, has a strong negative signal at 260 nm, reflecting the $\pi^* \leftarrow \pi$ transitions of the DNA bases, which are oriented at 86° from the long axis of the molecule [82]. With increasing EtBr concentration, the negative signal in this region increases, due to the contribution of the long axis polarised transition of the eithidium ion. The sign of this signal in the LD spectra is evidence of the intercalating mode of binding that the ethidium cation adopts in the complex.

It is also apparent from Figure 4.4, however, that it is very difficult to separate the signals coming from the DNA absorbance from those coming from EtBr, as they overlap one another in the UV region of the spectra. As the EtBr changes the orientation parameter (S in Equation 2.5), the DNA signal can not simply be subtracted. This lack of selectivity is a common problem with many spectroscopic techniques. Whilst in nuclear magnetic resonance (NMR) spectroscopy it is possible to reduce selectivity problems by taking actions such as substituting to a deuterated solvent, this is not achievable using absorbance methods. Numerical methods for resolving overlapping bands in absorbance spectra have been proposed by a number of investigators, which generally involve fitting either Gaussian or Lorentzian distribution to the band shapes [96–99]. However, these methods contain an error that can be large, especially if an inappropriate distribution is selected for the band shape [97]. Simply using a more selective technique would avoid this issue.

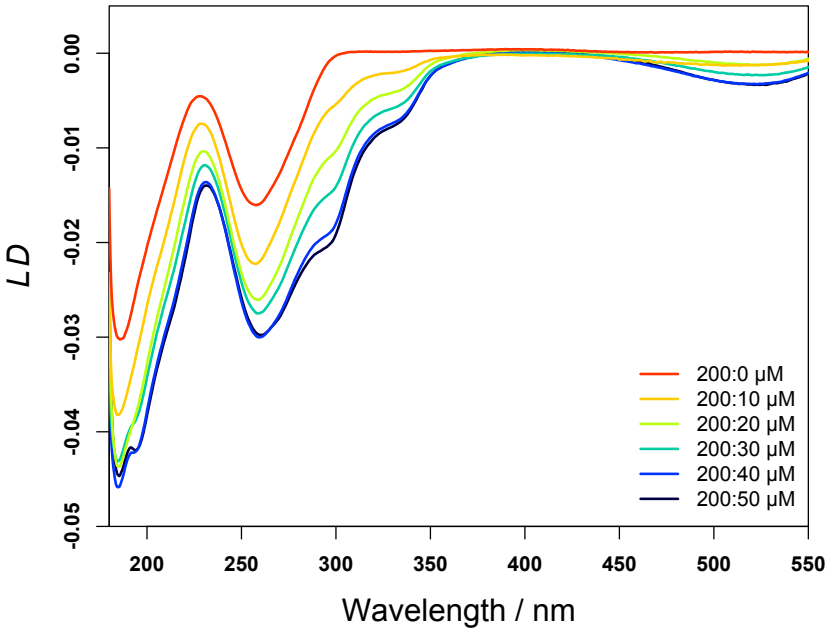

Figure 4.4: *Linear dichroism spectra of 200 μM DNA with increasing concentrations of ethidium bromide. All measurements were recorded using the parameters given in Table 4.2. Concentrations are as indicated in the figure legend.*

As DNA is not fluorescent and ethidium ions are, it is possible to record a spectrum from the ethidium alone by changing the detection system to detect fluorescence emissions only, as is done in $FDLD$. The Couette flow $FDLD$ spectra of DNA-EtBr complexes are given in Figure 4.5.

An immediately noticeable difference between Figures 4.4 and 4.5 is that the $FDLD$ spectra appear much noisier than LD, or indeed the film $FDLD$ spectra shown in Chapter 3. This is because in the Couette flow setup, the sample is farther away from the PMT and so the solid angle of the detector is reduced, and therefore fewer photons are collected than when measuring film $FDLD$ spectra. This has also been shown to be the case when measuring fluorescence detected circular dichroism ($FDCD$) [100]. However, it is still clear from the $FDLD$ spectra in Figure 4.5 that the molecule has adopted an intercalating binding mode by the sign of peaks, and that $FDLD$ signals have an increased magnitude when compared with the LD peaks at equal sample concentrations. These factors would be highly beneficial when investigating the binding mode of a fluorescence molecule whose absorbance signals

are completely obscured by the DNA or other bound compounds.

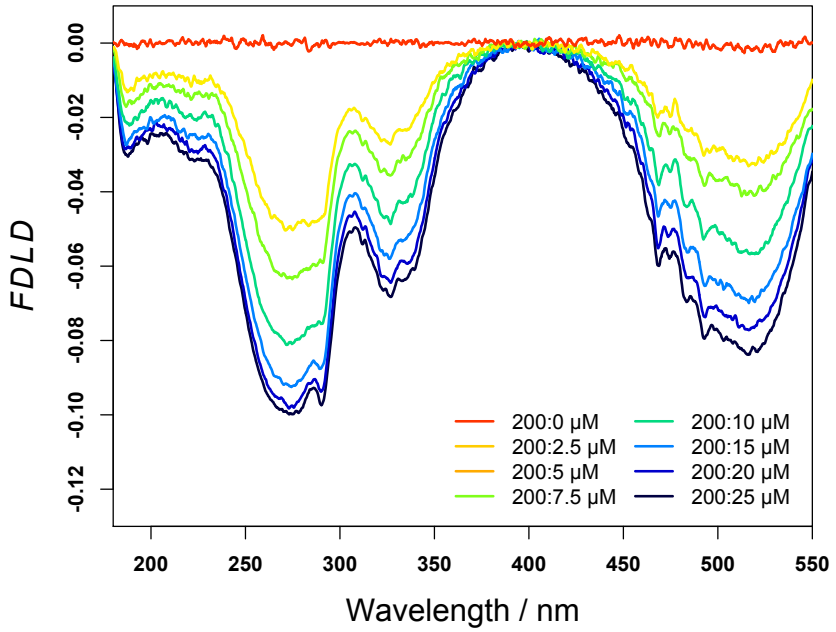

Figure 4.5: *Fluorescence detected linear dichroism spectra of 200 μM DNA with increasing concentrations of ethidium bromide. All measurements were recorded using the parameters given in Table 4.2.*

The propidium ion has a similar structure to that of the ethidium ion, as illustrated in Figure 4.2, and it also binds to DNA through intercalation. This is demonstrated in both the LD and $FDLD$ spectra of DNA-PI complexes, which are given in Figures 4.6 and Figure 4.7, respectively.

A further interesting difference between the LD and $FDLD$ spectra is the relative intensity of the long and short wavelength absorbance bands. In LD spectra of both EtBr and PI it is clear that the short wavelength absorption bands are much more intense than the long wavelength bands, which is visible even with the presence of the DNA signal. There is not such a difference in the relative magnitude of either of the sets of $FDLD$ spectra. This is because in the short wavelength transition we are exciting into the S_2 of the molecules, and fewer of the electrons decay to the ground state *via* a radiative process than in the $S_0 \leftarrow S_1$ decay of the long wavelength band, *i.e.* the short wavelength band has a lower fluorescence quantum yield than the long wavelength band.

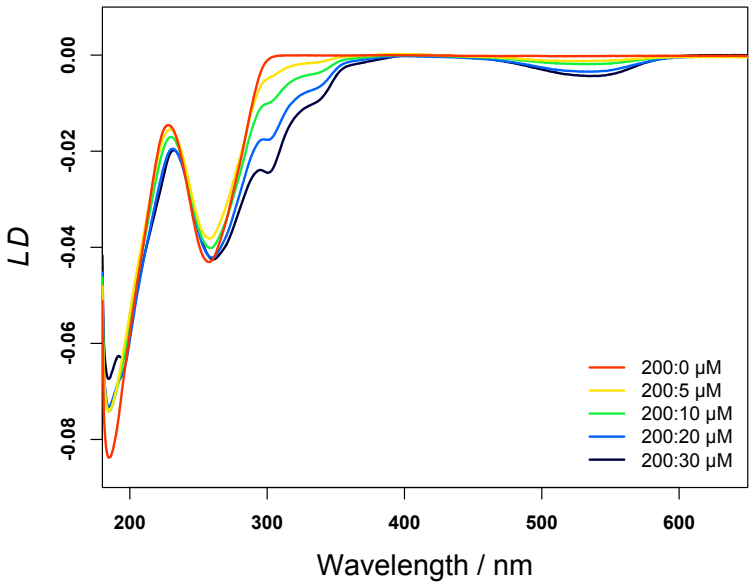

Figure 4.6: *Linear dichroism spectra of 200 µM DNA with increasing concentrations of propidium iodide bromide. All measurements were recorded using the parameters given in Table 4.2.*

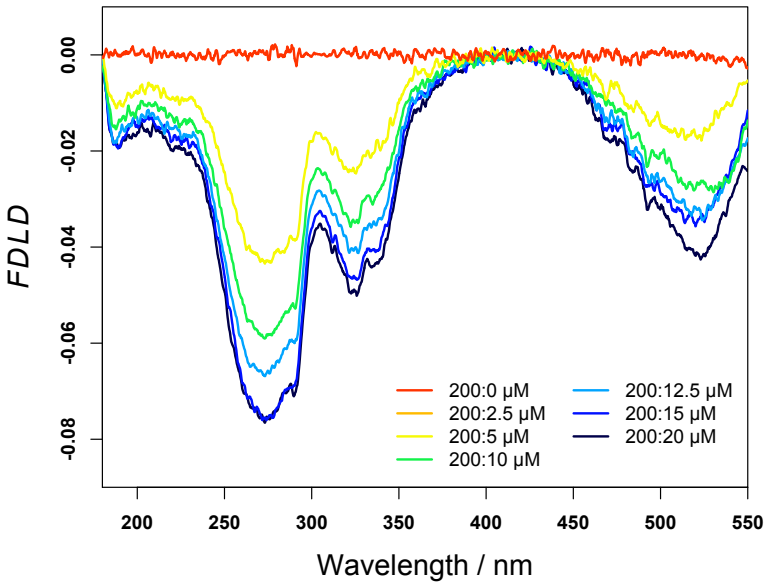

Figure 4.7: *Fluorescence detected linear dichroism spectra of 200 µM DNA with increasing concentrations of propidium iodide. All measurements were recorded using the parameters given in Table 4.2.*

4.3.2 DAPI and hoechst 33258

The UV-visible absorbance and fluorescence emission spectra of 20 μM of DAPI with increasing concentrations of DNA are given in Figure 4.8.

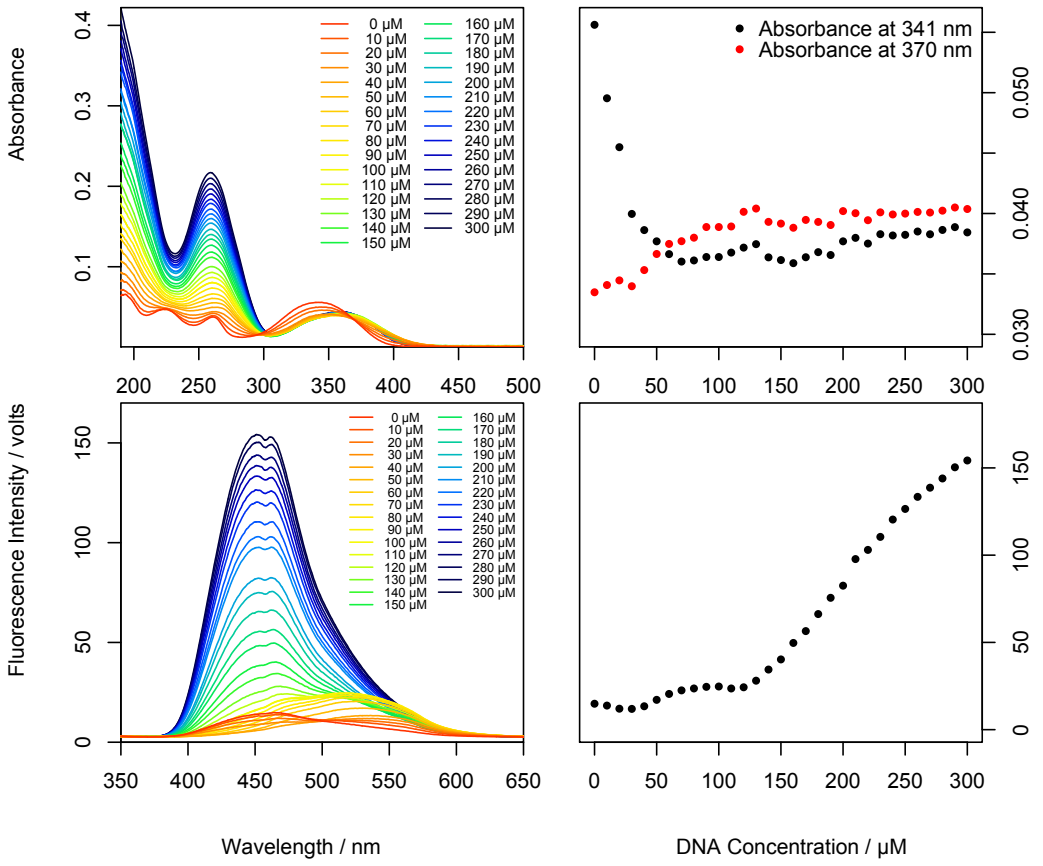

Figure 4.8: *UV-visible absorbance and fluorescence emission spectra of 20 μM DAPI and a range of concentrations of salmon sperm DNA. Top left: UV-visible absorbance spectra. Top right: Plot of the peak values at 341 and 370 nm, showing the bathochromic shift of the DAPI peak upon binding DNA. Bottom left: Fluorescence emission spectra, recorded using an excitation wavelength of 342 nm. Bottom right: Plot showing the change in fluorescence intensity with DNA concentration.*

Figure 4.8 shows that in the visible region, the DAPI maximum at 341 nm undergoes a large red (bathochromic) shift upon the addition of DNA. However, it is the very large increase in fluorescence emission intensity that is most apparent from the figure. This increase in sensitivity demonstrates the advantage of detecting fluorescence emissions for some DNA probes at low concentrations.

DAPI has been shown to be a groove binding dye from its *LD* spectra, which binds preferentially to AT rich regions of DNA [101]. The binding mode DAPI adopts

is illustrated in the LD spectra we have recorded, of 200 μM DNA and increasing concentrations of DAPI, which given in Figure 4.9.

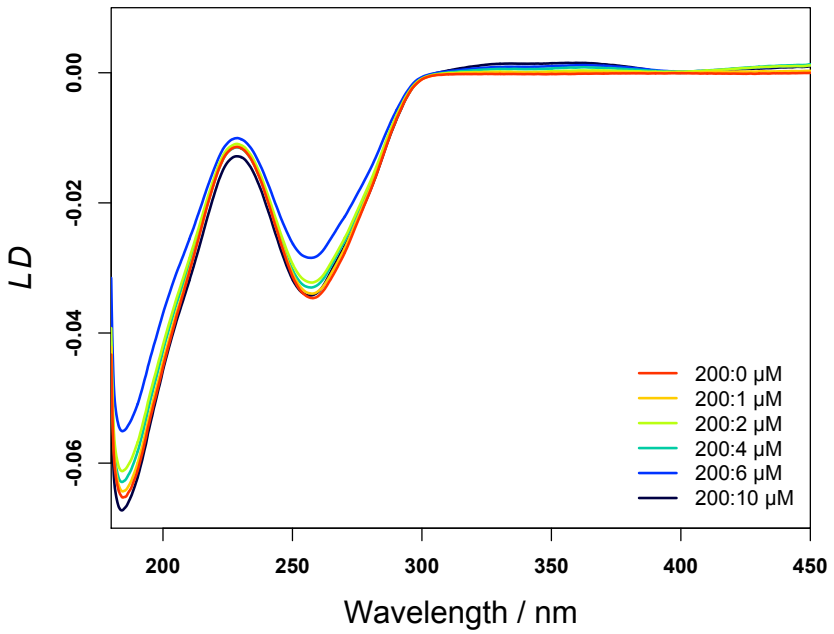

Figure 4.9: *Linear dichroism spectra of 200 μM DNA with increasing concentrations of DAPI. All measurements were recorded using the parameters given in Table 4.2.*

From Figure 4.9 we can see that at these concentration ratios, the DAPI signal is barely visible. Though a weak positive band around 370 nm can be seen, which is evidence of the groove binding mode adopted by DAPI. It is certainly not possible to observe any additional signals within the absorption band of the DNA itself. This is in contrast to the $FDLD$ spectra of the same samples, which are given in Figure 4.10.

With the exception of the red spectrum in Figure 4.10, which is of DNA only, all of the spectra show a strong positive peak with maximum at 370 nm. This clearly shows that the DAPI molecule has bound to a groove of the DNA, and is a further illustration of the increased measurement sensitivity of $FDLD$. In addition, it is also possible to observe smaller, negative bands in the $FDLD$ spectra, which were obscured by the DNA absorption in the LD spectra. The transition moment of the absorption band in this region has been shown to lie at 26° from the transition at 370 nm [35], and the fact that is gives a negative $FDLD$ signal shows that it is

angled towards the orientation direction of the DNA in flow.

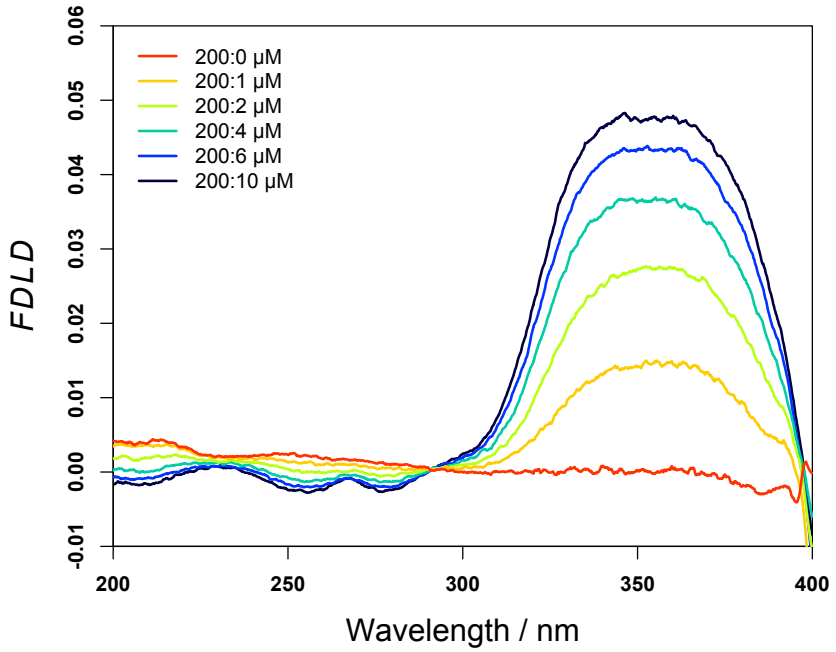

Figure 4.10: *Fluorescence detected linear dichroism spectra of 200 µM DNA with increasing concentrations of DAPI. All measurements were recorded using the parameters given in Table 4.2.*

Hoechst 33258 is another groove binding DNA probe and, like DAPI, it binds preferentially to AT-rich regions of DNA [102]. The UV-visible absorption and fluorescence emission spectra of Hoechst 33258 with increasing concentrations of DNA are given in Figure 4.11.

The UV-visible absorption spectra once again show a red shift in the long wavelength transition upon the addition of DNA, though Hoechst 33258 absorbs more strongly than DAPI in this region. From the bottom panels of Figure 4.11, it can be seen that the introduction of our DNA into the sample causes a large increase in fluorescence intensity. This is in agreement with what is in the literature [103, 104].

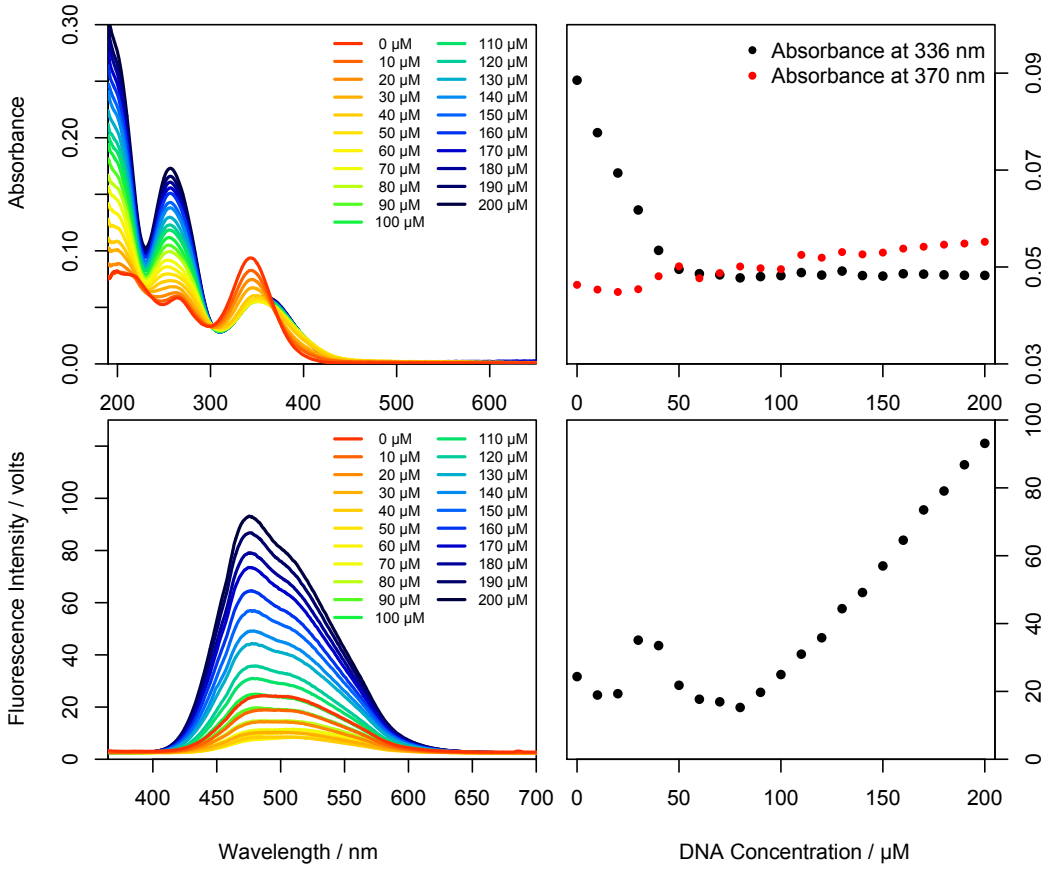

Figure 4.11: *UV-visible absorbance and fluorescence emission spectra of 20 µM Hoechst 33258 and a range of concentrations of salmon sperm DNA. Top left: UV-visible absorbance spectra. Top right: Plot of the peak values at 336 and 370 nm, demonstrating the bathochromic shift of the Hoechst 33258 peak upon binding DNA. Bottom left: Fluorescence emission spectra, recorded using an excitation wavelength of 346 nm. The sharp peak just below 700 nm in the spectra in from scattered incident light, and not from Hoechst 33258. Bottom right: Plot showing the change in fluorescence intensity with DNA concentration.*

The *LD* spectra of 200 µM DNA with increasing concentrations of Hoechst 33258 is given in Figure 4.12. This result is in agreement with previously published spectra of DNA-Hoechst 33258 complexes [5]. The positive signal in the near-UV region of the spectra shows that Hoechst 33258 is bound to a groove of the DNA. Relative to the DNA absorbance band, the signal magnitude from the dye here is slightly larger when compared with the DAPI-DNA complexes given in Figure 4.9, owing to the Hoechst 33258's stronger absorbance in this region. However, it is apparent that we would not be able to reduce the Hoechst 33258 concentration much further without losing the signal, and we cannot see any of the bands within the absorbance region

of the DNA, which we know are there from Figure 4.11.

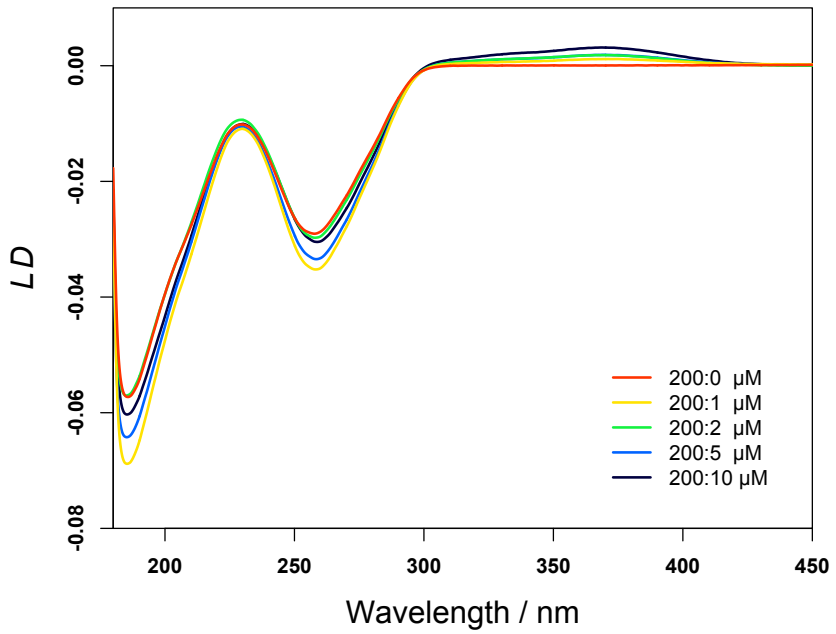

Figure 4.12: *Linear dichroism spectra of 200 μM DNA with increasing concentrations of Hoechst 33258. All measurements were recorded using the parameters given in Table 4.2.*

As a second illustration of results obtained from a DNA groove binding fluorescent probe, the $FDLD$ spectra of 200 μM DNA with a range of concentrations of Hoechst 33258 is given in Figure 4.13. Like DAPI, the $FDLD$ spectra of Hoechst 33258 show a large positive peak from the long-axis transition, centred around 370 nm, which is visible at dye concentrations in the 100s of nano-moles.

In Figure 4.13, however, the spectra have a slightly poorer signal to noise ratio compared with previous examples, possibly due to the lower dye concentrations used, which makes it difficult to pick out the vibrational structure within the absorbance band. Nevertheless, two dips in the spectra at 405.5 nm and 397 nm are visible in the spectra of the highest three concentrations of Hoechst 33258. Assuming these are from a 528 cm^{-1} progression, dashed grey lines have been overlaid to pick out other peaks with the same energy gap, that are barely visible above the noise.

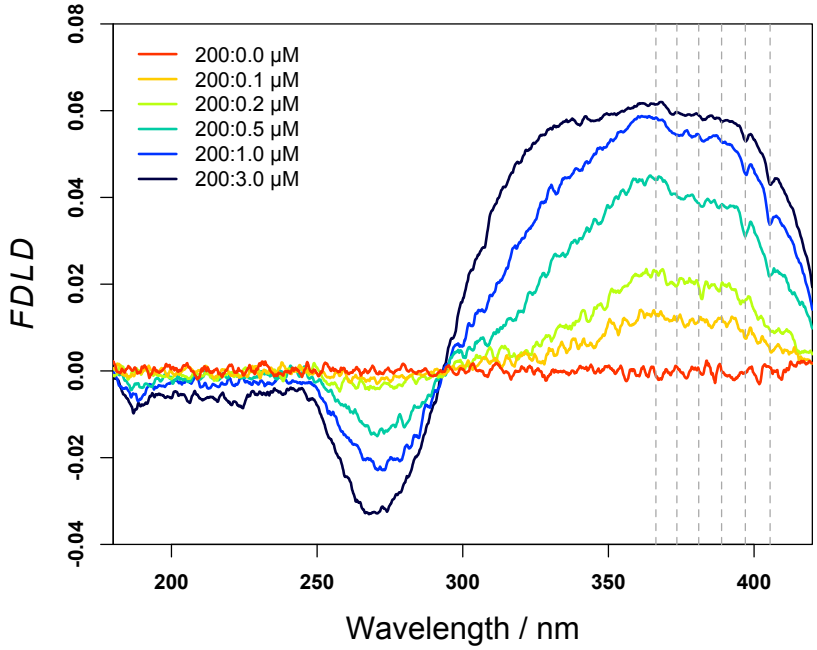

Figure 4.13: *Fluorescence detected linear dichroism spectra of 200 µM DNA with increasing concentrations of Hoechst 33258. The dashed grey lines at: 405.5 nm, 397 nm, 388.85 nm, 381 nm, 373.5 nm, and 366.3 nm highlight possible peaks from a 528 cm^{-1} vibronic progression. All measurements were recorded using the parameters given in Table 4.2.*

Figure 4.13 also shows that there is a relatively large negative peak around 260 nm in the $FDLD$ spectra of Hoechst 33258, which is obscured by the DNA's absorbance signal were we measuring LD spectra. This peak is visible in the Hoechst 33258-only absorbance spectrum in the top left panel of Figure 4.11. This transition has been shown previously to be oriented at 23° from the long axis of the molecule, and the fact that it gives a negative $FDLD$ signal shows that it is oriented towards the long axis of the DNA when bound to the molecule, enabling us to detect which way the Hoechst inserts in the groove [105].

Latt and Wohlleb made observations of the 260 nm transition of Hoechst 33258 when the molecule was bound to DNA and when it was on its own [106]. They used UV-visible absorbance spectroscopy, and by subtracting the spectrum of the Hoechst 33258-DNA complex from that of Hoechst 33258 on its own, found that when bound to DNA this absorbance maximum is blue shifted to 245 nm. We do not observe this shift in our $FDLD$ results in Figure 4.13, which may emphasise the benefit of

using a fluorescence detection system to selectively observe one fluorescent species in a sample, instead of having to obtain selective data through a more convoluted method.

4.3.3 Potential use to detect pathogenic bacteria

As is discussed in Chapter 5, finding new ways to detect pathogenic bacteria, either in the environment or in a living organism, is vital to reducing the amount of antibiotics we use and arresting the development of antimicrobial resistance. In 2012, Pacheco-Gómez *et al.* published their work towards developing an assay that detects the difference in the *LD* signal of an M13 bacteriophage-antibody complex in the presence or absence of pathogenic bacteria [107]. This assay was patented by Prof Timothy Dafforn and Dr Matthew Hicks prior to this publication [108]. Figure 4.14 illustrates the principle behind the detection system designed by Dafforn and Hicks.

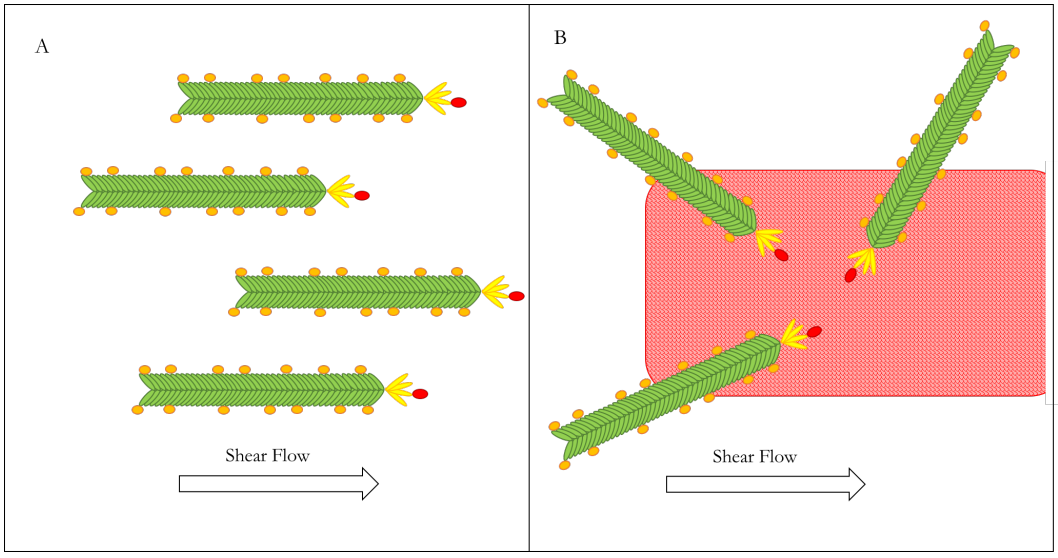

Figure 4.14: *Illustration of the LD assay to detect pathogens in solution. A: In the absence of any pathogen target, the M13 bacteriophage aligns very well, and hence gives a strong LD signal. B: Where a target bacterium is present (textured red), the M13 complexes bind to it and lose much of their freedom to align in the flow direction. Therefore, presence of a pathogen will be seen as a loss in LD signal.*

Figure 4.14 shows the outer pVIII proteins (green) and the end pIII proteins (yellow) endogenous to the M13 bacteriophage. Attached to the pIII proteins is an antibody

and secondary antibody complex (both grouped in solid red), which are selected to be specific to a pathogenic target. One may wish to use fluorophores attached to the pVIII proteins (orange) although these are not strictly necessary for the experiment, since aligned M13 has its own *LD* signal. Clearly, the assay is heavily reliant on the ability to detect an oriented M13 bacteriophage *LD* signal, and its sensitivity to relatively small concentrations of pathogens in solution is highly dependent on the ability of the detection system to measure small losses in M13 alignment. An example *LD* spectrum of 100 μg/mL of M13 bacteriophage, oriented in Couette flow, is given in Figure 4.15.

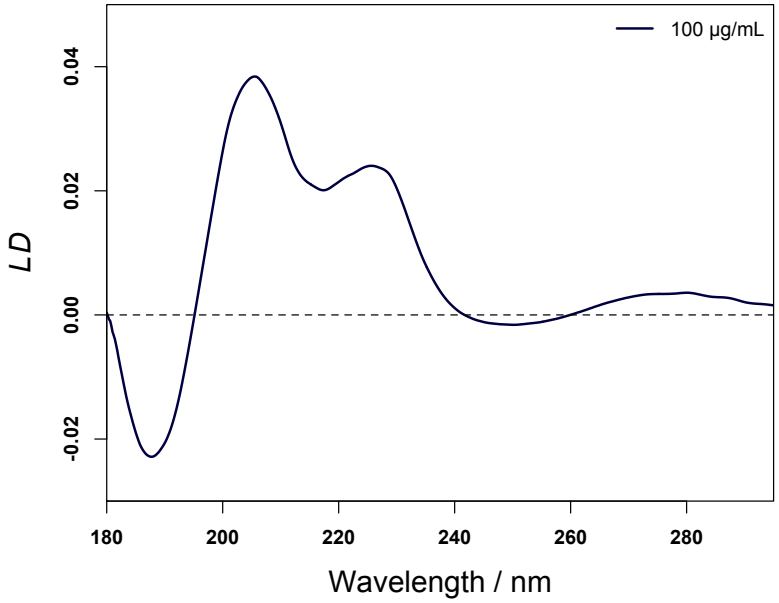

Figure 4.15: *LD spectrum of a 100 µg/mL sample of M13 bacteriophage, oriented in micro-volume Couette flow. The dashed grey line shows where LD is equal to zero. This spectrum was recorded using the instrument parameters given in Table 4.2.*

The largest peak in the *LD* spectrum of M13 bacteriophage, given in Figure 4.15, is in the far-UV region and comes from the $\pi^* \leftarrow \pi$ and $\pi^* \leftarrow n$ transitions of the peptide backbone [15]. In the near-UV region of the spectrum, the broad, shallow peak is from the absorbance of the aromatic amino acids, tryptophan and tyrosine. Like many biological samples, M13 bacteriophage is produced and purified in buffers that contain salts [107], which absorb light in the far-UV and can distort signals from the chromophore of interest. The sample used to record the *LD* spectrum in

Figure 4.15 was diluted down to 100 μg/mL from a 18 mg/mL stock solution with water, and so the effect of the salts in the buffer are negligible. However, when using high concentration buffers it would generally be preferable to use the signals in the near-UV to track changes in alignment.

As has been demonstrated in the spectra of the DNA binding fluorescent probes above, $FDLD$ has the potential to be used to detect a fluorophore at much lower concentrations than can be achieved when using absorbance methods. M13 bacteriophage contains one tryptophan and two tyrosines per PVIII protein, and each bacteriophage contains approximately 2,700 copies of this protein along its shaft [109]. As both of these amino acids are fluorescent we predicted we should be able to detect M13 bacteriophage alignment using $FDLD$. This is indeed the case, as illustrated in the $FDLD$ spectra given in Figure 4.16.

Figure 4.16 shows the $FDLD$ spectra of a range of concentrations of M13 bacteriophage. It is clear from the figure that it is possible to detect down to a concentration of 50 μg/mL, with a very good signal to noise ratio. This is despite using the same experimental setup as was used for the $FDLD$ measurements of the DNA-dye complexes. The reduced noise in this example may be due to the choice of long-pass filter collecting more of the emitted photons. Comparing the 100 μg/mL sample with the LD spectrum, given in Figure 4.15, we see that 17.5 times the signal magnitude in the aromatic region is obtained when using $FDLD$ ($LD_{280} = 0.00184646$, $FDLD_{280} = 0.0323457$). This shows that $FDLD$ could add a great deal to the efficiency of the detection of pathogenic bacteria assay described above.

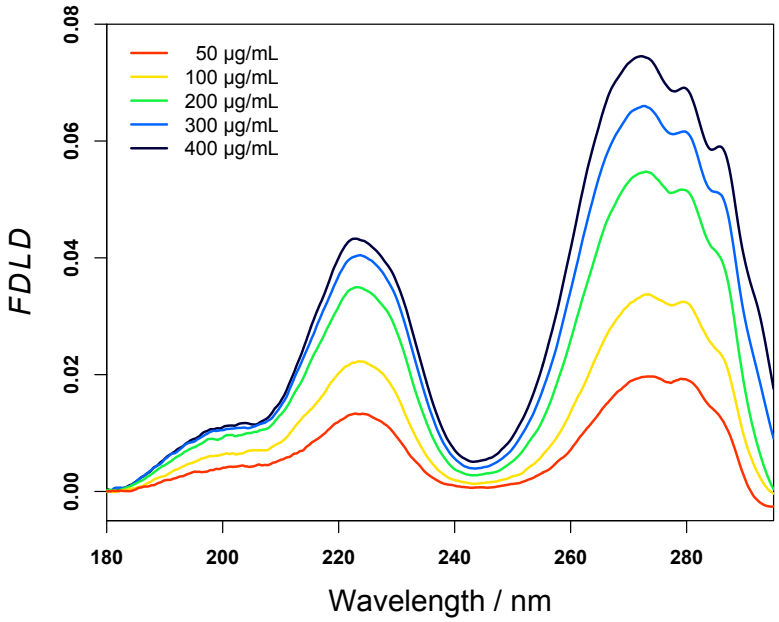

Figure 4.16: *FDLD spectra of a range of concentrations of M13 bacteriophage, oriented in micro-volume Couette flow. All spectra were recorded using the parameters given in Table 4.2, with a variable HT voltage. A Semrock 300 nm long-pass edge filter was used to block transmitted incident light in each measurement.*

It is also interesting to see the high resolution of the signature ^1L_a and ^1L_b bands of the tryptophan's indole chromophore around the 280 nm region of the spectra in Figure 4.16 [110]. Similar to the *FDLD* spectra of small molecules oriented on stretched PE^{OX}, given in Chapter 3, this is a further example of the increased ability of *FDLD* to resolve the individual contributions to an absorption band.

We know that each of the M13 bacteriophage particles possesses two fluorophores, tryptophan and tyrosine, however, we do not know the degree to which each was contributing to the *FDLD* spectra. To try and gain insight into this, we measured the intensity of fluorescence emissions over a range of excitation and emission wavelengths. The result is illustrated in Figure 4.17.

The fluorescence properties of the two fluorescent amino acids are well known — tryptophan possesses excitation and emission maxima at 280 nm and 350 nm, respectively [111], and tyrosine's excitation and emission maxima are at 275 nm and 303 nm [112]. Although tryptophan's emission wavelength is highly dependent on its surroundings, and in a hydrophobic environment can be 330 nm or lower [113].

From Figure 4.17 we can see that at both the excitation maxima in the phage $FDLD$ spectrum, the emission maxima are around 330 nm, which suggests the signal is predominately coming from the tryptophan residues, in hydrophobic environments.

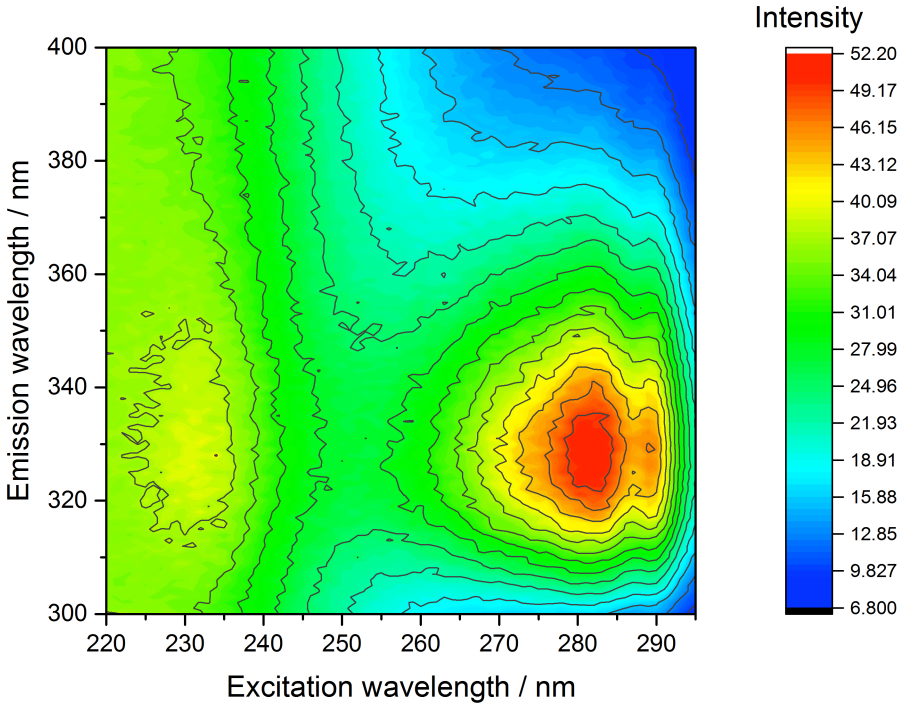

Figure 4.17: *3D plot showing the change in fluorescence emission intensity with excitation wavelength. This measurement was made on a Jasco FP-6500 spectrofluorimeter.*

A further confirmation of the fact that the signals present in the M13 bacteriophage $FDLD$ spectra originate from tryptophan, is that tyrosine fluorescence is reduced significantly by the presence of tryptophan and the peptide bonds in proteins, and so tyrosine will most likely have a lower quantum yield in the environment of our measurement than tryptophan [114]. Tyrosine fluorescence is also significantly effected by pH [115]. These factors are important in our discussion of the bacterial actin homologue MreB (Chapter 5), which contains five tyrosine and zero tryptophan residues.

4.4 Conclusions

In this section we have shown the utility of LD for determining the binding mode that small molecules adopt when bound to DNA. On observing any LD signal from the molecules we know that they are bound, as they are too small to orient in Couette flow on their own, and from the sign of the signal we can determine whether they are intercalated between the base pairs of the DNA (giving a negative LD signal) or bound to the major or minor groove of the molecule (giving a positive LD signal).

We have also shown that in cases where the bound molecule is a fluorophore, it is possible to record a micro-volume Couette flow $FDLD$ spectrum of the sample. Due to the distance of the oriented sample from the detector in the current Couette flow cell, these spectra have a decreased signal to noise ratio than the LD spectra of the same samples. However, they give signals of much higher magnitude in the examples given above, due to the inherent increased sensitivity of fluorescence detection, and a new design of Couette flow cell where the sample chamber is closer to the detector would increase the signal to noise ratio.

A further advantage of fluorescence detection is in the selectivity of the measurement when dealing with samples of complex mixtures, which is also clearly demonstrated in the $FDLD$ spectra given above. In the examples of the intercalating dyes ethidium bromide and propidium iodide, it is possible to see the the sign of the bands overlapping with the DNA's absorbance from their LD spectra, however, $FDLD$ reveals the full dye spectral shape, absorption maxima and the relative magnitude of peaks throughout this region.

The $FDLD$ spectra of the minor-groove binding dyes DAPI and Hoechst 33258 bound to DNA show a large increase in signal magnitude for their near-UV transitions, when compared to their LD spectra. Additionally, in both cases the transitions in the middle-UV region can also be observed in their $FDLD$ spectra — transitions that are completely obscured by the DNA's absorbance signal in the LD measurements. The negative sign of these peaks provides additional insight into the orientation of the bound dye.

Finally, we looked at the LD and $FDLD$ spectra of M13 bacteriophage solutions,

oriented by Couette flow. The $FDLD$ spectra showed a large enhancement of signal in the aromatic region of the spectra, which we argue would add significantly to the ability of a previously devised LD assay used to detect pathogenic bacteria in solution [107]. The $FDLD$ spectra also show highly resolved bands of the tryptophan residues, which further demonstates the additional information that can be obtained when using the technique.

CHAPTER 5

Expression and characterisation of the *E. coli* actin homologue MreB

5.1 Introduction

It is well known that antimicrobial resistance (AMR) is a serious threat to global public health. There have been numerous reports from the World Health Organisation that have emphasised the current — and not just future — danger of AMR [116]. The first World Antibiotic Awareness Week begun on the 16th November 2015, and the UK government has recently published its own five year strategy to tackle the problem [117]. The problem of AMR increased with the use of antimicrobial drugs [118]. These drugs, whilst creating an environment too hostile for most bacteria to survive, promotes the survival of pathogenic bacteria which have a mutation that makes them drug resistant. In the absence of any antibiotic it may be that mutant populations are less fit for survival, and so one strategy to help reduce AMR is to use fewer antibiotics [1].

Reducing the amount of antibiotics we use is critical to combatting AMR, and there is a global drive to increase awareness of the risks associated with the overuse of antibiotics. One example here in the UK is the Treat Yourself Better Campaign (www.treatyourselfbetter.co.uk). The need to use fewer antibiotics, however, will only serve as an afterthought to a dairy farmer whose livelihood *may* be jeopardised through mastitis in his herd, or a mother whose child *may* have a bacterial infection. In cases such as these, the real work must be done in the development of better diagnostics, so as to eliminate any doubt about whether or not the use of antibiotics is required. One way in which fluorescence detected linear dichroism may help achieve this goal is discussed in Chapter 4.3.3.

A second solution to the problem of AMR is to discover new drug targets and develop new antibiotics that function in a novel way [1]. With a large body a drugs that all kill pathogenic bacteria by a unique mechanism, it would be possible to cycle their use so that bacteria are less likely to evolve to become resistant to any one. The focus of this chapter is the expression, purification, and structural analysis of one such potential target: the bacterial actin homologue MreB (MreB). What follows is an introduction to this protein, our methods for obtaining it, and the results and conclusions of this work.

5.1.1 MreB

Bacterial cell morphology is determined by the peptidoglycan cell wall: a meshwork of glycan strands, which are cross-linked by peptide bridges [119]. This network of covalently bonded molecules makes the cell wall extremely strong, and resistant to the interior turgor pressure of the cell [120]. The biosynthesis of peptidoglycan begins in the cytoplasm, with the generation of soluble cell wall precursors, as is illustrated in Figure 5.1 [121].

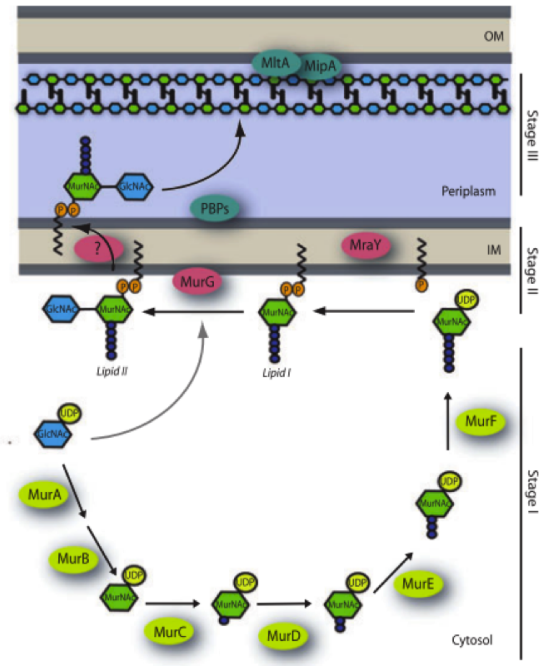

Figure 5.1: *Uridine diphosphate (UDP)-N-acetylglucosamine is converted into UDP-N-acetylmuramic acid, in reactions catalysed by the enzymes MurA and MurB. In a sequence of reactions catalysed by the other Mur enzymes: MurC, MurD, MurE and MurF; this goes on to form UDP-N-acetylmuramic acid pentapeptide. On the inner face of the cytoplasmic membrane, the membrane protein MraY then catalyses the formation of Lipid I from UDP-N-acetylmuramic acid pentapeptide. Subsequently, a UDP-N-acetylglucosamine molecule is ligated to Lipid I by MurG, to form Lipid II. Lipid II is then transported into the periplasm, where a group of enzymes called penicillin binding proteins insert it into the pre-existing cell wall. This figure is reproduced from reference [121].*

Bacterial cell morphogenesis is directly dependent on the proteins involved in peptidoglycan synthesis, such as the penicillin binding proteins (PBPs). PBPs are the target for β-lactam antibiotics, and fall into two classes: those of high molecular

weight, which can perform both the functions of assembling glycan chains and forming peptide links; and those of lower molecular weight, that solely function to form peptide bridges [122,123]. However, it is also indirectly dependent on cell-shape determining proteins, such as the bacterial-actin homologue MreB, which is found in most rod and spiral shaped bacteria [124]. This has been demonstrated by MreB depletions in: *Caulobacter crescentus*, where the phenotype of the mutation was the formation of lemon-shaped cells; *Bacillus subtillus*, where MreB-depleted mutants showed defects in chromosome segregation, followed by cell shape defects; and *E. coli*, where disruptions to *mreB* were found to promote the growth of rounded, inflated cells [122, 125, 126].

Fluorescence microscopy images of *C. crescentus* have shown that MreB has a very similar localisation pattern to the peptidoglycan synthesising enzyme MurG, in addition to PBP2 [119, 127]. These experiments suggest that MreB may act to spatially organise peptidoglycan synthesis. In their 2010 paper, White *et al.* looked to confirm this by testing whether any other *C. crescentus* peptidoglycan synthesising enzymes localise in a similar fashion to MreB [121]. To do this they tagged the C-teminal of the cytosolic proteins MurB, MurC, MurD, MurE and MurF, in addition to the integral membrane protein MraY, with the fluorescent protein mCherry. Using fluorescence microscopy they were able to confirm that all of these proteins did indeed exhibit similar localisation patterns to MreB.

White *et al.* used their result to construct a cellular model of MreB and its role in peptidoglycan synthesis, which is shown in Figure 5.2. They did not conduct experiments themselves on the cytosolic structure of MreB polymers, but used information from previously published reports, such as experiments performed by Shih *et al.* on *E. coli* MreB [128]. As will be discussed below, the cytoplasmic structure of MreB is currently a matter of debate in the literature.

It was thought that MreB dynamics were driven by its own polymerisation, however, the process was poorly understood. In their 2011 paper, van Teeffelen *et al.* attempted to investigate this by inhibiting peptidoglycan synthesis in *E. coli* [129]. They first tested mutants that cannot synthesise diaminopimelic acid, an intermediate in the biosynthetic pathway leading to the pentapeptide component

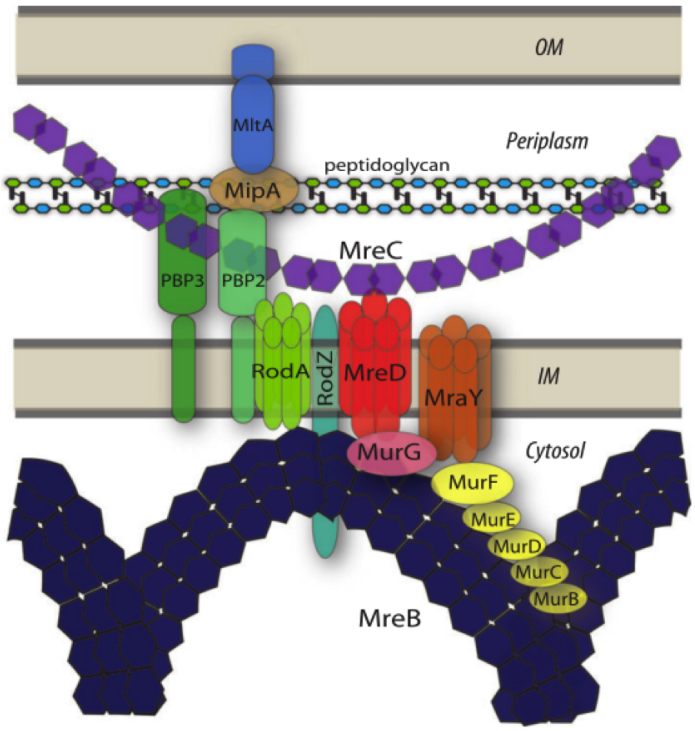

Figure 5.2: *Model of interactions between the bacterial morphogenetic proteins and the cell wall synthesising enzymes. MreB is shown to act to spatially organise the enzymes involved in synthesising peptidoglycan precursors in the cytoplasm, and through the integral membrane protein MreD, it also acts to position MreC, which positions peptidoglycan assembly in the periplasm. This figure is reproduced from reference [121]*

lysine [120]; they then used antibiotics such as fosfomycin, which targets the peptidoglycan synthesising enzyme MurA. Their epifluorescence microscopy images showed both of these treatments had the effect of reducing the intracellular motility of the short, membrane-associated MreB filaments — these are often referred to as 'patches' in the literature, as the filaments are too small to be properly resolved by light microscopy — and furthermore this occurred well before any effect on cell morphology was observed. This indicates that the cellular motion of MreB is dependent on the availability of peptidoglycan subunits [129].

Garner *et al.* went on to test this further by depleting three components of the *B. subtilis* peptidoglycan elongation machinery: RodA, RodZ and Pbp2A [130]. Over time these depletions resulted in the gradual cessation of MreB patch motility. They then introduced antibiotics that target peptidoglycan synthesis, which also halted MreB movement. Most notably, the minimum inhibitory concentrations that stopped MreB motion mirrored those that stopped cell growth. They therefore

concluded that MreB motion was driven by peptidoglycan synthesis.

Garner *et al.* also used single particle tracking to investigate the existence of a long range MreB cytoskeleton. It was found that there was no correlation in the motion of individual MreB complexes. Distinct patches were observed to pause or reverse direction, in a manner that was completely independent of its neighbour. These findings are inconsistent with the idea of a long, filamentous MreB cytoskeleton.

Domínguez-Escobar *et al.* used total internal reflection fluorescence (TIRF) microscopy to image GFP-tagged isoforms of MreB in *B. subtilis* [131]. They again showed that MreB complexes rotate perpendicular to the long axis of the cell in 'patches' during exponential growth. They suggested that the previously shown helical structure may have been a result of the increased depth of field of epifluorescence microscopy. The experiments were repeated using the Gram negative bacteria *E. coli* and *C. crescentus*, and these yielded the same results.

Domínguez-Escobar *et al.* then looked at the same question addressed by van Teeffelen *et al.*: What drives MreB patch motion? Fluorescence recovery after photobleaching (FRAP) experiments suggested that treadmilling was unlikely to be the dominant force, as the patches moved position with little change in their molecular composition. An example of one of their experiments is given in Figure 5.3.

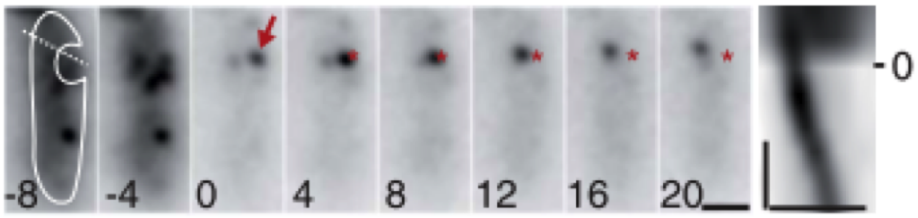

Figure 5.3: *An inverse FRAP experiment, showing the location of green fluorescent protein (GFP) labelled Mbl (an isoform of MreB in B. subtillus) on the cell wall. The region outlined in the first frame was bleached, leaving a single GFP-Mbl patch. The kymograph on the far right shows that the patch has moved, with no loss of fluorescence. This figure is reproduced from reference [131]*

Further work on the cellular structure of MreB was published in 2012 by Swulius *et al.* [132]. They used cryo-electron microscopy to visualise *E. coli* cells that over-expressed MreB with an N-terminal yellow fluorescent protein (YFP) tag, a strain that has commonly been used to show the extended cytoskeletal helix

formed by MreB. They confirmed previous results, however, when they repeated the experiment with other strains — such as FB76, where the chromosomal MreB gene was replaced with MreB-RFP^{SW}, and the resulting tag is positioned in an internal loop of the protein — they could not find any extended helical structures. They thus concluded that the proposed helical MreB cytoskeleton in *E. coli* is an artefact of using an N-terminal fluorescent tag [132].

Reimold *et al.*, using two super-resolution fluorescence microscopy techniques conclude that MreB forms "a discontinuous structure that is highly dynamic, including filaments as long as 3.4 μm" [133]. This is a compromise between the two extremes: the long range cytoskeleton similar to that formed by its eucharyotic counterpart and the short filaments that are too small to be resolved by light microscopy. So it would seem that much more work is required to understand the cytosolic structure of MreB, and its implications for the longitudinal growth of bacteria. Though what is clear, is that MreB is a key actor in the formation of the bacterial cell wall, and therefore, a good target for new antimicrobial compounds.

In the following sections the methods used to clone, express and purify MreB are described in detail. The structure of the MreB protein we obtained was then analysed using circular dichroism (CD) and fluorescence.

5.2 Materials and Methods

5.2.1 Molecular cloning

Molecular cloning techniques are used to obtain recombinant plasmid DNA, which is the template for expressing a desired protein when induced in a suitable host cell. A basic outline of this process may be given in four fundamental steps: firstly, one must obtain a fragment of DNA that contains the gene of interest, flanked by the recognition sequences of two restriction endonucleases; then, an appropriate expression vector must be selected that possesses these same recognition sequences; following this, both the gene and the plasmid are treated with the restriction endonucleases, so that the products possess short, complementary 'sticky ends';

and finally the two are covalently bound together with the use of a DNA ligase.

5.2.1.1 PCR amplification of MreB gene (*mreB*)

Nurse *et al.* have shown that *E. coli* MreB is capable of forming filamentous bundles *in vitro*, however, a precondition for this is that the first 20 residues of the protein must be removed [134]. This is because an N-terminal amphipathic helix that binds the protein to the *E. coli* inner membrane causes MreB to aggregate *in vitro*. We therefore started the sequence of the upstream primer from the ATG beginning 61 bases from the start of the *E. coli* MreB gene. The oligonucleotide primers used in the polymerase chain reaction (PCR) are given in Table 5.1. The recognition sequences of NcoI and XhoI are underlined in the upstream and downstream primers respectively. The *E. coli* MreB primary sequence from the twenty-first residue begins methionine–leucine; however, due to the NcoI recognition sequence encoding two guanines following the start codon, it was necessary to mutate the second residue from a leucine to a valine.

Table 5.1: Primers used to amplify the *mreB* gene using restriction enzymes

Primer	**Sequence**
Upsteam	5' - TTTGCGCCATGGTGAAAAAATTTCGTGGC ATGTTTTCCAATGACTTG
Downstream	5' -TTTGCGCTCGAGCTCTTCGCTGAACAGGTC GATC

The complete reaction mixture used for the PCR is given in Table 5.2. The DNA polymerase is added last, immediately prior to initiating the reaction, so to avoid the degradation of the primers due to the polymerases 3' to 5' exonuclease activity.

Table 5.2: Reaction Mixture (200 μL)

Reagent	**Concentration**	**Volume (μL)**
Phusion Reaction Buffer	5 ×	40
dNTPs	10 mM	4
Forward Primer	10 mM	10
Reverse Primer	10 mM	10
E. coli Genomic DNA	45.9 ng/μL	2.26
Nuclease-free H_2O	-	141.74
Phusion HF DNA polymerase	2 U/μL	2

The mixture was divided up between 8 PCR tubes (20 μL in each) and placed in the DNA Engine Tetrad 2 Peltier Thermal Cycler (BioRad). The reaction was set to proceed as described in Table 5.3.

Table 5.3: Conditions used for the PCR amplification of *E. coli* MreB. The initial denaturation step breaks the hydrogen bonds between the complementary strands on DNA. The temperature is then lowered, allowing the oligonucleotide primers to anneal to the sites they complement on the genomic DNA. Finally, the temperature is raised to 72°C to optimise the 5' to 3' polymerase activity of the enzyme. The process repeated a further 34 times to increase the amplicon concentration.

Step	**Temperature (°C)**	**Time (s)**
Initial Denaturation	98	30
35 cycles	98	10
	66	30
	72	45
Final Extension	72	600
Hold	4	∞

Following the procedure outlined in Appendix B.1, the DNA fragments in the PCR products were separated according to their size using gel electrophoresis.

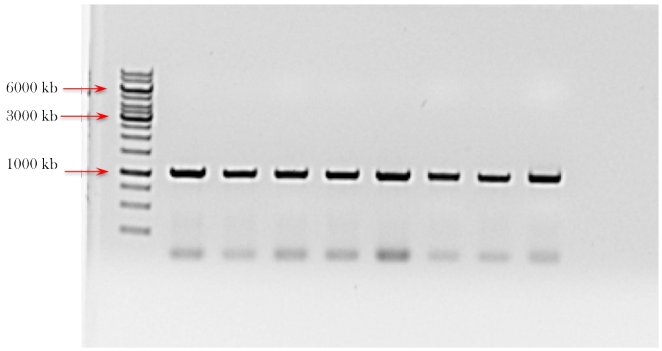

Figure 5.4: *Gel electrophoresis run using the PCR products. The length of our E. coli MreB is 1044 base pairs. All of our samples show a intense dark band just above the 1000 base pair marker, which most likely signals our desired product.*

From the result shown in Figure 5.4 it is clear that each of the samples contains a DNA fragment of approximately the size of the MreB gene. Therefore we could safely pool the samples together and remove any impurities, such as unreacted primers, using a PCR purification kit.

5.2.1.2 Expression vector

Our choice of expression vector was one of the pET System: pET28b. Genes cloned in to these vectors are under the control of bacteriophage T7 transcription [135]. T7 RNA polymerase is extremely selective, and when fully induced in bacterial cells, which have been engineered to express the bacteriophage polymerase, a large portion of resources are focussed on the expression of the target gene. The T7*lac* promoter included in pET28b uses the additional control of the *lac* operon. This measure means that its expression is negatively regulated by the binding of the *lac* repressor (LacI) to the *lac* operator, just upstream from where the *mreB* gene is to be inserted. The subsequent addition of isopropyl β-D-1-thiogalactopyranoside (IPTG) induces transcription by forming a complex with LacI, inhibiting its binding to the *lac* operator. This function could also be performed by lactose, however, IPTG is preferred as it is not broken down by β-galactosidase, and so its cellular concentration remains high [136].

The *lac* operon is part of a system that regulates the diauxic growth pattern of bacteria, in which they utilise metabolites sequentially, rather than in parallel [137]. Glucose is the preferred energy source, however, when its concentration is depleted

in the cell, the affinity of LacI for the operator is reduced, and lactose becomes the primary energy source. There is another upstream regulatory element in the *lac* operon, which binds a catabolite activator protein–cyclic adenosine monophosphate (CAP–cAMP) complex, and promotes transcription [138]. In the presence of glucose, cellular cAMP levels are low, thus transcription is once again inhibited by its presence. Therefore, including additional glucose to the medium in which the cells are being grown will maximally inhibit basal protein expression prior to the addition of IPTG, minimising its interference with the normal functioning of the cell [139].

The pET28b vector also contains a kanamycin resistance cassette, so that the bacterial cells it has been successfully transformed into may be selected for on an LB agar plate containing 50 μg/mL kanamycin. The full vector map showing all these sites, in addition to the multiple cloning site, is given in Figure 5.5.

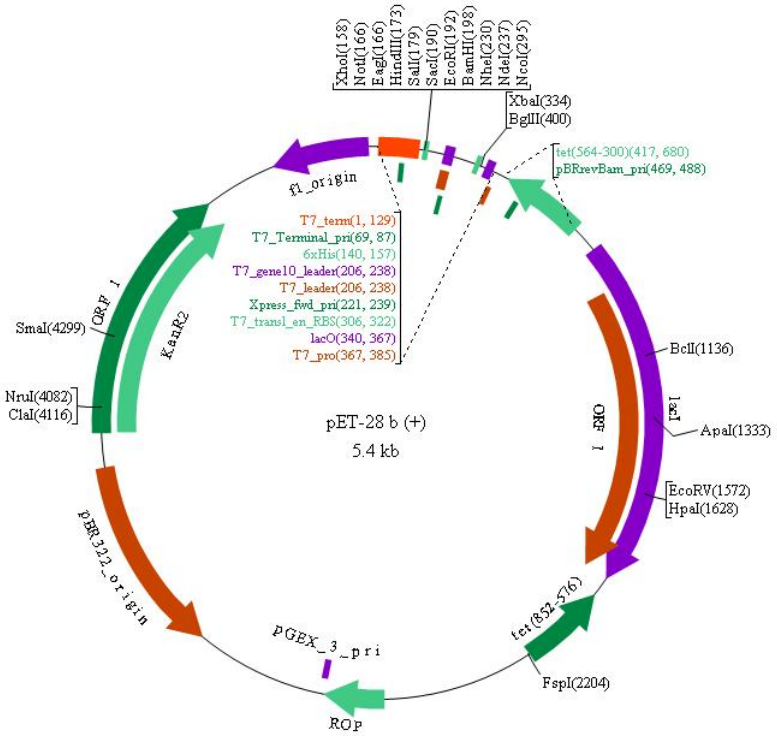

Figure 5.5: *Vector map of pET-28b*

5.2.1.3 Restriction digests

Restriction endonucleases are enzymes produced by bacteria to cleave DNA at specific sites, protecting the organisms from infection by bacteriophages. Once

isolated these enzymes can be used in the laboratory to cleave plasmid DNA, so that specific genes encoding a target protein may be inserted. To this end, the downstream restriction site we used was that of the enzyme XhoI, which after digestion leaves a 5' sticky end with sequence TCGA. Upstream from where the gene is to be inserted is the recognition sequence for the enzyme NcoI. This restriction enzyme leaves a 5' sticky end with sequence CATG following digestion, which like that left by XhoI, is an inverted repeat. Under certain conditions NcoI exhibits 'Star Activity', where the enzyme's specificity is relaxed, and cuts are made at a number of regions of DNA that are similar to the recognition sequence. For this reason we opted to use the high fidelity NcoI-HF enzyme (New England Biolabs) which has been engineered to reduce such effects.

The composition of the reaction mixture used to digest the PCR product, creating the 5' sticky ends on the amplicon, is given in Table 5.4. Bovine serum albumin (BSA) was added to the reaction to stabilise the enzymes and reduce enzyme loss due to attachment to the interior of the Eppendorf tube or pipette tip; this is particularly important when using XhoI.

Table 5.4: Digestion of PCR Product. Some concentrations are given in terms of units of activity (U).

Reagent	**Concentration**	**Volume (μL)**
Purified PCR Product	-	39.5
NEBuffer 4	10×	5
BSA	10 mg/mL	0.5
XhoI	20 U/μL	2.5
NcoI-HF	20 U/μL	2.5

The digestion of the expression vector proceeded with mixture detailed in Table 5.5.

Table 5.5: Digestion of pET-28b Vector DNA

Reagent	**Concentration**	**Volume (μL)**
Plasmid DNA	235.8 ng/μL	31.8 (7.5 μg)
NEBuffer 4	10×	5
BSA	10 mg/mL	0.5
H_2O	-	7.7
XhoI	20 U/μL	2.5
NcoI-HF	20 U/μL	2.5

The two restriction reactions are left at 37°C overnight. When the digestions are complete, the digested PCR product is placed on ice and the digested plasmid DNA is dephosphorylated with shrimp alkaline phosphatase (SAP). The 5' ends of the digested vector possess phosphate groups that are required for ligation. Removing these groups with SAP reduces the probability that self-ligation will occur, therefore reducing the number of background non-recombinants. The dephosphorylation reaction was performed by adding the mix given in Table 5.6 to the reaction and incubating at 37°C for a further 30 minutes.

Table 5.6: Dephosphorylation of Digested pET-28b Vector DNA

Reagent	**Concentration**	**Volume (μL)**
Dephosphorylation Buffer	10×	5
Shrimp Alkaline Phosphatase	1 Unit/μL	5
H_2O	-	40

A PCR purification kit can then be used to remove impurities, such as the restriction enzymes, from both digestions; this leaves only the DNA in a low salt buffer. In the case of the digested expression vector, however, the small fragment cut out between the two restrictions sites — XhoI (158) → NcoI (295) — is greater than 100 kb, and

so will also stick to the silica membrane assembly in the spin column. Therefore one may wish to separate the fragments using gel electrophoresis, and extract the larger of two from the gel. The number of background non-recombinants will consequently be lowered further. However, this benefit comes at the expense of linearised plasmid DNA concentration. We decided that this would be too costly for our purposes, and so proceeded having used only the PCR purification.

5.2.1.4 Ligation

DNA ligases fuse strands of DNA together by catalysing the formation of phosphodiester bonds between the 3'-hydroxyl and the 5'-phosphate ends of two nucleotides. For this to occur it is essential that the appropriate ends of the DNA fragments align, and are engaged long enough for the DNA ligase to act to bind them. To aid this, the ligation mixtures — which are displayed in Table 5.7 — are left to incubate overnight at 16°C instead of 37°C. The lower temperature slows down the molecules in the sample, and stabilises the hydrogen bonds between the complementary overhangs on the treated plasmid and gene insert.

Table 5.7: Composition of ligation mixtures

Reagent	**1:1**	**1:2**	**1:3**	**Vector Only Control**	**Insert Only Control**
Treated Plasmid (45.2 ng/μL)	2.21 μL	2.21 μL	2.21 μL	2.21 μL	-
Treated PCR Product (31.9 ng/μL)	3.13 μL	6.27 μL	9.40 μL	-	3.13 μL
10× T4 DNA Ligase Buffer	2 μL	2 μL	2 μL	2 μL	2 μL
Sterile Water	11.66 μL	8.52 μL	5.39 μL	14.79 μL	13.87 μL
NEB T4 DNA Ligase	1 μL	1 μL	1 μL	1 μL	1 μL

Following the ligation reaction, 5 μL was taken from each reaction mixture and

used to transform *E. coli* Top10 competent cells. Transformants are selected for by growing the small cultures on LB agar plates containing 50 μg/mL kanamycin. A selection of colonies were picked from each of the plates (with the exception of the controls) and grown overnight at 37°C, as outlined in Appendix B.4. The plasmid was subsequently extracted from each culture by mini-preparation and sequenced using the T7 promotor and terminator primers. A number of these sequences matched the MreB sequence, which is given in Appendix A.

5.2.2 Expression and purification

After obtaining the plasmid containing the gene of the protein we wish to express, we must over-express the gene in a suitable cell line, and then lyse the cells and separate our protein from the rest of mix. The following sections detail how this was achieved for the *E. coli* MreB used in this work.

5.2.2.1 Expression trial

The cell line we selected as an expression host was the *E. coli* strain C41(DE3). The C41(DE3) and C43(DE3) strains are derived from the BL21(DE3) strain, and are commonly used to overcome the effects of over-expressing toxic proteins. It has been shown empirically that the C43(DE3) strain is generally preferred in these cases [140], however, we found that this cell line over-expressed MreB to such a degree that it formed insoluble aggregates. Our recombinant pET28b-*mreB* DNA, in addition to 'empty' pET28b DNA, was transformed into the expression host cells, and successful transformants were again selected on LB agar antibiotic plates. A single colony was picked from each of the plates, and used to grow up overnight cultures, with the addition of glucose (see Appendix B.4). Two 100 μL aliquots of each of the overnight cultures were used to inoculate the solutions in 4 Falcon tubes, which each contained the following: 10 mL of LB media, 10 μL of 50 mg/mL kanamycin, and 40 μL of 50% w/v sterile glucose solution. All of the samples were then placed in a 37°C incubator, and shaken at 180 rpm until an optical density at 600 nm (OD_{600}) of $\sim$0.6 was reached. At this point IPTG was added to each culture to a final concentration of 1 mM.

One culture containing the recombinant DNA and one culture containing the empty vector were then placed in a 16°C incubator, and shaken at 180 rpm for 24 hours. The remaining two cultures were placed back in the 37°C incubator for four hours after the addition of IPTG.

When the cultures had reached the end of their respective incubation periods, they were centrifuged at 10,000 ×g for 15 minutes to pellet the cells. The pellets were resuspended in 1 mL of Buffer A (see Appendix B.5), and the cells were sonicated. The sample concentrations were measured using the BioRad assay, and the volume of each corresponding to 20 μg of protein was pipetted into labelled 500 μL Eppendorf tubes.

What remained in each culture was then centrifuged for a further 20 minutes at 10,000 ×g, to pellet the cell debris and other impurities. The BioRad assay was again used to measure the concentrations of soluble protein left in the supernatant, and the volume corresponding to 20 μg was pipetted into a further four labeled 500 μL Eppendorf tubes. The contents of the eight Eppendorfs were used to run a sodium dodecyl sulfate polyacrylamide gel electrophoresis (SDS-PAGE) gel, the result of which is given in Figure 5.6.

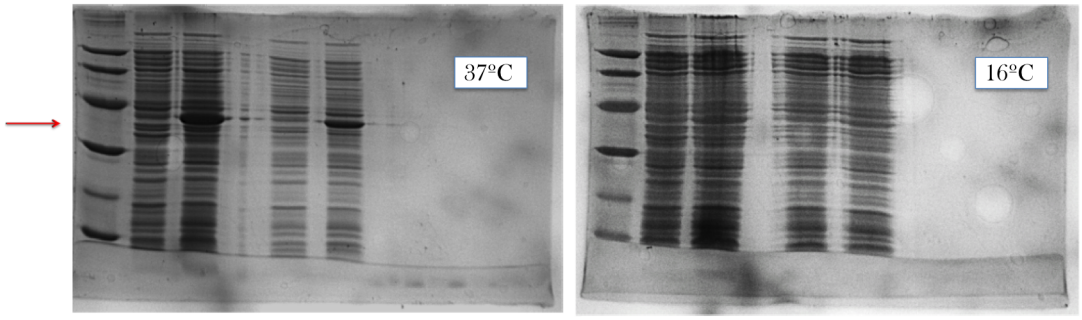

Figure 5.6: *SDS-PAGE gels of small scale expression. The lanes from left to right are as follows: whole cell fraction of C41(DE3) cells transformed with pET28b; whole cell fraction of C41(DE3) cells transformed with pET28b-mreB; soluble fraction of C41(DE3) cells transformed with pET28b; soluble fraction of C41(DE3) cells transformed with pET28b-mreB. The red arrow indicates the approximate distance a protein of the size of MreB (∼37 kDa) would travel on the gel, which is also the location of the dark bands on each of the cultures where our recombinant DNA was used.*

The expression trial indicated that the best conditions to express MreB in *E. coli* C41(DE3) cells is to grow at 37°C for 4 hours after induction with IPTG. Therefore,

it was with these conditions that we moved on to larger scale expression.

5.2.2.2 Large scale expression and purification

One litre cultures were grown using the procedure described above. Figure 5.7 shows an SDS-PAGE gel, which was run using the product of one of these cultures. The whole cell fractions, which are marked WC, show very intense bands at approximately 37 kDa. It is clear from these lanes that there is a large concentration of MreB being expressed in the cell. The two lanes marked ×10K and ×50K are the protein that remains in the supernatant, after the culture has been centrifuged for 15 minutes at 10,000 ×g and 30 minutes at 50,000 ×g, respectively. Although these show a good deal of soluble protein remains, the quantity putative MreB has depleted when compared with the whole cell fractions, most likely due to a small portion forming inclusion bodies. The next three lanes, marked HTin, FT and HT, are related to the HisTrap column used to purify the MreB, and denote the sample used to load the HisTrap column, the flow-through from the column, and the sample eluted from the column, respectively. The HisTrap purification is discussed further below.

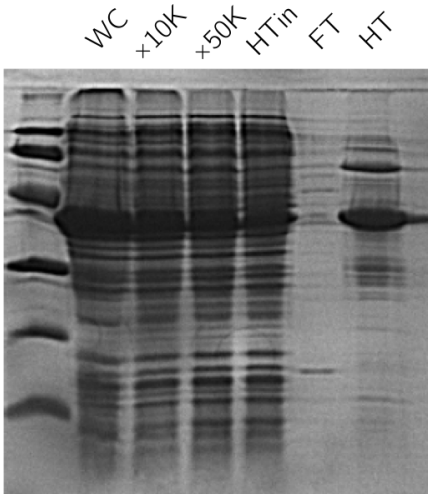

Figure 5.7: *SDS-PAGE gel of large scale expression of E. coli MreB in strain C41(DE3). The lanes from left to right are as follows: the protein markers (at 97 kDa, 66 kDa, 45 kDa, 30 kDa, 20 kDa and 14 kDa) the whole cell fraction following sonication of the culture; the soluble protein left after the cultures were centrifuged for 15 minutes at 10,000 ×g; the residual protein after the culture was centrifuged for a further 30 minutes at 50,000 ×g; the sample use to load the HisTrap column; the flow-through from the HisTrap column; and finally the sample eluted from the HisTrap column.*

As mentioned above, the MreB protein was expressed with a His-tag, so it can be purified using a HisTrap HP (5 mL, GE Life Sciences) column, which came pre-packed with nickel sepharose. After flushing through 100 mL of Buffer A, the protein was loaded onto the column on the bench, using a bench top peristaltic pump (Pharmacia LKB Pump P-1). The loaded column was then fitted to an ÄKTA Pure chromatography system, and eluted from the column in 1.5 mL fractions with an increasing gradient of Buffer B (Appendix B.5) flowing through the column. Figure 5.8 shows the result of the HisTrap elution.

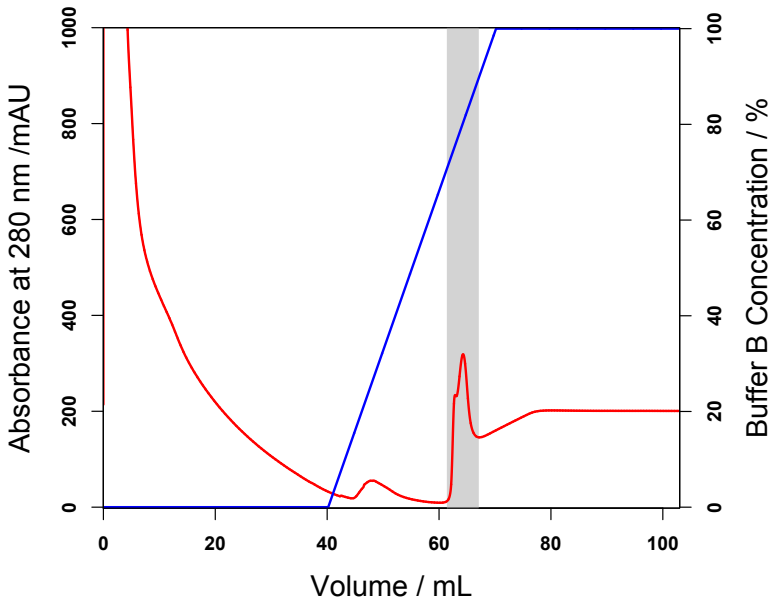

Figure 5.8: *Resulting chromatogram from the HisTrap elution of the MreB following its over-expression in the C41(DE3) cell line. The red line shows the absorbance of the eluted solution, and the grey box highlights the region where MreB is present. The blue line illustrates the percentage concentration of the high imidazole containing Buffer B. The figure shows that MreB comes elutes at a Buffer B concentration of ∼70-80%.*

The fractions from the region covered by the grey box in Figure 5.8 were collected and used to run an SDS-PAGE gel to confirm that MreB was present and check its purity, which is shown in Figure 5.7. It was found that MreB was present, but there were a number of other lighter bands on the gel, indicating that it was not absolutely pure. It was thought that these may be proteins that have a natural affinity to the HisTrap column, and so we next used TEV protease to cleave the His-tag from the

protein, and again run the protein through the HisTrap column using a bench top peristaltic pump. The TEV protease we used also contained a His-tag, and so it, in addition to the protein impurities, should stick to the column, whilst the flow through should contain only the pure MreB. However, a further SDS-PAGE gel was run using the flow through and some of the lighter bands were still present. This could be due to some additional proteins interacting with MreB itself, and not simply binding to the column. In an attempt to separate these impurities from the MreB in our sample, we used the ÄKTA Pure chromatography system with a gel filtration column to further purify the sample. The result of this is illustrated in Figure 5.9.

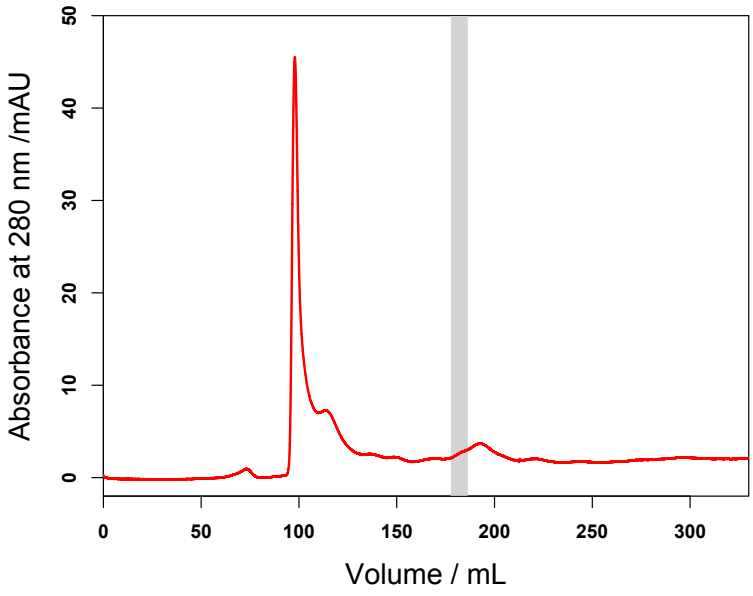

Figure 5.9: *Example chromatogram of the gel filtration of MreB. The column used was a HiPrep Sephacryl S-300 HR (GE Healthcare), which was equilibrated with 3 volumes of Buffer C (Appendix B.5) prior to use. A flow rate of 1 mL/min was used for this measurement.*

Figure 5.9 shows the result of the gel filtration of the MreB sample. The small band with maximum at 193 mL is the region where MreB came off the column. However, it was found that a number of impurities also came off here, and so to minimise their presence in the final sample, only the fractions within the grey region of the chromatogram were pooled. An SDS-PAGE gel was run of these pooled fractions, in addition to the fraction taken from the large peak at around 100 mL on the

chromatogram, and the result is given in Figure 5.10.

Figure 5.10 shows that the MreB protein is of high purity following gel filtration. Therefore the sample was concentrated using a VivaSpin® 20 sample concentrator with centrifugation at 3,200×g at 4°C. A small volume of dilute MreB solution was left following this method, which was sufficient for structural analysis using circular dichroism (CD).

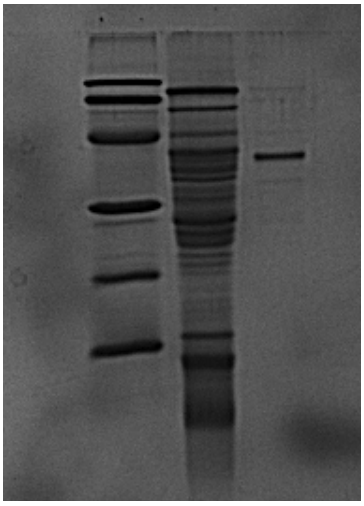

Figure 5.10: *Result of SDS-PAGE run on a 15% resolving gel. The lane on the far left are the protein markers (their sizes from top to bottom are: 97 kDa, 66 kDa, 45 kDa, 30 kDa, 20 kDa and 14 kDa). The lane in the middle is from the pooled fractions around the 100 mL region of Figure 5.9. The lane on the right is from the fractions within the grey region of Figure 5.9*

5.3 Results and Discussion

5.3.1 Circular dichroism and MreB secondary structure

Circular dichroism is the difference in the absorption of right (A_L) and left (A_R) circularly polarised light by an optically active material, as stated in Equation 5.1 [141].

$$CD = A_L - A_R \tag{5.1}$$

Samples of chiral molecules, where one enantiomer is in excess, are optically active — a fact that was first demonstrated by Pasteur in his observations of optical

activity in the two enantiomers of tartaric acid [142]. Proteins are made up of amino acids, which, with the exception on glycine, are chiral molecules, and only their L- enantiomer is produced by cells to make proteins. However, it is not only the components of proteins that are chiral, but also the regular structures they form when folded, known as secondary structure. The most common examples of secondary structure are α-helix, β-sheet and β-turn, and each of these elements produce distinct features in a far-UV CD spectrum. A CD spectrum of MreB is given in Figure 5.11.

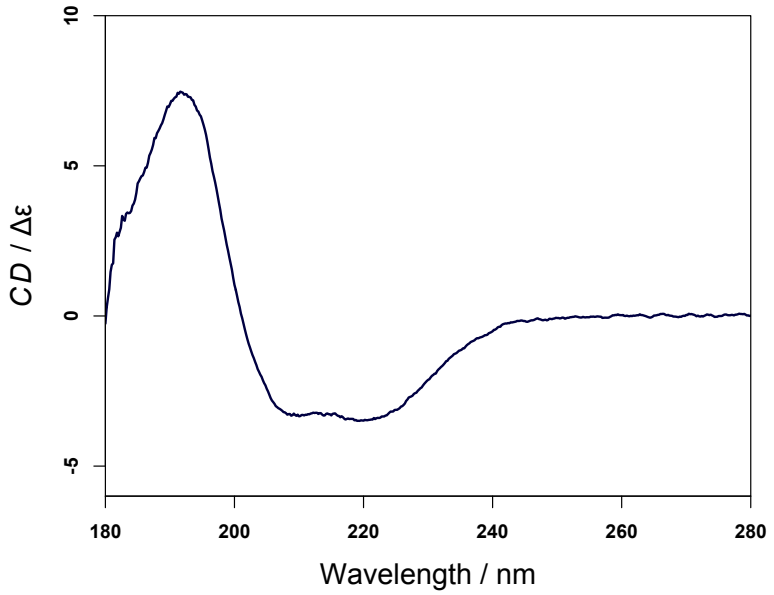

Figure 5.11: *Circular dichroism spectrum of E. coli MreB (with 20 residues omitted). This measurement was taken using the concentrated sample used to run the SDS-PAGE gel in Figure 5.10 in a 0.1 cm quartz cuvette. A Jasco J-1500 circular dichroism spectropolarimeter was used for the measurement. The concentration of the sample of 0.55 μM, which was determined using an extinction coefficient of ε_{280} = 7450 $M^{-1} cm^{-1}$*

Figure 5.11 shows that the protein appears to have a large amount of α-helix, as the large positive peak at 190 nm, in addition to the negative peaks to 208 and 222 nm, are signature spectral features of this structure [143]. To analyse the spectrum further, we used the online tool DichroWeb, developed by Whitmore and Wallace of the University of London [144].

DichroWeb allows users to predict the secondary structure elements of a protein

from its *CD* spectrum using one of five analysis algorithms: SELCON3 [145, 146]; CONTINLL [147, 148], K2D [149]; CDSSTR and VARSLC [150–152]. A number of reference data sets are also used in the analysis [152–155]. Figure 5.12 shows the results of the analysis of the MreB *CD* spectrum given in Figure 5.11, using the SELCON3, CONTINLL, CDSSTR and K2D algorithms. Reference set 7 was used for all with the exception of K2D, which is preprogrammed with its own reference set [155].

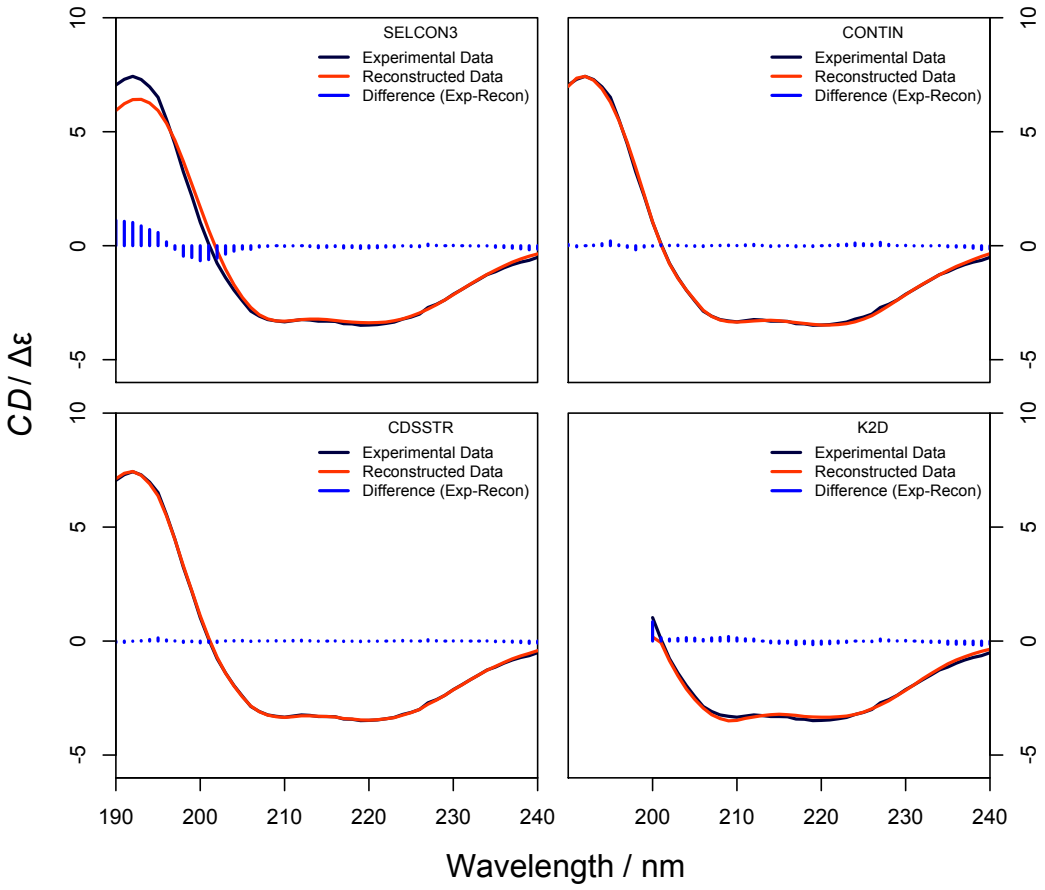

Figure 5.12: *Figure showing the output of DichroWeb using four of its algorithms: SELCON3 (top left), CONTINLL (top right), CDSSTR (bottom left) and K2D (bottom right). In each of the four panels the experimental input data are plotted along with the reconstructed data produced using the analysis algorithm. The figure also shows the difference between the experimental and reconstructed data.*

From Figure 5.12 it is apparent that the analysis algorithms provide a good spectral fit to the experimental data, with only the fit using the SELCON3 algorithm having any significant error in the far-UV of the spectrum. From these results we can be confident in the other output of DichroWeb, which are the predicted proportions of

secondary structure elements within the protein. These are given in Table 5.8, along with the normalised root mean square deviation (NRMSD) fit parameter [156].

Table 5.8: Secondary structure composition of MreB calculated using a range of algorithms in the online web server DichroWeb. The spectrum given in Figure 5.11 was used as input data. The far right column of the table contains the NRMSD parameter, which indicates the goodness of fit between the experimental and calculated spectra.

Analysis	**α-Helix**	**β-Sheet**	**β-Turn**	**Other**	**Total**	**Spectral NRMSD**
SELCON3	0.36	0.17	0.19	0.28	1.00	0.11
CONTIN	0.34	0.18	0.19	0.29	1.00	0.02
CDSSTR	0.38	0.16	0.19	0.27	1.00	0.01
K2D	0.32	0.18	-	0.50	1.00	0.07

The crystal structure of *C. crescentus* MreB has been published previously by van den Ent *et al.* [157]. The secondary structure reported in the protein data bank (PDB entry: 4czi) from the crystal structure the authors submitted — calculated using the DSSP hydrogen bond estimation algorithm [158] — contains 36% α-helix and 27% β-sheet. This is in reasonable agreement with the secondary structure composition of MreB calculated in DichroWeb, particularly the α-helix content. It is to be expected that the MreB measured here would have less ordered structure, as it was recorded in solution, whereas the *C. crescentus* MreB measured by van den Ent *et al.* was from crystal structure, which is an inherently more ordered and restricted environment.

The β-sheet content derived from our calculated MreB spectra is significantly lower than that reported in the literature for *C. crescentus* MreB [157]. Although the fact that our measurement was conducted in the solution phase will partially account for this discrepancy, a further reason in that 5.2% of the β-sheet content of the published structure comes from the structure within the first 20 residues of the protein, which we have excluded when expressing our *E. coli* MreB.

5.3.2 MreB fluorescence

Using the same sample as was used to record the *CD* spectrum in Figure 5.11, the fluorescence excitation and emission spectra of MreB were recorded on a Jasco FP-6500 spectrofluorometer. The result is given in Figure 5.13.

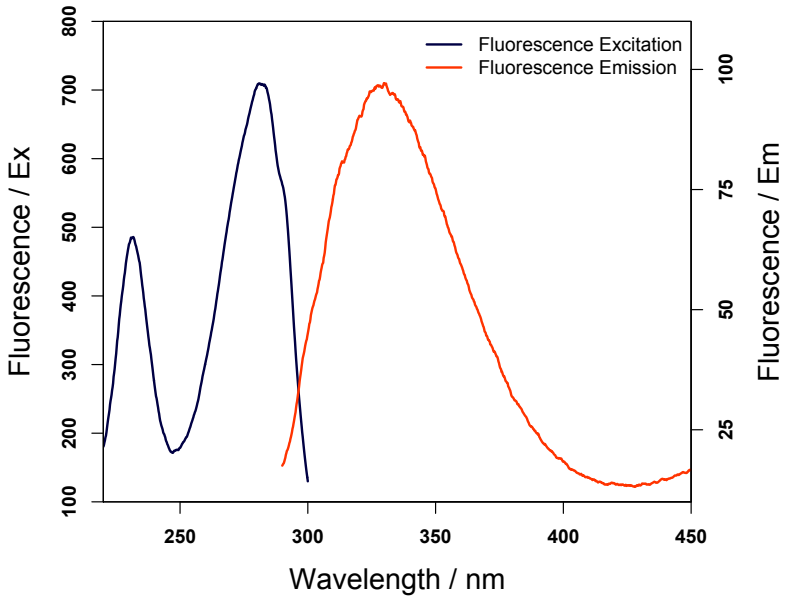

Figure 5.13: *Fluorescence excitation (blue) and emission (red) spectra of MreB, measured on a Jasco FP-6500 spectrofluorometer. For the excitation spectrum, the emission wavelength was set to 320 nm, and the excitation and emission bandwidths were set to 3 nm and of 10 nm, respectively. For the emission spectrum, the excitation wavelength was set to 280 nm, and the excitation and emission bandwidths were set to 5 nm and 3 nm, respectively.*

MreB does not contain any tryptophan residues, and so its fluorescence comes from its 5 tyrosine residues. As mentioned in Section 4.3.3, tyrosine is a poor fluorophore in proteins, and the measurements here were recorded with large excitation and emission bandwidths, and the PMT detector sensitivity set to high, giving it a high HT voltage. With these settings, we can see that good fluorescence spectra can be collected from the protein.

The spectra given in Figure 5.13 show that it may be possible to collect *FDLD* spectra of MreB if the protein can be oriented. We had attempted unsuccessfully a number of times to collect *FDLD* spectra of another protein that only contains a single tyrosine residue, FtsZ — a bacterial tubulin homologue whose *LD* spectrum

has been recorded and published [159] — but this result shows that MreB may be a more suitable candidate. Unfortunately, we were unable to adapt the purification protocol of MreB to obtain enough sample to develop a polymerisation kinetics assay using $FDLD$.

5.4 Conclusions

Here we have shown a method for the cloning, expression and purification of *E. coli* MreB with a cleavable poly-histidine tag. Its purity has been confirmed through SDS-PAGE, where a strong band was observed just below the 37 kDa marker — the molecular weight of our MreB is 36938.3 Da — with very few, faint bands appearing from contaminants. The structure of the purified MreB sample was analysed using CD, along with the online analysis tool DichroWeb, and it was found that the structure of our sample from *E. coli* was in good agreement with a previously published structure of MreB from *C. crescentus* [157].

We have also shown that a good fluorescence signal can be collected from MreB, despite tyrosine being its only fluorophore, which may indicate that its polymerisation kinetics could be studied using our $FDLD$ method. Unfortunately we were not able to optimise our method for purifying our product to obtain a high enough quantity of MreB to be able to develop this $FDLD$ assay during this project. The problems we had were in maintaining a high amount of soluble protein after lysing the cells, and then separating the soluble MreB from a large number of contaminants, even after HisTrap elution and gel filtration.

CHAPTER 6

Direct detection and measurement of wall shear stress using a filamentous bio-nanoparticle — M13 bacteriophage

6.1 Introduction

This chapter details the data processing and analysis contribution to a project that aimed to calculate the wall shear stress (WSS) a fluid exerts on a surface, which was published in the October 2015 issue of Nano Research [2]. WSS is a measure of the tangential component of the force exerted on a surface by a fluid flowing over it [160]. Abnormal WSS in the vasculature is associated with a number of medical conditions, such as atherogenesis [161], and aneurysms [162]. Therefore, our ability to accurately measure the WSS stress within the vasculature is highly valuable to diagnostic, and even preventative medicine.

Currently, the WSS within the vasculature is most commonly measured using bulk measurement techniques, such as particle image velocimetry (PIV) or particle tracking velocimetry (PTV) techniques [163, 164]. There have been a number of reported problems with these techniques for investigating WSS, one of which is their inherent bias, due to the concentrations of tracer particles decreasing as the surface boundary is approached [165]. Secondly, they make the assumption that both the flow and the surface over which the fluid is passing, is uniform. This means that the measured WSS is an average over that surface, and some of the information on the WSS dynamics critical to understanding diseases of the vasculature may be obscured.

This work uses fluorescently labelled M13-bacteriophage, with a surface binding agent attached to the end pIII proteins, as a nanosensor. The M13 bacteriophage complexes were attached to flow slides coated with either collagen IV or cultured human conditionally immortalised endothelial cells (GEnCs), and their response to a range of flow velocities allowed us to calculate the WSS at the point of attachment. The work was undertaken as part of a large collaborative project. The contribution of the author of this thesis to the work focussed around analysis of the fluorescence signals, which is the main content of this chapter.

6.2 Methods

This section presents an overview of all the methods used to determine the WSS exerted on a specific point of a surface by a fluid flowing over it. The focus of this chapter is data processing and analysis, and so these sections contain much more detailed information.

6.2.1 Experimental methods

All experimental procedures were carried out by Daniela P. Lobo, however, a brief outline of the experiment is presented here to help with understanding the subsequent data analysis.

Cultures of M13 bacteriophage were grown, purified, and fluorescently labelled with tetramethylrhodamine isothiocyanate (TRITC), as described by Pacheco-Gómez *et al.* [107], and subsequently derivatized with a protein anchor attached to the pIII protein, as illustrated in Figure 6.1. The protein anchors used were anti-collagen IV (aCol) and wheat germ aglutinnin (WGA) to be used in the collagen IV and GEnCs coated flow slide experiments, respectively.

Microchannel flow slides, coated with collagen IV were purchased from Ibidi, Munich, and human conditionally immortalized glomerular endothelial cells (GEnCs) were grown using a literature protocol [107, 166]. The completed M13-aCol-TRITC and M13-WGA-TRITC constructs were bound to a flow slide, coated in either collagen IV or GEnCs, and the slides were placed in a spinning disk confocal microscope. A pump was then attached to the slides to control the flow rate, and all fluorescent images were recorded using a nominal WSS of 0-3.5 dyn·cm^2.

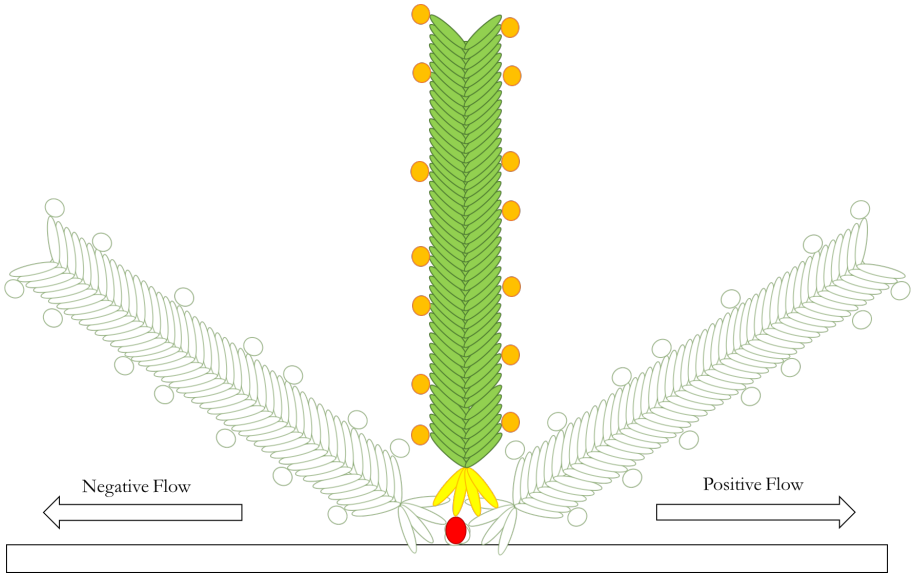

Figure 6.1: *Illustration of the derivatized M13-aCol-TRITC bacteriophage. The pVIII proteins (green) were labeled with the fluorescent dye TRITC (orange). The pIII proteins (yellow) were labelled with the anti-body anchor (red), which attached the whole complex onto a surface. The figure also shows how the particle responds to flow in the 'positive' and 'negative' directions.*

6.2.2 Phage orientation function

Microscopy experiments of two kinds were undertaken. Five image stacks recording the response to flow of M13-aCol-TRITC attached to collagen IV coated slides were obtained. Only one image stack for M13-WGA-TRITC attached to a GEnCs coated flow slide was collected. These image stacks were converted to AVI files using the program Fiji [167]. All subsequent data processing was performed in MATLAB (MATLAB R2014b, The MathWorks Inc., Natick, MA) with code written for the purpose.

The first step was to read in to MATLAB the .avi file containing the microscopy image stack. Following this, the number of frames and the frame rate was retrieved from the file, from which the time parameter was calculated.

```
cellObj = VideoReader('PhageMicroscopyMovie.avi');
vidFrames = read(cellObj);
```

```
numFrames = get(cellObj, 'NumberOfFrames');
frameRate = get(cellObj,  'FrameRate');
Time = ((1:numFrames)/frameRate)';
```

The method used to distinguish the M13 bacteriophage particles from the background is thresholding, where the image is segmented based on the fact that regions where the M13 is present have considerably higher pixel intensity than where it is absent [168]. To perform this action, the RGB images (from the RGB colour model) need to be converted to grayscale, and MATLAB requires the image intensity values to be converted to double precision format.

```
for k = 1 : numFrames
    img(k).gray = rgb2gray(vidFrames(:,:,:,k));
end

for k = 1 : numFrames
    img(k).double = im2double(img(k).gray);
end
```

To display an example image from the greyscale stack, the 'imshow' command is used. An example of this is given in Figure 6.2 to show one greyscale image of a fluorescent M13-aCol-TRITC particle. This frame of the image stack is used throughout this section to show the effect of the image processing commands.

```
figure(1)
imshow(img(45).gray,  'InitialMagnification', 'fit')
```

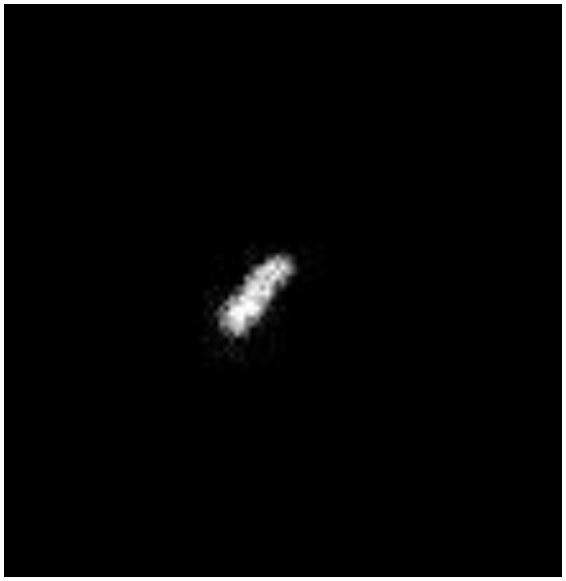

Figure 6.2: *Example of a greyscale image produced after reading a microcopy image stack in to MATLAB. This image shows a M13-aCol-TRITC particle, anchored to a collagen IV coated flow slide.*

The next step was to compute threshold values that will be used to convert the greyscale images to binary images. MATLAB has a global function for this, based on Otsu's method [169]. Once the threshold value was computed, it was used to binarise the images, so that pixels with an original value greater than the threshold were assigned a value of one, and those below are set a value of zero. A duplicate binary image stack was also created to be used for background subtraction.

```
level=zeros(numFrames,1);
for k=1:numFrames
    level(k)=graythresh(img(k).double);
end

for k = 1 : numFrames
    img(k).binary = im2bw(img(k).double,level(k));
end

for k = 1 : numFrames
```

```
    img(k).binary1 = img(k).binary;
end
```

After thresholding, the frame of the image stack shown above is now displayed in Figure 6.3.

```
figure(2)
imshow(img(45).binary1, 'InitialMagnification','fit')
```

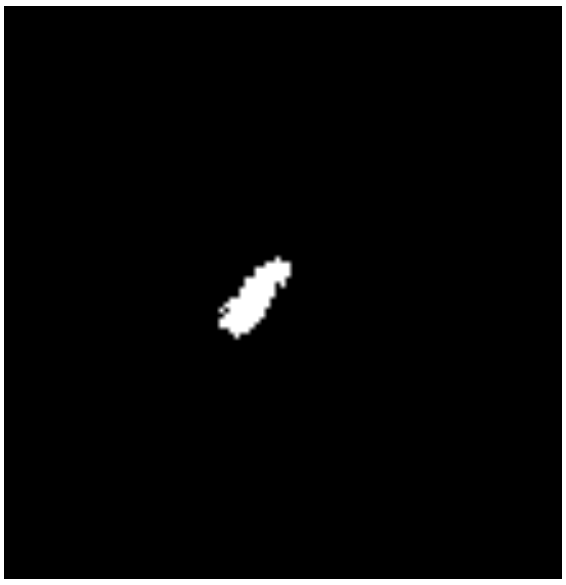

Figure 6.3: *The figure shows a product of the thresholding process, using the same image as is shown in Figure 6.2. The white region has a uniform pixel intensity of one, and all other pixels have a value of zero.*

At this point the images were binary, with the main region of ones being the M13 bacteriophage complex. This region was then defined as the region of interest by finding and grouping the connected ones in the image. To clean up any residual background regions of ones that made it through the thresholding process, the largest region (the M13) was deleted from the first image stack, and then this whole stack was subtracted from the duplicate made above.

```
for k = 1 : numFrames
    regions(k) = bwconncomp(img(k).binary);
end

for k = 1 : numFrames
    numPixels = cellfun(@numel,regions(k).PixelIdxList);
    [biggest,idx] = max(numPixels);
    img(k).binary(regions(k).PixelIdxListidx) = 0;
end

for k = 1 : numFrames
    img(k).subtracted = imsubtract(img(k).binary1,img(k).binary);
end
```

The final piece of image processing that was performed was to find the convex hull of the region, which fits a convex polygon within the M13 bacteriophage region of the binary image. This was included to deal with the potential problem of a group of pixels within the phage body having a pixel intensity below the threshold value (and hence would now have a intensity of zero), and also to help smooth the edges of the phage, as both of these issues may distort the information on the phage orientation and length.

```
for k = 1 : numFrames
    img(k).convhull = bwconvhull(img(k).subtracted);
end
```

An example image from the final processed image stack is given in Figure 6.4.

```
figure(3)
imshow(img(45).convhull,'InitialMagnification','fit')
```

Figure 6.4: *The figure displays and example of the processed images used to obtain orientation and major axis length data. It is once again the same image as was used in Figure 6.2, however this a convex polygon has been fit within the boundaries of this particle, and so the edges are considerably smoother.*

The function 'regionprops' was used to obtain the M13-aCol-TRITC and M13-WGA-TRITC orientation and major axis length from each image in the stack. The function was used to find the major axis of the M13 complexes by finding the longest straight line that can be drawn within the region of interest, in pixels. The function is then used to find the particle's orientation by calculating the angle between the major axis and the horizontal, or x axis of the image, in degrees.

```
for k = 1 : numFrames
Orientation(k).Orientation=regionprops(img(k).convhull,'Orientation');
end
```

```
for k = 1 : numFrames
Majoraxis(k).Majoraxis=regionprops(img(k).convhull,'MajorAxisLength');
end
```

At this point, all of the processed data were stored in structure arrays. To use the data for subsequent calculations more easily, and also to plot it, the relevant data needed to be extracted into vectors. This was done using the 'extractfield' commands. Here, the M13 length data was also converted from pixels to μm, which in this case required multiplication by 0.0693.

```
 Angle=zeros(numFrames,1);
for k = 1 : numFrames
 Angle(k)=extractfield(Orientation(k).Orientation,'Orientation');
end

 Length=zeros(numFrames,1);
 for k = 1 : numFrames
 Length(k)=extractfield(Majoraxis(k).Majoraxis,'MajorAxisLength');
 end

LengthNM = Length*0.0693;
```

The next problem that must be dealt with was to find a way of defining the times at which the flow was applied to the M13-aCol-TRITC, and when it was turned off. The defining characteristic of the flow being on is that the movement of the particle is restricted, and the variance in its angle relative to the horizontal axis is reduced. It is this property that we used to distinguish between the flow being on or off. First, a moving standard deviation of the orientation data was calculated. The minima of this vector corresponds to the times at which flow was applied. The

'findpeaks' function finds the local maxima of a vector, and so we simply calculated the inverse of the moving standard deviation vector and used this function to find the times at when flow is applied. These data were also smoothed prior to using the findpeaks function to ensure the maxima were found precisely.

```
MovStanDev = movingstd(Angle,51,'c');

InverseSmooth=-1*MovStanDev;

SmoothedData = smooth(InverseSmooth,0.1,'rloess');

findthepeaks=findpeaks(SmoothedData, 'MINPEAKHEIGHT', -30);

for k=1:length(findthepeaks)
    indvalues(k)=find(SmoothedData==findthepeaks(k));
end
```

The smoothed moving standard deviation data is displayed in Figure 6.5. It shows that there are nine peaks, and the modulus of their maximum values are trending to an increased magnitude as time increases, which tells us that the flow rates being applied are getting progressively weaker.

```
figure(4);
plot(Time, SmoothedData)
xlabel('Time / s')
ylabel('Smoothed Data')
```

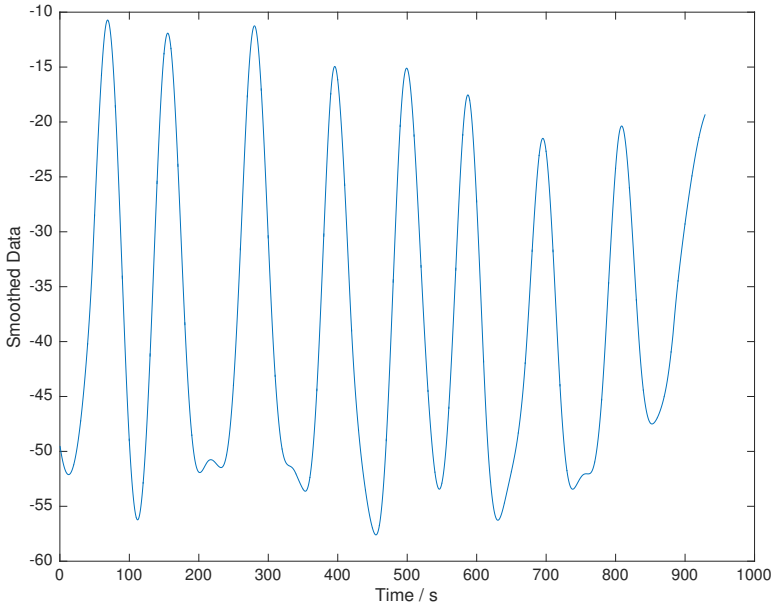

Figure 6.5: *The inverse moving standard deviation of the orientation data, obtained from one of the microscopy data sets using M13-aCol-TRITC bound to a collagen IV coated flow slide. The data has been smoothed so that the maxima are better defined.*

The maxima values from Figure 6.5 were then used to set a time frame over which flow was applied. Twenty seconds after the maxima and ten seconds prior was selected, so to allow the M13 bacteriophage complexes some time to settle following the application of shear flow. The average orientation and major axis length of the M13 particles over these time frames were calculated, in addition to the standard deviation of these properties.

```
LOW=49;
HIGH=101;

indvalues=[indvalues, numFrames-(HIGH+5)];

for k=1:length(indvalues)
    StdAngle(k) = std(Angle(indvalues(k)-LOW:indvalues(k)+HIGH));
end

for k=1:length(indvalues)
```

```
    StdLength(k) = std(LengthNM(indvalues(k)-LOW:indvalues(k)+HIGH));
end

for k=1:length(indvalues)
    Average_Angle(k) = mean(Angle(indvalues(k)-LOW:indvalues(k)+HIGH));
end

for k=1:length(indvalues)
Average_Length(k) = mean(LengthNM(indvalues(k)-LOW:indvalues(k)+HIGH));
end

for k=1:length(indvalues)
   TimeBars(k)=Time(ceil((indvalues(k)-LOW+indvalues(k)+HIGH)/2));
end

findthepeaks=findpeaks(SmoothedData, 'MINPEAKHEIGHT', -30);

for k=1:length(findthepeaks)
    indvalues(k)=find(SmoothedData==findthepeaks(k));
end
```

Finally, the processed data were grouped and exported to text files, so that they can be analysed and plotted in R [170].

```
DataMatrix=cat(2,Time,Angle,LengthNM);
header = 'Time', 'Angle', 'Length';
RawDataOut = dataset(DataMatrix,header:);

export(RawDataOut,'file','RawDataOut.txt','Delimiter',',')
% To export 'raw' data to a text file
```

```
DataMatrix=cat(2,TimeBars',Average_Angle',StdAngle',Average_Length',...
StdLength');
ProHeader = ('TimeBars','AverageAngle','StdAngle','AverageLength',...
'StdLength');
ProDataOut = dataset(DataMatrix,ProHeader:);

export(ProDataOut,'file','ProDataOut.txt','Delimiter',',')
% To export 'processed' data to a text file
```

6.2.3 Mathematical model

David J. Smith wrote a probability model for the orientation of the tethered bacteriophage particle in flow, which is presented in detail in the SI of our publication [171]. It begins by postulating a partial differential function — based on a random walk model, with additional parameters to account for the viscous restoring force of the fluid — and then uses a set of assumptions to present the ordinary differential equation:

$$D\frac{d^2p}{d\psi^2} + \frac{d(\beta\psi p)}{d\psi} = 0 \tag{6.1}$$

where D is the diffusion coefficient; ψ is the orientation of the particle; β is a positive constant that relates to the shear rate of the fluid; and $p = p(\psi)$, which is the probability of finding the particle in a given orientation. The key part for the experimental analysis is that one solution of this ODE is a normal distribution, where the mean equals zero and the standard deviation (σ) equals $\frac{D}{\beta}$:

$$p = A\exp(\frac{-\beta\psi^2}{2D}) \tag{6.2}$$

From here, as shown in the SI of the paper [2], we can say that:

$$\ln(\sigma) = -0.5\ln(\text{WSS}) - 1.5\ln(L) + k \tag{6.3}$$

where L the length of the particle and k is a constant, and:

$$\frac{1}{\sigma^2} \propto \text{Nominal WSS} \tag{6.4}$$

Therefore, the model predicts that a plot of $\ln(\sigma)$ *vs.* ln(WSS) will have a slope of -0.5 and that the nominal WSS is proportional to the inverse square of the standard deviation of the particle's adopted orientations at a given flow rate.

6.3 Results and discussion

6.3.1 Collagen IV coated flow slides

The experiments where the M13-aCol-TRITC was attached to a collagen IV coated slide were used as a simple model system, to show that the WSS can be predicted from the behaviour of the particle in flow, using the mathematical model described in Section 6.2.3 above. To confirm that the collagen IV coated slide results agree with the model, we first checked that the orientation data of M13-aCol-TRITC followed a normal distribution, at each flow rate, as predicted by Equation 6.2. To do this we used the Shapiro-Wilks test using the function shapiro.test(x) in *R*, and also the Anderson-Darling test, using the function ad.test(x) in the nortest package [172,173]. An example set of results from one of the image stacks is given in Table 6.1.

Table 6.1: Results of the Shapiro-Wilks and Anderson-Darling tests for the normality orientation data from one of the image stacks. The null hypothesis in the Shapiro-Wilks test is that the data is from a normal distribution, and so a p-value > 0.05 indicates that the data is normally distributed. Likewise, the null hypothesis of the Anderson-Darling test is that the data is normally distributed, and so a p-value > 0.05 would indicate that this is the case.

Nominal WSS ($\mathbf{dyn.cm^{-2}}$)	**p-value**	
	Shapiro-Wilks Test	**Anderson-Darling Test**
3.5	0.2606	0.05826
-3.5	0.2672	0.2321
2.5	0.4731	0.3933
-2.5	0.146	0.2865
1.5	0.9939	0.9953
-1.5	0.07569	0.06401
1.0	0.7106	0.5338
-1.0	0.6047	0.4769
0.5	0.1486	0.09329
0	2.321e-05	2.492e-05

Table 6.1 shows that when a shear flow is applied, all of the data agree with the null hypothesis of both tests: that the data comes from a normal distribution. This is a good indication that the mathematical model is correct. The extremely small p-values shown at a nominal WSS of 0 dyn.cm^{-2} shows that the orientation data is not normally distributed when no flow is applied, which was expected.

In the collagen IV coated slide experiments, the motion of a M13-aCol-TRITC particle was unhindered in all directions, and so it was equally likely to adopt any orientation relative to the horizontal axis of the image (in the range -90° to 90°) in either the positive or negative flow directions. Figure 6.6 illustrates this symmetrical response to flow direction.

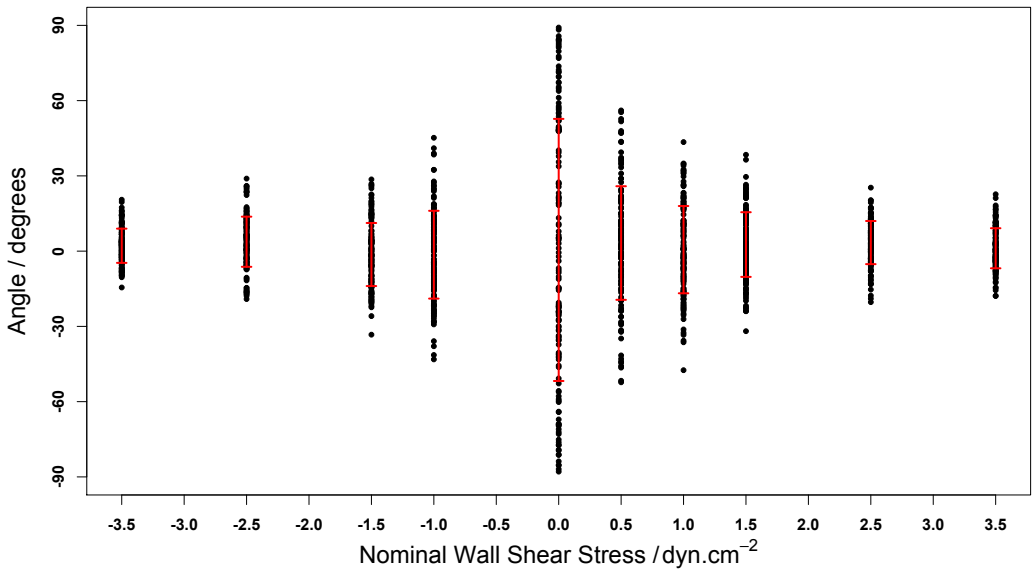

Figure 6.6: *Scatter plot of the orientations adopted by the M13-aCol-TRITC particle bound to a collagen coated flow slide at varying nominal WSS values. The red errors span $\pm\sigma$ around the mean value.*

Figure 6.6 shows that when no flow is applied, the phage particle freely adopts any orientation between $-90°$ and $+90°$, moving only under the influence of Brownian motion. It also shows that increasing the flow rate restricts the orientation of a particle, and the higher the flow rate the smaller the variance in particle orientation. So by observing the variance in the orientation of a particle at a given flow rate, we have a means of measuring the strength of that flow rate.

It is also apparent from Figure 6.6 that there is symmetry in the effect that the positive and negative flow rates have on the phage particle's orientation. As the particle responds the same way, irrespective of flow direction, we can group the orientation data based on the modulus of the nominal WSS values. These data were then used to calculate the frequency distribution of angles of the M13 particle in $3°$ bins, which was normalised to the number data points within each nominal WSS data set, as illustrated in Figure 6.7.

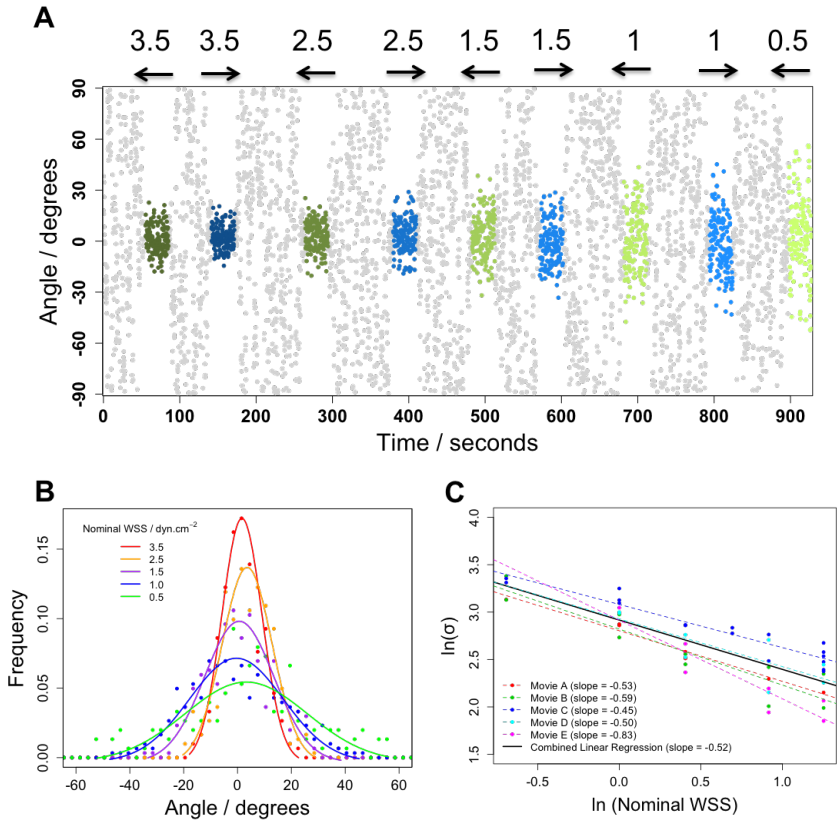

Figure 6.7: *(a) Example of the variation in angle of the M13-aCol-TRITC particle bound to a collagen IV coated flow with time when a shear flow is applied. The nominal WSS is indicated at the top in dyn.cm^{-2}. (b) Normalised frequency distribution of the orientation adopted by an M13 bacteriophage particle, tethered to a collagen IV coated slide, subject to a range of nominal WSS. (c)* $\ln(\sigma)$ *vs.* $\ln$*(Nominal WSS) for the 5 image stacks of M13-aCol-TRITC bound to collagen IV coated flow slides used in this work. The regression line is calculated from the combination of all of the data from the image stacks.*

Figure 6.7 A and B show that at higher nominal WSS, the distribution is much narrower around 0°, and as the WSS is relaxed, the distribution broadens as the M13 particle is less restricted. Figure 6.7 C shows that the data are in good agreement with the model shown in Equation 6.3, which allowed us to look at data where the particle was not on a uniform surface, and flow direction mattered.

6.3.2 Endothelial cell coated slides

The movie recorded of the M13-WGA-TRITC bacteriophage bound to a GEnCs coated flow slide was analysed in the same way as the above. The difference in this case was that the surface of the slide is not uniformly flat, and so depending on

the location on the GEnCs that the phage is bound to, its movement may be more restricted when subjected to flow in one direction than the opposite flow direction. The particle in our movie exhibits this behaviour, which is illustrated in Figure 6.8.

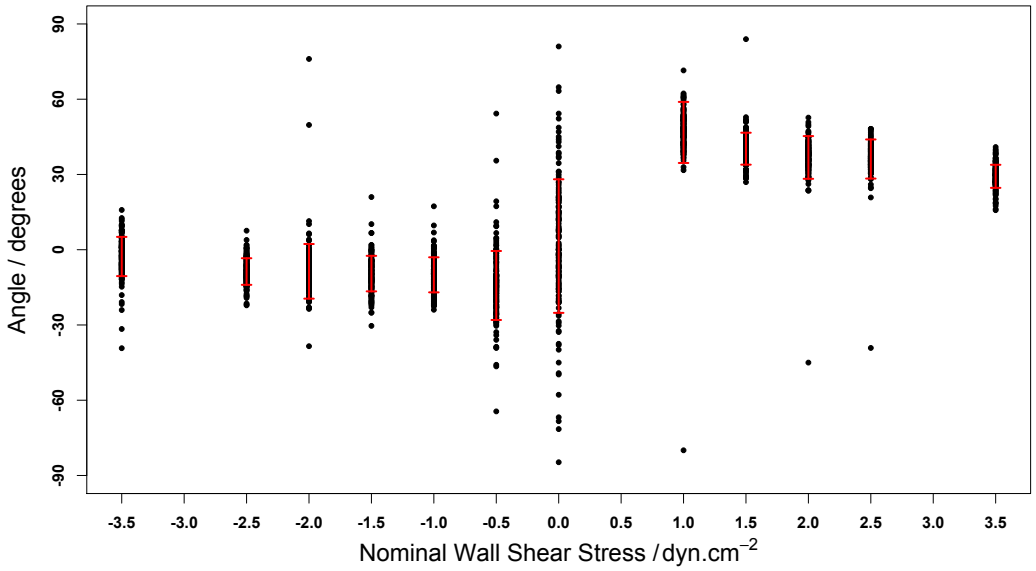

Figure 6.8: *Illustration of the asymmetrical response of the particle to flow direction. The points show the orientations adopted by the M13-WGA-TRITC particle bound to a GEnC coated flow slide at varying nominal WSS values and the red errors span* $\pm\sigma$ *around the mean value.*

Figure 6.8 shows that in the negative flow direction, the average orientation adopted by the M13-WGA-TRITC particle was ~ 0, whereas in the positive flow direction the average angle is higher and reduces with increasing nominal WSS. This shows that the particle's movement is restricted due to the position that it has bound to the cell. It can also be seen that the variance in the orientation of the particle is reduced when flow is applied in the positive direction. From Equation 6.4 this suggests that for equal flow rates in both directions, the positive flow direction would exert a higher WSS at the point where the particle is attached.

To assess the effect of the non-uniform surface on the exerted WSS more quantitatively, we can plot the $\ln(\sigma)$ vs. $\ln$(Nominal WSS), as we did for the collagen coated slides in Figure 6.7 C. The result is given in Figure 6.9.

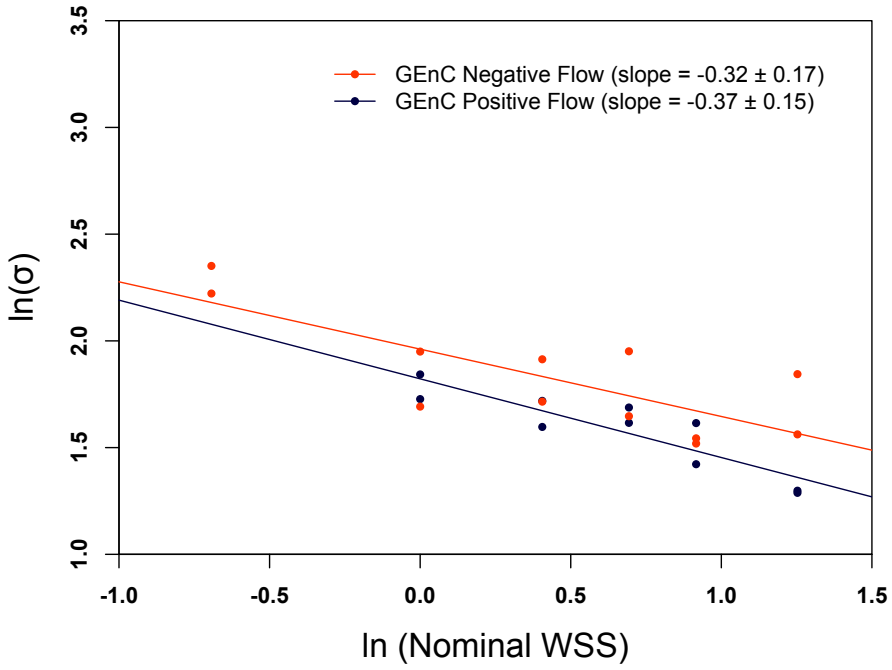

Figure 6.9: $\ln(\sigma)$ *vs.* $\ln$*(Nominal WSS) for the of M13-WGA-TRITC bound to GEnCs coated flow slides under shear flow in the positive and negative directions.*

Figure 6.9 shows the $\ln(\sigma)$ vs. ln(Nominal WSS) data for the M13-WGA-TRITC bacteriophage particle bound to a GEnCs coated flow slide, and the gradient of the calculated regression lines. Although the slopes of the regression lines appear smaller than the predicted value of -0.5 from Equation 6.3, they are in reasonable agreement within the large error of the experiment. More image stacks from these experiments would have reduced the error and allowed us to produce better statistics, which would have been preferable.

From Equation 6.4 we know that the nominal WSS is proportional to the inverse variance of the phage's orientation. To better illustrate the effect the GEnCs are having on the WSS, we can plot $1/\sigma^2$ versus the nominal WSS for both the collagen and GEnCs data. This is given in Figure 6.10.

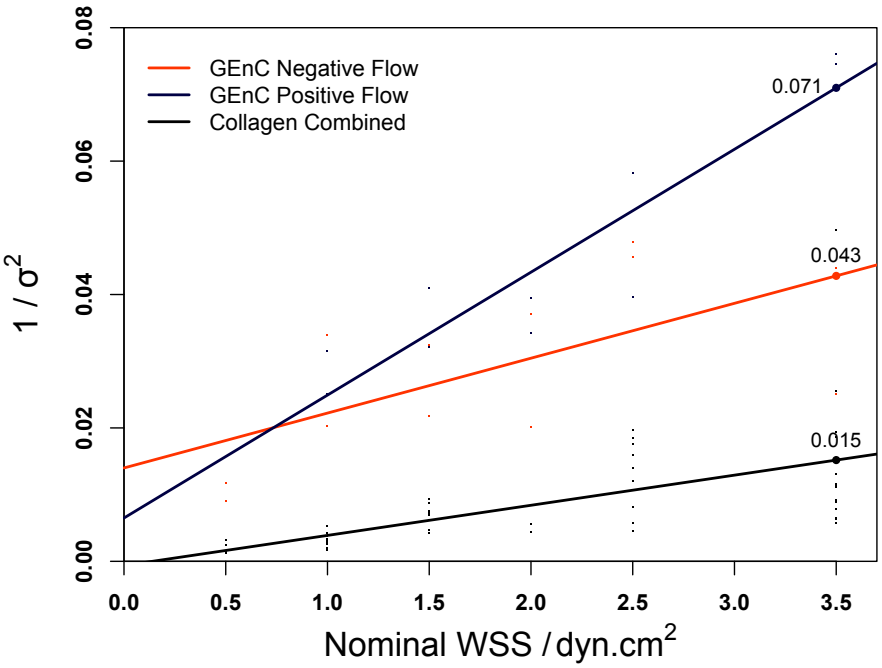

Figure 6.10: *Plot of the inverse variance ($1/\sigma^2$) versus nominal WSS from Figures 6.7 C and 6.9. The labelled points highlight the values at a nominal WSS of 3.5.*

From Figure 6.10 it is apparent that the presence of the GEnCs are having a large effect on the WSS at the point that the phage particle is attached, and also that the effect varies depending on the direction the fluid is flowing over it. As already shown by Barbee *et al.*, the presence of the endothelial cell significantly increases the WSS due to the shape of the protruding cell [174]. These results were corroborated by Pozrikidis, who mathematically modelled flow over protuberances in a plane surface in [175].

The effect of flow direction is also interesting. We can see that the WSS exerted is significantly higher when the flow is in the positive direction than when the flow is in the negative direction. We can see from Figure 6.8 that the particle is much more restricted in the orientation it can adopt when the flow is in the positive direction. This also give us an indication of where on the cell that the M13-WGA-TRITC particle may be bound, and shows that the WSS exerted in a surface by a fluid flowing over it is not uniform over that surface.

6.4 Conclusion

This work shows a method of measuring the WSS exerted on a surface by a fluid flowing over it with vastly increased spatial resolution than other commonly used methods, such as PIV and PTV. The method was calibrated using a simple model system of M13-aCol-TRITC particles bound to a collagen coated flow slides, where the WSS was calculated from the particle's flow behaviour using a mathematical model. This method was then applied to an irregular surface — M13-WGA-TRITC particles bound to GEnCs coated flow slides — and we showed that it is possible to measure the local WSS at the point of the particle's attachment. This experiment also highlights the deficiency in other methods that average over local WSS dynamics, by showing that the WSS exerted can be very different across a non-uniform surface.

This chapter was particularly focussed on the data processing and analysis elements of this work. The image stacks, which were collected on a Nikon Eclipse inverted microscope, were analysed using a custom made algorithm that was written in MATLAB. The images were binarised using a thresholding technique, and the background noise was subtracted from our region of interest (ROI). A convex polygon was then fit into the ROI to smooth its edges, and remove any dark pixels within it. The length and angle of the ROI was then tracked throughout each image stack, and a code was implemented to determine times where a shear flow had been applied. This process provided the data required to test the predicted phage behaviour using our mathematical model, and show the differences in WSS exerted on a surface by a constant shear rate, which depend on the uniformity of surface and the direction of the flow.

CHAPTER 7

Conclusions and future work

The aim of this work was to develop experimental and analytical methods, which enhance our ability to study samples of anisotropically oriented fluorophores. The primary development here is the novel fluorescence detection method for linear dichroism spectroscopy. Using this technique, we have shown that information on the relative orientation of chromophores in a sample can be obtained with increased sensitivity and selectivity than is achievable when using absorption LD. A particular motivation for this was to make LD more suitable for studying biological systems, which are often obtained in small quantities, in solutions that contain complex mixtures of molecules. We also explained whether flow fluorescence methods could be used more generally. To this end a new production method for MreB is reported, and the analysis of fluorescence data for tethered M13 bacteriophage is also presented.

The theory behind our $FDLD$ experiment, with a particular focus on how to produce an $FDLD$ spectrum from the currents generated in the PMT detector of a commercial CD spectropolarimeter, is derived in Chapter 2. The first experimental results of small molecules oriented on stretched PE^{OX} films is presented in Chapter 3, and in all of these experiments we demonstrated the large increase in sensitivity of $FDLD$, showing that signals of similar magnitude or larger were attainable with only a fraction of the amount of sample. Interestingly, some of the $FDLD$ spectra given in this chapter also showed an increased resolution of the vibronic components within an absorption band, illustrating that in some cases more information about a molecule may be obtained by using $FDLD$.

The LD and $FDLD$ spectra of complexes of DNA and ethidium bromide, propidium iodide, 4',6-diamidino-2-phenyindole (DAPI), and Hoechst 33258 are compared in Chapter 4. Here, we again showed the increased sensitivity of $FDLD$, though in this case the signal to noise of the spectra was poorer due to the distance between the sample in the Couette flow cell and the detector. However, we also demonstrated the increased selectivity of the measurement, as we were detecting signals from the fluorescent dyes only, and not the DNA, which often dominates the middle-UV region of LD spectra. In doing so, we were able to see in greater detail the sign and relative magnitude of the dye signals within this region, which adds to the information we know about how the molecules are bound to DNA.

In Chapter 4 we also gave the LD and $FDLD$ spectra of M13 bacteriophage oriented in Couette flow, where in addition to simply being able to detect tryptophan signals at lower M13 concentrations when using $FDLD$, we again showed the higher resolution of the different absorption bands of the indole chromophore attained when using $FDLD$. We propose that these properties would improve the detection capabilities of an LD assay designed to detect pathogenic bacteria in solution [107, 108].

We developed a protocol for the cloning, expression and purification of the *E. coli* actin homologue MreB, which is given in Chapter 5. We demonstrated that our product was pure using SDS-PAGE, and analysed its structure using circular dichroism and the online analysis tool: DichroWeb. We found that the structure of our protein was in good agreement with the published crystal structure of *C. crescentus* MreB, though ours showed slightly less ordered secondary structure, which would be expected as our measurement was performed in solution. Although we were not able to obtain MreB in a high enough quantity to develop an $FDLD$ assay to study its *in vitro* polymerisation kinetics, we did show that a good fluorescence signal can to obtained from the protein, indicating that this may be achievable.

We were also involved in a work which showed that the WSS could be calculated at a specific point by attaching a fluorescently labelled M13 bacteriophage to the surface, and gave the full details in Chapter 6. Our focus was primarily on the data processing and image analysis, and so these sections are given in greater detail. We showed that by using a global thresholding process in MATLAB, a background subtracted microcopy image stack containing a particle of interest can be binarised, and the particle's size and orientation can be tracked throughout the image stack. The data obtained using this algorithm were then used to calculate the WSS at the point of the particle's attachment, and clearly showed that it varied when the surface is not uniform. Future work using this method will involve the analysis of images obtained from a labelled particle bound to the wall of the vasculature *in vivo*. The ability to observe the effect of vascular surface dynamics should increase our understanding of diseases related to WSS.

Following on from the work of this thesis, the development of a new flow cell for micro-volume Couette flow $FDLD$ would greatly improve the signal to noise ratio of the measurement. The new design would have the sample chamber closer to the detector, with focussing lenses directing a higher proportion of the fluorescence emissions towards the detector. Although we were not able to achieve it during the course of this work, an area of high potential for $FDLD$ lies in observing the polymerisation process of proteins, and other monomers, to form long chain fibres. Using $FDLD$ one would be able to test the effect of a range of conditions, such as temperature, pH, or concentration, on the polymerisation of such a sample. To this end, an $FDLD$ Couette flow cell would also greatly benefit from including an injection system, so that reaction initiators (or terminators) could be introduced during the course of the measurement, and one could observe the propagation of the reaction in full.

A key measure of the usefulness of an analytical technique is how readily one can obtain information about a sample or a process of interest when using it. For investigations into the relative orientation of chromophores in complexes that possess a high aspect ratio, or when seeking to find the optimum conditions for molecules to polymerise to form fibres, Couette flow LD possesses a degree of selectivity, as only information on chromophores with a macroscopic alignment is obtained. Including the additional selectivity of fluorescence detection to the experiment broadens its utility, as data from samples of complex mixtures can more easily be recorded. This is also true of microscopy based experiments, such as our method for detecting WSS. By using a fluorescently labelled particle we were able to selectively detect its response to an applied shear flow, to the exclusion of all other particles carried in the solution, which would have been present were the experiment performed using a simple optical microscope. The synthesis of orientational and chromophoric selectivity in the methods developed in this work increase their utility, allowing one to directly record data from processes that may otherwise only be obtainable through a complex post-analysis — if at all. On this evidence, the design of composite experimental and analytical techniques should serve as a fruitful strategy for future investigations.

Bibliography

[1] C. E. Broughton, H. A. Van Den Berg, A. M. Wemyss, D. I. Roper, and A. Rodger, "Beyond the Discovery Void : New targets for antibacterial compounds," *Science Progress*, vol. 99, no. 2, pp. 153–182, 2016.

[2] D. P. Lobo, A. M. Wemyss, D. J. Smith, A. Straube, K. B. Betteridge, A. H. J. Salmon, R. R. Foster, H. E. Elhegni, S. C. Satchell, H. A. Little, R. Pacheco-Gómez, M. J. Simmons, M. R. Hicks, D. O. Bates, A. Rodger, T. R. Dafforn, and K. P. Arkill, "Direct detection and measurement of wall shear stress using a filamentous bio-nanoparticle," *Nano Research*, vol. 8, no. 10, pp. 3307–3315, 2015.

[3] L. D. Barron, *Molecular Light Scattering and Optical Activity*. New York, NY, USA: Cambridge University Press, 2nd ed., 2009.

[4] H. Ambronn, "Ueber den pleochroismus pflanzlicher zellmembranen," *Annalen der Physik*, vol. 270, no. 6, pp. 340–347, 1888.

[5] R. Marrington, T. R. Dafforn, D. J. Halsall, and A. Rodger, "Micro-volume couette flow sample orientation for absorbance and fluorescence linear dichroism.," *Biophysical journal*, vol. 87, pp. 2002–12, September 2004.

[6] D. E. Waldron, R. Marrington, M. C. Grant, M. R. Hicks, and A. Rodger, "Capillary circular dichroism," *Chirality*, vol. 22, no. 1E, pp. E136–E141, 2010.

[7] J. R. Lakowicz, *Principles of Fluorescence Spectroscopy*. Kluwer Academic/Plenum Publishers, second ed., 1999.

[8] M. Bloemendal and R. van Grondelle, "Linear-dichroism spectroscopy for the study of structural properties of proteins," *Moleular Biology Reports*, vol. 18, pp. 49–69, 1993.

[9] B. Nordén, C. Elvingson, M. Kubista, B. Sjöberg, H. Ryberg, M. Ryberg, K. Mortensen, and M. Takahashi, "Structure of RecA-DNA complexes studied by combination of linear dichroism and small-angle neutron scattering measurements on flow-oriented samples.," *Journal of molecular biology*, vol. 226, pp. 1175–91, August 1992.

[10] E. W. Thulstrup and J. Michl, "Orientation and linear dichroism of symmetrical aromatic molecules imbedded in stretched polyethylene," *Journal of the American Chemical Society*, vol. 104, pp. 5594–5604, October 1982.

[11] E. W. Thulstrup and J. Michl, "Polarized absorption spectroscopy of molecules aligned in stretched polymers bl," *Spectrochimica Acta Part A: Molecular Spectroscopy*, vol. 44, pp. 767–782, January 1988.

[12] S. E. Howson, A. Bolhuis, V. Brabec, G. J. Clarkson, J. Malina, A. Rodger, and P. Scott, "Optically pure, water-stable metallo-helical 'flexicate' assemblies with antibiotic activity.," *Nature chemistry*, vol. 4, pp. 31–6, January 2012.

[13] F. R. Svensson, P. Lincoln, B. Nordén, and E. K. Esbjörner, "Tryptophan orientations in membrane-bound gramicidin and melittin-a comparative linear dichroism study on transmembrane and surface-bound peptides.," *Biochimica et biophysica acta*, vol. 1808, pp. 219–28, January 2011.

[14] M. R. Hicks, A. Rodger, Y.-P. Lin, N. C. Jones, S. V. Hoffmann, and T. R. Dafforn, "Rapid injection linear dichroism for studying the kinetics of biological processes.," *Analytical chemistry*, vol. 84, pp. 6561–6, August 2012.

[15] T. R. Dafforn and A. Rodger, "Linear dichroism of biomolecules: which way is up?," *Current Opinion in Structural Biology*, vol. 14, pp. 541–546, October 2004.

[16] A. Wada, "Dichroic Spectra of Biopolymers Oriented by Flow," *Applied Spectroscopy Reviews*, vol. 6, no. 1, pp. 1–30, 1972.

[17] T. R. Dafforn, J. Rajendra, D. J. Halsall, L. C. Serpell, and A. Rodger, "Protein Fiber Linear Dichroism for Structure Determination and Kinetics in a Low-Volume, Low-Wavelength Couette Flow Cell," *Biophysical Journal*, vol. 86, pp. 404–410, August 2004.

[18] W. T. Astbury, "Molecular Biology or Ultrastructural Biology?," *Nature*, vol. 190, p. 1124, June 1961.

[19] O. T. Avery, C. M. MacLeod, and M. McCarty, "Studies on the chemical nature of the substance inducing transformation of pneumococcal types: INduction of transformation by a deoxyribonucleic acid fraction isolated from pneumococcus type III," *The Journal of Experimental Medicine*, vol. 79, pp. 137–158, February 1944.

[20] J. D. Watson and F. H. C. Crick, "Molecular structure of nucleic acids," *Nature*, vol. 171, no. 4356, pp. 737–738, 1953.

[21] F. Crick, "Central dogma of molecular biology," *Nature*, vol. 227, no. 5258, pp. 561–563, 1970.

[22] B. Alberts, A. Johnson, J. Lewis, M. Raff, K. Roberts, and P. Walker, *Molecular Biology of the Cell*. Garland Seience, 6th ed., 2015.

[23] K. B. Mullis, "Process for amplifying nucleic acids," 1985.

[24] J. Geliebter, "Polymerase chain reaction (current communications in molecular biology)," *Trends in Genetics*, vol. 6, pp. 229–230, August 2016.

[25] B. Weiss and C. C. Richardson, "Enzymatic breakage and joining of deoxyribonucleic acid, I. Repair of single-strand breaks in DNA by an enzyme system from Escherichia coli infected with T4 bacteriophage.," *Proceedings of*

the National Academy of Sciences of the United States of America, vol. 57, pp. 1021–1028, April 1967.

[26] W. Gilbert and B. Müller-Hill, "Isolation of the LAC repressor," *Proceedings of the National Academy of Sciences of the United States of America*, vol. 56, pp. 1891–1898, December 1966.

[27] P. N. Nge, C. I. Rogers, and A. T. Woolley, "Advances in Microfluidic Materials, Functions, Integration, and Applications," *Chemical Reviews*, vol. 113, pp. 2550–2583, April 2013.

[28] P. Ertl, D. Sticker, V. Charwat, C. Kasper, and G. Lepperdinger, "Lab-on-a-chip technologies for stem cell analysis," *Trends in Biotechnology*, vol. 32, no. 5, pp. 245 – 253, 2014.

[29] C. K. Zarins, D. P. Giddens, B. K. Bharadvaj, V. S. Sottiurai, R. F. Mabon, and S. Glagov, "Carotid bifurcation atherosclerosis. Quantitative correlation of plaque localization with flow velocity profiles and wall shear stress.," *Circulation Research*, vol. 53, pp. 502–514, October 1983.

[30] Y. S. Chatzizisis, A. U. Coskun, M. Jonas, E. R. Edelman, C. L. Feldman, and P. H. Stone, "Role of Endothelial Shear Stress in the Natural History of Coronary Atherosclerosis and Vascular Remodeling: Molecular, Cellular, and Vascular Behavior," *Journal of the American College of Cardiology*, vol. 49, pp. 2379–2393, June 2007.

[31] R. S. Reneman and A. P. G. Hoeks, "Wall shear stress as measured in vivo: consequences for the design of the arterial system," *Medical & Biological Engineering & Computing*, vol. 46, no. 5, pp. 499–507, 2008.

[32] D. Katritsis, L. Kaiktsis, A. Chaniotis, J. Pantos, E. P. Efstathopoulos, and V. Marmarelis, "Wall Shear Stress: Theoretical Considerations and Methods of Measurement," *Progress in Cardiovascular Diseases*, vol. 49, pp. 307–329, August 2016.

[33] B. Nordén, A. Rodger, and T. Dafforn, *Linear Dichroism and Circular Dichroism*. The Royal Society of Chemistry, 2010.

[34] B. Nordén, "Applications of linear Dichroism Spectroscopy," *Applied Spectroscopy Reviews*, vol. 14, no. 2, pp. 157–248, 1978.

[35] K. Razmkhah, N. P. Chmel, M. I. Gibson, and A. Rodger, "Oxidized polyethylene films for orienting polar molecules for linear dichroism spectroscopy," *The Analyst*, vol. 139, pp. 1372–82, March 2014.

[36] R. Marrington, T. R. Dafforn, D. J. Halsall, J. I. MacDonald, M. Hicks, and A. Rodger, "Validation of new microvolume couette flow linear dichroism cells," *Analyst*, vol. 130, pp. 1608–1616, 2005.

[37] Jasco, *CD Spectrometer Hardware / Function Manual*. No. June, 2013.

[38] S. Flyckt and C. Marmonier, "Photomultiplier tubes: Principles and applications," *Photonis, Brive, France*, no. September, 2002.

[39] J. C. Kemp, "Piezo-Optical Birefringence Modulators: New Use for a Long-Known Effect," *J. Opt. Soc. Am.*, vol. 59, no. 8, pp. 950–953, 1969.

[40] K. W. Hipps and G. A. Crosby, "Applications of the Photoelastic Modulator to Polarization Spectroscopy," *The Journal of Physical Chemistry*, vol. 83, no. 5, pp. 555–562, 1979.

[41] A. F. Drake, "Polarisation modulation - the measurement of linear and circular dichroism," *Journal of Physics E: Scientific Instruments*, vol. 170, no. 5, pp. 170–179, 1986.

[42] W. C. Johnson, "A Circular Dichroism Spectrometer for the Vacuum Ultraviolet," *Review of Scientific Instruments*, vol. 42, no. 9, p. 1283, 1971.

[43] O. Schnepp, S. Allen, and E. F. Pearson, "The Measurement of Circular Dichroism in the Vacuum Ultraviolet," *Review of Scientific Instruments*, vol. 41, no. 8, p. 1136, 1970.

[44] A. Jabłoński, "Über den Mechanismus der Photolumineszens von Farbstoffphosphoren," *Zeitschrift für Physik*, vol. 94, no. 1, pp. 38–46.

[45] G. G. Stokes, "On the Change of Refrangibility of Light," *Philosophical Transactions of the Royal Society of London*, vol. 142, no. 1852, pp. 463–562, 1852.

[46] M. Kasha, "Characterization of electronic transitions in complex molecules," *Discussions of the Faraday Society*, vol. 9, no. 0, pp. 14–19, 1950.

[47] C. A. Parker and W. T. Rees, "Fluorescence Spectrometry," *Analyst*, vol. 87, no. 1031, pp. 83–111, 1962.

[48] J. R. Albani, "New insights in the interpretation of tryptophan fluorescence : Origin of the fluorescence lifetime and characterization of a new fluorescence parameter in proteins: The emission to excitation ratio," *Journal of Fluorescence*, vol. 17, no. 4, pp. 406–417, 2007.

[49] K. Muto, H. Mochizuki, R. Yoshida, T. Ishii, and T. Handa, "Circular Dichroism of the Backbone and Side Chains Separated from Natural Circular Dichroism of Poly-L-tryptophan by the Fluorescence Detected Circular Dichroism Method," *J. Am. Chem. Soc.*, vol. 108, no. 6, pp. 6416–6417, 1986.

[50] J. R. Lakowicz, *Principles of fluorescence spectroscopy*. 2006.

[51] G. Muller, F. C. Muller, C. L. Maupin, and J. P. Riehl, "The measurement of the fluorescence detected circular dichroism (FDCD) from a chiral Eu(III) system," *Chemical Communications*, no. 28, pp. 3615–3617, 2005.

[52] J. C. Sutherland, "Measuurement of Circular Dichroism and Related Spectroscopies with Conventional and Synchrotron Light Sources : Theory and Instrumentation," 2009.

[53] Å. Davidsson and B. Nordén, "Polarised absorption spectra of benzene, naphtalene and anthracene obtained with a high sensitive linear dichroism technique.," *Tetrahedron Letters*, vol. 13, no. 30, pp. 3093–3096, 1972.

[54] S. F. Mason and R. D. Peacock, "The location of the 1Lb transition of anthracene by dichroism techniques," *Chemical Physics Letters*, vol. 21, no. 2, pp. 406–408, 1973.

[55] J. Kolc, J. Michl, and E. Vogel, "Excited states of bridged [14]annulenes with anthracene perimeter: absorption, polarized emission, linear dichroism, and magnetic circular dichroism," *Journal of the American Chemical Society*, vol. 98, no. 13, pp. 3935–3948, 1976.

[56] D. M. Friedrich, R. Mathies, and A. C. Albrecht, "Studies of excited electronic states of anthracene and some of its derivatives by photoselection and PPP-SCF calculations," *Journal of Molecular Spectroscopy*, vol. 51, no. 1, pp. 166–188, 1974.

[57] D. Grunberger, R. Haimovitz, and M. Shinitzky, "Resolution of plasma membrane lipid fluidity in intact cells labelled with diphenylhexatriene," *Biochimica et Biophysica Acta (BBA) - Biomembranes*, vol. 688, no. 3, pp. 764–774, 1982.

[58] J. Plášek and P. Jarolím, "Interaction of the fluorescent probe 1, 6-diphenyl-1, 3, 5-hexatriene with biomembranes," *Gen. Physiol. Biophys*, pp. 425–448, 1987.

[59] Lentz B.R., "Membrane "fluidity" as detected by diphenylhexatriene probes," *Chem. Phys. Lipids*, vol. 50, pp. 171–190, 1989.

[60] R. D. Kaiser and E. London, "Location of Diphenylhexatriene (DPH) and Its Derivatives within Membranes: Comparison of Different Fluorescence Quenching Analyses of Membrane Depth," *Biochemistry*, vol. 37, pp. 8180–8190, June 1998.

[61] P. C. Alford and T. F. Palmer, "Photophysics of derivatives of all-trans-1,6-diphenyl-1,3,5- hexatriene (DPH). 1. Model involving fluorescence fom S2 and S1 excited-states," *J.Chem.Soc.Faraday Trans.II*, vol. 79, pp. 433–447, 1983.

[62] A. Kawski, A. Kubicki, B. Kukliński, and G. Piszczek, "Isomerization of Diphenyl Polyenes. Part V. The Origin of Fluorescence of l, 6-Diphenyl-1, 3, 5-hexatriene in Poly (vinyl alcohol) Films," *Zeitschrift für Naturforschung A*, vol. 48, no. 8-9, pp. 861–867, 1993.

[63] J. Saltiel and S. Wang, "Absorption and Fluorescence Spectra of a Rigid Analog of all-trans-1,6-Diphenyl-1,3,5-hexatriene. Solvent-Controlled Order Inversion of 21Ag and 11Bu Energy Levels," *Journal of the American Chemical Society*, vol. 117, pp. 10761–10762, November 1995.

[64] M. T. Allen and D. G. Whitten, "The photophysics and photochemistry of .alpha.,.omega.-diphenylpolyene singlet states," *Chemical Reviews*, vol. 89, no. 8, pp. 1691–1702, 1989.

[65] P. C. Alford and T. F. Palmer, "Fluorescence of DPH derivatives. Evidence for emission from S2 and S1 excited states," *Chemical Physics Letters*, vol. 86, no. 3, pp. 248–253, 1982.

[66] J. B. Birks, G. N. R. Tripathi, and M. D. Lumb, "The fluorescence of all-trans diphenyl polyenes," *Chemical Physics*, vol. 33, no. 2, pp. 185–194, 1978.

[67] J. H. Clark, M. G. Dekamin, and F. M. Moghaddam, "Genuinely catalytic Fries rearrangement using sulfated zirconia," *Green Chemistry*, vol. 4, pp. 366–368, 2002.

[68] G. D. Scholes, K. P. Ghiggino, A. M. Oliver, and M. N. Paddon-Row, "Intramolecular electronic energy transfer between rigidly linked naphthalene and anthracene chromophores," *The Journal of Physical Chemistry*, vol. 97, pp. 11871–11876, November 1993.

[69] E. S. Boiadjiev and A. D. Lightner, "Exciton Chirality. (A) Origins of and (B) Applications from Strongly Fluorescent Dipyrrinone Chromophores," *Monatshefte für Chemie / Chemical Monthly*, vol. 136, no. 3, pp. 489–508, 2005.

[70] A. M. Turek, G. Krishnamoorthy, D. F. Sears, I. Garcia, O. Dmitrenko, and J. Saltiel, "Resolution of Three Fluorescence Components in the Spectra of all-trans-1,6-Diphenyl-1,3,5-hexatriene under Isopolarizability Conditions," *The Journal of Physical Chemistry A*, vol. 109, pp. 293–303, January 2005.

[71] Y. S. Kim and C. S. P. Sung, "UV and fluorescence characterization of styrene and methyl methacrylate polymerization," *Journal of Applied Polymer Science*, vol. 57, pp. 363–370, July 1995.

[72] N. C. Maiti, S. Mazumdar, and N. Periasamy, "J- and H-Aggregates of Porphyrin-Surfactant Complexes: Time-Resolved Fluorescence and Other Spectroscopic Studies," *The Journal of Physical Chemistry B*, vol. 102, pp. 1528–1538, February 1998.

[73] U. Rösch, S. Yao, R. Wortmann, and F. Würthner, "Fluorescent H-Aggregates of Merocyanine Dyes," *Angewandte Chemie*, vol. 118, pp. 7184–7188, October 2006.

[74] M. Van der Auweraer, B. Verschuere, and F. C. De Schryver, "Absorption and fluorescence properties of Rhodamine B derivatives forming Langmuir-Blodgett films," *Langmuir*, vol. 4, pp. 583–588, May 1988.

[75] M. S. Kinch, A. Haynesworth, S. L. Kinch, and D. Hoyer, "An overview of FDA-approved new molecular entities: 1827âĂŞ2013," *Drug Discovery Today*, vol. 19, no. 8, pp. 1033–1039, 2014.

[76] M. Sirajuddin, S. Ali, and A. Badshah, "Drug-DNA interactions and their study by UV-Visible, fluorescence spectroscopies and cyclic voltametry," *Journal of Photochemistry and Photobiology B: Biology*, vol. 124, no. November 2015, pp. 1–19, 2013.

[77] L. S. Lerman, "Structural considerations in the interaction of DNA and acridines.," *Journal of molecular biology*, vol. 3, no. 1, pp. 18–30, 1961.

[78] B. Nordén, M. Kubista, and T. Kurucsev, "Linear dichroism spectroscopy of nucleic acids.," *Quarterly reviews of biophysics*, vol. 25, no. 1, pp. 51–170, 1992.

[79] K. Yamaoka and E. Charney, "Electric dichroism studies of macromolecules in solutions. II. Measurements of linear dichroism and birefringence of deoxyribonucleic acid in orienting electric fields," *Macromolecules*, vol. 6, no. 1, pp. 66–76, 1973.

[80] B. Nordén and F. Tjerneld, "Structure of Methylene-Blue DNA Complexes Studied by Linear and Circular-Dichroism Spectroscopy," *Biopolymers*, vol. 21, no. 1, pp. 1713–1734, 1982.

[81] C. Bailly, P. Colson, J. P. Hénichart, and C. Houssier, "The different binding modes of Hoechst 33258 to DNA studied by electric linear dichroism.," *Nucleic acids research*, vol. 21, no. 16, pp. 3705–3709, 1993.

[82] Y. Matsuoka and B. Nordén, "Linear dichroism studies of nucleic acid bases in stretched poly(vinyl alcohol) film. Molecular orientation and electronic transition moment directions," *The Journal of Physical Chemistry*, vol. 86, no. 8, pp. 1378–1386, 1982.

[83] T. I. Watkins and G. Woolfe, "Effect of Changing the Quaternizing Group on the Trypanocidal Activity of Dimidium Bromide," *Nature*, vol. 169, p. 506, March 1952.

[84] J. Olmsted and D. R. Kearns, "Mechanism of ethidium bromide fluorescence enhancement on binding to nucleic acids.," *Biochemistry*, vol. 16, no. 16, pp. 3647–3654, 1977.

[85] O. Dann, G. Bergen, E. Demant, and G. Volz, "Trypanocide Diamidine des 2-Phenyl-benzofurans, 2-Phenyl-indens und 2-Phenyl-indols," *Justus Liebigs Annalen der Chemie*, vol. 749, no. 1, pp. 68–89, 1971.

[86] M. Couette, "Oscillations tournantes d'un solide de révolution en contact avec un fluide visqueux," *Compt. Rend. Acad. Sci. Paris*, vol. 105, pp. 1064–1067, 1887.

[87] A. Wada and S. Kozawa, "Instrument for the studies of differential flow dichroism of polymer solutions," *Journal of Polymer Science Part A: General Papers*, vol. 2, pp. 853–864, 1964.

[88] G. Viola, E. Uriarte, O. Gia, and S. Moro, "Interactions between DNA and benzo- and tetrahydrobenzofurocoumarins: thermodynamic and molecular modeling studies.," *Farmaco (Società chimica italiana : 1989)*, vol. 55, no. 4, pp. 276–86, 2000.

[89] P. O. Vardevanyan, A. P. Antonyan, M. A. Parsadanyan, H. G. Davtyan, Z. R. Boyajyan, and A. T. Karapetian, "Complex-formation of Ethidium Bromide with poly[d(A-T)].poly[d(A-T)]," *J Biomol Struct Dyn*, vol. 22, no. 4, pp. 465–470, 2005.

[90] J. Fried, A. G. Perez, and B. D. Clarkson, "Flow cytofluorometric analysis of cell cycle distributions using propidium iodide. Properties of the method and mathematical analysis of the data," *Journal of Cell Biology*, vol. 71, no. 1, pp. 172–181, 1976.

[91] M. Kubista, B. Akerman, and B. Norden, "Characterization of Interaction between DNA and 4 ', 6-Diamidino-2-phenylindole by Optical Spectroscopy," *Biochemistry*, vol. 26, no. 14, pp. 4545–4553, 1987.

[92] C. Bailly, P. Colson, J.-P. Hénichart, and C. Houssier, "The different binding modes of Hoechst 33258 to DNA studied by electirc linear dichroism," *Nucleic Acids Research*, vol. 21, no. 16, pp. 3705–3709, 1993.

[93] B. Rafique, A. M. Khalid, K. Akhtar, and A. Jabbar, "Interaction of anticancer drug methotrexate with DNA analyzed by electrochemical and spectroscopic methods," *Biosensors and Bioelectronics*, vol. 44, no. 1, pp. 21–26, 2013.

[94] A. R. Morgan, J. S. Lee, D. E. Pulleyblank, N. L. Murray, and D. H. Evans, "Ethidium fluorescence assays. Part 1. Physicochemical studies," *Nucleic Acids Research*, vol. 7, pp. 547–565, October 1979.

[95] B. Nordén and F. Tjerneld, "High-sensitivity linear dichroism as a tool for equilibrium analysis in biochemistry. Stability constant of DNA-ethidium bromide complex," *Biophysical Chemistry*, vol. 4, no. 2, pp. 191–198, 1976.

[96] J. T. Bell and R. E. Biggers, "The absorption spectrum of the uranyl ion in perchlorate media," *Journal of Molecular Spectroscopy*, vol. 18, no. 3, pp. 247–275, 1965.

[97] D. B. Siano and D. E. Metzler, "Band Shapes of the Electronic Spectra of Complex Molecules," *The Journal of Chemical Physics*, vol. 51, no. 5, 1969.

[98] L. Antonov and S. Stoyanov, "Analysis of the Overlapping Bands in UV-Vis Absorption Spectroscopy," *Applied Spectroscopy*, vol. 47, no. 7, pp. 1030–1035, 1993.

[99] L. Antonov and D. Nedeltcheva, "Resolution of overlapping UV-Vis absorption bands and quantitative analysis," *Chemical Society Reviews*, vol. 29, no. 3, pp. 217–227, 2000.

[100] E. Castiglioni, S. Abbate, F. Lebon, and G. Longhi, "Chiroptical spectroscopic techniques based on fluorescence," *Methods and Applications in Fluorescence*, vol. 2, no. 2, p. 024006, 2014.

[101] B. Nordén and T. Kurucsev, "Analysing DNA complexes by circular and linear dichroism," *Journal of Molecular Recognition*, vol. 7, no. 2, pp. 141–155, 1994.

[102] B. Weisblum and E. Haenssler, "Fluorometric properties of the bibenzimidazole derivative hoechst 33258, a fluorescent probe specific for AT concentration in chromosomal DNA," *Chromosoma*, vol. 46, no. 3, pp. 255–260, 1974.

[103] F. G. Loontiens, P. Regenfuss, A. Zechel, L. Dumortier, and R. M. Clegg, "Binding characteristics of Hoechst 33258 with calf thymus DNA, poly[d(A-T)] and d(CCGGAATTCCGG): multiple stoichiometries and determination of tight binding with a wide spectrum of site affinities," *Biochemistry*, vol. 29, pp. 9029–9039, September 1990.

[104] I. Haq, J. E. Ladbury, B. Z. Chowdhry, T. C. Jenkins, and J. B. Chaires, "Specific binding of hoechst 33258 to the d(CGCAAATTTGCG)2 duplex: calorimetric and spectroscopic studies," *Journal of Molecular Biology*, vol. 271, pp. 244–257, August 1997.

[105] J.-H. Moon, S. K. Kim, U. Sehlstedt, A. Rodger, and B. Nordï£¡n, "DNA structural features responsible for sequence-dependent binding geometries of Hoechst 33258," *Biopolymers*, vol. 38, no. 5, pp. 593–606, 1996.

[106] S. A. Latt and J. C. Wohlleb, "Optical studies of the interaction of 33258 Hoechst with DNA, chromatin, and metaphase chromosomes," *Chromosoma*, vol. 52, no. 4, pp. 297–316, 1975.

[107] R. Pacheco-Gómez, J. Kraemer, S. Stokoe, H. J. England, C. W. Penn, E. Stanley, A. Rodger, J. Ward, M. R. Hicks, and T. R. Dafforn, "Detection of pathogenic bacteria using a homogeneous immunoassay based on shear alignment of virus particles and linear dichroism," *Analytical Chemistry*, vol. 84, no. Figure 1, pp. 91–97, 2012.

[108] T. R. Dafforn and M. Hicks, "Molecular detection system," 2013.

[109] W.-J. Chung, D.-Y. Lee, and S. Y. Yoo, "Chemical modulation of M13 bacteriophage and its functional opportunities for nanomedicine," *International Journal of Nanomedicine*, vol. 9, pp. 5825–5836, December 2014.

[110] E. H. Strickland, J. Horwitz, E. Kay, L. M. Shannon, M. Wilchek, and C. Billups, "Near-ultraviolet absorption bands of tryptophan. Studies using horseradish peroxidase isoenzymes, bovine and horse heart cytochrome c, and N-stearyl-L-tryptophan n-hexyl ester," *Biochemistry*, vol. 10, pp. 2631–2638, June 1971.

[111] A. B. T. Ghisaidoobe and S. J. Chung, "Intrinsic Tryptophan Fluorescence in the Detection and Analysis of Proteins: A Focus on Förster Resonance Energy Transfer Techniques," *International Journal of Molecular Sciences*, vol. 15, pp. 22518–22538, December 2014.

[112] P. G. Coble et al., eds., *Aquatic Organic Matter Fluorescence*. Cambridge University Press, 2014.

[113] J. T. Vivian and P. R. Callis, "Mechanisms of tryptophan fluorescence shifts in proteins.," *Biophysical Journal*, vol. 80, pp. 2093–2109, May 2001.

[114] R. W. Cowgill, "Fluorescence and the structure of proteins V. Ionization of tyrosyl residues," *Biochimica et Biophysica Acta (BBA) - Biophysics including Photosynthesis*, vol. 94, no. 1, pp. 81–88, 1965.

[115] S. G. Shulman, *Molecular Luminescence Spectroscopy: Methods & Applications âPart 1*. Gainesville, Florida: John Wiley & Sons.

[116] WHO, "ANTIMICROBIAL RESISTANCE: Global Report on surveillance," 2014.

[117] Department of Health and Department for Environment Food and Rural Affairs, "UK Five Year Antimicrobial Resistance Strategy 2013 to 2018," *Department of Health Department for Environment Food and Rural Affairs*, p. 43, 2013.

[118] J. Anomaly, "Combating resistance: The case for a global antibiotics treaty," *Public Health Ethics*, vol. 3, no. 1, pp. 13–22, 2010.

[119] R. A. Daniel and J. Errington, "Control of cell morphogenesis in bacteria: two distinct ways to make a rod-shaped cell.," *Cell*, vol. 113, pp. 767–76, June 2003.

[120] J.-v. Höltje, "Growth of the Stress-Bearing and Shape-Maintaining Murein Sacculus of Escherichia coli Growth of the Stress-Bearing and Shape-Maintaining Murein Sacculus of Escherichia coli," *Microbiology and molecular biology reviews*, vol. 62, no. 1, pp. 181–203, 1998.

[121] C. L. White, A. Kitich, and J. W. Gober, "Positioning cell wall synthetic complexes by the bacterial morphogenetic proteins MreB and MreD.," *Molecular microbiology*, vol. 76, pp. 616–33, May 2010.

[122] R. M. Figge, A. V. Divakaruni, and J. W. Gober, "MreB , the cell shape-determining bacterial actin homologue , co-ordinates cell wall morphogenesis in Caulobacter crescentus," *Molecular Microbiology*, vol. 51, no. 5, pp. 1321–1332, 2004.

[123] E. Sauvage, F. Kerff, M. Terrak, J. A. Ayala, and P. Charlier, "The penicillin-binding proteins: structure and role in peptidoglycan biosynthesis.," *FEMS microbiology reviews*, vol. 32, pp. 234–58, March 2008.

[124] C. E. Broughton, H. A. Van Den Berg, A. M. Wemyss, D. I. Roper, and A. Rodger, "Beyond the Discovery Void : New targets for antibacterial compounds," *Science Progress*, vol. 99, no. 2, pp. 153–182, 2016.

[125] H. J. D. Soufo and P. L. Graumann, "Actin-like Proteins MreB and Mbl from Bacillus subtilis Are Required for Bipolar Positioning of Replication Origins," *Current Biology*, vol. 13, pp. 1916–1920, October 2003.

[126] T. Kruse, J. Møller-Jensen, A. Løbner-Olesen, and K. Gerdes, "Dysfunctional MreB inhibits chromosome segregation in Escherichia coli.," *The EMBO journal*, vol. 22, pp. 5283–92, October 2003.

[127] A. V. Divakaruni, C. Baida, C. L. White, and J. W. Gober, "The cell shape proteins MreB and MreC control cell morphogenesis by positioning cell wall synthetic complexes.," *Molecular microbiology*, vol. 66, pp. 174–88, October 2007.

[128] Y.-L. Shih, T. Le, and L. Rothfield, "Division site selection in Escherichia coli involves dynamic redistribution of Min proteins within coiled structures that extend between the two cell poles.," *Proceedings of the National Academy of Sciences of the United States of America*, vol. 100, pp. 7865–70, June 2003.

[129] S. van Teeffelen, S. Wang, L. Furchtgott, K. C. Huang, N. S. Wingreen, J. W. Shaevitz, and Z. Gitai, "The bacterial actin MreB rotates, and rotation depends on cell-wall assembly.," *Proceedings of the National Academy of Sciences of the United States of America*, vol. 108, pp. 15822–7, September 2011.

[130] E. C. Garner, R. Bernard, W. Wang, X. Zhuang, D. Z. Rudner, and T. Mitchison, "Coupled, circumferential motions of the cell wall synthesis machinery and MreB filaments in B. subtilis.," *Science (New York, N.Y.)*, vol. 333, pp. 222–5, July 2011.

[131] J. Domínguez-Escobar, A. Chastanet, A. H. Crevenna, V. Fromion, R. Wedlich-Söldner, and R. Carballido-López, "Processive movement of MreB-associated cell wall biosynthetic complexes in bacteria.," *Science (New York, N.Y.)*, vol. 333, pp. 225–8, July 2011.

[132] M. T. Swulius and G. J. Jensen, "The helical mreb cytoskeleton in Escherichia coli MC1000/pLE7 is an artifact of the N-terminal yellow fluorescent protein tag," *Journal of Bacteriology*, vol. 194, no. 23, pp. 6382–6386, 2012.

[133] C. Reimold, H. Soufo, F. Dempwolff, and P. L. Graumann, "Motion of variable-length MreB filaments at the bacterial cell membrane influences cell morphology," *Molecular Biology of the Cell*, 2013.

[134] P. Nurse and K. J. Marians, "Purification and characterization of Escherichia coli MreB protein.," *The Journal of biological chemistry*, vol. 288, pp. 3469–75, February 2013.

[135] Novagen, "pET System Manual," *www.novagen.com*, pp. 1–68, 2003.

[136] R. M. Atlas, *Principles of Microbiology*. Wm. C. Brown Publishers, second ed., 1997.

[137] M. Lewis, "The lac repressor.," *Comptes rendus biologies*, vol. 328, pp. 521–48, June 2005.

[138] R. M. Twyman, *Advanced Molecular Biology: A Concise Reference*. BIOS Scientific Publishers Limited, 1998.

[139] R. Novy and B. Morris, "Use of glucose to control basal expression in the pET System," *inNovations*, no. 1, pp. 13–15.

[140] L. Dumon-Seignovert, G. Cariot, and L. Vuillard, "The toxicity of recombinant proteins in Escherichia coli: a comparison of overexpression in BL21(DE3), C41(DE3), and C43(DE3).," *Protein expression and purification*, vol. 37, pp. 203–6, September 2004.

[141] B. M. Bulheller, A. Rodger, and J. D. Hirst, "Circular and linear dichroism of proteins," *Physical Chemistry Chemical Physics*, vol. 9, no. 17, pp. 2020–2035, 2007.

[142] L. Pasteur, "Mémoire sur la relation qui peut exister entre la forme cristalline et la composition chimique, et sur la cause de la polarisation rotatoire,"

Comptes rendus hebdomadaires des séances de l'Académie des Sciences, vol. 26, pp. 535–538, 1848.

[143] D. W. Urry, "Circular-dichroism pattern of methylpyrrolidone can resemble that of the .alpha. helix," *The Journal of Physical Chemistry*, vol. 72, pp. 3035–3038, August 1968.

[144] L. Whitmore and B. A. Wallace, "DICHROWEB, an online server for protein secondary structure analyses from circular dichroism spectroscopic data," *Nucleic Acids Research*, vol. 32, pp. W668–W673, July 2004.

[145] N. Sreerama and R. W. Woody, "A Self-Consistent Method for the Analysis of Protein Secondary Structure from Circular Dichroism," *Analytical Biochemistry*, vol. 209, no. 1, pp. 32–44, 1993.

[146] N. Sreerama, S. Y. U. Venyaminov, and R. W. Woody, "Estimation of the number of α-helical and β-strand segments in proteins using circular dichroism spectroscopy," *Protein Science*, vol. 8, no. 2, pp. 370–380, 1999.

[147] S. W. Provencher and J. Gloeckner, "Estimation of globular protein secondary structure from circular dichroism," *Biochemistry*, vol. 20, pp. 33–37, January 1981.

[148] I. H. M. van Stokkum, H. J. W. Spoelder, M. Bloemendal, R. van Grondelle, and F. C. A. Groen, "Estimation of protein secondary structure and error analysis from circular dichroism spectra," *Analytical Biochemistry*, vol. 191, no. 1, pp. 110–118, 1990.

[149] M. A. Andrade, P. Chacón, J. J. Merelo, and F. Morán, "Evaluation of secondary structure of proteins from UV circular dichroism spectra using an unsupervised learning neural network," *Protein Engineering*, vol. 6, no. 4, pp. 383–390, 1993.

[150] L. A. Compton and W. Johnson, "Analysis of protein circular dichroism spectra for secondary structure using a simple matrix multiplication," *Analytical Biochemistry*, vol. 155, no. 1, pp. 155–167, 1986.

[151] P. Manavalan and W. Johnson, "Variable selection method improves the prediction of protein secondary structure from circular dichroism spectra," *Analytical Biochemistry*, vol. 167, no. 1, pp. 76–85, 1987.

[152] N. Sreerama and R. W. Woody, "Estimation of Protein Secondary Structure from Circular Dichroism Spectra: Comparison of CONTIN, SELCON, and CDSSTR Methods with an Expanded Reference Set," *Analytical Biochemistry*, vol. 287, no. 2, pp. 252–260, 2000.

[153] N. Sreerama, S. Y. Venyaminov, and R. W. Woody, "Estimation of Protein Secondary Structure from Circular Dichroism Spectra: Inclusion of Denatured Proteins with Native Proteins in the Analysis," *Analytical Biochemistry*, vol. 287, no. 2, pp. 243–251, 2000.

[154] J. G. Lees, A. J. Miles, F. Wien, and B. A. Wallace, "A reference database for circular dichroism spectroscopy covering fold and secondary structure space," *Bioinformatics*, vol. 22, no. 16, pp. 1955–1962, 2006.

[155] A. Abdul-Gader, A. J. Miles, and B. A. Wallace, "A reference dataset for the analyses of membrane protein secondary structures and transmembrane residues using circular dichroism spectroscopy," *Bioinformatics*, vol. 27, pp. 1630–1636, June 2011.

[156] D. Mao, E. Wachter, and B. A. Wallace, "Folding of the mitochondrial proton adenosine triphosphatase proteolipid channel in phospholipid vesicles," *Biochemistry*, vol. 21, pp. 4960–4968, September 1982.

[157] F. van den Ent, T. Izoré, T. A. M. Bharat, C. M. Johnson, and J. Löwe, "Bacterial actin MreB forms antiparallel double filaments," *eLife*, vol. 3, p. e02634, May 2014.

[158] W. Kabsch and C. Sander, "Dictionary of protein secondary structure: Pattern recognition of hydrogen-bonded and geometrical features," *Biopolymers*, vol. 22, no. 12, pp. 2577–2637, 1983.

[159] B. M. Bulheller, A. Rodger, M. R. Hicks, T. R. Dafforn, L. C. Serpell, K. E. Marshall, E. H. C. Bromley, P. J. S. King, K. J. Channon, D. N. Woolfson, and

J. D. Hirst, "Flow Linear Dichroism of Some Prototypical Proteins," *Journal of the American Chemical Society*, vol. 131, pp. 13305–13314, September 2009.

[160] A. M. Shaaban and A. J. Duerinckx, "Wall shear stress and early atherosclerosis: a review.," *AJR. American journal of roentgenology*, vol. 174, no. 6, pp. 1657–1665, 2000.

[161] M. I. Cybulsky and M. A. Gimbrone, "Endothelial expression of a mononuclear leukocyte adhesion molecule during atherogenesis.," *Science (New York, N.Y.)*, vol. 251, no. 4995, pp. 788–791, 1991.

[162] M. L. Raghavan, D. A. Vorp, M. P. Federle, M. S. Makaroun, and M. W. Webster, "Wall stress distribution on three-dimensionally reconstructed models of human abdominal aortic aneurysm.," *Journal of vascular surgery*, vol. 31, no. 4, pp. 760–9, 2000.

[163] M. L. Smith, D. S. Long, E. R. Damiano, and K. Ley, "Near-wall micro-PIV reveals a hydrodynamically relevant endothelial surface layer in venules in vivo.," *Biophysical journal*, vol. 85, no. 1, pp. 637–45, 2003.

[164] A. Balducci, M. Grigioni, G. Querzoli, G. P. Romano, C. Daniele, G. D'Avenio, and V. Barbaro, "Investigation of the flow field downstream of an artificial heart valve by means of PIV and PTV," *Experiments in Fluids*, vol. 36, no. 1, pp. 204–213, 2004.

[165] C. J. Kähler, S. Scharnowski, and C. Cierpka, "On the uncertainty of digital PIV and PTV near walls," *Experiments in Fluids*, vol. 52, no. 6, pp. 1641–1656, 2012.

[166] S. C. Satchell, C. H. Tasman, a. Singh, L. Ni, J. Geelen, C. J. von Ruhland, M. J. O'Hare, M. a. Saleem, L. P. van den Heuvel, and P. W. Mathieson, "Conditionally immortalized human glomerular endothelial cells expressing fenestrations in response to VEGF.," *Kidney international*, vol. 69, no. 9, pp. 1633–1640, 2006.

[167] J. Schindelin, I. Arganda-Carreras, E. Frise, V. Kaynig, M. Longair, T. Pietzsch, S. Preibisch, C. Rueden, S. Saalfeld, B. Schmid, J.-Y. Tinevez,

D. J. White, V. Hartenstein, K. Eliceiri, P. Tomancak, and A. Cardona, "Fiji: an open-source platform for biological-image analysis.," *Nature methods*, vol. 9, no. 7, pp. 676–82, 2012.

[168] M. Sezgin and B. Sankur, "Survey over image thresholding techniques and quantitative performance evaluation," *Journal of Electronic Imaging*, vol. 13, no. 1, pp. 146–165, 2004.

[169] N. Otsu, "A Threshold Selection Method from Gray-Level Histograms," *IEEE*, vol. 20, no. 1, pp. 62–66, 1979.

[170] R Core Team, *R: A Language and Environment for Statistical Computing*. R Foundation for Statistical Computing, Vienna, Austria, 2015.

[171] D. P. Lobo, A. M. Wemyss, D. J. Smith, A. Straube, K. B. Betteridge, A. H. J. Salmon, R. R. Foster, H. E. Elhegni, S. C. Satchell, H. A. Little, R. Pacheco-Gómez, M. J. Simmons, M. R. Hicks, D. O. Bates, A. Rodger, T. R. Dafforn, and K. P. Arkill, "Direct detection and measurement of wall shear stress using a filamentous bio-nanoparticle," *Nano Research*, vol. 8, no. 10, pp. 3307–3315, 2015.

[172] J. Gross and U. Ligges, *nortest: Tests for Normality*, 2015.

[173] H. W. Lilliefors, "On the Kolmogorov-Smirnov Test for Normality With Mean and Variance Unknown," *Journal of the American Statistical Association*, vol. 62, no. 318, pp. 399–402, 1967.

[174] K. A. Barbee, T. Mundel, R. Lal, and P. F. Davies, "Subcellular distribution of shear stress at the surface of flow-aligned and nonaligned endothelial monolayers," *American Journal of Physiology - Heart and Circulatory Physiology*, vol. 268, pp. H1765–H1772, April 1995.

[175] C. Pozrikidis, "Shear flow over a protuberance on a plane wall," *Journal of Engineering Mathematics*, vol. 31, no. 1, pp. 29–42, 1997.

[176] M. Singh, A. Yadav, X. Ma, and E. Amoah, "Plasmid DNA transformation in Escherichia Coli: effect of heat shock temperature, duration, and cold

incubation of CaCl2 treated cells," *International Journal of Biotechnology and Biochemistry*, vol. 6, no. 4, pp. 561–568, 2010.

Appendices

APPENDIX A

E. coli MreB Sequence

M	V	K	K	F	R	G	M	F	S
ATG	GTG	AAA	AAA	TTT	CGT	GGC	ATG	TTT	TCC
N	D	L	S	I	D	L	G	T	A
AAT	GAC	TTG	TCC	ATT	GAC	CTG	GGT	ACT	GCG
N	T	L	I	Y	V	K	G	Q	G
AAT	ACC	CTC	ATT	TAT	GTA	AAA	GGA	CAA	GGC
I	V	L	N	E	P	S	V	V	A
ATC	GTA	TTG	AAT	GAG	CCT	TCC	GTG	GTG	GCC
I	R	Q	D	R	A	G	S	P	K
ATT	CGT	CAG	GAT	CGT	GCC	GGT	TCA	CCG	AAA
S	V	A	A	V	G	H	D	A	K
AGC	GTA	GCT	GCA	GTA	GGT	CAT	GAC	GCG	AAG
Q	M	L	G	R	T	P	G	N	I
CAG	ATG	CTG	GGC	CGT	ACG	CCG	GGC	AAT	ATT
A	A	I	R	P	M	K	D	G	V
GCT	GCC	ATT	CGC	CCA	ATG	AAA	GAC	GGC	GTT
I	A	D	F	F	V	T	E	K	M
ATC	GCC	GAC	TTC	TTC	GTG	ACT	GAA	AAA	ATG
L	Q	H	F	I	K	Q	V	H	S
CTC	CAG	CAC	TTC	ATC	AAA	CAA	GTG	CAC	AGC
N	S	F	M	R	P	S	P	R	V
AAC	AGC	TTT	ATG	CGT	CCA	AGC	CCG	CGC	GTT
L	V	C	V	P	V	G	A	T	Q
CTG	GTT	TGT	GTG	CCG	GTT	GGC	GCG	ACC	CAG
V	E	R	R	A	I	R	E	S	A
GTT	GAA	CGC	CGC	GCA	ATT	CGT	GAA	TCC	GCG

Q	G	A	G	A	R	E	V	F	L
CAG	GGC	GCT	GGT	GCC	CGT	GAA	GTC	TTC	CTG
I	E	E	P	M	A	A	A	I	G
ATT	GAA	GAA	CCG	ATG	GCT	GCC	GCA	ATT	GGT
A	G	L	P	V	S	E	A	T	G
GCT	GGC	CTG	CCG	GTT	TCT	GAA	GCG	ACC	GGT
S	M	V	V	D	I	G	G	G	T
TCT	ATG	GTG	GTT	GAT	ATC	GGT	GGT	GGT	ACC
T	E	V	A	V	I	S	L	N	G
ACT	GAA	GTT	GCT	GTT	ATC	TCC	TTG	AAC	GGT
V	V	Y	S	S	S	V	R	I	G
GTG	GTT	TAC	TCC	TCT	TCT	GTG	CGC	ATT	GGT
G	D	R	F	D	E	A	I	I	N
GGT	GAC	CGT	TTC	GAC	GAA	GCT	ATC	ATC	AAC
Y	V	R	R	N	Y	G	S	L	I
TAT	GTG	CGT	CGT	AAT	TAC	GGT	TCT	CTG	ATC
G	E	A	T	A	E	R	I	K	H
GGT	GAA	GCC	ACC	GCA	GAA	CGT	ATC	AAG	CAC
E	I	G	S	A	Y	P	G	D	E
GAA	ATC	GGT	TCG	GCT	TAT	CCG	GGC	GAT	GAA
V	R	E	I	E	V	R	G	R	N
GTC	CGT	GAA	ATC	GAA	GTT	CGT	GGC	CGT	AAC
L	A	E	G	V	P	R	G	F	T
CTG	GCA	GAA	GGT	GTT	CCA	CGC	GGT	TTT	ACC
L	N	S	N	E	I	L	E	A	L
CTG	AAC	TCC	AAT	GAA	ATC	CTC	GAA	GCA	CTG

Q	E	P	L	T	G	I	V	S	A
CAG	GAA	CCG	CTG	ACC	GGT	ATT	GTG	AGC	GCG
V	M	V	A	L	E	Q	C	P	P
GTA	ATG	GTT	GCA	CTG	GAA	CAG	TGC	CCG	CCG
E	L	A	S	D	I	S	E	R	G
GAA	CTG	GCT	TCC	GAC	ATC	TCC	GAG	CGC	GGC
M	V	L	T	G	G	G	A	L	L
ATG	GTG	CTC	ACC	GGT	GGT	GGC	GCA	CTG	CTG
R	N	L	D	R	L	L	M	E	E
CGT	AAC	CTT	GAC	CGT	TTG	TTA	ATG	GAA	GAA
T	G	I	P	V	V	V	A	E	D
ACC	GGC	ATT	CCA	GTC	GTT	GTT	GCT	GAA	GAC
P	L	T	C	V	A	R	G	G	G
CCG	CTG	ACC	TGT	GTG	GCG	CGC	GGT	GGC	GGC
K	A	L	E	M	I	D	M	H	G
AAA	GCG	CTG	GAA	ATG	ATC	GAC	ATG	CAC	GGC
G	D	L	F	S	E	E	*		
GGC	GAC	CTG	TTC	AGC	GAA	GAG	TAA		

APPENDIX B

General Biological Protocols

Below is list of protocols for the some of the fundamental techniques that would be required to reproduce the work detailed in this report.

B.1 Gel electrophoresis

First make up a 0.8% agarose gel by weighing out 3.2 g of electrophoresis grade agarose, and making it up to 400 mL using TAE buffer (containing a mixture of Tris base, acetic acid and EDTA).

Add 1 μL ethidium bromide per 20 μL of 0.8% agarose gel, and pour mixture into a gel tray with the well comb in place.

Allow to set in the cold room - approximately 10 minutes.

Remove ends of gel tray, along with the well comb, and place tray into the gel box (electrophoresis unit).

Fill gel box with 1×TAE until the gel is covered.

Add 5 μL of GeneRuler 1 kb DNA Ladder (0.5 μg/μL) to left hand well. Then mix 5 μL of each DNA sample with 1 μL of 6× TriTrack DNA Loading Dye, and pipette into the other wells.

Run for 25 minutes at 110 V.

Transfer the gel to the SYNGENE G:BOX gel imaging plate (black surface for DNA gels). Then use the GeneSnap software to view the gel, by setting the light source to 'Transilluminator' and pressing the green button.

B.2 Prepare LB agar antibiotic plates

Melt 200 mL of LB agar in the microwave and allow to cool slightly in a biological containment cabinet.

Add the appropriate volume of antibiotic. For kanamycin resistance this should be 200 μL of 50 mg/mL stock solution, so that the final concentration of kanamycin in the solution is 50 μg/mL.

Lay out 6 sterile 92×16 mm petri dishes in the containment cabinet, with the lids slightly ajar.

Pour in the LB agar antibiotic solution, leaving the lids ajar for 5 minutes to reduce condensation.

Once the LB agar antibiotic solution has gone opaque, it has set and can be removed from the containment hood.

Label the underside of each plate with the name of the antibiotic used.

B.3 Plasmid transformation

Plasmid transformation is the transfer of plasmid DNA into competent *E. coli* cells, which are able to take in exogenous DNA.

Add 3 μL of plasmid to 50 μL of competent *E. coli* Top10 cells, and incubate on ice for 30 minutes.

'Heat shock' the mixture by placing it in a 45°C water bath for 45 seconds. This increases the efficiency of transforming into *E. coli* cells approximately 15 fold [176].

Incubate on ice for a further 2.5 minutes, and add 150 μL of LD media to the mix.

Place in an incubator at 37°C, and shake at 180 rpm for 60 minutes. This time allows the newly transformed cells to express the antibiotic resistance genes.

After the hour has passed, remove the cells from the incubator and aseptic technique pipette 75 μL onto an LB agar antibiotic plate. Flame a glass spreader to remove any residual ethanol, and spread the solution over the plate.

Finally, incubate the plate upside down at 37°C overnight.

B.4 Overnight cultures

Pipette 5 mL of LB media into a universal tube, in addition an appropriate volume of antibiotic; 5 μL of 50 mg/mL kanamycin solution for plasmids with kanamycin resistance. If the overnight culture is to be used for the expression of a protein from a pET vector, one may wish to add glucose to a mass concentration of 0.2.

Pick a single colony of cells transformed with the plasmid (Appendix B.3) with a small inoculating loop, and add to the solution contained within the universal tube.

Place the universal tubes in an incubator at 37°C, and shake at 180 rpm overnight.

The resulting culture may be used to inoculate a larger volume of media for protein expression, or it can be used to harvest more plasmid from the cells by mini-preparation.

B.5 Buffer preparation

The mass of each element of the buffer to make the concentration given below in a 1 L volume are weighed out and placed in a large beaker. Deionised water is added to the beaker, up to a volume of approximately 950 mL. The solution is stirred to dissolve the solid constituents, and its pH measured with a pH meter. Concentrated HCl or NaOH is added to the solution to correct the pH to the desired value, before the whole solution is poured into a 1 L measuring cylinder. Deionised water is then added up to a volume of 1 L. Finally, the buffer is filter sterilised.

Buffer A ($pH = 8$)

TRIS: 10 mM
KCl: 0.1 M
Imidazole: 10 mM

Buffer B ($pH = 8$)

TRIS: 10 mM
KCl: 0.1 M
Imidazole: 500 mM

Buffer C ($pH = 8$)

Sodium Phosphate Buffer: 10 mM
KCl: 0.1 M

B.6 SDS-PAGE

To prepare an SDS-PAGE, first a resolving gel must be prepared, as given in Table B.1. The TEMED initiator must be added last and then the mixture is immediately pipetted into a gel caster. Once the gel has set, a stacking gel is prepared using the ingredients given in Table B.2. The stacking gel is added on top of the revolving gel in the gel caster, and a comb is inserted into it to leave gaps for the denatured protein-loading dye mix to be added. It is useful to also add a small amount of bromophenol blue to the stacking gel so that these gaps are more visible. After the protein has been added, the gel can be places in an electrophoresis machine connected to a power source, and run at 180 V for 45 minutes.

Table B.1: 15% Resolving Gel

Reagent	**Volume (μL)**
H_2O	2.3 mL
1.5 M Tris, pH 8.8	2.5 mL
30 % Acrylamide mix	5 mL
10 % SDS	100 μL
10 % ammonium persulphate	100 μL
TEMED	4 μL

Table B.2: 5% Stacking Gel

Reagent	**Volume (μL)**
H_2O	2.7 mL
1 M Tris, pH 6.8	500 μL
30 % Acrylamide mix	670 μL
10 % SDS	40 μL
10 % ammonium persulphate	40 μL
TEMED	4 μL

APPENDIX C

Publications

C.1 Beyond the Discovery Void: New targets for antibacterial compounds

Science Progress (2016), 99(2), 153–182
Paper 1600170 doi:10.3184/003685016X14616130512308

Beyond the Discovery Void: New targets for antibacterial compounds

CLAIRE E. BROUGHTON, HUGO A. VAN DEN BERG, ALAN M. WEMYSS, DAVID I. ROPER and ALISON RODGER

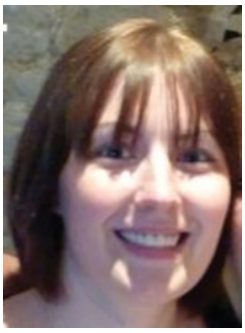

Claire E. Broughton studied Mathematical Biology and Biophysical Chemistry at the University of Warwick, obtaining an MSc in 2011 and a PhD at the Doctoral Training Centre for Molecular Organisation and Assembly in Cells in 2015. Her thesis focussed on the elucidation of interactions between the proteins that drive bacterial cell division. E-mail: c.broughton@warwick.ac.uk

Hugo A. van den Berg teaches mathematics at the University of Warwick, with an emphasis on mathematical models of biological systems, evolutionary dynamics, and the mathematical relationships between traits and genes.

Alan M. Wemyss also studied Mathematical Biology and Biophysical Chemistry at the Molecular Organisation and Assembly in Cells Doctoral Training Centre, obtaining an MSc in 2012. His PhD topic is the development and application of a fluorescence detection methodology for linear dichroism spectroscopy. This has enhanced our ability to study the relative orientation of chromophores in biological macromolecules.

David I. Roper is Reader in Structural Biology at the University of Warwick. He uses X-ray structural determination in combination with molecular biology and biochemical approaches, to investigate the molecular basis of antimicrobial resistance. His research encompasses fundamental and translation approaches including assay development and drug discovery.

Alison Rodger is Professor of Biophysical Chemistry at the University of Warwick. Her research interests include structure and function of bio-macromolecules such as DNA, membrane proteins, and fibrous proteins with application to bacterial cell division. She has developed innovative polarised spectroscopy techniques for bio-macromolecules.

ABSTRACT

Antibiotics save many lives, but their efficacy is under threat: overprescription, population growth, and global travel all contribute to the rapid origination and spread of resistant strains. Exacerbating this threat is the fact that no new major classes of antibiotics have been discovered in the last 30 years: this is the "discovery void." We discuss the traditional molecular targets of antibiotics as well as putative novel targets.

Keywords: *antibiotics, bacterial resistances to antibiotics, MRSA, discovery void, cell wall, cell division.*

1. Introduction

Antimicrobial drugs are among the resounding triumphs of modern medical science[1]. Millions of people alive today probably owe their lives, directly or indirectly, to our ability to halt the spread of dangerous bacteria inside the human body. Despite these successes, there are dark clouds on the horizon. As there are more people on the planet, and as they are travelling further, there are many more opportunities for resistant strains to arise and proliferate rapidly. Routine prescription of antibiotics, even when not strictly needed, adds further to the evolutionary pressure on pathogenic bacteria to develop resistance since a resistant mutant may actually be less fit than a wild-type in a non-antibiotic environment and thus not likely to take over in the absence of the drug.

Taken together, these worrying developments mean that our arsenal of antibiotics desperately needs to be broadened, and novel molecular targets must be found. Here, we review the history of antibiotics and we consider in detail what makes a good antibiotic. This review is written from the perspective that if we understand bacterial cell division at the molecular level then we may be able to identify new targets for antibacterial drug design, since this process is currently unexploited. We discuss the molecular machinery of the classic antibacterial target, the peptidoglycan cell wall, in the model Gram-negative organism *Escherichia coli*, and we describe the protein factors involved in the switch from peptidoglycan synthesis in cell elongation to peptidoglycan synthesis in cell division. We describe the structural components of the cell division machinery and the progress to date in the development of antibacterial drugs targeted to the inhibition of cell division.

2. A brief history of antibiotic drug discovery and an emerging threat

Ever since the germ theory of disease gained acceptance following Pasteur's discoveries and the formulation of Koch's postulates[2] in the late 19th century[3], the search has been on for a "magic bullet" that would subdue these germs. Following the early successes of synthetic agents such as Salversan and the sulfa drugs[3–5], efforts shifted towards natural compounds when Fleming demonstrated the antibacterial properties of *Penicillium* and the subsequent

purification of the active compound penicillin by Florey and Chain in 1940[6] made its use practicable. Many more natural antibacterial compounds followed during the so-called "golden era" of antibiotic drug discovery from 1940 to 1960. In the 1970s the focus shifted once more, this time toward chemical modification of the antimicrobial compounds that were already in use[3].

The discovery of daptomycin in 1987 marked the last novel class of antimicrobial compounds[7], although additional chemical structures have found use in the clinic, by virtue of chemical modification strategies. The dearth of novel classes becomes an ever more pressing problem as clinically relevant bacteria develop resistance to the compounds used in the clinic. Whenever resistance to one class becomes widespread, that class can no longer be used with guaranteed success and no novel class resides in the pipeline to replace it. The result is the so-called *Discovery Void* (Figure 1).

Modern antibacterial drug design still relies on the well-established strategies of whole-cell screening of natural fermentation products and the systematic chemical modification of lead compounds. However, these techniques are now used in conjunction with high-throughput, *in vitro* screens for inhibition of activity of a purified protein. In addition, the binding of

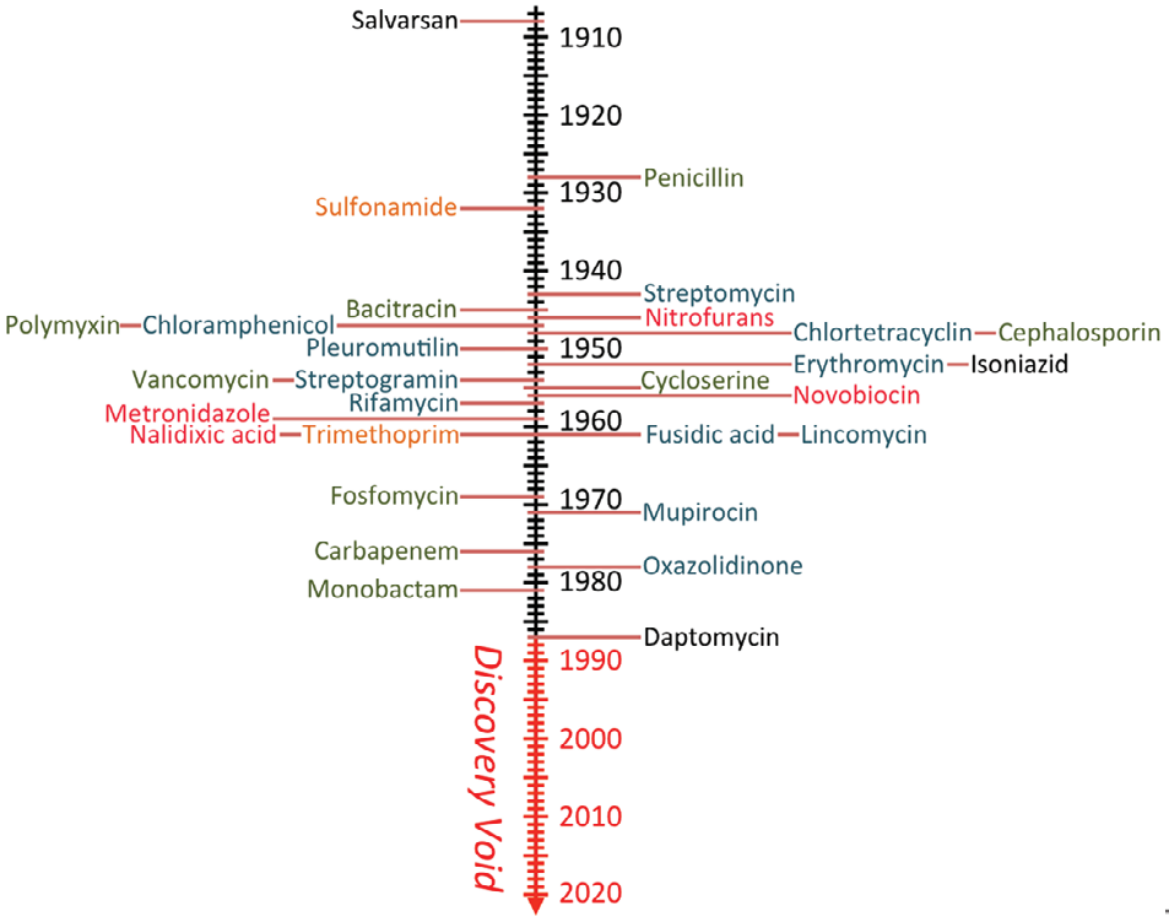

Figure 1 *Antimicrobial drug discovery timeline. Dates indicate initial discovery or patent registration. Compounds named are exemplars for classes, colour-coded by target process as follows: green: cell wall formation; orange: folate metabolism; blue: protein synthesis; red: DNA replication; black: unique modes of action. Adapted from Silver*[7].

a compound to an individual drug target may be tested *in silico* by running "docking" simulations. Indeed, the molecular structure of a large number of putative targets has been resolved as a result of the widespread use of protein X-ray crystallography.

Resistance is fast becoming a clear and present danger. In 2013 the UK Chief Medical Officer (CMO) recommended that antimicrobial resistance be put on the national risk register for civil emergencies[1]. This was one of a score of recommendations put forward in the CMO Annual Health Report to address the emerging crisis[1]. Other recommendations included improved international collaboration in research, more thorough global surveillance and data collection, and the implementation of significant changes to clinical practice in the prescription of antimicrobial drugs to both humans and animals[1]. The UK Government responded with the publication of its Five Year Antimicrobial Resistance Strategy 2013–2018 that detailed targets to improve public awareness and understanding of the issue, which should increase patient compliance with treatment regimes, and the decisions to conserve the currently available treatments, and to invest in new treatments with a focus on vaccination which will reduce the requirement for antibacterial drugs. Further improvements are a reduction of the number of antibacterial prescriptions and the introduction of genomic-level pathogen identification at the point of care. Finally, the report envisages changes to the EU regulatory landscape, for instance with regards to the agricultural use of antibiotics, tighter research collaboration between universities and industry, and financial incentives to commit the pharmaceutical industry to carry out more research[8].

There are several mechanisms that confer antibacterial resistance. These include modification of the drug target by mutation, modification of transport proteins which decreases the uptake of the drug into the bacterial cell, drug inactivation by enzyme activity, and an increase in the efflux of the drug from the cell[7]. The adaptations that confer resistance may be constitutively active, or they may be inducible, for instance as part of a generalised stress response, or specifically in response to exposure to the particular drug. Examples of the latter are the induction of β-lactamase and aminoglycoside kinase enzymes, which are expressed specifically in response to β-lactam- and aminoglycoside-type drugs, respectively[3].

Once resistance-conferring genes have arisen, they can spread. Such genes are often acquired through horizontal gene transfer *via* plasmids, which often encode resistance to more than one drug class[3]. The timescales of resistance development are quite unpredictable. For example, resistance of *Staphylococcus aureus* to β-lactam drugs was reported immediately after the introduction of penicillin. In contrast, 33 years went by before vancomycin resistance was finally recognised[7].

Although the incidence of the notorious "superbug" methicillin-resistant *S. aureus* (MRSA) has been in decline in the UK since its peak in 2003 (largely

due to improved hospital procedures) MRSA and other drug-resistant strains are still of major concern. Carbapenem-resistant Enterobacteriaceae, penicillin-resistant *Streptococcus pneumoniae*, vancomycin-resistant *Enterococci*, and multidrug-resistant *Mycobacterium tuberculosis* and *Neisseria gonorrhoeae* have been earmarked as serious threats[1,3,9].

Antibacterial drugs in current use mainly target the synthesis of macromolecular assemblies, such as deoxyribonucleic acid (DNA), ribonucleic acid (RNA), proteins, or the cell wall. Examples include fluoroquinolones, which are DNA topoisomerase inhibitors and rifamycins, which are RNA polymerase inhibitors. Drugs that target protein synthesis are named for the ribosomal subunit they attack (50S inhibitors include macrolides and amphenicols, whereas 30S inhibitors include tetracyclines and aminoglycosides), and drugs acting at the level of cell wall synthesis include penicillin binding protein (PBP) inhibitors such as β-lactams and transpeptidase inhibitors such as glycopeptides[10]. The success of the inhibitors of cell wall synthesis is due to the uniqueness of the molecular targets to the prokaryotes. This is also true of many of the components of the cell division machinery which therefore forms an attractive new target, although compounds acting at this level have yet to reach the market[10].

3. What makes a good antimicrobial agent?

An ideal antibacterial target molecule fulfils several desiderata[7]. First, it should be essential to life so that the bacteria perish when the target's regular physiological function is disrupted. Second, the target should be well conserved across a range of pathogens so that the drug has a wide range of applicability. Third, the target machinery should exhibit little functional redundancy so that the bacteria cannot readily evolve a "work-around" that bypasses the need for whatever component is targeted. Finally, the target should have no structural homologue in mammalian cells (or be unlike mammalian machinery serving a comparable function) so that the compound is not toxic to mammalian patients. For the antibacterial drugs targeted to DNA synthesis, RNA synthesis and protein synthesis, the drug must be highly specific for the prokaryotic target since the functions are also essential to the eukaryotic host. Several proteins of the machinery that drives cell division meet these desiderata and are hence potential targets[11]. While a compound that hits one of them may be discovered serendipitously, it seems reasonable to suppose that an understanding of the macromolecular machinery will aid the design and development of new antibacterial drugs.

4. A classic target: the cell wall and its associated machinery

Many of the components of the cell wall synthesis machinery were first identified as "penicillin-binding proteins" (PBPs). The naming convention has retained this reference to the interaction with penicillin, although the binding of

an antibiotic can hardly be considered to be their primary physiological role. As a detailed discussion of this machinery will naturally lead us to putative novel targets, this will be our point of departure.

4.1 The prokaryotic cell wall

The cell wall of a Gram-negative bacterium such as *E. coli* consists of an inner plasma membrane, a 3–6 nm thick, single-molecule, peptidoglycan layer, and an outer membrane[12], as shown in Figure 2. The peptidoglycan layer, also known as the murein cell wall, forms a net-like structure, the sacculus, which allows the cell to withstand the large internal turgor pressure and to maintain cell morphology. Seemingly at odds with this load-bearing "exoskeletal" role, the sacculus must somehow permit growth to take place; this requires a degree of dynamic adaptability while new material is added and the ability of the cell envelope to separate into two components when the cell divides[13]. During growth, the rod-shaped cell elongates while the diameter remains constant. Once the cell has approximately doubled in length, it divides by the controlled invagination and separation of both inner and outer membrane, sandwiching the periplasmic space between them[14].

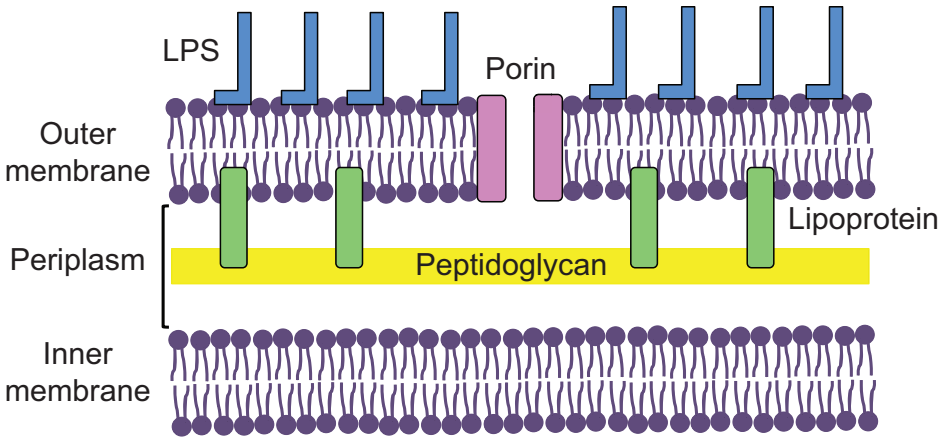

Figure 2 *The cell wall of Gram-negative bacteria. LPS: lipopolysaccharide. Adapted from Cabeen and Jacobs-Wagner[13].*

The sacculus consists of glycan chains that are covalently cross-linked by peptides forming a network that lies in an orientated fashion on the cell surface, in a single layer (Figure 3), as has been demonstrated by electron cryo-tomography; in particular, the structure was found to be fairly disordered, with the glycan chains lying mainly perpendicular to the long axis of the cell[15].

The glycan chains of peptidoglycan consist of alternating units of N-acetyl-glucosamine (GlcNAc) and N-acetyl-muramic acid (MurNAc), linked by a β-1,4-glycosidic bond, and the MurNAc subunit bears a pentapeptide *via* a peptide bond. These linear glycan strands are cross-linked by peptide bonds that link the pentapeptides on adjacent strands, the result being an extended

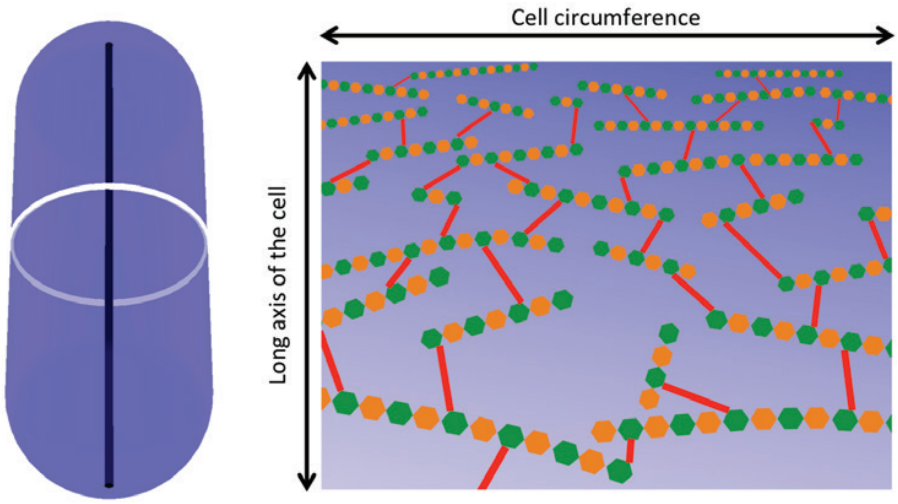

Figure 3 *The organisation of the peptidoglycan cell wall in* E. coli. *Left: bacterial cell with long axis indicated as a black line and circumference as a white band. Right: glycan strands (green and amber) lying approximately perpendicular to the long axis of the cell, in an otherwise fairly disorganised arrangement, with peptide links between these strands shown in red. Adapted from Gan* et al.[15].

peptidoglycan network[16], as shown in Figure 4 (the arrangement in this figure is more regular than is likely to be the case *in vivo*; *cf*. Figure 3).

Peptidoglycan synthesis begins in the cytoplasm where a series of enzymes generates uridine-5′-diphosphate (UDP)-GlcNAc from fructose-6-phosphate. MurA and MurB enzymes then catalyse the formation of UDP-MurNAc from UDP-GlcNAc[12,17,18] as shown in Figure 5.

Next, the enzymes MurC–F sequentially add the pentapeptide stem to the carboxyl group of the lactoyl moiety of MurNAc (Figure 5): MurC adds

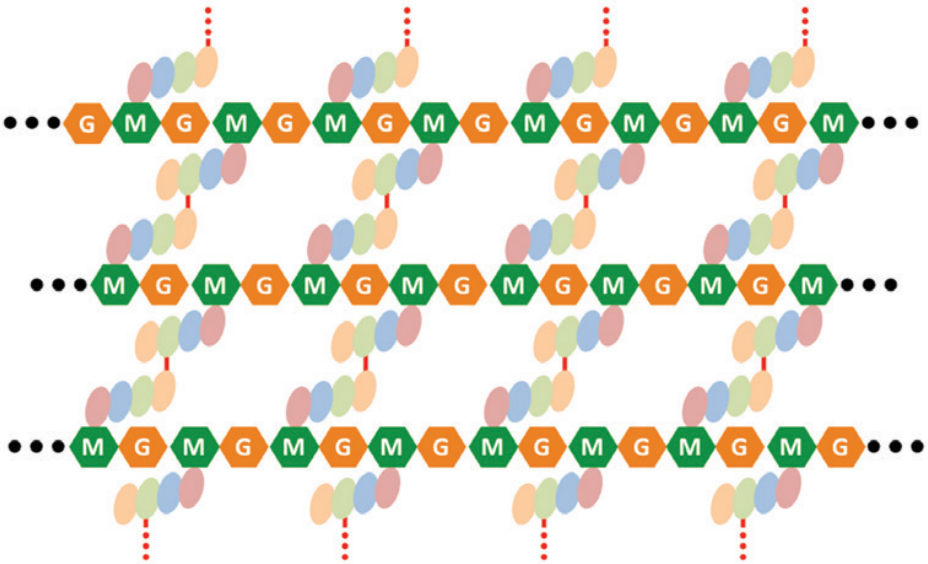

Figure 4 *Idealised chemical structure of* E. coli *peptidoglycan, adapted from Vollmer* et al.[17]. *M and G correspond to MurNAc and GlcNAc, respectively, and amino acid residues are represented as elliptical beads. Peptide bonds that link the glycan strands are indicated in red.*

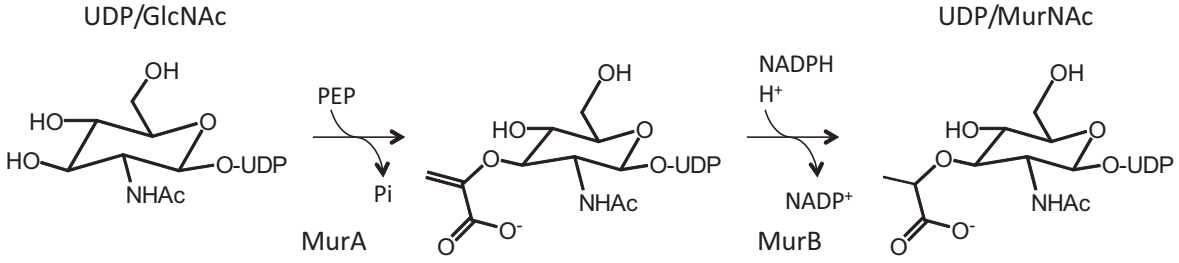

Figure 5 *The synthesis of UDP-MurNAc from UDP-GlcNAc by MurA and MurB. PEP is phosphoenolpyruvate. Adapted from Barreteau* et al.[19].

L-alanine and MurD follows, adding D-glutamate, MurE adds meso-2,6-diaminopimelic acid (an intermediate in lysine biosynthesis) to the γ-carboxylate group of the D-glutamate, and MurF adds the D-Ala-D-Ala dipeptide that has previously been dimerised by Ddl[19].

Next, the phosphorylated MurNAc-pentapeptide precursor is transferred by MraY to the membrane-embedded acceptor undecaprenyl-phosphate, yielding undecaprenyl-pyrophosphoryl-MurNAc (lipid I); uridine-5′-monophosphate is released. Lipid I then receives a GlcNAc donated by UDP-GlcNAc; this step is catalysed by MurG and results in undecaprenyl-pyrophosphoryl-MurNAc-pentapeptide-GlcNAc (lipid II) with the release of UDP[20].

Lipid II (a lipid-disaccharide-protein conjugate) then moves to the periplasmic phase, where the disaccharide group will be linked up into glycan chains (Figure 6). This "volte-face" is mediated by an enzyme whose identity remains unclear, FtsW being one candidate[21] and MurJ another[22].

Once lipid II has been transported to the periplasmic face of the inner membrane, glycosyltransferase enzymes (GTases) catalyse the addition of the GluNAc-MurNAc disaccharide to a growing glycan chain while transpeptidases (TPases) catalyse the peptide crosslinking reactions, the peptidoglycan synthases being anchored to the inner membrane[12,17,18]. The peptide crosslink usually observed in *E. coli* cell walls consists of a peptide bond between the carboxyl terminus of the D-Ala of position 4 and the free amino group of meso-2,6-diaminopimelic acid. The terminal D-Ala of the original pentapeptide stem is discarded in the process. Each glycan strand terminates with a 1,6-anhydro-MurNAc residue, which contains an intra-molecular ring from carbon 1 to carbon 6 of the sugar; this prevents any further elongation of the glycan chain but it is unclear if this structure is formed during synthesis or in later remodelling[18]. The average glycan chain length is estimated to be between 20 and 35 disaccharide units for *E. coli*. Lengths vary from as little as 10 units to as high as 45 and growth conditions may be relevant, since in the transition from exponential phase to stationary phase, peptide cross linkage and lipoprotein content increase and the mean glycan chain length decreases[23–25]. There are three classes of peptidoglycan synthase enzymes, the monofunctional GTases, the monofunctional TPases, and the bifunctional GTase and TPases[26]. The proteins were originally identified as ligands of penicillin and are still referred

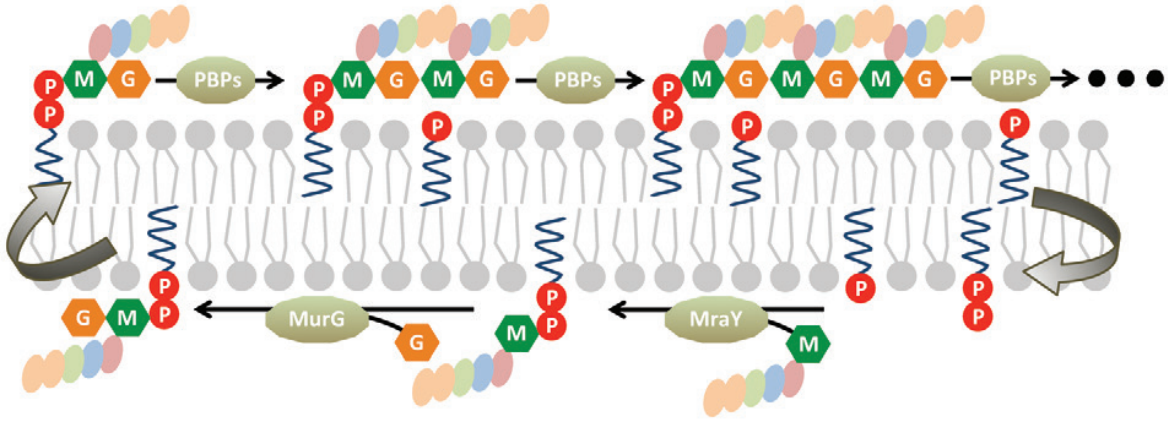

Figure 6 *Peptidoglycan synthesis at the inner membrane. M and G correspond to MurNAc and GlcNAc, respectively. The pentapeptide stem is represented as a string of coloured beads. On the periplasmic side of the membrane (top), the polysaccharide is formed by the polymerisation of the basic GlcNAc-MurNAc-pentapeptide disaccharide subunit (M-G-pentapeptide); PBPs are penicillin binding proteins. The units are delivered to the cytoplasmic face of the membrane (bottom) by the enzymes MraY and MurG. Adapted from Bouhss* et al.[20].

to as the penicillin-binding proteins (PBPs)[27,28]. *E. coli* has three class-A bifunctional PBPs (PBP1A, PBP1B, and PBP1C) and two monofunctional TPases (PBP2 and PBP3). The presence of either PBP1A or PBP1B is essential for life[29]. Although PBP1A has been shown to act in elongation and PBP1B in cell division, each protein can compensate for the absence of the other. PBP1C is non-essential and its over-expression cannot compensate for the loss of both PBP1A and PBP1B[30]. The monofunctional GTase MtgA is non-essential in *E. coli* and may play a role in cell division[31].

The peptidoglycan wall is also linked to the outer membrane *via* Braun's lipoprotein (Lpp), a small 58-residue protein with an S-glycerylcysteine at the N-terminus, which is modified with three fatty acids. These are embedded in the outer membrane *in vivo*. The C-terminal lysine residue is covalently attached to peptidoglycan *via* a peptide bond between the ε-amino group of the lysine side chain and the α-carbonyl of meso-2,6-diaminopimelic acid[32,33].

4.2 The elongasome

Cell growth and division both require that new peptidoglycan be synthesised and covalently linked to the old peptidoglycan sacculus within the periplasm[13,14]. In cell division this is achieved by the organisation and activation of the divisome protein complex[34], which is discussed below. In cell growth, a different set of proteins assembles at the inner membrane; this is the "elongasome", named as such since the addition of new cell wall material results in cell growth along the long axis in rods such as *E. coli*[35]. Whereas mutations of the divisome components result in cell filamentation, a loss of function within the elongasome results in a spherical phenotype[35,36].

Elongasome complexes are dispersed along the entire cell wall, so that new peptidoglycan is incorporated diffusely along the long axis of the cell while the length of the short axis remains constant[14]. Polar peptidoglycan is stable and tends not to be remodelled over time[37].

The elongasome comprises MreB, MreC, and MreD, proteins that are essential for the maintenance of the rod shape of *E. coli*[38]. MreB is an actin homologue[39] that was shown to form polymers *in vitro* in the presence of ATP, when purified from *Thermotoga maritima*[40]. MreB polymerises *in vivo* and binds directly to the inner cell membrane *via* an amphipathic helix[41]. This protein was once believed to form a large helical structure that extended along the long axis of the cell in both *E. coli* and *Bacillus subtilis*[42], but this has since been disputed[43]. It is now thought that MreB forms short filaments *in vivo* and that elongasome complexes form discrete patches in the membrane that move along the cell wall[41]. However, the mechanism of movement is as yet unclear. Discrete foci appear to move around the circumference of the cell, which suggests that the complex may follow the direction of the glycan chains of peptidoglycan. This rotation depends on the synthesis of peptidoglycan in the periplasm, and not on the ATPase activity of MreB[44]. On the cytoplasmic face of the inner membrane, MreB recruits components of the lipid II synthesis machinery MurG and MraY to the elongasome complex[45]. The RodZ protein, which contains a single transmembrane domain is also recruited to the elongasome *via* a direct interaction with MreB[46,47].

Interestingly, the diameter of the round cells produced on RodZ mutation is close to that of the short axis of wild-type cells, whereas treatment of cells with the MreB inhibitor A22, which causes MreB to dissociate from the membrane[48], results in spherical cells whose diameter is close to the length of the long axis of the wild-type cells. This suggests that MreB controls the maintenance of the short-axis length while RodZ determines the long-axis length[49].

MreC is an inner membrane protein with a large C-terminal periplasmic domain that forms filaments *in vivo*[50]. MreC interacts with MreB, MreD, and with large periplasmic PBPs, thus recruiting peptidoglycan synthetic enzymes to the elongasome[50]. Sequence analysis indicates that the protein is mostly hydrophobic with several transmembrane domains[51].

Another elongasome component is RodA; loss of this protein also results in a spherical phenotype. It has been suggested that RodA may mediate lipid II translocation in the elongasome, since it shares 30% sequence identity with FtsW[35,52]. However, as discussed, the lipid II translocase activity of FtsW is disputed[21,22].

The “diffuse” insertion of new peptidoglycan, associated with the elongasome, is quite distinct from the insertion of material at the midcell/cell pole (every cell pole is a former midcell), associated with the divisome: the two processes appear to employ different (but overlapping) sets of enzymes, as attested by the fact that cells treated with PBP2-specific mecillinam become

spherical and then lyse, whereas cells treated with PBP3-specific aztreonam become filamentous, with aborted Z-ring constrictions. This suggests that PBP2 is an elongasome component while PBP3 belongs with the divisome[27]. In fact, although PBP2 is part of the elongasome, it may also contribute to the initial stages of cell division as it transiently localises to the midcell, a process that requires active PBP3, as PBP2 did not localise to the midcell under aztreonam treatment[26].

As previously noted, notwithstanding the apparent different physiological functions of PBP1A and PBP1B, each can compensate for the absence of the other *in vivo*[29]. Whereas PBP1A binds PBP2 and is thought to be active in cell elongation and in the early stage of cell division[26], PBP1B binds PBP3, suggestive of a role in late cell division[53]. In the absence of PBP1A, cells have a smaller diameter with a longer time period between cell divisions, indicative of sluggish elongation[54]. The "diffuse" localisation of PBP1A supports a role in elongation, although in the absence of PBP1B, the midcell localisation of PBP1A increases in keeping with its compensatory role[54]. The activators of PBP1A and PBP1B, LpoA and LpoB respectively, do localise to the midcell during cell division, although LpoA localisation is relatively weak[55,56].

Some components of the elongasome complex, such as MreB, PBP2, and MurG, migrate simultaneously to the midcell, which might underpin the transition from elongating growth to the formation of the septum that will divide the daughter cells[57]. A transitory elongasome/FtsZ complex prevails between 20% to 60% of the cell cycle time, when the preseptal peptidoglycan synthesis occurs; an interaction between PBP2 and PBP3 was also measured during the mixed phase by Förster resonance energy transfer (FRET)[57]. When the elongasome components leave the complex, the late divisome completes cell separation[57].

4.3 Peptidoglycan turn-over and remodelling

Half of the cell wall material is turned over during each cell generation and most of this material is re-incorporated into the sacculus. The products of peptidoglycan hydrolysis accumulate in the periplasm and are transported back into the cytoplasm for recycling[58].

There are several enzymes that degrade peptidoglycan (Figure 7): N-acetylmuramidases and N-acetylglucosaminidases hydrolyse the β-1,4-glycosidic bonds of the glycan chains; N-acetylmuramidases cleave between MurNAc and GlcNAc subunits to produce a GlcNAc-MurNAc product (these enzymes are further categorised as lysozymes and lytic transglycosylases based on their generation of reduced MurNAc or 1,6-anhydro-MurNAc respectively)[59,60]; N-acetylglucosaminidases cleave between successive GlcNAc and MurNAc units to produce a MurNAc-GlcNAc degradation product[60]; DD-endopeptidases including PBP4, PBP7, and MepA cleave

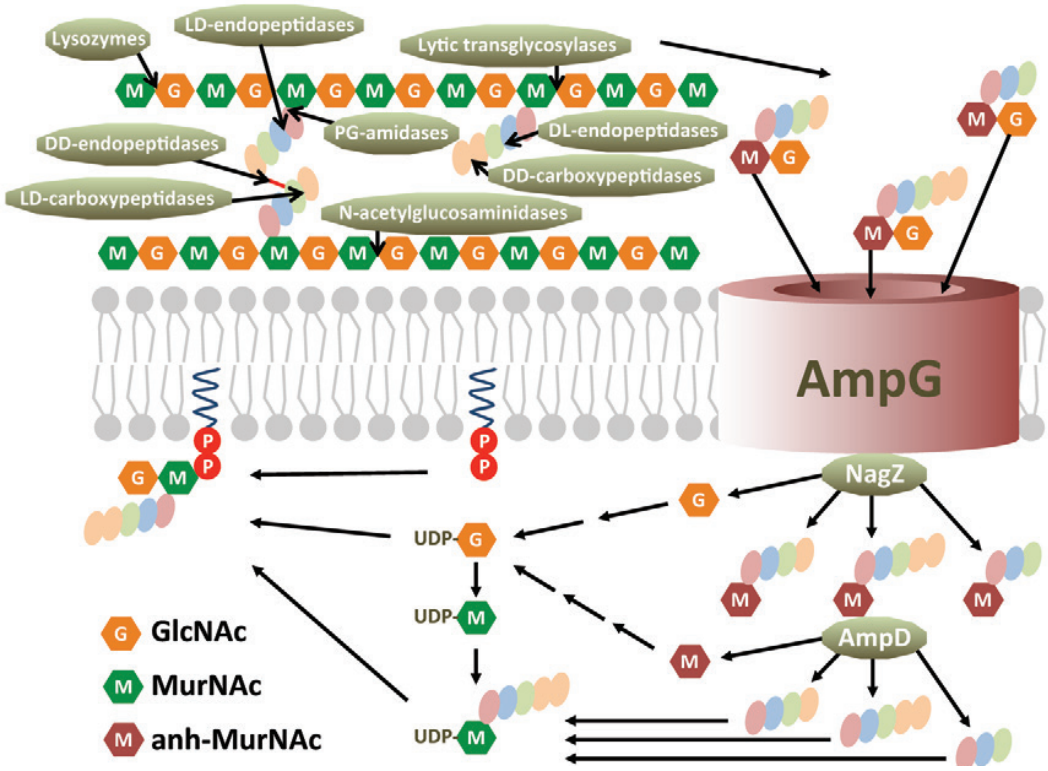

Figure 7 *Peptidoglycan degradation and recycling. Several peptidoglycan hydrolysis enzymes act in the periplasm; the resulting degradation products are transported back to the cytoplasm by AmpG and subsequently processed and regenerated into lipid II; "anh-MurNAc" stands for 1,6-anhydro-MurNAc. Adapted from Sobhanifar* et al.[60].

the crosslink peptide bond between the D-Ala of one strand and the meso-2,6-diaminopimelic acid of the neighbouring strand[60,61]; MurNAc-L-alanine amidases or peptidoglycan amidases including AmiA, AmiB, and AmiC hydrolyse the peptide bond between MurNAc and L-Ala at the first position of the peptide side chain[62]; LD-endopeptidases cleave between L-Ala and D-Glu at positions 1 and 2 of the peptide stem; DL-endopeptidases cleave between D-Glu and meso-2,6-diaminopimelic at positions 2 and 3; LD-carboxypeptidases cleave between meso-2,6-diaminopimelic and D-Ala at positions 3 and 4, and D,D-carboxypeptidases such as PBP4, PBP5, and PBP6 cleave between D-Ala and D-Ala at positions 4 and 5 [60,63].

The peptides released into the periplasm are transported back into the cytoplasm by the MppA-OppBCDF permease complex[64]. Penta-, tetra-, and tripeptide GlcNAc-1,6-anhydro-MurNAc degradation products are transported into the cytoplasm by the inner membrane AmpG permease[65]. Subsequently, the enzyme NagZ cleaves the glycosidic bond of the disaccharide[66,67], AmpD removes the peptide stem of 1,6-anhydro-MurNAc peptides[68,69], and LD-carboxypeptidase (LdcA) removes the D-Ala from the tetrapeptides[70]. The peptides are also directly recycled by the formation of a peptide bond with MurNAc, catalysed by Mpl[60,61,71]. The monosaccharide units are fed back into the UDP-GlcNAc synthesis pathway by conversion to glucosamine-6-phosphate[60,72].

A cut-and-insert model of peptidoglycan synthesis was originally proposed in which the peptidoglycan must be locally degraded, before insertion of new material that is then crosslinked[73,74]. Later work suggested that new material was added as single strands[75]. However, in another model of peptidoglycan synthesis, three new peptidoglycan strands are synthesised and inserted into the sacculus with degradation of one old glycan strand[14,25], every second strand being replaced by three new strands per cell generation[76]. Possibly, a monofunctional transglycosylase synthesises a glycan strand, while one or more bifunctional PBPs synthesise a strand on either side and catalyse the attachment of the outer strands to the central strand. In this model, PBP4 or PBP7 cut the old inter-strand linkages whereas PBP2 or PBP3 link the new glycan triplet to the sacculus. An outer membrane lytic transglycosylase such as Slt70, MltA, or MltB might then remove the original docking strand[76]. In this manner, multiprotein complexes would co-ordinate the synthesis and degradation of peptidoglycan and the pre-existing peptidoglycan matrix can serve as a template to maintain a constant cell diameter through each generation[77].

Notwithstanding the attractiveness of this model, a discrete macromolecular complex remains to be identified *in vivo*. Nevertheless, an interaction between PBP1B and MltA was observed *in vitro*[78], and the formation of a complex of the lytic transglycosylase Slt70, the DD-endopeptidase PBP7 and PBP3 has been reported[79]. Furthermore, MltB interacts with PBP1B, PBP1C, and PBP3[80], which might contribute to septum formation[79].

4.4 PBP3-independent peptidoglycan synthesis at the midcell region

E. coli is characterised by a constrictive mode of cell division in which the invagination of the inner and outer membranes and the synthesis of new cell wall material occur simultaneously; this stands in contrast to many Gram-positive bacteria in which the new cell wall is synthesised along the midcell before membrane invagination[18,35,58]. In *E. coli*, peptidoglycan remodelling may contribute a pushing force from outside of the inner membrane in the periplasm in addition to the inner pull from the constriction machinery[81].

Whereas the Z-ring forms at 39% of the way through the cell cycle time, PBP3 (also separately named as FtsI) and the cell-division trigger FtsN (see Section 5.4) are not recruited until 59% of the cell cycle time, a delay that allows the PBP3-independent synthesis of pre-septal peptidoglycan at the division site[82]. This was confirmed by a pulse-chase labelling experiment using D-cysteine which indicated that the “diffuse” insertion of new peptidoglycan during growth and cell elongation is followed by “local” synthesis at the midcell consequent on the formation of the Z-ring that drives septum formation and constriction at the midcell[37], as shown in Figure 8. Following cell division, the peptidoglycan synthesised at the new cells’ poles remains stable throughout the following division cycles[37]. This division-zone peptidoglygan synthesis is critically dependent on the presence of a Z-ring[83].

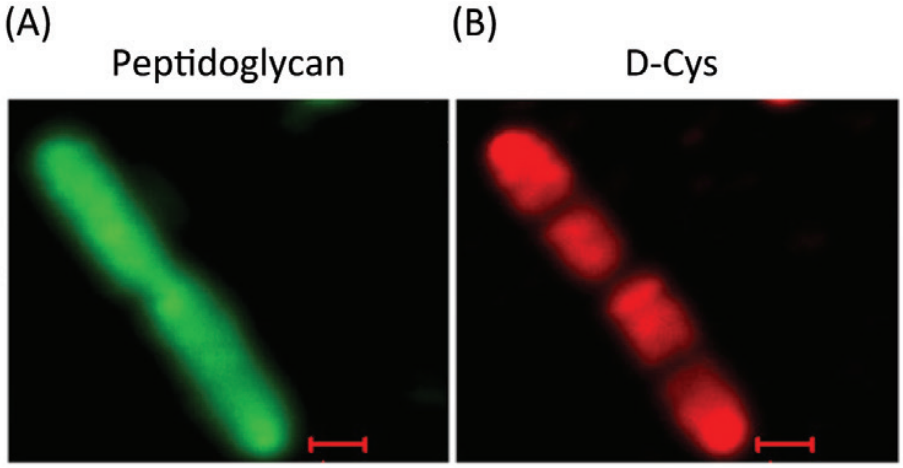

Figure 8 *PBP3-independent peptidoglycan synthesis at the midcell. A temperature-sensitive PBP3* E. coli *strain was grown at 42 °C during the chase period. (A) Sacculi were purified and labelled using an anti-peptidoglycan antibody. (B) D-Cys residues incorporated during the pulse phase were biotinylated and labelled with an anti-biotin antibody. Dark regions in (B) that are stained in (A) indicate new peptidoglycan synthesised in the chase phase. Scale bar indicates 1 μm. From Potluri* et al.[83].

5. Putative novel targets: the divisome and the Z-ring

Cell constriction, septal/polar peptidoglycan synthesis, and the coordination of cytokinesis go hand in hand. We have previously reviewed the divisome[84], represented schematically in Figure 9, in full detail and therefore will focus our attention here on critical processes that might pose good candidates for novel antibiotics.

5.1 Breaking down the Z-ring: ClpXP

The core component of the division machinery is the Z-ring (Figure 9), which is composed of filaments of the FtsZ protein. Enhancing the turn-over of this key protein could be one avenue of disrupting cell division.

FtsZ is degraded by ClpXP[85], a complex of ClpX and ClpP. The former belongs to the AAA+ protein family and can either act alone, remodelling proteins and disassembling polymers, or it may engage the serine protease ClpP in protein degradation, where ClpP forms two stacked heptameric rings, capped at one or both sides by a hexameric ring of ClpX, which controls the transfer of substrates into the proteolytic cavity[86].

ClpXP degrades FtsZ polymers *in vitro* in the presence of ATP and GTP, with polymers being the preferred substrate although monomers are also degraded[87]. The C-terminal tail of FtsZ is required for efficient ClpXP binding and degradation[87] and MinC competes with ClpXP for binding to FtsZ[88]. In the absence of ATP, ClpX appears to exist predominantly as a dimer with the N-terminal domain accessible for FtsZ binding, sequestering FtsZ and inhibiting polymerisation, whereas in the presence of ATP, the ATP-independent sequestering effect becomes sterically less favoured but ATP-dependent degradation of FtsZ by the ClpXP complex can proceed[89].

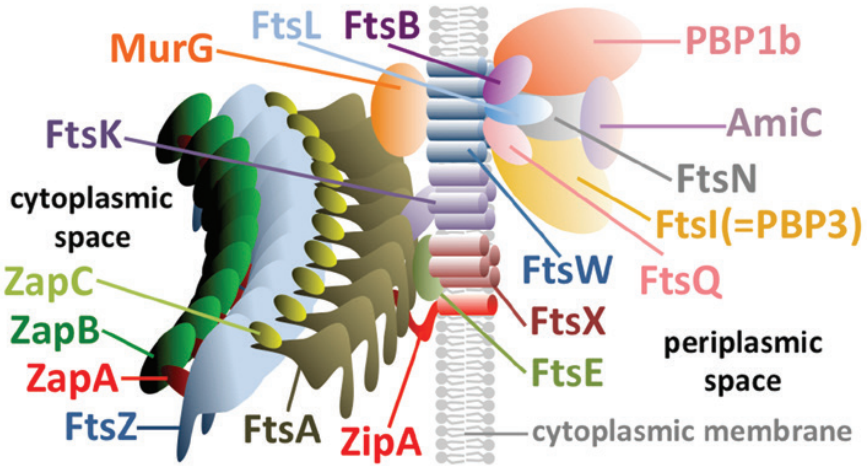

Figure 9 *The prokaryotic divisome, the complex of proteins that orchestrates cytokinesis in prokaryotic cells. Cylinders represent transmembrane domains.*

The ClpXP complex was shown to interact with FtsZ *in vivo*. On addition of spectinomycin to prevent protein synthesis, the half-life of FtsZ in wild-type cells was 115 minutes, which corresponds to a loss of 13% of FtsZ per cell cycle. In cells lacking ClpX, the FtsZ half-life increased to 205 minutes whereas in cells over-expressing ClpXP, it decreased to 45 minutes[87]. The ATPase activity of ClpX is required for FtsZ turnover *in vivo*[90].

5.2 Z-ring stability: the Zap proteins

The Z-ring associated proteins ZapA–E support the stability and efficiency of the Z-ring[91]. Light scattering and electron microscopy indicated that ZapA induces the bundling of FtsZ polymers[92]. In contrast to the lack of phenotype on the loss of ZapA in *B. subtilis*, deletion of the *zapA* gene in *E. coli* has been shown to affect cell growth[93], as localisation of the Z-ring becomes less reliable[94]. In *E. coli*, ZapA interacts with FtsZ which promotes polymer bundling and reduces GTPase activity by 20–24%[93,95].

ZapA is a dimer of dimers where each of the N-terminal domains interacts with an FtsZ subunit[96]. The ZapA tetramer therefore crosslinks two FtsZ filaments that each contain two FtsZ polymers arranged antiparallel. The ZapA tetramer links FtsZ filaments in a "rungs of a ladder" structure[93,96,97].

ZapA also interacts with ZapB, possibly *via* an interaction at the coiled-coil domain of ZapA[94]. In the absence of ZapB in *E. coli*, division is delayed and ectopic Z-rings are observed[98]. The ZapB protein is a coiled-coil dimer and it was shown to polymerise into filaments *in vitro*[98], whereas *in vivo* it forms a ring at the midcell with a slightly smaller diameter than the FtsZ ring, constricting just prior to the FtsZ-ring during cytokinesis[99]. This ZapB ring has been suggested to stabilise the FtsZ ring at its inner face[94]. ZapB has also been shown to interact with MatP (see Section 5.5), suggestive of a link between DNA replication and cytokinesis[100]. Indeed, on ZapB over-expression, the

nucleoid appears condensed and aberrant cell division occurs, resulting in very small cells as well as filaments[98].

ZapC localises to the Z-ring as an early cell division protein *in vivo*; cells lacking ZapC are elongated. Moreover, at high concentrations, ZapC causes the formation of ectopic Z-rings, leading to cell filamentation[101]. ZapC binds directly to FtsZ, promoting bundling *in vitro*[102] with a reduction of the GTPase activity of FtsZ of up to 60%[101].

ZapD binds directly to FtsZ, inducing FtsZ polymer bundling and a reduction of GTPase activity *in vitro* of up to 60%[91]. Purified as a dimer *in vitro*, ZapD binds to the C-terminal tail of FtsZ[91]. Whereas ZapD is non-essential, combined loss of ZapA and ZapD leads to cells that are longer than is observed on loss of either gene by itself. Overexpression of ZapD led to cell filaments and aberrant Z-ring formation[91].

In contrast to the other Zap proteins, ZapE is a late recruit to the divisome, as was confirmed when the midcell localisation of ZapE was found to coincide with cell constriction[103]. ZapE disrupts the formation of Z-rings when over-expressed *in vivo* and cells become filamentous; no Z-rings have been observed when ZapE is overexpressed[103]. This effect may be linked to ZapE's ability to hydrolyse ATP *in vitro* and to bundle FtsZ polymers into large, destabilised three-dimensional structures in the presence of ATP[103].

5.3 Coordination of midcell peptidoglycan remodelling: FtsEX

FtsEX is an apparent ABC transporter, consisting of FtsX, which is an integral membrane protein, and FtsE, which contains the ATP binding domain and interacts directly with FtsZ (Figure 10). The interaction does not appear to require ZipA, FtsA, or the C-terminal tail of FtsZ[104,105]. Loss of the FtsEX complex is conditionally lethal in *E. coli*. When grown in low-salt medium (less than 0.5% NaCl) cells filament, despite apparent Z-ring formation, as late cell

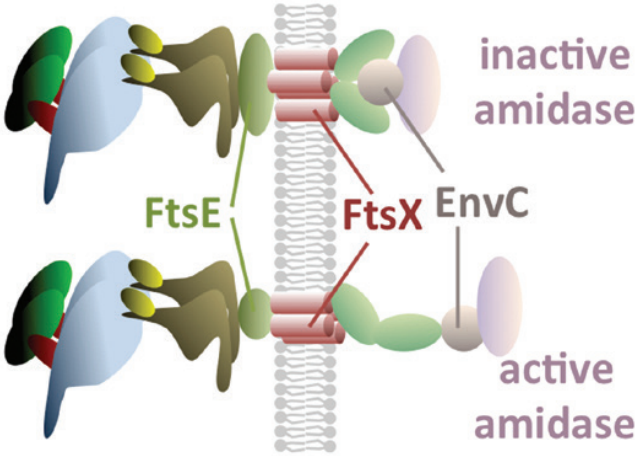

Figure 10 *Recruitment and activation of peptidoglycan amidases by the FtsEX complex. The periplasmic loop of FtsX is required for the recruitment of the amidase activator EnvC[109].*

division proteins fail to be recruited[104,106]. Supplementation of other osmolytes including glucose, sucrose, or glycerol to the growth medium can rescue the loss of FtsEX.

In bacterial two-hybrid screens, FtsX was found to interact with FtsA and with FtsQ[107]. Moreover, FtsEX recruits and controls the activity of EnvC, an activator of the peptidoglycan amidases AmiA and AmiB, which are key to splitting the peptidoglycan sacculus during cell separation[108]. The large periplasmic loop of FtsX binds to EnvC and is required for the recruitment of the latter to the divisome. The ATPase activity of FtsE is thought to be required for EnvC activation as mutations of FtsE that are predicted to cause ATP-binding or ATPase deficiencies did not affect the recruitment of EnvC to the midcell, however, division was impaired in these cells. Measurement of the ATPase activity of the mutant proteins has not been completed due to the poor solubility of purified FtsE *in vitro*[109]. A model for the activation of peptidoglycan amidases *via* FtsEX is given in Figure 10.

5.4 Triggering Z-ring constriction: the late division proteins

The late division proteins from FtsK to FtsN appear to assemble at the midcell concurrently[82]. FtsK is a DNA translocase. It resolves DNA dimers formed due to incomplete homologous recombination and may contribute to the link between chromosome segregation and cytokinesis[110,111]. The FtsK N-terminal domain, which contains four membrane-spanning helices, is required for the localisation of the protein to the midcell *in vivo* and therefore is essential, whereas the DNA translocase activity of its C-terminal domain was found to be non-essential[112,113].

FtsBLQ is recruited to the midcell as a complex. FtsB and FtsL both contain a single transmembrane domain and a short C-terminal periplasmic domain that form a putative leucine zipper, which may mediate the FtsLB heterodimerisation. FtsQ also has a single transmembrane domain but with a large periplasmic C-terminal domain of unknown function[34,114]. It is thought that the BLQ complex has two stable configurations, one that blocks cell constriction, and one that promotes or triggers it. Interactions with FtsA and FtsN lead to transitions between these states[115], as shown in Figure 11.

FtsW and FtsI(PBP3) also interact and form a complex, independently of the other late cell division proteins[116]. FtsW, which contains 10 transmembrane domains, features a 66-residue periplasmic loop region between transmembrane domains 7 and 8 that appears to be essential for the function of FtsW *in vivo*. FtsW may act as the lipid II translocase[21], or this role may be served by MurJ[22], or by both these proteins. The loop between transmembrane domains 9 and 10 of FtsW mediates the docking of FtsI[117]. In addition to its role as a monofunctional transpeptidase in peptidoglycan synthesis, FtsI(PBP3) interacts with the bifunctional enzyme PBP1B *in vitro* as well as *in vivo*[118]. FtsI(PBP3) was also shown to interact directly with FtsN *in vitro*[119].

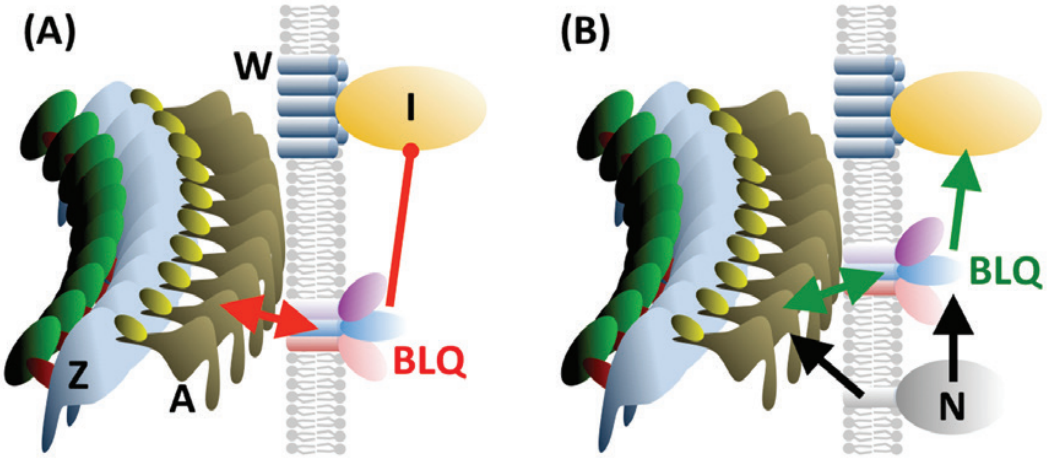

Figure 11 *A model for the activation of Z-ring constriction in* E. coli. *(A) Prior to the recruitment of FtsN, the FtsBLQ complex suppresses FtsI. (B) On recruitment of FtsN* via *an interaction with FtsA, the FtsBLQ complex is activated, leading to the initiation of peptidoglycan remodelling. The contraction of the Z-ring is activated* via *FtsA.*

Cell constriction commences upon the arrival of the final essential cell division protein, FtsN, suggesting that this membrane protein acts as a trigger[120,121]. FtsN interacts directly with the early cell division protein FtsA, *via* domain 1C of FtsA, an interaction that may signal the completion of divisome assembly to FtsZ[122].

Overexpression of FtsN can be used to compensate for the depletion of FtsA, FtsK, FtsI, and FtsQ[123] and to restore cell division in cells lacking FtsEX grown in low salt medium[124]. FtsN was also the only late cell division protein to bypass the requirement for ZipA in *E. coli* when overexpressed[125]. Although ZipA is required for the recruitment of the downstream cell division proteins, it has been shown that only FtsA interacts with them directly[121].

The interaction of FtsN with FtsA depends on the first 55 residues of FtsN, which comprise a short cytoplasmic region (residues 1–28) and the transmembrane domain (residues 29–55), a conserved motif at residues 4–6 (R/KDY) of FtsN being the FtsA binding site[125]. This binding apparently promotes oligomerisation of FtsN which drives the accumulation of FtsN at the midcell[120,122]. Midcell localisation of FtsN is further enhanced by the C-terminal, periplasmic SPOR domain of FtsN (residues 242–316), which binds to glycan strands that lack stem peptides, and these are generated by the activity of the peptidoglycan amidases AmiA–C[120,121,126]. The enhanced localisation of FtsN *via* the SPOR domain depends on the presence of FtsI and at least one of AmiA–C at the midcell[120]. The essential function of FtsN resides in a small region, residues 71 to 105. When targeted to the periplasm, this peptide supported the growth of *ftsN*$^{-}$ cells, although division was relatively inefficient and the fusion protein was found to be dispersed throughout the periplasm, rather than specifically localised to the midcell[120].

In sum, it appears that the FtsBLQ complex localises to the midcell in the state where it suppresses cell constriction and peptidoglycan synthesis,

involving perhaps a direct interaction with FtsWI. Binding of FtsN to FtsA supports initial midcell accumulation of FtsN, which interacts with the FtsBLQ complex and induces a state transition in the latter, which relieves the FtsBLQ-mediated suppression of peptidoglycan synthesis and remodelling. As the latter two processes are disinhibited, cell separation can commence. The mechanism is represented schematically in Figure 11.

The peptidoglycan amidases AmiB and AmiC, as well as the AmiC activator protein NlpD[108], are recruited downstream of FtsN[127,128] and their presence, coupled with the activation of FtsWI by FtsBLQ leads to an increase in the local concentration of the substrate for binding of the SPOR region of FtsN. This acts as a positive feedback loop for the further recruitment of FtsN and maintains and augments the pro-constriction state.

Oligomerisation of FtsA may sterically hinder its binding to FtsN[121]. A mutant form, FtsA*, has a reduced self-interaction and appears to be more potent than wild-type FtsA, *e.g.* bypassing the ZipA requirement; in the wild-type, ZipA may antagonise the self-interaction of FtsA, in addition to anchoring the Z-ring to the membrane[125,129].

5.5 Formation and localisation of the Z-ring: SulA, Min, nucleoid occlusion, and MatP

In *E. coli*, the SulA protein, which is expressed in response to DNA damage, inhibits the formation of the Z-ring, and this arrests cell division until the DNA damage has been repaired[130–133]. If the latter is prevented from being completed, the persistent block on cell division leads to the filamentous phenotype[134]. SulA can arrest cell division even when expressed artificially, in the absence of DNA damage[130,135].Once the DNA damage is repaired, recovery of cell division function is rapid[134,136], due to the short half-life (~1 min) of SulA. When protein expression is blocked with spectinomycin, SulA is rapidly removed by Lon protease and a new Z-ring forms[135].

Z-ring formation is restricted to the midcell region, as the Min system blocks Z-ring formation at the cell poles. As it is essential that chromosome replication and segregation are complete prior to cytokinesis, lest the nucleoid (the DNA-containing region of the cell) is severed by the contracting Z-ring[137], a "nucleoid occlusion" (NO) mechanism bars Z-ring formation in regions of the cell that contain genetic material. The *B. subtilis* protein Noc was the first nucleoid occlusion factor found[138] and SlmA was subsequently identified in *E. coli*[139]. The two proteins have no sequence or structural similarity and contain different DNA-binding domains[137]: Noc is similar to the ParB family[140] whereas SlmA contains a TetR-like DNA-binding domain[141].

SlmA inhibits FtsZ polymerisation *in vitro* and increases the GTPase activity of FtsZ by 36%. By binding to the C-terminal tail of FtsZ, SlmA induces polymer destabilisation and breakage of the filament[142]. Moreover, SlmA dimers may sequester FtsZ polymers into structures that are incompatible with Z-ring formation[141].

A third mechanism in Z-ring positioning, besides Min and NO, acts at the level of the replication termination region (Ter) of the *E. coli* chromosome, which is localised near the cell pole that arises upon cell division[143]. In particular, the MatP dimer binds to the Ter region and the two then move to the midcell. Moreover, the MatP focus splits and separates as Ter segregates[143]. Deletion of the *matP* gene causes cell filamentation, cell elongation, and the appearance of anucleate minicells in rich medium, whereas in minimal medium there is no division defect. In the absence of MatP, the positioning of the Ter region at the midcell is less precise and the separation of the Ter region occurs earlier in the cell cycle[100,143].

The MatP protein provides a link between chromosome segregation and cell division as it has been shown to interact with ZapB, in the presence of ZapA[100]. MatP binding to the Ter region of DNA acts as a positive signal for Z-ring formation in the absence of the negative regulators MinC and SlmA[144].

6. Drug candidates that target FtsZ

FtsZ appears to satisfy the criteria outlined in Section 3: it is essential to life and is well-conserved across most bacterial species; it is the first protein to localise to the midcell and is required for the downstream recruitment of all other cell division proteins[18]. Therefore, an inhibitor of the function of FtsZ is likely to be lethally disruptive to the division process. Although FtsZ is a structural homologue of eukaryotic tubulin, the disparate primary structures suggest that FtsZ-specific inhibitors are feasible[11]. Intriguingly, this has not been found to date, so in the final section of this review we consider what is known and suggest possible ways forward. We also refer to our mathematical model titled Critical Accumulation of Membrane-bound FtsZ Fibres (CAM-FF) that describes the formation of the Z-ring and the initiation of cell division. CAM-FF was used to assess the efficiency of the biochemical drug targets of the FtsZ molecule by the definition of a drug sensitivity co-efficient. A high co-efficient value corresponds to a site at which inhibition is highly toxic to the cell division process[145,146].

A drug molecule might compete with GTP at the GTP-binding pocket, thus blocking FtsZ polymerisation. However, this approach risks toxicity to other processes that require GTP binding, such as protein synthesis, signal transduction, and tubulin polymerisation in mammalian cells. Alternatively, a drug that mimics the SulA:FtsZ interaction at the T7 loop of FtsZ could block FtsZ polymerisation. Other possibilities include a drug that stabilises polymers to prevent subsequent depolymerisation, or one that blocks the interaction of FtsZ with its binding partners through its C-terminal tail[11].

The discovery of a specific inhibitor of FtsZ function is only part of the process, however. The drug's pharmacokinetics, as well as access of the drug to the target in cells, must be addressed in drug development[7]. This stage of the drug design process suffers from poor follow-up of previously reported inhibitors in the literature[147].

To date, there have been several examples of success in the search for small molecule inhibitors of FtsZ. Several compounds found to have anti-FtsZ activity are shown in Figure 12. Both naturally-derived and synthetic inhibitors have been identified using whole-cell filamentation tests, high-throughput FtsZ *in vitro* assays, as well as computational and structure-based design initiatives[148]. Although an antibacterial drug active against the cell division machinery is yet to reach the market, the examples below demonstrate the potential for exploitation of this system in the design and development of the antibacterial drugs of the future[11,148].

6.1 GTP analogues

To block the GTP-dependent polymerisation of FtsZ, C8-substituted GTP analogues have been tested and were shown to inhibit FtsZ polymerisation *in vitro*[149,150]. The small substitutions did not inhibit tubulin assembly[150]. Unfortunately, the C8-substituted guanine, guanosine, guanosine-5′-monophosphate (GMP), and guanosine-5′-triphosphates were later found to be ineffective antibacterial agents against *E. coli*, despite the strong inhibition of FtsZ polymerisation *in vitro*; moreover, the lack of toxicity was not due to low intracellular accumulation, nor to the absence of conversion of the analogue to the inhibitory triphosphate form[151]. The solutions of the mathematical equations of CAM-FF may explain this result. According to CAM-FF, the GTP-binding site is a poor antibacterial target since the drug sensitivity co-efficient is low at 0.043[145,146]. As an alternative approach to blocking the N-terminal FtsZ polymerisation surface, Sorto *et al*. designed T7-loop mimics by *in silico* docking of compounds into the T7 binding region of the SulA:FtsZ co-crystal structure from *Pseudomonas aeruginosa*[152]. These compounds have been synthesised and tests of activity are under way[153]. According to CAM-FF, the T7 loop is a highly efficient antibacterial target since a low level of inhibition results in the disruption of cell division; the drug sensitivity coefficient is high at 1.035 [145,146].

6.2 3-Methoxybenzamide analogues

An inhibitor of ADP-ribosyltransferase, 3-methoxybenzamide (3-MBA), was found to cause filamentation of *B. subtilis* but the phenotype could be suppressed by mutations in the *ftsZ* gene. This suggested that the target of 3-MBA was the FtsZ protein[154]. Subsequently, 500 analogues of 3-MBA were synthesised and tested for antibacterial activity; among these, the difluorobenzamide PC190723 (3-[(6-chloro[1,3]thiazolo[5,4-b]pyridin-2-yl)methoxy]-2,6-difluorobenzamide) turned out to be a potent inhibitor of both *B. subtilis* and *S. aureus*. In the latter, both single-drug-resistant and multi-drug-resistant strains were susceptible, while PC190723 was non-toxic to human hepatocytes[155,156]. Furthermore, in a mouse model of *S. aureus* infection, all animals survived following a single intravenous dose of PC190723, compared to nil survivors without treatment[155].

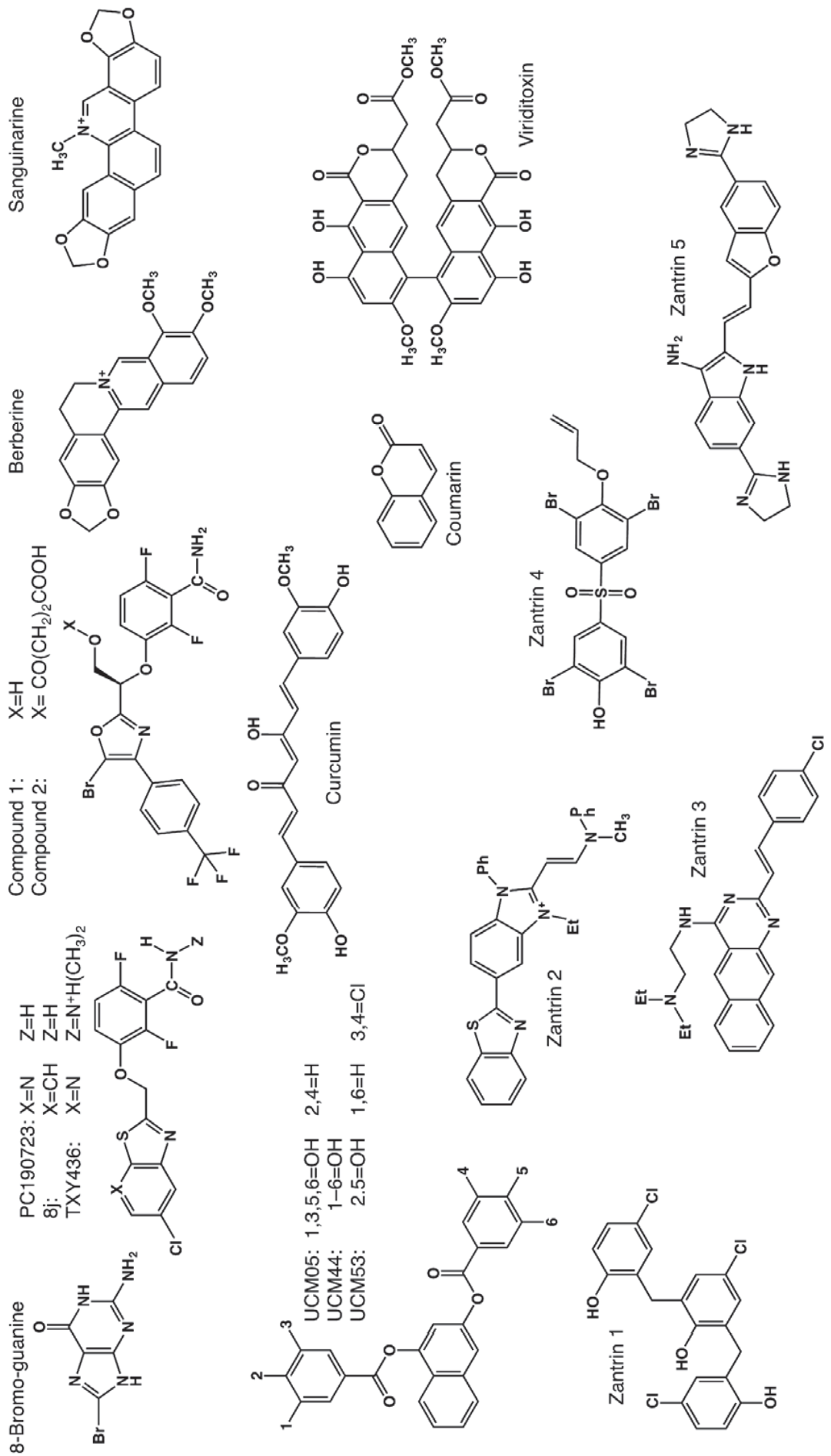

Figure 12 *Small molecule inhibitors of FtsZ*[148].

In later work, PC190723 was shown to be more effective than vancomycin and linezolid against MRSA growth, with a minimum inhibitory concentration of 0.2 μg/mL, compared to 2 μg/mL for vancomycin and linezolid. PC190723 was also shown to act synergistically with imipenem and other β-lactam antibiotics *in vivo*. In a mouse model of MRSA infection, neither imipenem nor PC190723 (at higher doses than used in the original study) resolved the infection as a single agent. However, when co-administered, a significant reduction in the number of colony forming units in mouse thigh homogenates was observed[156].

FtsZ-cyan-fluorescent-protein and green-fluorescent-protein-FtsZ fusions exhibited disrupted localisation in MRSA and *B. subtilis,* respectively, on treatment with PC190723: multiple rings and arcs of FtsZ, not restricted to the midcell, were observed[155,156]. PC190723 was shown to stabilise polymers of *B. subtilis* and *S. aureus* FtsZ and to reduce their GTPase activity. Curved structures, bundles, toroids, and helices of FtsZ were also observed *in vitro* using electron microscopy[157]. These effects were not observed for FtsZ purified from *E. coli*, which is not susceptible to growth inhibition by PC190723[155,157].

The binding of PC190723 to *S. aureus* FtsZ stabilises the active form to promote polymerisation. This reduces the concentration required for polymerisation and leads to loss of the critical concentration and co-operativity of FtsZ polymerisation that is observed in the absence of the compound[158]. The crystal structure of *S. aureus* FtsZ in complex with PC190723, shown in Figure 13, revealed that the compound binds in the cleft between the interdomain helix H7 and the C-terminal domain with the benzamide moiety close to the T7 loop. The site is similar to the taxol binding site of tubulin[159]. The stabilisation of FtsZ polymers may be initially beneficial to the cell in the formation of the Z-ring. Indeed, CAM-FF predicts that cells are better able to form the Z-ring and to initiate cell division if polymers are stabilised and the GTPase activity is reduced. However, the subsequent depolymerisation of the Z-ring is inhibited and this will prevent the progression of cell division after initiation[145,146].

The low solubility of PC190723 hampers its use as an oral drug; to address this, a prodrug derivative referred to as TXY436 was developed. Whereas PC190723 was ineffective as an oral preparation, 100% of methicillin-sensitive *S. aureus* (MSSA)-infected mice that were treated with oral TXY436 survived, as did 67% of mice infected with MRSA, compared to 0% survival without treatment. Moreover, TXY436 had minimal toxicity to monkey kidney epithelial cells[160]. Compound 8j, shown in Figure 12 is closely related to PC190723 and was found to be more potent[161]. An alternative 3-MBA derivative, referred to as compound 1 (Figure 12), also displayed antibacterial activity as a single drug. Compound 1 and its succinate prodrug (referred to as compound 2) were both effective in the reduction of bacterial load in the murine model of *S. aureus* infection[162].

6.3 Nature's pharmacopoeia

Several naturally occurring molecules have also been shown to inhibit FtsZ activity. For example, in a screen of $>10^5$ extracts of microbial fermentation broths and plants, viriditoxin was identified as an inhibitor of the polymerisation and GTPase activity of *E. coli* FtsZ *in vitro*. Viriditoxin was purified from an *Aspergillus viridinutans* fermentation broth and was found to inhibit the growth of all of the drug-sensitive and multi-drug-resistant strains of *Staphylococcus*, *Enterococcus*, and *S. pneumoniae* that were tested[163]. However, viriditoxin was later synthesised[164] but was found to be inactive against FtsZ from both *B. subtilis* and *E. coli*; chemical lability of the preparation was suggested to be the cause but a trace impurity may have been the active compound in the original study[148].

Plant-derived compounds have also been reported to be active against FtsZ; these include curcumin (1,7-bis-(4-hydroxy-3-methoxy-phenyl)hepta-1,6-diene-3,5-dione), which inhibits the growth of *E. coli* and *B. subtilis* and disrupts FtsZ polymerisation by an increase in the rates of GTPase activity and the subsequent depolymerisation[165]. However, curcumin has also been shown to inhibit other proteins including FabI in *E. coli*, as well as HIV integrase and human glyoxylase I and monoamine oxidase, which suggests that curcumin is a promiscuous inhibitor and therefore may not be useful as a drug lead[7].

The plant-based polyphenol coumarins were also shown to inhibit *B. subtilis* cell division and to inhibit *E. coli* FtsZ polymerisation and GTPase activity *in vitro*. Docking studies suggested that they bind to the T7 loop of FtsZ. These compounds were also shown to be non-toxic to NIH/3T3 mouse

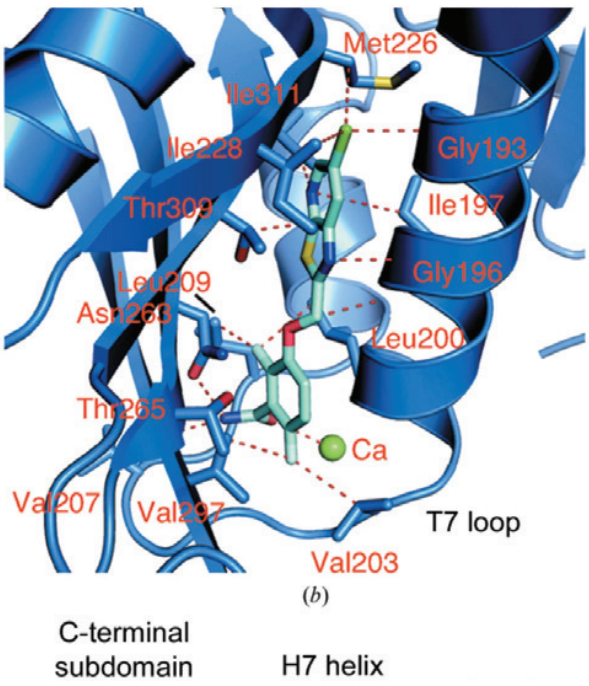

Figure 13 S. aureus *FtsZ in complex with PC190723. The compound binds in the cleft between the inter-domain helix H7 and the C-terminal domain*[159].

embryonic fibroblasts and to human embryonic kidney cell lines[166]. Berberine has also been shown to inhibit the growth of several species including *E. coli*, *S. aureus* (including MRSA), *Streptococcus pyogenes*, *Vibrio cholerae*, *Clostridium perfringens*, and multi-drug-resistant *M. tuberculosis*. Berberine inhibits *E. coli* FtsZ polymerisation and GTPase activity by competition with GTP for binding to FtsZ[167]. The plant compound sanguinarine was also found to inhibit the growth of several Gram-negative and Gram-positive species and to inhibit FtsZ polymerisation and GTPase activity *in vitro*[168]. However, sanguinarine also inhibits tubulin *in vitro* and may be toxic to eukaryotic cells[168]. Finally, cinnamaldehyde also inhibited *E. coli* FtsZ polymerisation and GTPase activity *in vitro* and was antibacterial against *E. coli* and *B. subtilis*[169].

6.4 The chemist's pharmacopoeia

Several high-throughput screens of chemical libraries have yielded further small molecules that are active against FtsZ. For example, the five chemically distinct Zantrins were identified in a screen of over 18,000 chemicals for inhibition of the GTPase activity of *E. coli* FtsZ[170]. These compounds were also shown to inhibit the GTPase activity of FtsZ from *M. tuberculosis*. Zantrins Z1 and Z4 were shown to decrease the number and length of *E. coli* FtsZ filaments using electron microscopy, whereas Z2, Z3, and Z5 stabilised the filaments. The compound Z1 abolished growth of *P. aeruginosa*, *S. pneumonia*, and *Bacillus cereus* and Z1 and Z2 killed *E. coli*, as did Z3 and Z5 in an *E. coli* strain lacking the major drug pump AcrAB. Furthermore, Z1–Z3 were active against *Shigella dysenteriae* and *Vibrio cholera* and Z1–Z4 were active against MRSA. Zantrins were also shown to perturb Z-ring assembly in *E. coli*[170].

Competitive ligands UCM05, UCM44, and UCM53 were likewise identified by means of a chemical library screen by using FtsZ from *B. subtilis* and detection of competitive binding to FtsZ with mant-GTP. UCM53 was found to be active against *B. subtilis* and drug-resistant strains of *S. aureus*, as well as ampicillin- and levofloxacin-resistant *Enterococcus faecium*[171]. Finally, in a cell filamentation screen of 151 rhodanine compounds, compound CCR-11 was identified as an inhibitor of *B. subtilis*; this compound was subsequently shown to disrupt the localisation of Z-rings in cells and to inhibit the assembly and GTPase activity of *B. subtilis* FtsZ *in vitro*[172].

6.5 Blocking interactions with ZipA

The search for small molecule inhibitors of the FtsZ:ZipA interaction is hampered by the fact that protein–protein interactions are difficult to disrupt using small molecules since large areas of the two protein surfaces are buried in the interaction[173]. However, in a high-throughput screen of 250,000 compounds, 29 were found to compete for the FtsZ binding site of ZipA. The most successful competitor was co-crystallised with ZipA from *E. coli* and was found to bind to the FtsZ-binding cleft of ZipA[174]. Top-scoring compounds that were found

to bind to different but overlapping sites of the ZipA cleft were chemically combined and these hybrid molecules were found to have increased potency. However, their antibacterial activity against Gram-positive bacteria suggests that the compound is acting on additional cell targets, since ZipA homologues appear to be absent in these species[175].

An NMR-based assay was used to screen 825 compounds for binding to ZipA[173]. Seven compounds showed binding to residues at the ZipA:FtsZ interface. Building on the highest affinity hit, a further 87 chemically similar molecules were tested with some improvement to ZipA affinity, although the latter remained too low at 2 mM[173]. CAM-FF predicts that the inhibition of the FtsZ:ZipA interaction has an intermediate effect on the cell division process; for the inhibition of the T7 loop of FtsZ, the drug sensitivity co-efficient is 0.204 [145,146].

7. Conclusion

Taken together, these studies show that the road to drug discovery is long and arduous, most compounds fall by the wayside for some reason or other. However, the divisome complex represents a collection of numerous possible targets within the bacterium's machinery that remains to be explored and exploited. As the threat of a post-antibiotic era looms, the search for potential drug interactions must utilise all of the available tools. *In silico* experimentation will aid the discovery of drug leads and, as in the application of CAM-FF, mathematical descriptions of the cell division process should be employed to target the research effort. Despite the setbacks, the examples presented here give hope that the cell division machinery will hold a way to fill the Discovery Void.

CEB and AMW gratefully acknowledge support by the EPSRC (grant EP/F500378/1).

Published online: 8 June 2016

8. References

1. Anonymous. (2013) Less talk, more action. *Nat. Rev. Microbiol.,* **11**, 295.
2. Evans, A. (1978) *Am. J. Epidemiol.*, **108**, 249–258.
3. Wright, G.D. (2007) *Nat. Rev. Microbiol.*, **5**, 175–186.
4. Winau, F., Westphal, O. and Winau, R. (2004) *Microbes Infect.*, **6**, 786–789.
5. Aminov, R.I. (2010) *Front. Microbiol.*, **1**, 134.
6. Bentley, R. (2009) *J. Ind. Microbiol. Biotechnol.*, **36**, 775–786.
7. Silver, L. (2011) *Clin. Microbiol. Rev.*, **24**, 71–109.
8. (2013) UK 5 year antimicrobial resistance strategy 2013 to 2018. *Dep. Heal.*
9. Chopra, I. (2013) *J. Antimicrob. Chemother.*, **68**, 496–505.
10. Kohanski, M.A., Dwyer, D.J. and Collins, J.J. (2010) *Nat. Rev. Microbiol.*, **8**, 423–435.
11. Den Blaauwen, T., Andreu, J.M. and Monasterio, O. (2014) *Bioorg. Chem.*, **55**, 27–38.
12. Vollmer, W. and Seligman, S.J. (2010) *Trends Microbiol.*, **18**, 59–66.
13. Cabeen, M.T. and Jacobs-Wagner, C. (2005) *Nat. Rev. Microbiol.*, **3**, 601–610.

14. Vollmer, W. and Höltje, J.V. (2001) *Curr. Opin. Microbiol.*, **4**, 625–633.
15. Gan, L., Chen, S. and Jensen, G.J. (2008) *Proc. Natl. Acad. Sci. U. S. A.*, **105**, 18953–18957.
16. Schleifer, K. and Kandler, O. (1972) *Bacteriol. Rev.*, **36**, 407–477.
17. Vollmer, W., Blanot, D. and De Pedro, M.A. (2008) *FEMS Microbiol. Rev.*, **32**, 149–167.
18. Egan, A.J.F. and Vollmer, W. (2013) *Ann. N. Y. Acad. Sci.*, **1277**, 8–28.
19. Barreteau, H., Kovač, A., Boniface, A., *et al*. (2008) *FEMS Microbiol. Rev.*, **32**, 168–207.
20. Bouhss, A., Trunkfield, A.E., Bugg, T.D.H. and Mengin-Lecreulx, D. (2008) *FEMS Microbiol. Rev.*, **32**, 208–233.
21. Mohammadi, T., van Dam, V., Sijbrandi, R., *et al*. (2011) *EMBO J.*, **30**, 1425–1432.
22. Sham, L., Butler, E., Lebar, M., *et al*. (2014) *Science*, **345**, 220–222.
23. Gmeiner, J., Essig, P. and Martin, H. (1982) *FEBS Lett.*, **138**, 109–112.
24. Glauner, B., Holtje, J.V. and Schwarz, U. (1988) *J. Biol. Chem.*, **263**, 10088–10095.
25. Höltje, J.V. and Glauner, B. (1990) *Res. Microbiol.*, **141**, 75–89.
26. Den Blaauwen, T., Aarsman, M.E.G., Vischer, N.O.E. and Nanninga, N. (2003) *Mol. Microbiol.*, **47**, 539–547.
27. Spratt, B.G. (1975) *Proc. Natl. Acad. Sci. U. S. A.*, **72**, 2999–3003.
28. Spratt, B.G. (1977) *Eur. J. Biochem.*, **72**, 341–352.
29. Suzuki, H., Nishimura, Y. and Hirota, Y. (1978) *Proc. Natl. Acad. Sci. U. S. A.*, **75**, 664–668.
30. Schiffer, G. and Höltje, J.V. (1999) *J. Biol. Chem.*, **274**, 32031–32039.
31. Derouaux, A., Wolf, B., Fraiport, C., *et al*. (2008) *J. Bacteriol.*, **190**, 1831–1834.
32. Hantke, K. and Braun, V. (1973) *Eur. J. Biochem.*, **34**, 284–296.
33. Dramsi, S., Magnet, S., Davison, S. and Arthur, M. (2008) *FEMS Microbiol. Rev.*, **32**, 307–320.
34. Goehring, N.W. and Beckwith, J. (2005) *Curr. Biol.*, **15**, R514–26.
35. Den Blaauwen, T., de Pedro, M.A., Nguyen-Distèche, M. and Ayala, J.A. (2008) *FEMS Microbiol. Rev.*, **32**, 321–344.
36. De Pedro, M., Donachie, W.D., Höltje, J.V. and Schwarz, H. (2001) *J. Bacteriol.*, **183**, 4115–4126.
37. De Pedro, M.A., Quintela, J.C., Höltje, J.V. and Schwarz, H. (1997) *J. Bacteriol.*, **179**, 2823–2834.
38. Kruse, T., Bork-Jensen, J. and Gerdes, K. (2005) *Mol. Microbiol.*, **55**, 78–89.
39. Van den Ent, F., Amos, L.A. and Löwe, J. (2001) *Nature*, **413**, 39–44.
40. Esue, O., Cordero, M., Wirtz, D. and Tseng, Y. (2005) *J. Biol. Chem.*, **280**, 2628–2635.
41. Salje, J., van den Ent, F., de Boer, P. and Löwe, J. (2011) *Mol. Cell*, **43**, 478–487.
42. Shih, Y.L., Le, T. and Rothfield, L. (2003) *Proc. Natl. Acad. Sci. U. S. A.*, **100**, 7865–7870.
43. Swulius, M. and Jensen, G. (2012) *J. Bacteriol.*, **194**, 6382–6386.
44. Van Teeffelen, S., Wang, S., Furchtgott, L., *et al*. (2011) *Proc. Natl. Acad. Sci.*, **108**, 15822–15827.
45. Mohammadi, T., Karczmarek, A., Crouvoisier, M., *et al*. (2007) *Mol. Microbiol.*, **65**, 1106–1121.
46. Bendezu, F., Hale, C., Bernhardt, T. and de Boer, P. (2009) *EMBO J.*, **28**, 193–204.
47. Van den Ent, F., Johnson, C.M., Persons, L., *et al*. (2010) *EMBO J.*, **29**, 1081–1090.
48. Karczmarek, A., Baselga, R.M.A., Alexeeva, S., *et al*. (2007) *Mol. Microbiol.*, **65**, 51–63.
49. Shiomi, D., Sakai, M. and Niki, H. (2008) *EMBO J.*, **27**, 3081–3091.
50. Van den Ent, F., Leaver, M., Bendezu, F., *et al*. (2006) *Mol. Microbiol.*, **62**, 1631–1642.
51. Leaver, M. and Errington, J. (2005) *Mol. Microbiol.*, **57**, 1196–1209.
52. Ikeda, M., Sato, T., Wachi, M., *et al.* (1989) *J. Bacteriol.*, **171**, 6375–6378.
53. Weiss, D., Pogliano, K., Carson, M., *et al.* (1997) *Mol. Microbiol.*, **25**, 671–681.
54. Banzhaf, M., van den Berg van Saparoea, B., Terrak, M., *et al.* (2012) *Mol. Microbiol.*, **85**, 179–194.
55. Paradis-Bleau, C., Markovski, M., Uehara, T., *et al.* (2010) *Cell*, **143**, 1110–1120.
56. Typas, A., Banzhaf, M., van den Berg van Saparoea, B., *et al.* (2010) *Cell*, **143**, 1097–1109.
57. Van der Ploeg, R., Verheul, J., Vischer, N.O.E., *et al.* (2013) *Mol. Microbiol.*, **87**, 1074–1087.
58. Typas, A., Banzhaf, M., Gross, C.A. and Vollmer, W. (2011) *Nat. Rev. Microbiol.*, **10**, 123–36.
59. Scheurwater, E., Reid, C.W. and Clarke, A.J. (2008) *Int. J. Biochem. Cell Biol.*, **40**, 586–591.

60. Sobhanifar, S., King, D.T. and Strynadka, N.C.J. (2013) *Curr. Opin. Struct. Biol.*, **23**, 695–703.
61. Park, J.T. and Uehara, T. (2008) *Microbiol. Mol. Biol. Rev.*, **72**, 211–227.
62. Heidrich, C., Templin, M.F., Ursinus, A., *et al.* (2001) *Mol. Microbiol.*, **41**, 167–178.
63. Ghosh, A.S., Chowdhury, C. and Nelson, D.E. (2008) *Trends Microbiol.*, **16**, 309–317.
64. Park, J.T., Raychaudhuri, D., Li, H., *et al.* (1998) *J. Bacteriol.*, **180**, 1215–1223.
65. Cheng, Q. and Park, J.T. (2002) *J. Bacteriol.*, **184**, 6434–6436.
66. Cheng, Q., Li, H., Merdek, K. and Park, J.T. (2000) *J. Bacteriol.*, **182**, 4836–4840.
67. Vötsch, W. and Templin, M.F. (2000) *J. Biol. Chem.*, **275**, 39032–39038.
68. Jacobs, C., Joris, B., Jamin, M., *et al.* (1995) *Mol. Microbiol.*, **15**, 553–559.
69. Lee, M., Zhang, W., Hesek, D., *et al.* (2009) *J. Am. Chem. Soc.*, **131**, 8742–8743.
70. Templin, M.F., Ursinus, A. and Höltje, J.V. (1999) *EMBO J.*, **18**, 4108–4117.
71. Van Heijenoort, J. (2011) *Microbiol. Mol. Biol. Rev.*, **75**, 636–663.
72. Plumbridge, J. (2009) *J. Bacteriol.*, **191**, 5641–5647.
73. Burman, L.G. and Park, J.T. (1984) *Proc. Natl. Acad. Sci. U. S. A.*, **81**, 1844–1848.
74. Park, J. and Burman, L. (1985) *Ann. l'Institut Pasteur / Microbiol.*, **136**, 51–58.
75. De Jonge, B., Wientjes, F., Jurida, I., *et al.* (1989) *J. Bacteriol.*, **171**, 5783–5794.
76. Höltje, J.V. (1998) *Microbiol. Mol. Biol. Rev.*, **62**, 181–203.
77. Höltje, J.V. (1996) *Microbiology*, **142**, 1911–1918.
78. Vollmer, W., Von Rechenberg, M. and Höltje, J.V. (1999) *J. Biol. Chem.*, **274**, 6726–6734.
79. Romeis, T. and Höltje, J.V. (1994) *J. Biol. Chem.*, **269**, 21603–21607.
80. Von Rechenberg, M., Ursinus, A. and Höltje, J.V. (1996) *Microb. Drug Resist.*, **2**, 155–157.
81. Erickson, H.P., Anderson, D.E. and Osawa, M. (2010) *Microbiol. Mol. Biol. Rev.*, **74**, 504–528.
82. Aarsman, M.E.G., Piette, A., Fraipont, C., *et al.* (2005) *Mol. Microbiol.*, **55**, 1631–1645.
83. Potluri, L.P., Kannan, S. and Young, K.D. (2012) *J. Bacteriol.*, **194**, 5334–5342.
84. Broughton, C.E., Roper, D.I., van den Berg, H.A. and Rodger, A. (2015) *Sci. Prog.*, **98**, 313–345.
85. Flynn, J.M., Neher, S.B., Kim, Y.I., *et al.* (2003) *Mol. Cell*, **11**, 671–683.
86. Hanson, P.I. and Whiteheart, S.W. (2005) *Nat. Rev. Mol. Cell Biol.*, **6**, 519–529.
87. Camberg, J.L., Hoskins, J.R. and Wickner, S. (2009) *Proc. Natl. Acad. Sci. U. S. A.*, **106**, 10614–10619.
88. Camberg, J.L., Viola, M.G., Rea, L., *et al.* (2014) *PLoS One* **9**, e94964.
89. Sugimoto, S., Yamanaka, K., Nishikori, S., *et al.* (2010) *J. Biol. Chem.*, **285**, 6648–6657.
90. Camberg, J.L., Hoskins, J.R. and Wickner, S. (2011) *J. Bacteriol.*, **193**, 1911–1918.
91. Durand-Heredia, J., Rivkin, E., Fan, G., *et al.* (2012) *J. Bacteriol.*, **194**, 3189–3198.
92. Gueiros-Filho, F.J. and Losick, R. (2002) *Genes Dev.*, **16**, 2544–2556.
93. Mohammadi, T., Ploeger, G.E.J., Verheul, J., *et al.* (2009) *Biochemistry,* **48**, 11056–11066.
94. Galli, E. and Gerdes, K. (2012) *J. Bacteriol.*, **194**, 292–302.
95. Small, E., Marrington, R., Rodger, A., *et al.* (2007) *J. Mol. Biol.*, **369**, 210–221.
96. Low, H.H., Moncrieffe, M.C. and Löwe, J. (2004) *J. Mol. Biol.*, **341**, 839–852.
97. Pacheco-Gómez, R., Cheng, X., Hicks, M., *et al.* (2013) *Biochem. J.*, **449**, 795–802.
98. Ebersbach, G., Galli, E., Møller-Jensen, J., *et al.* (2008) *Mol. Microbiol.*, **68**, 720–735.
99. Buss, J., Coltharp, C., Shtengel, G., *et al.* (2015) *PLOS Genet.*, **11**, e1005128.
100. Espéli, O., Borne, R., Dupaigne, P., *et al.* (2012) *EMBO J.*, **31**, 3198–3211.
101. Hale, C., Shiomi, D., Liu, B., *et al.* (2011) *J. Bacteriol.*, **193**, 1393–1404.
102. Durand-Heredia, J.M., Yu, H.H., De Carlo, S., *et al.* (2011) *J. Bacteriol.*, **193**, 1405–1413.
103. Marteyn, B.S., Karimova, G., Fenton, A.K., *et al.* (2014) *MBio* **5**, e00022–14.
104. Schmidt, K.L., Peterson, N.D., Kustusch, R.J., *et al.* (2004) *J. Bacteriol.*, **186**, 785–793.
105. Corbin, B.D., Wang, Y., Beuria, T.K. and Margolin, W. (2007) *J. Bacteriol.*, **189**, 3026–3035.
106. De Leeuw, E., Graham, B., Phillips, G.J., *et al.* (1999) *Mol. Microbiol.*, **31**, 983–993.
107. Karimova, G., Dautin, N. and Ladant, D. (2005) *J. Bacteriol.*, **187**, 2233–2243.
108. Uehara, T., Parzych, K.R., Dinh, T. and Bernhardt, T.G. (2010) *EMBO J.*, **29**, 1412–1422.
109. Yang, D.C., Peters, N.T., Parzych, K.R., *et al.* (2011) *Proc. Natl. Acad. Sci.*, **108**, E1052–E1060.
110. Aussel, L., Barre, F.X., Aroyo, M., *et al.* (2002) *Cell*, **108**, 195–205.

111. Pease, P.J., Levy, O., Cost, G.J., *et al.* (2005) *Science*, **307**, 586–590.
112. Yu, X.C., Tran, A.H., Sun, Q. and Margolin, W. (1998) *J. Bacteriol.*, **180**, 1296–1304.
113. Draper, G.C., McLennan, N., Begg, K., *et al.* (1998) *J. Bacteriol.*, **180**, 4621–4627.
114. Buddelmeijer, N. and Beckwith, J. (2004) *Mol. Microbiol.*, **52**, 1315–1327.
115. Tsang, M. and Bernhardt, T. (2015) *Mol. Microbiol.*, **95**, 925–944.
116. Fraipont, C., Alexeeva, S., Wolf, B., *et al.* (2011) *Microbiology*, **157**, 251–259.
117. Pastoret, S., Fraipont, C., den Blaauwen, T., *et al.* (2004) *J. Bacteriol.*, **186**, 8370–8379.
118. Bertsche, U., Kast, T., Wolf, B., *et al.* (2006) *Mol. Microbiol.*, **61**, 675–690.
119. Müller, P., Ewers, C., Bertsche, U., Anstett, M., *et al.* (2007) *J. Biol. Chem.*, **282**, 36394–36402.
120. Gerding, M.A., Liu, B., Bendezú, F.O., *et al.* (2009) *J. Bacteriol.*, **191**, 7383–7401.
121. Weiss, D. (2015) *Mol. Microbiol.*, **95**, 903–909.
122. Busiek, K.K., Eraso, J.M., Wang, Y. and Margolin, W. (2012) *J. Bacteriol.*, **194**, 1989–2000.
123. Dai, K., Xu, Y. and Lutkenhaus, J. (1993) *J. Bacteriol.*, **175**, 3790–3797.
124. Reddy, M. (2007) *J. Bacteriol.*, **189**, 98–108.
125. Pichoff, S., Du, S. and Lutkenhaus, J. (2015) *Mol. Microbiol.*, **95**, 971–987.
126. Busiek, K. and Margolin, W. (2014) *Mol. Microbiol.*, **92**, 1212–1226.
127. Uehara, T., Dinh, T. and Bernhardt, T.G. (2009) *J. Bacteriol.*, **191**, 5094–5107.
128. Peters, N.T., Dinh, T. and Bernhardt, T.G. (2011) *J. Bacteriol.*, **193**, 4973–4983.
129. Pichoff, S., Shen, B., Sullivan, B. and Lutkenhaus, J. (2012) *Mol. Microbiol.*, **83**, 151–167.
130. Huisman, O., D'Ari, R. and Gottesman, S. (1984) *Proc. Natl. Acad. Sci. U. S. A.*, **81**, 4490–4494.
131. Dajkovic, A., Mukherjee, A. and Lutkenhaus, J. (2008) *J. Bacteriol.*, **190**, 2513–2526.
132. Chen, Y., Milam, S.L. and Erickson, H.P. (2012) *Biochemistry,* **51**, 3100–3109.
133. Mukherjee, A., Cao, C. and Lutkenhaus, J. (1998) *Proc. Natl. Acad. Sci. U. S. A.*, **95**, 2885–2890.
134. Janion, C. (2008) *Int. J. Biol. Sci.*, **4**, 338–344.
135. Bi, E. and Lutkenhaus, J. (1993) *J. Bacteriol.*, **175**, 1118–1125.
136. Mizusawa, S. and Gottesman, S. (1983) *Proc. Natl. Acad. Sci. U. S. A.*, **80**, 358–362.
137. Wu, L.J. and Errington, J. (2012) *Nat. Rev. Microbiol.*, **10**, 8–12.
138. Wu, L.J. and Errington, J. (2004) *Cell*, **117**, 915–925.
139. Bernhardt, T.G. and de Boer, P. (2005) *Mol. Cell*, **18**, 555–564.
140. Wu, L.J., Ishikawa, S., Kawai, Y., *et al.* (2009) *EMBO J.*, **28**, 1940–1952.
141. Tonthat, N.K., Arold, S.T., Pickering, B.F., *et al.* (2011) *EMBO J.*, **30**, 154–164.
142. Du, S. and Lutkenhaus, J. (2014) *PLoS Genet.*, **10**, e1004460.
143. Mercier, R., Petit, M., Schbath, S., *et al.* (2008) *Cell*, **135**, 475–485.
144. Bailey, M., Bisicchia, P., Warren, B., *et al.* (2014) *PLOS Genet.*, **10**, e1004504.
145. Dow, C.E., Rodger, A., Roper, D.I. and van den Berg, H.A. (2013) *Integr. Biol. (Camb).,* **5**, 778–95.
146. Dow, C.E., van den Berg, H.A., Roper, D.I. and Rodger, A. (2015) *Biochemistry,* **54**, 3803–3813.
147. Schaffner-Barbero, C., Martín-Fontecha, M., Chacón, P. and Andreu, J.M. (2012) *ACS Chem. Biol.*, **7**, 269–277.
148. Anderson, D.E., Kim, M.B., Moore, J.T., *et al.* (2012) *ACS Chem. Biol.*, **7**, 1918–1928.
149. Läppchen, T., Hartog, A.F., Pinas, V.A., *et al.* (2005) *Biochemistry,* **44**, 7879–7884.
150. Läppchen, T., Pinas, V.A., Hartog, A.F., *et al.* (2008) *Chem. Biol.*, **15**, 189–199.
151. Läppchen, T. (2007) Synthesis of GTP analogues and evaluation of their effect on the antibiotic target FtsZ and its eukaryotic homologue tubulin, University of Amsterdam.
152. Cordell, S.C., Robinson, E.J.H. and Lowe, J. (2003) *Proc. Natl. Acad. Sci. U. S. A.*, **100**, 7889–7894.
153. Sorto, N.A., Painter, P.P., Fettinger, J.C., *et al.* (2013) *Org. Lett.*, **15**, 2700–2703.
154. Ohashi, Y., Chijiiwa, Y., Suzuki, K., *et al.* (1999) *J. Bacteriol.*, **181**, 1348–1351.
155. Haydon, D.J., Stokes, N.R., Ure, R., *et al.* (2008) *Science*, **321**, 1673–1675.
156. Tan, C.M., Therien, A.G., Lu, J., *et al.* (2012) *Sci. Transl. Med.*, **4**, 126ra35.
157. Andreu, J.M., Schaffner-Barbero, C., Huecas, S., *et al.* (2010) *J. Biol. Chem.*, **285**, 14239–14246.
158. Elsen, N.L., Lu, J., Parthasarathy, G., *et al.* (2012) *J. Am. Chem. Soc.*, **134**, 12342–12345.

159. Matsui, T., Yamane, J., Mogi, N., *et al.* (2012) *Acta Crystallogr. Sect. D Biol. Crystallogr.*, **68**, 1175–1188.
160. Kaul, M., Mark, L., Zhang, Y., *et al.* (2013) *Antimicrob. Agents Chemother.*, **57**, 5860–5869.
161. Adams, D.W., Wu, L.J., Czaplewski, L.G. and Errington, J. (2011) *Mol. Microbiol.*, **80**, 68–84.
162. Stokes, N.R., Baker, N., Bennett, J.M., *et al.* (2013) *Antimicrob. Agents Chemother.*, **57**, 317–325.
163. Wang, J., Galgoci, A., Kodali, S., *et al.* (2003) *J. Biol. Chem.*, **278**, 44424–44428.
164. Park, Y., Grove, C., Gonzalez-Lopez, M., *et al.* (2011) *Angew. Chemie - Int. Ed.*, **50**, 3730–3733.
165. Rai, D., Singh, J.K., Roy, N. and Panda, D. (2008) *Biochem. J.*, **410**, 147–155.
166. Duggirala, S., Nankar, R.P., Rajendran, S. and Doble, M. (2014) *Appl. Biochem. Biotechnol.*, **174**, 283–296.
167. Domadia, P.N., Bhunia, A., Sivaraman, J., *et al.* (2008) *Biochemistry,* **47**, 3225–3234.
168. Beuria, T.K., Santra, M.K. and Panda, D. (2005) *Biochemistry,* **44**, 16584–16593.
169. Domadia, P., Swarup, S., Bhunia, A., *et al.* (2007) *Biochem. Pharmacol.*, **74**, 831–840.
170. Margalit, D.N., Romberg, L., Mets, R.B., *et al.* (2004) *Proc. Natl. Acad. Sci. U. S. A.*, **101**, 11821–11826.
171. Ruiz-Avila, L.B., Huecas, S., Artola, M., *et al.* (2013) *ACS Chem. Biol.*, **8**, 2072–2083.
172. Singh, P., Jindal, B., Surolia, A. and Panda, D. (2012) *Biochemistry,* **51**, 5434–5442.
173. Tsao, D., Sutherland, A.G., Jennings, L., *et al.* (2006) *Bioorganic Med. Chem.*, **14**, 7953–7961.
174. Kenny, C., Ding, W., Kelleher, K., *et al.* (2003) *Anal. Biochem.*, **323**, 224–233.
175. Sutherland, A.G., Alvarez, J., Ding, W., *et al.* (2003) *Org. Biomol. Chem.*, **1**, 4138–4140.

C.2 Direct detection and measurement of wall shear stress using a filamentous bio-nanoparticle

Nano Research 2015, 8(10): 3307–3315
DOI 10.1007/s12274-015-0831-x
Research Article
ISSN 1998-0124
CN 11-5974/O4

Direct detection and measurement of wall shear stress using a filamentous bio-nanoparticle

Daniela P. Lobo[1], Alan M. Wemyss[1,2], David J. Smith[3], Anne Straube[4], Kai B. Betteridge[5], Andrew H. J. Salmon[5], Rebecca R. Foster[6], Hesham E. Elhegni[6], Simon C. Satchell[6], Haydn A. Little[7], Raúl Pacheco-Gómez[8], Mark J. Simmons[9], Matthew R. Hicks[8], David O. Bates[10], Alison Rodger[1] (✉), Timothy R. Dafforn[8], and Kenton P. Arkill[11]

[1] *Department of Chemistry and Warwick Analytical Science Centre, University of Warwick, Coventry CV4 7AL, UK*
[2] *MOAC Doctoral Training Centre, University of Warwick, Coventry CV4 7AL, UK*
[3] *Mathematics, University of Birmingham, Edgbaston, Birmingham, West Midlands B15 2TT, UK*
[4] *Centre for Mechanochemical Cell Biology, Warwick Medical School, University of Warwick, Coventry CV4 7AL, UK*
[5] *Physiology and Pharmacology, University of Bristol, University Walk, Bristol BS8 1TD, UK*
[6] *Clinical Sciences, Whitson Street, University of Bristol, Bristol BS1 3NY, UK*
[7] *School of Chemistry, University of Birmingham, Edgbaston, Birmingham, West Midlands B15 2TT, UK*
[8] *Biosciences, University of Birmingham, Edgbaston, Birmingham, West Midlands B15 2TT, UK*
[9] *Chemical Engineering, University of Birmingham, Edgbaston, Birmingham, West Midlands B15 2TT, UK*
[10] *School of Medicine, University of Nottingham, Queen's Medical Centre, Nottingham NG2 7UH, UK*
[11] *Biochemistry, University of Bristol, University Walk, Bristol BS8 1TD, UK*

Received: 19 February 2015
Revised: 4 June 2015
Accepted: 8 June 2015

KEYWORDS
microfluidics,
nanoparticle,
M13 bacteriophage,
wall shear stress,
fluorescent microscopy

ABSTRACT

The wall shear stress (WSS) that a moving fluid exerts on a surface affects many processes including those relating to vascular function. WSS plays an important role in normal physiology (e.g. angiogenesis) and affects the microvasculature's primary function of molecular transport. Points of fluctuating WSS show abnormalities in a number of diseases; however, there is no established technique for measuring WSS directly in physiological systems. All current methods rely on estimates obtained from measured velocity gradients in bulk flow data. In this work, we report a nanosensor that can directly measure WSS in microfluidic chambers with sub-micron spatial resolution by using a specific type of virus, the bacteriophage M13, which has been fluorescently labeled and anchored to a surface. It is demonstrated that the nanosensor can be calibrated and adapted for biological tissue, revealing WSS in micro-domains of cells that cannot be calculated accurately from bulk flow measurements. This method lends itself to a platform applicable to many applications in biology and microfluidics.

Address correspondence to a.rodger@warwick.ac.uk

1 Introduction

The interaction between flowing liquids and solid surfaces, such as blood and endothelial cells, affects the function of both the surface and liquid. The force per unit area that a moving fluid exerts parallel to a surface or wall is known as the wall shear stress (WSS). This parameter affects cellular and biochemical reactions and is therefore important for a range of fields, including microfluidic system design [1], and in understanding disease states of the vascular system [2]. WSS plays an important role in normal physiology and affects the microvasculature's primary function of molecular transport [3–7]. Points of fluctuating WSS show abnormalities in diseases such as atherosclerosis, diabetes, and cancer. Measuring WSS directly is currently possible only on a relatively large scale by techniques such as microelectromechanical sensors [8] and quasi-direct methods such as deformable micropillars (a micropillar device is ~100 μm tall) [9, 10]. There is no established technique for measuring WSS directly in physiological systems. All methods rely on the estimation of WSS by using velocity gradients measured close to the wall, the fluid rheology, and the assumption of a boundary condition at the surface (e.g. the Dirichlet no-slip condition). Such methods are unreliable when applied to the circulatory system, which exhibits pulsatile three-dimensional flow containing fluid particulates and has elastic walls of varying geometries. Thus, development of new methods to measure WSS is important.

In the vasculature, the velocity gradient at the wall is currently measured by bulk flow techniques such as micro-particle image velocimetry (μPIV) [11] to calculate the velocity gradient at the wall by making assumptions including uniformity of flow and the surface. Such an average measurement may hide variability critical to the understanding of disease states in complex, dynamic, and variable systems such as a blood vessel. μPIV methods struggle with the complex nature of blood and are limited by the particle size used (as well as viable flow ranges). Furthermore, interpreting experimental data is dependent on the computational models (and associated assumptions) used to determine WSS in medicine [12].

Any fluid moving along a solid boundary induces a shear stress on that boundary. For a Newtonian fluid in laminar flow, such as blood plasma, the WSS is

$$\mathrm{WSS} = \eta \left.\frac{\partial V}{\partial y}\right|_0 \quad (1)$$

where η is the dynamic viscosity of the fluid, V is its velocity, and y is the height above the boundary. The horizontal axis refers to WSS as calculated from a model of laminar flow in a smooth rectangular channel (numerical values taken from manufacturer's data). This quantity is a "nominal" value because it does not correct for local variations such as roughness over the surfaces of cells.

Reported here is a strategy for measuring WSS by using labeled M13 bacteriophage (M13) as a microfluidic reporter. Previous work has reported its use as a scaffold for nanowires [13–15] and fibres [16, 17], as a biosensor [18], in drug delivery [19], as a cancer marker [20], and in the detection of biological molecules [18]. M13 is a long (~900 nm) and thin (~7 nm) semi-rigid construct whose persistence length is ~1,400 nm [21]. The alignment in flow and spectroscopy of this filamentous particle has recently been exploited in our previous work for a variety of diagnostic assays [22]. We have generated chemical modification protocols to label M13 with fluorophores that provide a suite of signals detectable by using linear dichroism (a differential polarized light spectroscopy technique). A number of methods have been developed to modify chemically the surface of the M13, adding an extensive list of moieties to the surface of the virus.

The M13 naturally possesses different chemical groups at each end [23]. Therefore, it is theoretically possible to chemically tether one end to a surface and visualize it under various shear conditions as a nanotuft (Fig. 1). In this work, we report our observations of the behavior of M13 in fluid flow together with the chemical modification protocols developed in our laboratory [22] to produce a system that can be used to study flow at surfaces. It results in a simple, novel, scalable, synthetic biology method for measuring WSS on a sub-micron scale by using fluorescent microscopy. The nanosensor is an M13 with a specific binding agent (e.g. an antigen-specific antibody) attached to

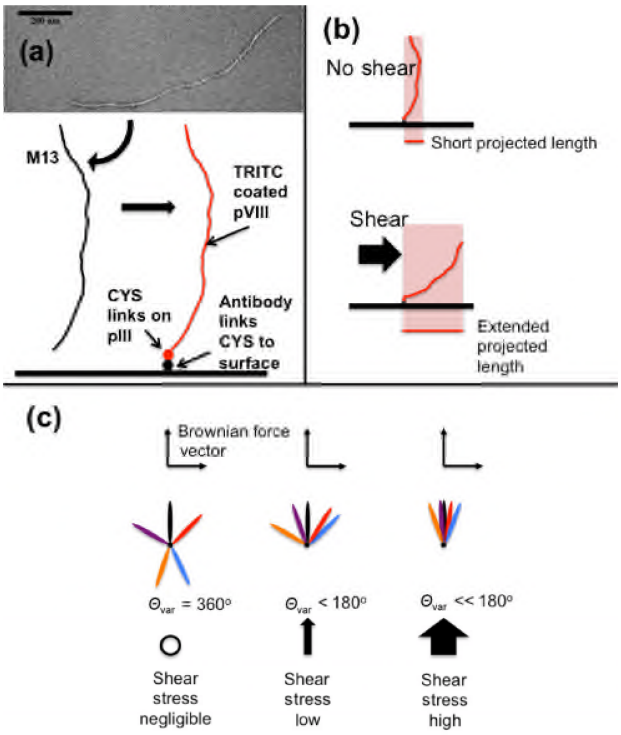

Figure 1 Principles and design of bacteriophage construct. (a) Transmission electron micrograph of M13 with uranyl acetate stain. A schematic of the M13 followed by our process of using cysteines (CYS) on the pIII proteins to bind a molecule designed to affix the M13 to a target surface. pVIII proteins are covalently labeled with a fluorescent isothiocyanate derivative TRITC for fluorescent imaging. (b) A possible method of detection by length. (c) A possible method of detection by variation in angle.

one end via pIII proteins and fluorophores attached to the pVIII proteins (Fig. 1). The appropriate antigen was attached to the surface of the flow cell and its behavior visualized in flow. Subsequent data analysis allowed us to determine the WSS for both the collagen and cultured endothelial cells affixed to coated plastic slides. The result is a nanosensor that is potentially usable *in vivo*.

2 Experimental

Wheat germ agglutinin (WGA) was obtained from Sigma-Aldrich, Poole, UK and the anti-collagen antibody from Abcam, Cambridge, UK. Other chemicals were obtained from the suppliers given in the Electronic Supplementary Material (ESM) and used as received unless stated otherwise. M13 were grown, purified, and fluorescently labeled as described in detail elsewhere [22] and outlined in the ESM. M13 was derivatized with the protein anchor attached to the pIII protein as described in the ESM. The structure of the nanosensor construct is schematically illustrated in Fig. 1(a). Collagen IV-coated microchannel plates (μ-Slide $I^{0.8}$ Luer, ibidi, Munich) were assembled into a controlled flow system by using a pump (ibidi, Munich). We have previously shown that ibidi systems are able to orient semi-rigid molecular systems [24]. Human conditionally immortalized glomerular endothelial cells (GEnCs) [25] were grown as described in the ESM. The completed M13 construct was bound to the flow slide coating (collagen IV or endothelial cells) and any unbound M13 was rinsed off.

A nominal WSS (0–3.5 dyn·cm^{-2}) was applied. See ESM and the ibidi website for further details. The fluorescent images of the derivatized and labeled M13 construct in flow were measured by using either a spinning disk confocal microscope (Ultraview spinning disk confocal microscope with a 1.4 NA, 100× oil immersion objective, 561 nm laser, tetramethylrhodamine-5-(and-6)-isothiocyanate (TRITC) filter sets (Croma), and an ORCA R^2 camera (Hamamatsu) under control of Volocity 6.3, Perkin-Elmer) at 10 frames per second or a Nikon Ti Eclipse inverted microscope through a 60× oil immersion objective 1.4 (Nikon Plan Apo VC 60× Oil DIC N2).

Recorded time-lapse images of collagen-coated slides were post-analyzed by using a bespoke function in MATLAB 2014b (MATLAB R2014b, The MathWorks Inc., Natick, MA). Videos and more details are available in the ESM.

From our analysis, we determined the orientation angle and approximate length and width of the M13 nanosensor in each frame. Using MATLAB, the region that the M13 occupies on each frame was first defined by finding a threshold pixel intensity below which all pixels were set to zero and above which they were set to one (Otsu method [26]). The pixels with value one whose nearest neighbor also had value one were then defined as regions of interest (ROI). The largest of these was assumed to be the M13. An image stack with the largest ROI subtracted out was created to be the background and was subtracted from the original binary image, leaving only a M13 nanosensor

in each image. To smooth the edges of this ROI and fill any pixels of zero intensity in its interior – both of which would affect subsequent analysis – a convex polygon was fitted to the ROI. The major axis was then defined as the longest possible straight line that could be drawn within the ROI, and its angle, determined relative to the horizontal axis of the image, defined the bacteriophage's orientation. The directionality plugin in Fiji/ImageJ [27] gave comparable results.

The tethered nanoparticle motion under Brownian effects and flow was modeled phenomenologically by a random walk with spatially homogeneous jump probability, but a spatially-varying difference in the probability of left or right jumps, modeling the biasing effect of the viscous restoring force as described in the ESM.

3 Results and discussion

3.1 Production and microscopy of labeled and derivatized nanosensors

Two systems were developed using a novel M13 nanosensor to determine WSS.

(i) Fluorescent M13 constructs derivatized with anti-collagen IV antibodies (M13-aCol-TRITC) attached to a collagen IV-coated microchannel plate substrate. The collagen IV was designed to act as a relatively flat surface to test the principles of the nanosensor.

(ii) Fluorescent M13 constructs derivatized with WGA (M13-WGA-TRITC) attached to cultured endothelial cells (GEnCs) via the glycocalyx (WGA binds to sialic acid residues on the surface of glycoproteins that form the glycocalyx on most endothelial cells). The endothelial cells were designed to act as a model blood vessel.

3.2 Detection of WSS on collagen coated slides

Spinning disc images of M13-aCol-TRITC exposed to a range of nominal WSS (0–3.5 dyn·cm^{-2}) were collected. The data from these experiments take the form of time-lapse images of individual M13-aCol-TRITC constructs on the surface. The constructs could be recognized under the microscope as bright points, agitating in the buffer. Once under high digital magnification, the M13-aCol-TRITC constructs appear as elliptical shapes, owing to the diffraction limit of light, that adopt different angles as a function of time (Fig. 2(a)). Fourteen independent M13-aCol-TRITC data sets were collected at each flow condition. Once an M13-aCol-TRITC construct was in focus, the flow was induced to test if the construct was bound. Images of the flow slide with no shear flow applied suggested that the M13-aCol-TRITC construct is on the surface and oriented in a random fashion (in response to Brownian motion, Fig. 2(c)). The reaction to flow-induced shear is obvious by eye: The fluorescent ellipse orients, seemingly instantaneously, with its long axis preferentially aligned with the shear flow direction. The degree of orientation increases with flow rate. The microscope focus typically required adjustment to achieve optimal imaging. The signal to noise decreased over time as would be expected if bleaching was occurring; however, more than 10 min of continuous imaging was possible with both the spinning disk confocal and wide-field microscopes. An example of a M13-aCol-TRITC video (Movie S1) is available in the ESM.

3.3 Measurement of WSS on GEnCs

GEnCs, normally used as a model capillary system for kidney disease, were seeded onto sterile, collagen-coated flow slides. These kidney-derived cells provide an intellectual bridge to future work on how complications of diabetes (e.g. nephropathy) affects flow in kidneys. WGA conjugated to the pIII protein of M13 (M13-WGA-TRITC) made a body that was visualized by using a wide-field fluorescent microscope showing that the bacteriophage had successfully adhered to cells on the flow slide surface (Fig. 2(b)) and had formed a confluent layer.

Time-lapse images show that in the absence of flow the conjugates move fairly randomly in response to Brownian motion in a manner consistent with attachment to the cellular surface at only one end. The angle space it explores is reduced compared with the collagen-only slides (Figs. 2(c) and 2(d)) and the mean angles in both negative and positive flow directions are non-zero, in contrast to the collagen surfaces. This suggests the bacteriophage is located

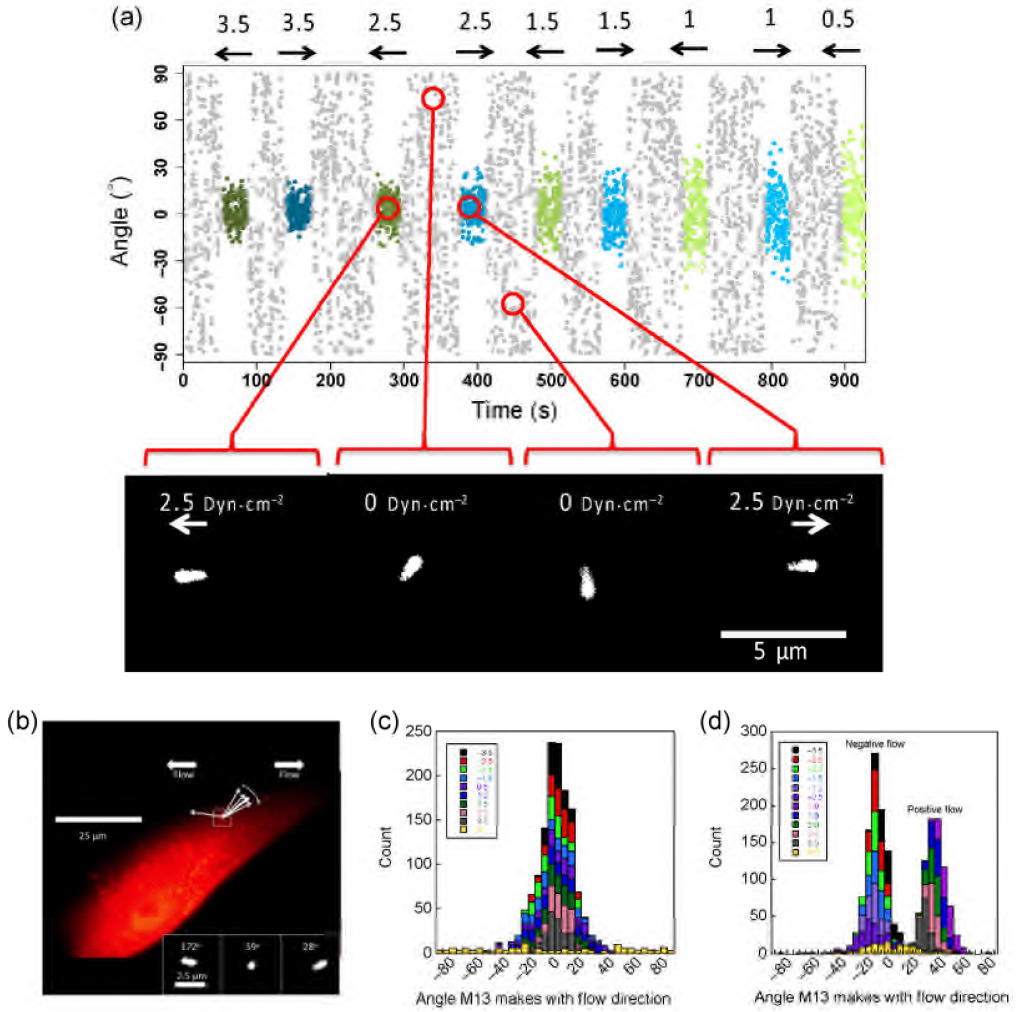

Figure 2 (a) Example of wall shear stress visualized by M13-aCol-TRITC bound to a collagen IV coated flow slide. M13 orientation vs. time in a typical experiment. The nominal wall shear stress (assuming a linear relationship between bulk fluid flow and WSS) is indicated at the top in dyn·cm^{-2}. The flow direction and magnitude at each time point are indicated by the arrows and by the color and intensities of the overlays (negative (blue), positive (green), and zero (grey)). Example images at time points corresponding to the red circles in background subtracted spinning disk confocal image frames are shown below. (b) Wall shear stress effect on a M13-WGA-TRITC bound to the surface of a cultured GEnC demonstrated by inset snapshots of three flows, giving the indicated nominal wall shear stress and the average orientation. Additive histograms for angles made by a bound M13 with (c) a collagen-only coated slide and (d) a surface layered with GEnCs.

on the side of a cell, near the top, with the cell surface forcing minimum angles of approximately –10° for negative flow and +30° for positive flow.

3.4 Quantitation of response of M13-aCol-TRITC construct to flow and WSS

To use the above data to quantify WSS, a robust data analysis methodology was required. This has two parts.

3.4.1 Turning the videos into orientation data of the type summarized in Fig. 2(a)

MATLAB code was written to extract the bacteriophage orientation and major axis length data. Its angle relative to the horizontal axis of the image defined the bacteriophage's orientation as summarized in Figs. 2(a) and 2(c). The MATLAB segmentation code was found to be accurate by eye and gave similar results to the ImageJ directionality plugin. A video comparison is

shown in Movie S2 (in the ESM). Both methods gave erratic readings when there was poor focus or other poor signal-to-noise-ratio situations. Moreover, if the M13 appeared round (due to pointing straight up) the angles derived were erratic by both methods.

3.4.2 Development of a theoretical model of how the bacteriophage orientation relates to the flow

Both the apparent mean length of the bacteriophage and the variation of its orientation in flow will depend on the shear stress it experiences. If a theoretical model is to be of any use, it must be consistent with the experimental data. The maximum mean length in most examples was ~1.3 μm, which is consistent with the expected M13 length plus the expected Airy disk, indicating the M13 is almost parallel to the surface at maximum flow and the measured length decreased with flow velocity. There was a correlation between length and nominal WSS; however, as there are only a few pixels between maximum and minimum lengths the resolution was too low for WSS measurement. Fortunately, the variation in angle showed more resolution.

A simple two-dimensional random walk model predicts a normal distribution of angle about a mean direction with the logarithm of the standard deviation of the angle (σ) being linearly related to the logarithm of the WSS, with a slope of 0.5 (see ESM)

$$\ln(\sigma) = -0.5\ln(\mathrm{WSS}) - 1.5\ln(L) + k \quad (2)$$

where L is the particle length and k is a constant. The data in Figs. 3(a) (Run A) and 3(b) (collagen combined

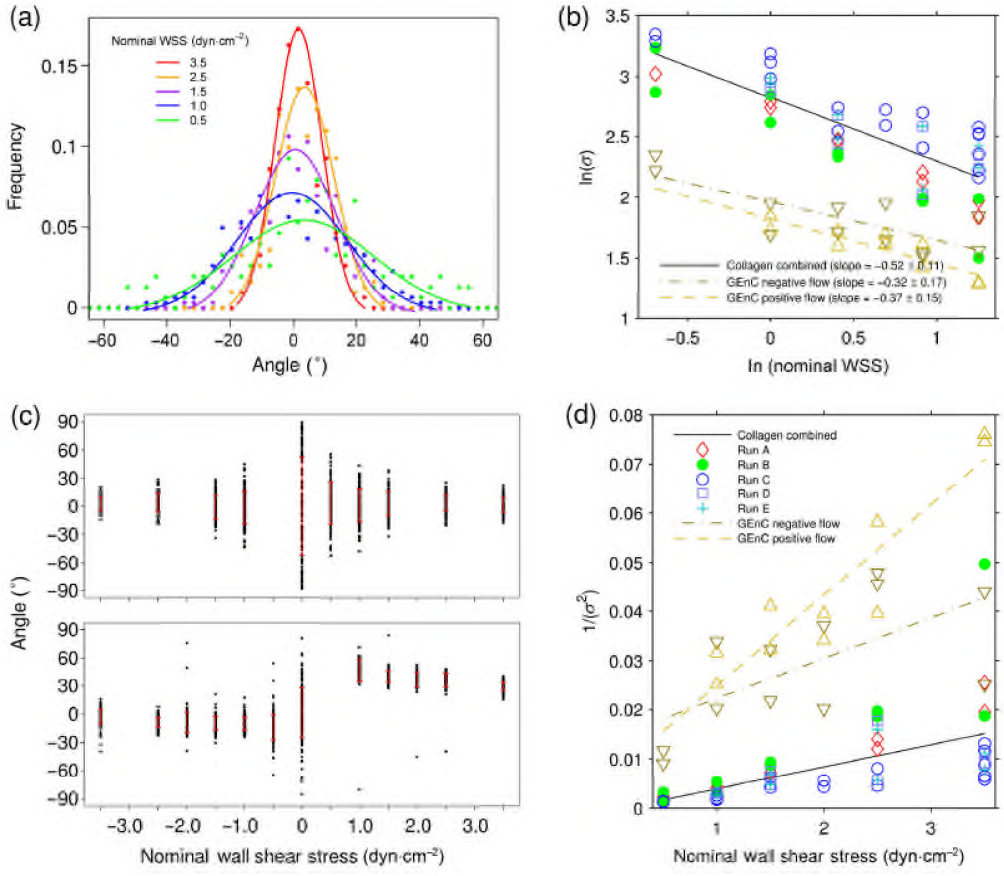

Figure 3 (a) The normalized frequency distribution of angles for an M13 bacteriophage anchored to a collagen coated slide with a Gaussian fit to the original data points (Run A in (b)) as a function of nominal-flow-induced-WSS in dyn·cm^{-2}. (b) ln(σ) vs. ln(nominal WSS) for 5 measured M13-aCol-TRITC movies and one GEnC movie all involving both positive and negative direction flows, for σ the standard deviation of the angle at each flow rate. (c) Orientation vs. nominal WSS for an M13 anchored to collagen (top) and GEnC coated slides (bottom), negative flow (left), positive flow (right). σ is denoted by the bold red bar for each flow. (d) Plots of inverse variance vs. nominal WSS for the data plotted in (b). Quoted errors on the slopes are 95% confidence intervals of the fit to a straight line.

data) for 5 independent runs of an M13 bacteriophage anchored onto a collagen-coated flat slide were in accord with such a model, where WSS on the horizontal axis was a nominal value calculated from bulk flow rates (see ESM). The GEnC data (Fig. 3(a)) were also consistent with the model within the larger experimental error of these experiments. Better statistics, either from a higher frame rate, longer runs, or more bacteriophage would be desirable.

The scatter plots of Fig. 3(c) show clearly the different behavior of the flat collagen coated slides and the two opposite flow directions of the GEnC coated slides: The flow direction has no significant effect on the average M13-aCol-TRITC angle or the standard deviation of its observed angles for the collagen coated slides but has a significant effect on both the average angle and standard deviation of angles of the GEnC slides. The reduced angle space of the GEnC data sets (Fig. 2(d)) may suggest some degree of non-specific interaction of M13 with the cell surface. However, the space sampled in zero flow is still bigger than at the lowest flow rates, so these interactions will not significantly affect the analysis.

Although the x-intercepts of the ln/ln plots of Fig. 3(b) contain the information to determine the true WSS from ln(σ) and ln(nominal WSS), the error in the intercept is large. So instead Eq. (3) was plotted.

$$\frac{1}{\sigma^2} \propto \text{nominal WSS} \tag{3}$$

Nominal WSS is the value of the WSS if the bulk flow is a correct predictor of the flow at the surface. We expect this to be accurate for the collagen experiments. By way of contrast, even though the slopes of the two GEnC lines in Fig. 3(d) have a large error, they are clearly larger than those of the collagen-coated slides, indicating that the bulk-flow-determined nominal WSS is not a good estimate of WSS at the cell surface. The slopes of Fig. 3(d) suggest that the negative flow direction has WSS of more than twice the nominal value and the positive direction over three times the nominal value.

The μ-slide is approximately 80× deeper than the cell so the enhanced WSS of the GEnC experiments is unlikely to be from channel narrowing. Various other factors presumably contribute to the observation, including roughness of the surface, local viscosity effects, and the shape of the protrusion into the μ-slide. Barbee et al. [28] measured the height of endothelial cells above a surface by using atomic force microscopy and approximated the shear stress due to flow across the surface through a simplified computational fluid dynamics approach: Their result suggests approximately 50% enhancement of WSS due to the shape protrusion of the cells. Pozrikidis [29] mathematically modeled flow over protuberances on a plane wall: For an elongated hemispheroid with an aspect ratio of 0.2 (similar to the [28] cells) WSS was calculated to increase by 1.5×; for an aspect ratio of 0.5 this factor increased to 2.5×. Thus, much of the increase in WSS with our GEnC experiments is due to the shape of the cells compared with the flat collagen slides; however, other factors are also involved and show the importance of being able to measure WSS locally.

4 Conclusions

WSS is usually calculated by using flow velocity gradients measured close to the wall with boundaries and Newtonian assumptions that are often approximations. Here, we have shown that by anchoring one end of a fluorescent M13 bacteriophage onto a surface, the free body of the nanoreporter repositions itself in response to directional flow, resulting in a novel nanosensor that can be used to measure WSS with a 1 μm spatial resolution, which is 100× better than currently implemented methods.

We calibrated the approach with a model system to demonstrate that we could predict the relationship, by using a simple theoretical model, between particle flow behavior and WSS. We were then able to measure local WSS of the irregular surface of a cultured cell, proving the concept and showing that the normal predictions by bulk flow cannot be relied upon. The system is adaptable and can in principle be used in *in vivo* systems, as it requires only wide-field fluorescent microscopy. The technique and production methodology have been demonstrated on two types of surfaces: relatively flat collagen-coated slides, which compare well with bulk flow expectations, and an endothelial cell-coated surface, which show higher WSS than bulk flow values. Our data therefore suggest

that WSS operative in physiological systems is likely to deviate significantly from that expected on the basis of bulk flow estimates.

There are several key areas to develop, none of which we believe are insurmountable, before the technique can be used *in vitro* or *in vivo* to explore how differences in cell surfaces are affected by local flow effects. The physical properties of the nanofibre–cell binding, in particular its compliance, may affect the precise details of the response to shear. However, provided that the fibre is able to undergo relatively free rotation as exhibited in the present data, the balance between Brownian rotation and shear flow deflection will provide a sensitive and accurate indication of WSS once calibrated to the particular construct.

In summary, although further construct and data-quality developments are needed, this bacteriophage construct, with low manufacturing costs and high adaptability, suggests a way to map flow and WSS on a micron scale in biological systems, thus opening up a wide range of potential applications in fundamental research and diagnosis.

Acknowledgements

The technical expertise of Ian Hands-Portman at the Imaging Suite, of Life Sciences, University of Warwick, Coventry, CV4 7AL contributed significantly to this work. The funding from a variety of sources to support this work is gratefully acknowledged: Engineering and Physical Sciences Research Council (Impact Acceleration Account EP/K503873/1: M. J. S., K. P. A., T. R. D., M. R. H.); European Union FP7 Marie Curie Initial Training Network (Innovative Doctoral Programme: D. P. L., A. R.); The Science City Research Alliance (K. P. A.); Bizkaia Talent Fellowship (No. AYD-000-256); Engineering and Physical Sciences Research Council (MOAC Doctoral Training Centre, No. EP/F500378/1: A. W.); Medical Research Council (No. G0802829: A. H. J. S., K. B. B.); British Heart Foundation (No. FS/10/017/28249: R. R. F.; No. FS/13/42/30377: A. S.; No. PG/15/37/31438: K. P. A., D. O. B., T. R. D.) and the Libyan higher education ministry (No. 9139, H. E. E.).

Electronic Supplementary Material: Supplementary material (protocols, the basis of the theoretical analysis used, and time-lapses of the figures) is available in the online version of this article at http://dx.doi.org/10.1007/s12274-015-0831-x.

References

[1] Nge, P. N.; Rogers, C. I.; Woolley, A. T. Advances in microfluidic materials, functions, integration, and applications. *Chem. Rev.* **2013**, *113*, 2550–2583.

[2] Zarins, C. K.; Giddens, D. P.; Bharadvaj, B. K.; Sottiurai, V. S.; Mabon, R. F.; Glagov, S. Carotid bifurcation atherosclerosis. Quantitative correlation of plaque localization with flow velocity profiles and wall shear-stress. *Circ. Res.* **1983**, *53*, 502–514.

[3] Chatzizisis, Y. S.; Coskun, A. U.; Jonas, M.; Edelman, E. R.; Feldman, C. L.; Stone, P. H. Role of endothelial shear stress in the natural history of coronary atherosclerosis and vascular remodeling: Molecular, cellular, and vascular behavior. *J. Am. Coll. Cardiol.* **2007**, *49*, 2379–2393.

[4] Katritsis, D.; Kaiktsis, L.; Chaniotis, A.; Pantos, J.; Efstathopoulos, E. P.; Marmarelis, V. Wall shear stress: Theoretical considerations and methods of measurement. *Prog. Cardiovasc. Dis.* **2007**, *49*, 307–329.

[5] Reneman, R. S.; Hoeks, A. P. G. Wall shear stress as measured *in vivo*: Consequences for the design of the arterial system. *Med. Biol. Eng. Comput.* **2008**, *46*, 499–507.

[6] Reneman, R. S.; Arts, T.; Hoeks, A. P. G. Wall shear stress-an important determinant of endothelial cell function and structure-in the arterial system *in vivo*. *J. Vasc. Res.* **2006**, *43*, 251–269.

[7] Young, E. W. K.; Beebe, D. J. Fundamentals of microfluidic cell culture in controlled microenvironments. *Chem. Soc. Rev.* **2010**, *39*, 1036–1048.

[8] Naughton, J. W.; Sheplak, M. Modern developments in shear-stress measurement. *Prog. Aerosp. Sci.* **2002**, *38*, 515–570.

[9] Große, S.; Schröder, W. Mean wall-shear stress measurements using the micro-pillar shear-stress sensor MPS3. *Meas. Sci. Technol.* **2008**, *19*, 015403.

[10] Brücker, C.; Spatz, J.; Schröder, W. Feasability study of wall shear stress imaging using microstructured surfaces with flexible micropillars. *Exp. Fluids.* **2005**, *39*, 464–474.

[11] Smith, M. L.; Long, D. S.; Damiano, E. R.; Ley, K. Near-wall μ-PIV reveals a hydrodynamically relevant endothelial surface layer in venules *in vivo*. *Biophys. J.* **2003**, *85*, 637–645.

[12] Samady, H.; Eshtehardi, P.; McDaniel, M. C.; Suo, J.; Dhawan, S. S.; Maynard, C.; Timmins, L. H.; Quyyumi, A. A.; Giddens, D. P. Coronary artery wall shear stress is associated with

progression and transformation of atherosclerotic plaque and arterial remodeling in patients with coronary artery disease. *Circulation* **2011**, *124*, 779–788.

[13] Mao, C. B.; Solis, D. J.; Reiss, B. D.; Kottmann, S. T.; Sweeney, R. Y.; Hayhurst, A.; Georgiou, G.; Iverson, B.; Belcher, A. M. Virus-based toolkit for the directed synthesis of magnetic and semiconducting nanowires. *Science* **2013**, *303*, 213–217.

[14] Murugesan, M.; Abbineni, G.; Nimmo, S. L.; Cao, B. R.; Mao, C. B. Virus-based photo-responsive nanowires formed by linking site-directed mutagenesis and chemical reaction. *Sci. Rep.* **2013**, *3*, 1820.

[15] Nam, K. T.; Kim, D. W.; Yoo, P. J.; Chiang, C. Y.; Meethong, N.; Hammond, P. T.; Chiang, Y. M.; Belcher, A. M. Virus-enabled synthesis and assembly of nanowires for lithium ion battery electrodes. *Science* **2006**, *312*, 885–888.

[16] Chiang, C. Y.; Mello, C. M.; Gu, J.; Silva, E. C. C. M.; Van Vliet, K. J.; Belcher, A. M. Weaving genetically engineered functionality into mechanically robust virus fibers. *Adv. Mater.* **2007**, *19*, 826–832.

[17] Niu, Z. W.; Bruckman, M. A.; Harp, B.; Mello, C. M.; Wang, Q. Bacteriophage M13 as a scaffold for preparing conductive polymeric composite fibers. *Nano Res.* **2008**, *1*, 235–241.

[18] Domaille, D. W.; Lee, J. H.; Cha, J. N. High density DNA loading on the M13 bacteriophage provides access to colorimetric and fluorescent protein microarray biosensors. *Chem. Commun.* **2013**, *49*, 1759–1761.

[19] Suthiwangcharoen, N.; Li, T.; Li, K.; Thompson, P.; You, S. J.; Wang, Q. M13 bacteriophage-polymer nanoassemblies as drug delivery vehicles. *Nano Res.* **2011**, *4*, 483–493.

[20] Carrico, Z. M.; Farkas, M. E.; Zhou, Y.; Hsiao, S. H.; Marks, J. D.; Chokhawala, H.; Clark, D. S.; Francis, M. B. N-terminal labelling of filamentous phage to create cancer marker imaging agents. *ACS Nano* **2012**, *6*, 6675–6680.

[21] Khalil, A. S.; Ferrer, J. M.; Brau, R. R.; Kottmann, S. T.; Noren, C. J.; Lang, M. J.; Belcher, A. M. Single M13 bacteriophage tethering and stretching. *Proc. Nat. Acad. Sci. USA* **2007**, *104*, 4892–4897.

[22] Pacheco-Gómez, R.; Kraemer, J.; Stokoe, S.; England, H. J.; Penn, C. W.; Stanley, E.; Rodger, A.; Ward, J.; Hicks, M. R.; Dafforn, T. R. Detection of pathogenic bacteria using a homogeneous immunoassay based on shear alignment of virus particles and linear dichroism. *Anal. Chem.* **2012**, *84*, 91–97.

[23] Sidhu, S. S. Engineering M13 for phage display. *Biomol. Eng.* **2001**, *18*, 57–63

[24] Cheng, X.; Joseph, M. B.; Covington, J. A.; Dafforn, T. R.; Hicks, M. R.; Rodger, A. Continuous-channel flow linear dichroism. *Anal. Methods* **2012**, *4*, 3169–3173.

[25] Satchell, S. C.; Tasman, C. H.; Singh, A.; Ni, L.; Geelen, J.; von Ruhland, C. J.; O'Hare, M. J.; Saleem, M. A.; van den Heuvel, L. P.; Mathieson, P. W. Conditionally immortalized human glomerular endothelial cells expressing fenestrations in response to VEGF. *Kidney Int.* **2006**, *69*, 1633–1640.

[26] Otsu, N. A threshold selection method from gray-level histogram. *IEEE Trans. Syst. Man Cybernetics.* **1979**, *9*, 62–66.

[27] Schindelin, J.; Arganda-Carreras, I.; Frise, E. Kaynig, V.; Longair, M.; Pietzsch, T.; Preibisch, S.; Rueden, C.; Saalfeld, S.; Schmid, B. et al. Fiji: An open-source platform for biological-image analysis. *Nat. Methods* **2012**, *9*, 676–682.

[28] Barbee, K. A.; Mundel, T.; Lal, R.; Davies, P. F. Subcellular distribution of shear stress at the surface of flow-aligned and nonaligned endothelial monolayers. *Am. J. Physiol.* **1995**, *268*, H1765–H1772.

[29] Pozrikidis, C. Shear flow over a protuberance on a plane wall. *J. Eng. Math.* **1997**, *31*, 29–42.

[30] Arkill, K. P.; Neal, C. R.; Mantell, J. M.; Michel, C. C.; Qvortrup, K.; Rostgaard, J.; Bates, D. O.; Knupp, C.; Squire, J. M. 3D reconstruction of the glycocalyx structure in mammalian capillaries using electron tomography. *Microcirculation* **2012**, *19*, 343–351.